COMPUTATIONAL MODELING OF OTOACOUSTIC EMISSIONS

A Dissertation

Presented to

The Academic Faculty

by

Thomas Bowling

In Partial Fulfillment

of the Requirements for the Degree

Doctor of Philosophy in the

George W. Woodruff School of Mechanical Engineering

Georgia Institute of Technology

December, 2019

COMPUTATIONAL MODELING OF OTOACOUSTIC EMISSIONS

Approved by:

Dr. Julien Meaud
Advisor, Committee Chair
School of Mechanical Engineering
Georgia Institute of Technology

Dr. Kenneth Cunefare
School of Mechanical Engineering
Georgia Institute of Technology

Dr. Michael Leamy
School of Mechanical Engineering
Georgia Institute of Technology

Dr. Karim Sabra
School of Mechanical Engineering
Georgia Institute of Technology

Dr. Wei Dong
Department of Otolaryngology & Head and Neck Surgery, School of Medicine
Loma Linda University

Date Approved: August 12, 2019

ACKNOWLEDGMENTS

First and foremost, I want to acknowledge my thesis advisor, Dr. Julien Meaud, for his continued guidance and support. Working for him has been a real pleasure and his mentorship made me a better researcher, engineer, and communicator.

I would also like to thank my thesis committee for their continued time: Dr. Ken Cunefare, Dr. Michael Leamy, Dr. Karim Sabra, and Dr. Wei Dong. A special thanks goes to Dr. Cunefare for his guidance. During this thesis work, it was all too easy to focus on small details and lose sight of the big picture; my meetings with him pushed me to re-evaluate how to present my work effectively. Additionally, I would like to thank Dr. Wei Dong for our discussions on distortion products and for experimental data she has provided.

Next, I would like to thank current and former members of the Meaud lab group: Charlsie Lemons, Kaikai Che, Haiqi Wen, Elisa Boatti, and Michael Rouleau. Working with such smart and kind people is one of the highlights of my graduate studies. Finally I would like to thank my family, especially my parents, for their constant support and encouragement over my many years of schooling.

Financial support for this research has been provided by Georgia Tech, the National Science Foundation, and the Department of Defense through the National Defense Science and Engineering Graduate Fellowship (NDSEG) Program.

TABLE OF CONTENTS

LIST OF TABLES

LIST OF FIGURES

NOMENCLATURE

BM	basilar membrane
BP	best place
CF	characteristic frequency
DOF	degree of freedom
DP	distortion product
DPOAE	distortion product otoacoustic emission
HB	hair bundle
iDP	intracochlear distortion product
MET	mechanoelectrical transduction
NIHL	noise-induced hearing loss
OAE	otoacoustic emission
OCT	optical coherence tomography
OHC	outer hair cell
RL	reticular lamina
RS	random seed
SFOAE	stimulus frequency otoacoustic emission
SM	scala media
SOAE	spontaneous otoacoustic emission
ST	scala tympani
SV	scala vestibuli
TEOAE	transient evoked otoacoustic emission
TM	tectorial membrane

SUMMARY

The mammalian ear is a remarkable sensory system with wide dynamic range and sharp frequency selectivity. These impressive characteristics are products of an active feedback mechanism within the cochlea. A consequence of this active feedback mechanism is that, in addition to detecting sound, the cochlea can also generate sounds, called otoacoustic emissions, that can be measured in the ear canal to provide a noninvasive assessment of hearing. There are several types of otoacoustic emissions, including distortion product otoacoustic emissions (that are generated in response to a stimulus of two tones) and spontaneous otoacoustic emissions (self-sustained oscillations that occur without any applied stimulus). Distortion product otoacoustic emissions are commonly used clinically and in research labs; however, key aspects of how these emissions are generated and propagate within the cochlear are debated. In this thesis, the properties of distortion product generation and propagation are investigated using a computational model of the mammalian cochlea. Additionally, this computational model is used to demonstrate that altering the viscoelastic properties of the tectorial membrane (a structure in the cochlea) affects spontaneous otoacoustic emission generation and the ability of the cochlea to detect low level sounds.

CHAPTER 1

INTRODUCTION

1.1 Hearing physiology and mechanics

The ear can be divided into three distinct parts (see Figure 1.1): the outer ear, middle ear, and inner ear. The outer ear includes the pinna and focuses sounds into the auditory

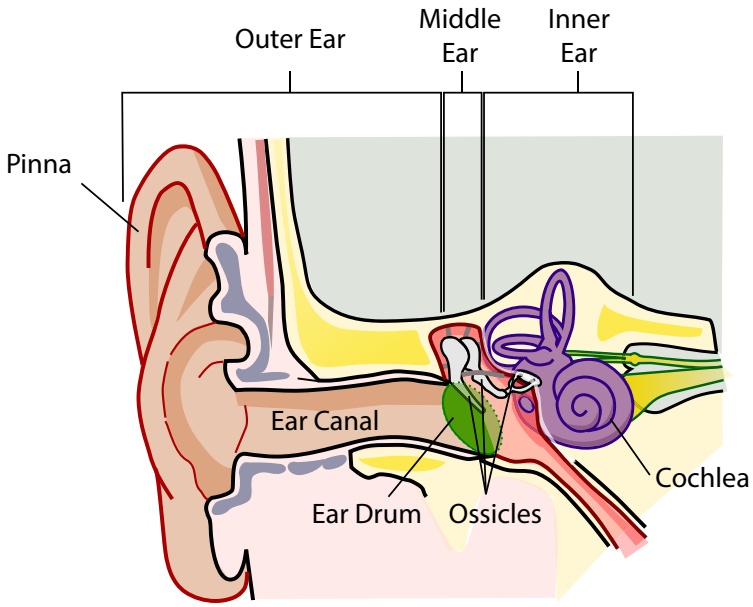

FIGURE 1.1. Diagram of the human ear. Figure modified from figure by Lars Chittka and Axel Brockmann [1] distributed under a Creative Commons 2.5 license.

canal. Once at the end of the auditory canal, the sound waves hit the tympanic membrane (eardrum) and cause the three bones of the middle ear to vibrate. The last of these three bones, the stapes, is connected to the fluid-filled cochlea. Although the cochlea is wrapped like a snail shell, it is convenient to imagine the cochlea unwrapped as shown in Figure 1.2.

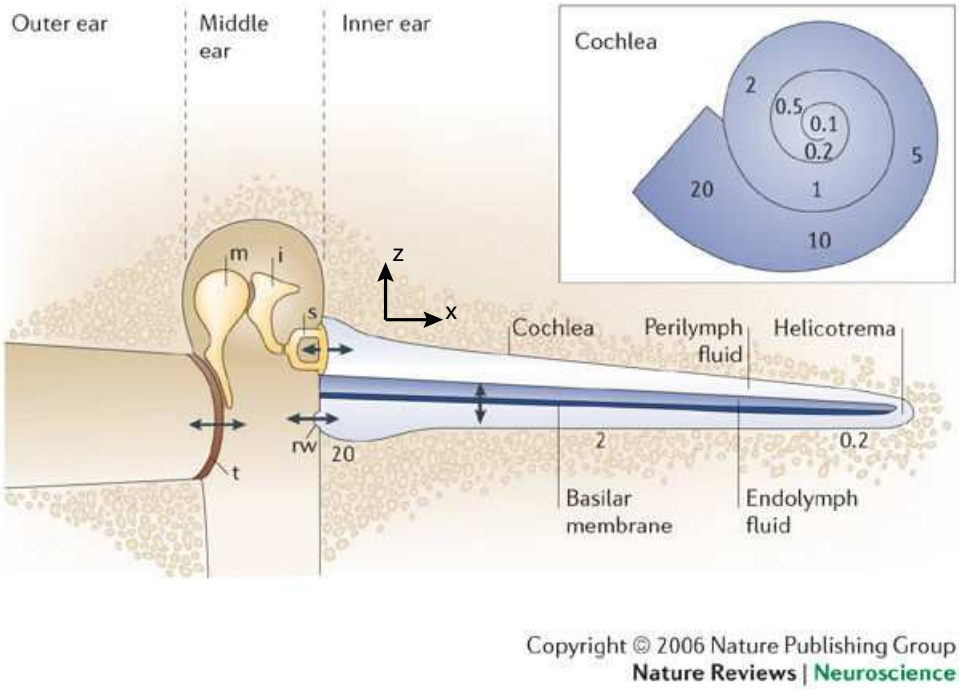

FIGURE 1.2. Diagram of the unwrapped human cochlea and place-frequency map. t: tympanic membrane; m: malleus; i: incus; s: stapes; rw: round window. The number listed in the spiral of the inset figure correspond to the frequency in kHz of the pure-tone response that peaks at the corresponding position. Reprinted by permission from R. Fettiplace and C. M. Hackney, "The sensory and motor roles of auditory hair cells," *Nature Reviews Neuroscience*, vol. 7, no. 1, pp. 19–29, 2006, copyright 2006.

The cochlea is tonotopic, in that higher frequencies have larger responses at the base near the stapes, while lower frequencies have larger responses at the apex closer to the helicotrema, as shown in Figure 1.2. This mapping of frequency to position is called the place-frequency map[3]. For a given position, the characteristic frequency (CF) is the frequency at which it is most sensitive (i.e. has the largest vibrations in response to a low level sound near the hearing threshold). Similarly, the best place (BP) is the position most sensitive to a given frequency. Different species have different hearing frequency ranges; the place-frequency maps for the gerbil, mouse, and human are compared in Figure 1.3.

The cochlea is embedded in bone and has three fluid filled ducts: the scalae vestibuli (SV) and tympani (ST), which are filled with perilymph fluid (a high-sodium solution), and the scala media, which contains endolymph fluid (a high-potassium solution)[5]. A

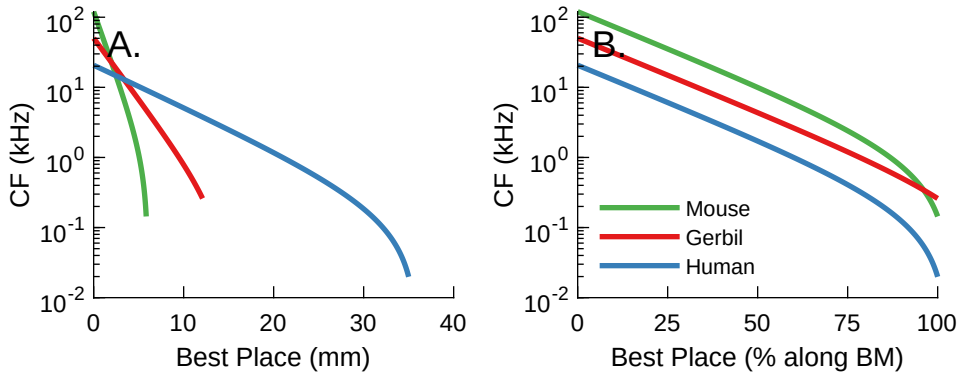

FIGURE 1.3. Comparison of Greenwood's[4] place-frequency maps for the mouse, gerbil, and human. A. Distance along the BM shown in millimeters. B. Distance along the BM shown as percent of total BM length.

cross-section diagram of the cochlea is shown in Figure 1.4. The scalae vestibuli and media are separated by the very thin (only two cell layers thick[6]) Reissner's membrane. Separating the scala tympani and scala media (SM) is the cochlear partition, which includes the tectorial membrane (TM), basilar membrane (BM), and organ of Corti. The organ of Corti includes the outer hair cells (OHCs), inner hair cells, and other supporting structures. The inner hair cells are the primary sensory cell and transduce the motion of the cochlear fluid into nerve signals, while the OHCs are key components in a feedback loop that adds mechanical energy to the system and amplifies low amplitude sounds[5,7]. Both the inner and outer hair cells have stereocilia (hair bundles, HB), which protrude from the top of the hair cells; the inner hair cell stereocilia extend freely into the endolymphatic space while the apical ends of the OHC stereocilia are connected to the tectorial membrane[6].

At the apex of the cochlea, the scalae vestibuli and tympani are connected by the helicotrema (see Figure 1.4). At the base of the cochlea, the stapes is coupled to the fluid in the scala vestibuli and the vibration of the stapes causes pressure waves within the cochlea (see Figure 1.2). These waves result in a pressure difference between the scalae vestibuli and media and the scala tympani, causing the cochlear partition to vibrate. The relative motions of the tectorial and basilar membranes cause deflection of the hair bundles[5]. Neighboring hair bundles are connected via tip links, which extend from the tip of the shorter HB to

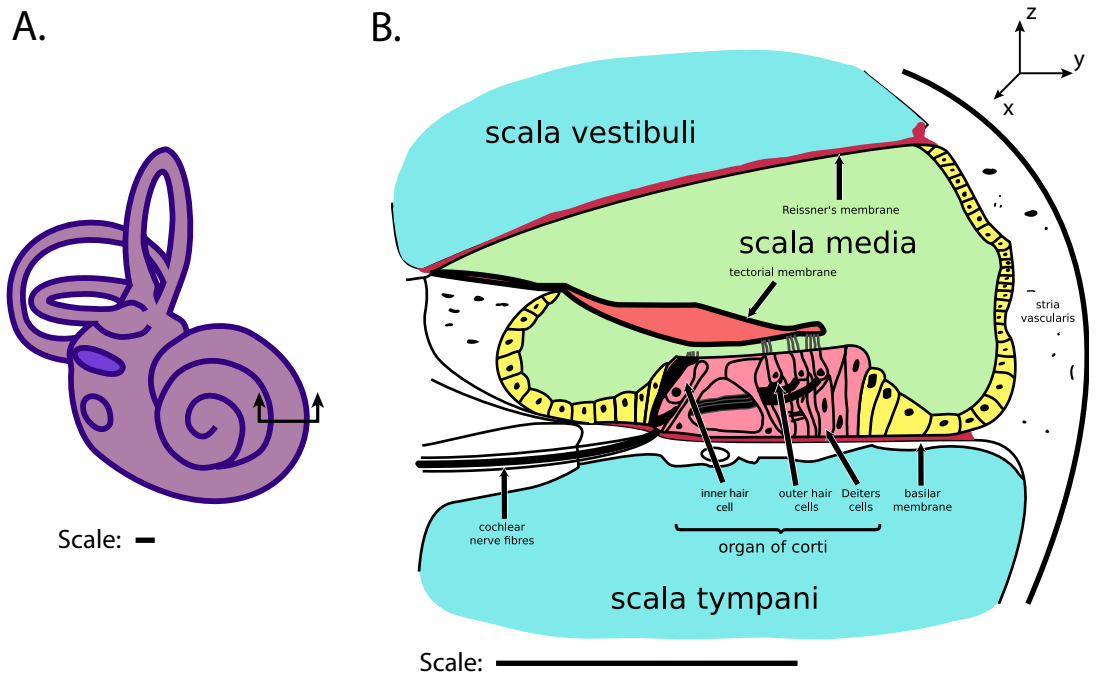

FIGURE 1.4. (A.) Human cochlea from Figure 1.1. Arrows indicate the section view shown in B. (B.) Diagram of a cross-section of the cochlea and the organ of Corti. Modified from figure by Oarih Ropshkow[8] distributed under a Creative Commons Attribution-Share Alike 3.0 Unported license. Scale bars are shown in give a rough estimate of the difference in dimensions scales of the cochlea and organ of Corti.

the side of the neighboring HB[5]. Upward motion of the BM causes the tip links to stretch, when in turn causes mechanoelectrical transduction (MET) channels on the tips of the hair cells to open, allowing ions to flow into the cell, generating a current and voltage change[5,3]. Deflection of the HBs towards the tallest stereocilia is excitatory (opens the channels, towards the right side in Figure 1.4B) and deflection in the opposite direction is inhibitory (closes the channels)[5]. This MET current flow causes the OHCs to depolarize *in vivo*[6].

The depolarization of the OHCs causes them to contract (in a piezoelectric-like process termed somatic electromotility[9]) and pull on the attached tectorial and basilar membranes, amplifying their motion. This positive feedback, called the "cochlear amplifier", is most effective at low sound pressure levels and in fact the cochlea exhibits a strong compressive nonlinearity[10,7]. In mammals, a 0 dB SPL stimulus results in basilar membrane vibrations on the order of ± 0.1 nm while a 120 dB SPL stimulus (six orders of magnitude larger) re-

sults in basilar membrane vibrations on the order of ± 10 nm, only two orders of magnitude larger[10]. This compressive nonlinearity occurs due to a saturation of the mechanoelectrical transduction current flowing through the OHCs.

In response to an acoustic stimulus in the ear canal, a wave propagates on the BM in the forward direction, i.e., from the base toward the apex of the cochlea. The magnitude of the wave peaks at a location that depends on the stimulus frequency. As the wave propagates from the base towards its best place, it grows in amplitude and slows down. At the base the wave travels at speeds of tens of m/s, while around the best place is only a few m/s. Because these speeds are much smaller than the speed of sound in water, this wave is commonly called the "slow forward traveling wave". After the wave reaches its best place, it continues propagating towards the apex but decreases in amplitude until it becomes evanescent.

Historically, much of the focus in hearing mechanics was on the response of the basilar membrane (e.g.[11,12]) and the entire organ of Corti was assumed to have similar motion. Within the last several years, the advent of optical coherence tomography (OCT, an imaging technique based on low-coherence interferometry) to hearing mechanics has enabled the study of the structures within the organ of Corti[13,14,15,16,17]. These studies have revealed that the motions within the organ of Corti are much more complicated than previous expected. Although the BM displays amplification and nonlinearity only around the peak frequency, the reticular lamina shows both amplification and nonlinearity around the peak and frequencies well below CF[13,15,16,17]. These studies also suggest that near CF, structures like the TM and RL have larger displacements than the BM[13,14,16]. In classical computational models of the cochlea[18,19], the cochlear partition is represented either as a single structure[18] or as a two degree of freedom system[19] that does not consider the anatomy of the organ of Corti. To accurately represent the vibrations of the structures in the organ of Corti reported from the OCT measurements, a more detailed model of the organ of Corti is required. Although not a focus of this thesis, the computational model used in this work is able to match some of the characteristics of the OCT data (e.g. larger motion of the RL than

the BM at CF and nonlinearity of the RL at frequencies below CF), but does not match others (e.g. the model underpredicts the motion of the RL at low frequencies relative to CF). Methods for modifying the model to more accurately match the experiment measurements are discussed in the future work (Section 7.2).

1.2 Otoacoustic emissions

Otoacoustic emissions (OAEs) are sound generated by the cochlea that can be measured in the ear canal and provide a noninvasive method for determining the health and functionality of the cochlea's active and sensory mechanisms[20]. Otoacoustic emissions can be divided into two categories by how they are generated (Figure 1.5): (1) evoked emissions that occur in response to some external stimulus and (2) spontaneous emissions that need no external stimulus[21].

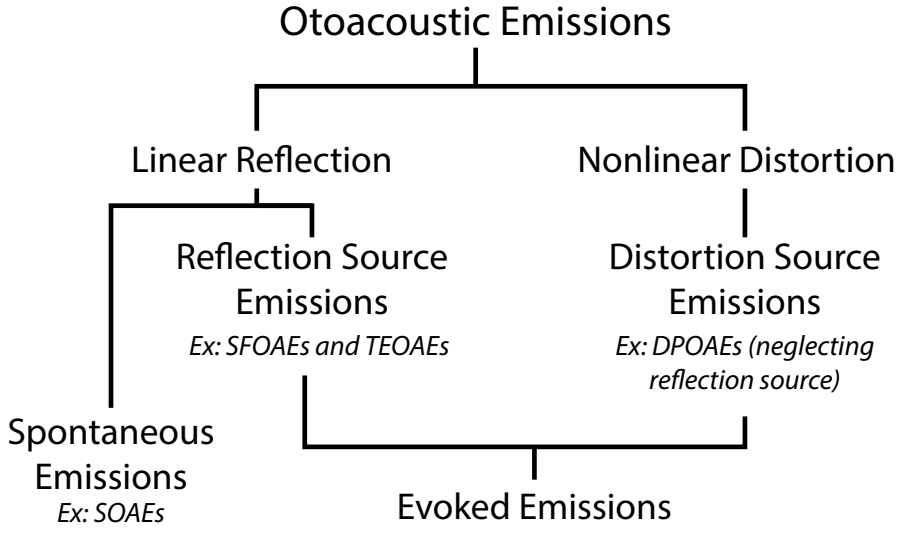

FIGURE 1.5. Mechanisms for otoacoustic emissions. Adopted with permission from Figure 10 of C. A. Shera and J. J. Guinan Jr, "Evoked otoacoustic emissions arise by two fundamentally different mechanisms: a taxonomy for mammalian OAEs," *Journal of the Acoustical Society of America*, vol. 105, no. 2, pp. 782–798, 1999. Copyright 1999, Acoustical Society of America.

Evoked emissions may be separated into emissions due to linear reflection and those due to nonlinear distortion[22]. Mechanical impedance perturbations along the length of the

cochlea result in reflections of an incoming wave (similar to Bragg scattering)[23]. According to a well established theory, these impedance perturbations are randomly distributed throughout the cochlear partition; the most effective region for generating reflection is around the best place[23,22]. A potential source of these impedance perturbations are the hair cells and other cellular architectures in the organ of Corti, which are discrete structures superimposed upon the more graduation variation of parameters related to the place-frequency map[24,25]. In response to a pure tone stimulus, these impedance perturbations cause reflections that propagate backwards through the cochlea, middle ear, and into the ear canal where they can be measured at stimulus frequency otoacoustic emissions (SFOAEs). In response to the pure tone stimulus, interactions between the backward traveling wave and stimulus create quasi-periodic variations in the ear canal pressure called fine structure.

Distortion product otoacoustic emissions (DPOAEs) are generated due to nonlinear distortion in response to two stimulus tones (of frequencies f_1 and f_2, where $f_2 > f_1$)[26]. Intracochlear measurements of the BM velocity[27,28,29] or fluid pressure[30] in response to a two-tone stimulus have confirmed that distortion products (DPs) are generated in the cochlea. It is generally agreed that DPs are generated by the OHCs[27] due to the nonlinearity of the mechanoelectrical transduction (MET) channel[2]. In any nonlinear system, DPs occur at linear combinations of the two stimulus tones, such as $2f_1 - f_2$, $2f_2 - f_1$, $f_2 - f_1$, $f_1 + f_2$ (Figure 1.6). Due to the specific form of cochlear nonlinearity, the low-side cubic DP of frequency $f_{DP} = 2f_1 - f_2$ tends to have the highest amplitude and is the most commonly studied DP[29]. After the low-side cubic DP, the high-side cubic DP of frequency $f_{DP} = 2f_2 - f_1$ is one of the DPs most commonly studied[28,30,31]. According to the theory of coherent reflection, DPs are generated not only by the nonlinear interactions (distortion source) of the two stimulus tones, but also due to linear reflection (reflection source)[22,32]. While the exact locations of DP generation are still being debated, there is general agreement that the distortion source component originates from near the f_2 best place and the reflection source component of the $2f_1 - f_2$ DP originates from a more apical position close

to the $2f_1 - f_2$ best place[32].

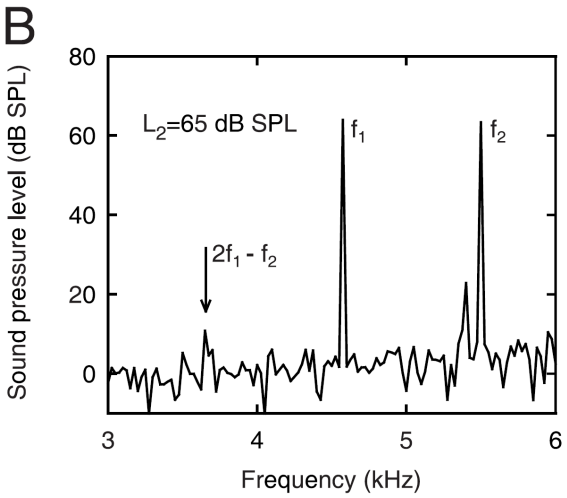

FIGURE 1.6. Example of DPOAE measured in a human. Figure source: E. Dalhoff, D. Turcanu, H.-P. Zenner, and A. Gummer, "Distortion product otoacoustic emissions measured as vibration on the eardrum of human subjects," *Proceedings of the National Academy of Sciences*, vol. 104, no. 5, pp. 1546–1551, 2007. Copyright 2007 National Academy of Sciences.

When measured in the ear canal, interactions between the distortion and reflection source components of the DPOAE result in quasi-periodic variations across frequency, called fine-structure[34,35,22]. The presence of two sources of DPOAEs in the ear canal complicates the efficacy of using DPOAEs to assess cochlear function[36,37]. As a result, there has been much effort to develop techniques for separating the two components[38,39,37,40,41,42] in the ear canal pressure, but these techniques cannot be applied to separate the two components from intracochlear measurements. The focus of this work is on the distortion source component, which tends to be the dominant component when the primary frequency ratio, f_2/f_1, is sufficiently larger than 1; other recent work within the Meaud lab group has focused on the reflection source[43].

Because of the cochlear amplifier, the cochlea is an active system that, at low stimulus levels, operates close to a dynamic instability[44,45]. Due to this instability, the cochlea is sometimes in an oscillatory regime characterized by the presence of self-sustained oscillations. These self-sustained oscillations were originally predicted by Gold in 1948[44] and

observed more than 30 years later as spontaneous otoacoustic emissions (SOAEs) in the ear canal pressure[46]. SOAEs are narrow-band oscillations that are fairly common in humans and can be measured in about 70% of the population[47]. Two typical human SOAE frequency spectra are shown in Figure 1.7.

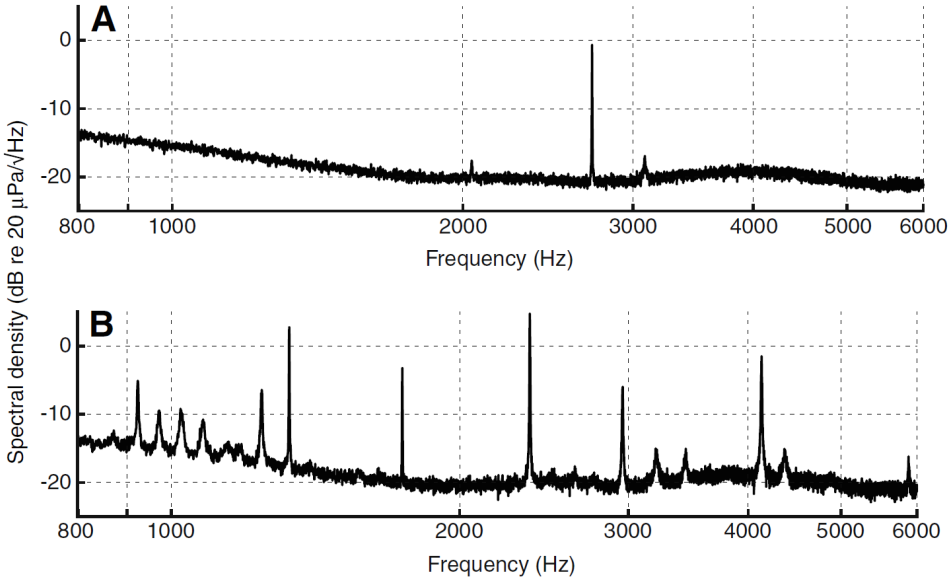

FIGURE 1.7. Frequency spectrum for typical human SOAEs measured in two individuals. The spectral peaks correspond to the SOAEs. Figure distributed under a Creative Commons Attribution Noncommercial License from P. van Dijk, B. Maat, and E. de Kleine, "The effect of static ear canal pressure on human spontaneous otoacoustic emissions: spectral width as a measure of the intra-cochlear oscillation amplitude," *Journal of the Association for Research in Otolaryngology*, vol. 12, no. 1, pp. 13–28, 2011.

In addition to somatic electromotility, a different active process, called HB motility (*i.e.*, motility of the hair-like filaments located on top of the OHCs) might play a role in cochlear amplification and SOAE generation[49]. Somatic electromotility is known to be essential for mammalian cochlear amplification[50,7]; additionally, experiments and theoretical models[51,52,53,54] have shown that HB motility might also be an important component of the cochlear amplifier. Because spontaneous oscillations of HBs have been observed in non-mammalian vertebrates[55,56], HB motility has often been hypothesized to underlie the generation of SOAEs in these species. However, spontaneous oscillations of mammalian HBs have never been observed, even though some evidence of mammalian HB motility has

been observed[57,58]. Due to the inherent coupling between OHCs linked to the presence of a traveling wave and of structural coupling[59,60], mammalian SOAEs might not be the result of activity of individual HBs or OHCs but rather a global phenomenon that emerges from the active dynamics of the overall system[61,45]. In the theory of coherent reflection[61], the cochlea acts like a laser cavity; SOAE generation requires coherent reflection of traveling waves by putative inhomogeneities in the cochlear partition and amplification of waves by the OHCs. While alternative theoretical models exist[62,63], this theory has been implemented in physically-motivated cochlear models[64] and successfully captures many of the key characteristics of SOAEs, such as the presence of discrete spectral peaks with a common spacing between adjacent SOAEs[35,64]. Interestingly, recent experiments in genetically modified mice have demonstrated that mutations of the genes expressed in the tectorial membrane can significantly enhance the generation of SOAEs[65,66,67].

1.3 Noise-Induced Hearing Loss

An estimated one in five people in the United States (20% or 48 million) have some form of hearing loss[68] and a study by the Centers for Disease Control[69] found that 16% of Americans reported having trouble hearing. Although hearing loss generally occurs with aging (presbycusis), noise-induced hearing loss (NIHL) can occur at any age. NIHL can be caused by short exposure to intense impulsive sounds (e.g. an explosion) or by continuous exposure to loud sound over an extended period of time. The etiology of NIHL is the damage or loss of hair cells (Figure 1.8) and up to 30-50% of hair cells can be damaged before any hearing loss is detected[70].

Damaged or destroyed OHCs will result in either reduced or no OAEs. Therefore, OAEs provide a powerful, and importantly noninvasive, tool for assessing cochlear function and hearing loss[72]. The OAEs most commonly used in clinics for assessing cochlear function are transient evoked otoacoustic emissions (TEOAEs, which occur in response to an impulse, i.e., acoustic click)[73]. DPOAEs, however, have several benefits over TEOAEs:

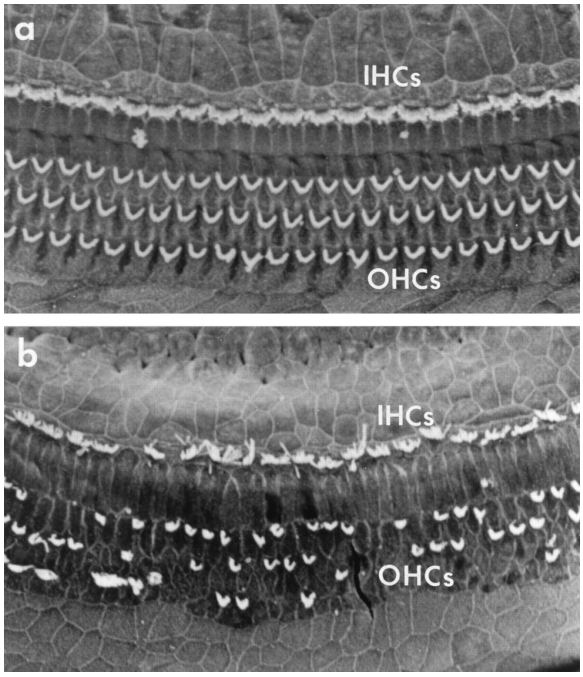

FIGURE 1.8. Scanning electron micrographs of normal (a) and damaged (b) sensory epithelium. Figure source: A. F. Ryan, "Protection of auditory receptors and neurons: evidence for interactive damage," *Proceedings of the National Academy of Sciences*, vol. 97, no. 13, pp. 6939–6940, 2000. Copyright 2000 National Academy of Sciences.

finer frequency specificity and wider dynamic range[73]. Indeed, while TEOAEs provide a qualitative assessment of cochlear function, DPOAEs can provide quantitative information about the range and operational characteristics of the cochlear amplifier[72]. What's more, DPOAEs can study OHC function in ears with up to 45 to 55 dB HL (hearing loss), while TEOAEs are unable to assess function >30 dB HL[73]. Measuring DPOAEs thus provides a mechanism for evaluating the health of the cochlea and OHCs. Correct interpretation of DPOAE measurements, however, requires correct understanding of where the DPs are generated and how they propagate within the cochlea.

1.4 Thesis overview and outline

While ultimately knowledge about human hearing is the most useful, animal experiments are needed in order to obtain direct *in vivo* information about hearing mechanics. Of the rodents most commonly used in hearing mechanics (chinchilla, guinea pig, mouse, ger-

bil), the gerbil is the species of choice for a significant fraction of the studies due to a hearing range similar to that of humans (Figure 1.3). In recent years, most studies that involve intracochlear measurements (e.g. fluid pressure, OCT) are performed in either the gerbil or mouse (e.g. Refs. 14, 15, 74, 75, 17, 76). Of particular interest to this work, the intracochlear DP measurements by Dong and Olson are made in the gerbil[77,30,31,74]. Previous work in the Grosh and Meaud labs have utilized a model of the guinea pig cochlea[78,79,60,80,81,82]. Although both the guinea pig and gerbil are rodents, many of the properties of their cochleae are different, including the overall lengths of the basilar membranes (12 vs 18 mm)[83], place-frequency maps[4,84], and sharpness of tuning[12,85,86]. To give the best comparison to experimental gerbil data, the previously developed model of the guinea pig was modified to represent the gerbil.

The overall objective of this thesis is to improve the basic understanding of hearing mechanics and OAE generation. The long term motivation for this is that gaining a better understanding of hearing mechanics can foster better treatment of hearing loss and answering remaining questions on OAEs can improve their clinical use as a diagnostic. In this thesis, this computational model of the gerbil ear was used to study various aspects of OAEs in the cochlea. The formulation of this model is given in Chapter 2. Calibration and validation, along with a sensitivity study of the mechanical parameters, are discussed in Chapter 3. In Chapter 4, how DPs propagate in the cochlea on their way towards the middle ear is determined. The study in Chapter 5 aims to determine the locations of DP generation. In Chapter 6, the role of the TM in maintaining cochlear stability, preventing the generation of many SOAEs, and detection of low level sounds is evaluated.

CHAPTER 2

MODEL FORMULATION

2.1 Chapter overview

Most aspects of the computational model of the mammalian cochlea used for this research were formulated in a series of papers[78,79,60,80,81,82] by the Grosh and Meaud groups before the start of this thesis work. With the exception of Ramamoorthy et al.[79] (and Ramamoorthy's PhD dissertation[87]), for which many parts of the model were new, these papers generally only provided an overview of the model or discussed the differences from the preceding paper. Because several features have been to added to the model since its original introduction[79], including longitudinal coupling to the BM and TM[60] and a state space formulation[82], a complete description of the current model formulation is not available in the literature. To fill this gap, this chapter provides a comprehensive presentation of key model assumptions and derivation of the governing equations. Much of the development of the model is not new to this work, but is included here for completeness and to serve as a reference for future researchers. The origins of each part of the model are cited as appropriate and additions or changes made are stated explicitly. The model is formulated with the finite element method and includes acoustic (fluid), mechanical, and electrical physics. The governing equations for the model are given in Sections 2.2 and 3.3. The finite element and state space formulations of the model are given in Section 2.4.

2.2 Cochlear model

The multi-physics model of the cochlea includes acoustic (fluid), mechanical, and electrical domains (Figure 2.1). The acoustic domain represents the fluid mechanics within the cochlear ducts. The mechanical domain represents the vibrations of the structures in the cochlear partition. The electrical domain represents the electrodynamics of the OHCs and cochlear ducts. Mechanoelectric transduction and somatic electromotility couple the mechanical and electrical domains.

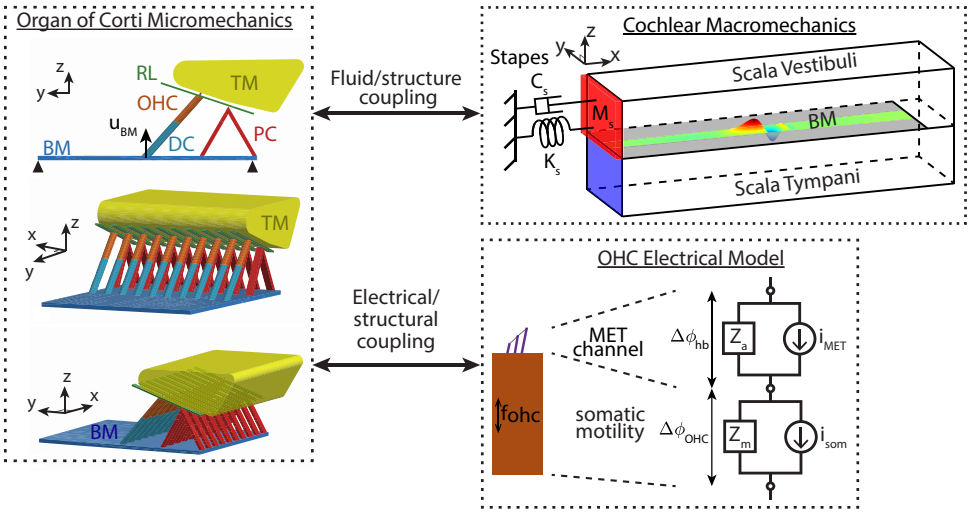

FIGURE 2.1. Schematic of the 3D cochlear model. Acoustic pressure in the cochlear ducts excited the BM. The BM is coupled to a micromechanical model of the organ of Corti. In the schematic of the micromechanical model, the spacing between cross sections has been exaggerated for visualization purposes. This micromechanical model is coupled to an electrical model of the OHCs. The cochlear model is coupled to a one degree of freedom middle ear model.

2.2.1 Acoustic domain

In modeling efforts to represent the cochlea, the cochlear ducts are commonly represented by a straight box with two cochlear ducts (the scala media is merged with the scala vestibuli)[88,78]. The cochlear fluid is assumed to be incompressible (which implies that the speed of sound is infinite in the model) and inviscid (the effect of viscosity is lumped into the damping

parameters of the structural model), such that the governing equation for the fluid is

$$\nabla^2 P(x,y,z,t) = 0 \tag{2.1}$$

where P is the pressure of the fluid; x, y, and z are the distance in the longitudinal (from the stapes), radial (from the center of the duct), and transverse (from the BM) directions, respectively; t is time. A schematic of the fluid box model is shown in Figure 2.2. Given that the cochlea is modeled as a rectangular box, using the term *lateral* instead of *radial* is arguably be a better choice of terminology, but because it is more commonly cited in the literature and the actual cochlea is curved, the term *radial* will be used throughout this work when describing the direction perpendicular to the longitudinal axis and parallel to the cochlear partition.

The linearized Euler relationships coupling the fluid in the scalae vestibuli and tympani, respectively, to the BM are

$$\left.\frac{\partial P}{\partial z}\right|_{z=0^+} = \left.\frac{\partial P}{\partial z}\right|_{z=0^-} = -\rho_f \ddot{u}_{BM} \tag{2.2}$$

where $z = 0^+$ and $z = 0^-$ correspond to $z = 0$ (at the BM) in the scala vestibuli (SV) and scala tympani (ST), respectively; ρ_f is the density of the cochlear fluid; u_{BM} is the displacement of the BM (positive u_{BM} is in the $+z$ direction, towards the SV).

At the oval window, the linearized Euler relationship coupling the fluid in the scala vestibuli to the stapes is

$$\left.\frac{\partial P}{\partial x}\right|_{x=0,z\geq 0} = -\rho_f \ddot{u}_s \tag{2.3}$$

where u_s is the displacement of the stapes (positive displacement is the $+x$ direction). The round window is modeled as a pressure release:

$$P|_{x=0,z\leq 0} = 0 \tag{2.4}$$

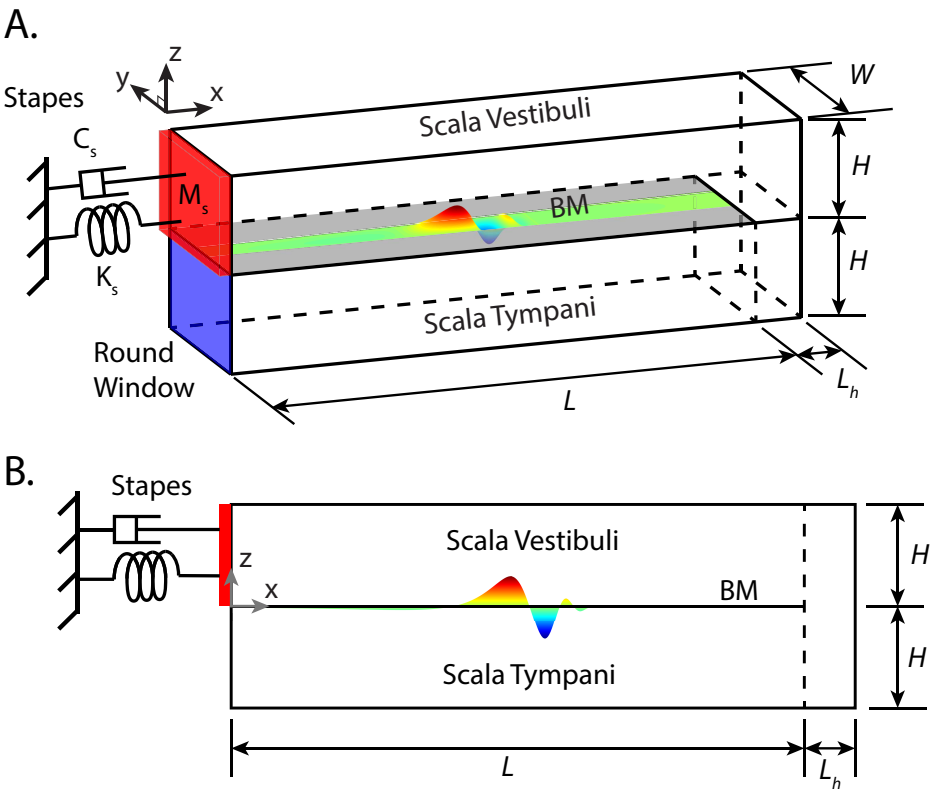

FIGURE 2.2. Box model of the cochlea. A. Isometric view of the box model. B. Side view of the box model. L is the length of the BM; L_h is the length of the helicotrema; H and W are the height and width, respectively, of the cochlear ducts; M_s, C_s, and K_s are the mass, damping, and resistance, respectively, of the stapes. The displacement of the BM has been exaggerated for visualization purposes.

and the other walls of the cochlea are assumed to be rigid:

$$\left.\frac{\partial P}{\partial y}\right|_{y=\pm W/2} = \left.\frac{\partial P}{\partial z}\right|_{z=\pm H} = \left.\frac{\partial P}{\partial x}\right|_{x=L+L_h} = 0 \tag{2.5}$$

where H is the height of the cochlear duct; L is the length of the BM; L_h is the length of the helicotrema.

As introduced by Parthasarathi et al.[78], the pressure, $P(x,y,z,t)$, is decomposed into radial (y direction) mode shapes so that a 2D mesh can give a 3D solution:

$$P(x,y,z,t) = \sum_{m=0,2,4,\ldots}^{M} P^{(m)}(x,z,t)\phi_m(y), \tag{2.6}$$

where

$$\phi_m(y) = \cos\left[\frac{m\pi(y+W/2)}{W}\right], \tag{2.7}$$

where m is the mode number; $P^{(m)}$ is the modal amplitude of the mth mode; $\phi_m(y)$ is the mth mode shape; and W is the width of the cochlear duct. Radial symmetry is assumed so that only the even modes are necessary.

2.2.2 Mechanical domain

2.2.2.1 Kinematics

Figure 2.3 shows the geometry of the organ of Corti model. This kinematic model was originally introduced by Ramamoorthy *et al.*[79] and is based work by Dallos[89]. The geometric parameters for the gerbil models were determined during model calibration and are based on images of the gerbil organ of Corti taken by Edge *et. al*[90].

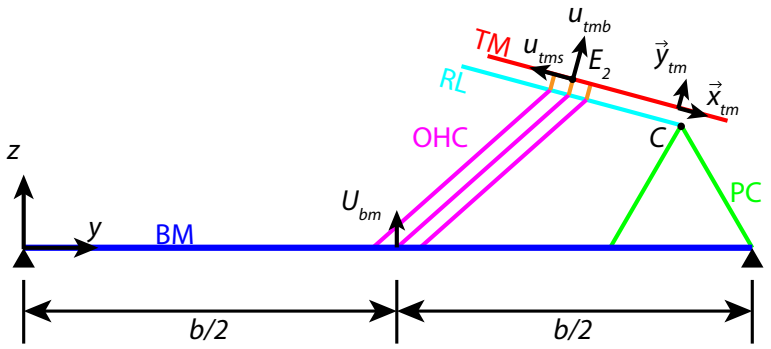

FIGURE 2.3. Geometric model of the organ of Corti (not to scale). BM: basilar membrane; TM: tectorial membrane; RL: reticular lamina; OHC: outer hair cell; PC: pillar cells; b is the width of the BM; U_{bm}, u_{tms}, and u_{tmb} are the displacements of the BM, TM-shear mode, and TM-bending mode, respectively.

The Ramamoorthy model[79] includes a physiologically based model of the organ of Corti with degrees-of-freedom (DOFs) for the basilar membrane and tectorial membrane in bending and shear (u_{tmb} and u_{tms}, respectively). The basilar membrane is modeled as an

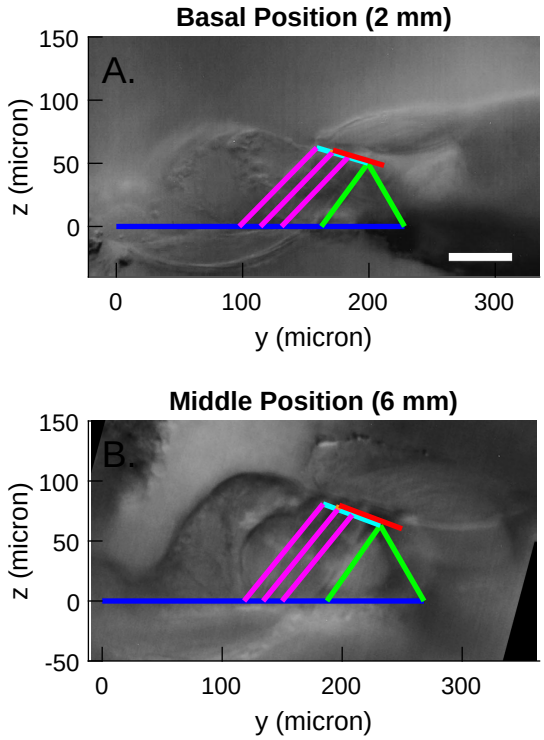

FIGURE 2.4. Geometric model of the organ of Corti overlapped with images of the organ of Corti[90] at a basal and middle turn location.

orthotropic plate that can vibrate in its first mode[79]:

$$u_{bm}(x,y) = U_{bm}(x)\psi(y) \tag{2.8}$$

where U_{bm} is displacement of the BM at the center of the cross section ($y = 0$) and

$$\psi(y) = \sin\left[\frac{\pi(y+b/2)}{b}\right] \tag{2.9}$$

where b is the width of the basilar membrane. The pillar cells are assumed to be rigid so that the apical end of the pillar cells (point C in Figure 2.3) rotates as the BM is displaced and is given by[79]:

$$u_{ap} = D_1 U_{bm} \tag{2.10}$$

where D_1 is a geometric coupling coefficient defined in Appendix A.

Each cross section of the TM is assumed to vibrate as a rigid body that can translate in plane in two directions (but does not rotate):

$$\vec{u}_{E_2} = -u_{tms}\vec{x}_{tm} + u_{tmb}\vec{y}_{tm} \tag{2.11}$$

where $\vec{x}_{tm}$ is defined to be parallel to the RL. Using this convention, positive TM-shear displacement corresponds to the HBs rotating in the excitatory direction (the tops of the HBs move away from the pillar cells).

As in the original formulation[79], the deflection of the j-th HB (u_{hb/rl_j}), compression of the j-th OHC ($u^{comp}_{ohc_j}$), and deflection of the RL at the top of the j-th OHC (u_{rl_j}) relative to the tip of the pillars cells are related to the displacements of the BM, TM-shear (u_{tms}), and TM-bending (u_{tmb}):

$$u_{hb/rl_j} = \left(A_{j1} + B_{j1}\frac{L_{st}}{L_{ro}}\right)U_{bm} + \left(A_{j3} + B_{j3}\frac{L_{st}}{L_{ro}}\right)u_{tms} + \left(A_{j4} + B_{j4}\frac{L_{st}}{L_{ro}}\right)u_{tmb} \tag{2.12}$$

$$u^{comp}_{ohc_j} = (E_{j1} + C_{j1})U_{bm} + C_{j3}u_{tms} + C_{j4}u_{tmb} \tag{2.13}$$

$$u_{rl_j} = B_{j1}U_{bm} + B_{j3}u_{tms} + B_{j4}u_{tmb} \tag{2.14}$$

where L_{st} is the length of the HBs; L_{ro} is the distance between the RL pivot and the middle OHC; $A_{j1}, A_{j3}, A_{j4}, B_{j1}, B_{j3}, B_{j4}, C_{j1}, C_{j3}, C_{j4}$, and E_{j1} are geometric coupling coefficients defined in Appendix A. Positive deflection of the HBs relative to the RL is in the excitatory direction. The averages of the HB deflection relative to the RL and OHC compression for the three HBs and OHCs within each longitudinal cross-section are:

$$u^{avg}_{hb/rl} = \frac{1}{3}\sum_{j=1}^{3} u_{hb/rl_j} \tag{2.15}$$

$$u^{comp}_{ohc}|_{avg} = \frac{1}{3}\sum_{j=1}^{3} u^{comp}_{ohc_j} \tag{2.16}$$

2.2.2.2 *Dynamics*

Within the micromechanical model, the BM, TM-shear, and TM-bending all have associated masses: M_{bm}, M_{tms}, and M_{tmb}, respectively. The masses M_{tms} and M_{tmb} are the effective TM mass in the shear and bending directions, respectively. The BM is modeled as an orthotropic plate. As introduced by Meaud and Grosh[60], the model includes longitudinal coupling between cross sections for both the BM and TM. The discussion of the mechanical model thus far has only considered the in-plane motion occurring at a single cross-section. Although neighboring cross sections are coupled by the cochlear fluid, longitudinal coupling between cross sections in the BM and TM provides an additional mechanism by which neighboring cross sections may interact. In the model from Meaud and Grosh and in the Bowling 2018 model, only the TM-shear mode has longitudinal coupling, while the Bowling 2019 and current models include longitudinal coupling for both the TM-shear and TM-bending modes.

The total kinetic energy for the model can be written as:

$$T = \int_0^L \left(\int_{-b/2}^{b/2} \frac{1}{b} M_{bm} \ddot{u}_{bm}^2 dy + \frac{1}{2} M_{tms} \ddot{u}_{tms}^2 + \frac{1}{2} M_{tmb} \ddot{u}_{tmb}^2 \right) dx \tag{2.17}$$

and the total potential energy can be written as:

$$
\begin{aligned}
V = \int_0^L \Bigg[& \frac{1}{2} \int_{-b/2}^{b/2} \Bigg(D_{xx} \Big(\frac{\partial^2 u_{bm}}{\partial x^2} \Big)^2 + D_{yy} \Big(\frac{\partial^2 u_{bm}}{\partial y^2} \Big)^2 + 2 D_{xy} \frac{\partial^2 u_{bm}}{\partial x^2} \frac{\partial^2 u_{bm}}{\partial y^2} \\
& + D_s \Big(\frac{\partial^2 u_{bm}}{\partial x \partial y} \Big)^2 \Bigg) dy \\
& + \int_{A_{tm}} \frac{1}{2} G_{tm} \Bigg(\Big(\frac{\partial u_{tms}}{\partial x} \Big)^2 + \delta_m \Big(\frac{\partial u_{tmb}}{\partial x} \Big)^2 \Bigg) dA + \frac{1}{2} K_{tms} u_{tms}^2 + \frac{1}{2} K_{tmb} u_{tmb}^2 \\
& + \frac{1}{2} K_{hb} \Bigg(\Big(u_{hb_1} + u_{rl_1} \frac{L_{st}}{L_{ro} - L_1} \Big)^2 + \Big(u_{hb_2} + u_{rl_2} \frac{L_{st}}{L_{ro}} \Big)^2 + \Big(u_{hb_3} + u_{rl_3} \frac{L_{hb}}{L_{ro} + L_1} \Big)^2 \Bigg) \\
& + \frac{1}{2} K_{rl} \Big(u_{rl} + u_{ap} \frac{L_{ro}}{L_{pc}} \Big)^2 + \frac{1}{2} \sum_{j=1}^{3} K_{ohc} \big(u_{ohc_j}^{comp} \big)^2 \Bigg] dx
\end{aligned}
\tag{2.18}
$$

where D_{xx}, D_{yy}, D_{xy}, and D_s are the orthotropic plate bending stiffnesses of the BM; G_{tm} is the TM shear modulus; A_{tm} is the effective area of the TM; K_{tms} and K_{tmb} are the attachment stiffnesses of the TM shear mode and TM bending mode, respectively, to the spiral limbus; K_{hb} is the HB stiffness; K_{rl} is the stiffness of the RL; K_{ohc} is the stiffness of the OHCs; L_{pc} is distance between the left edge of the BM and the outer pillar cell; L_1 is the radial distance between HBs. To account for the addition of longitudinal coupling to the TM-bending mode for the later two iterations of the model, the value of δ_m is 0 for the Bowling 2018 model (used in Chapter 4) and 1 for the Bowling 2019 and current models (used in Chapters 5 and 6). The generalized work done by external, viscous, and electromotile

(piezoelectric-like) forces is:

$$Q = \int_0^L \Bigg[\int_{-b/2}^{b/2} \Bigg(-(\frac{2}{b} C_{bm} \dot{u}_{bm}) u_{bm} - \sum_{m=0}^{M} (P_{sv}^{(m)} - P_{st}^{(m)}) u_{bm} \Bigg) dy \\ - \int_{A_{tm}} \eta_{tm} \Big(\frac{\partial \dot{u}_{tms}}{\partial x} \frac{\partial u_{tms}}{\partial x} + \delta_m \frac{\partial \dot{u}_{tmb}}{\partial x} \frac{\partial u_{tmb}}{\partial x} \Big) dA \\ - \big(C_{tms} \dot{u}_{tms}\big) u_{tms} - \big(C_{tmb} \dot{u}_{tmb}\big) u_{tmb} - \big(C_f \dot{u}_{hb/rl}\big) u_{hb/rl} - \sum_{j=1}^{3} f_{ohc_j} u_{ohc_j}^{comp} \Bigg] dx \tag{2.19}$$

where C_{bm}, C_{tms}, and C_{tmb} are the viscous damping coefficients for the BM, TM in shear, and TM in bending, respectively; $P_{sv}^{(m)}$ and $P_{st}^{(m)}$ are the pressures in the SV and ST, respectively, at the BM ($z = \pm 0$) for the m-th fluid mode; η_{tm} is the TM shear viscosity; f_{ohc} is the force applied by the OHCs due to somatic motility (see Section 2.2.3). Damping from the fluid in the subtectorial space is taken into account by a term proportional to the HB velocity with an effective damping coefficient, C_f. Because the BM is assumed to vibrate in its first mode and the TM is assumed to vibrate as a rigid body within each longitudinal cross-section, the total kinetic and potential energies and the generalized work may be written as:

$$T = \int_0^L \Big(\frac{1}{2} M_{bm} \dot{U}_{bm}^2 + \frac{1}{2} M_{tms} \dot{u}_{tms} + \frac{1}{2} M_{tmb} \dot{u}_{tmb}^2 \Big) dx \tag{2.20}$$

$$V = \int_0^L \Bigg[D_{xx} \frac{b}{4} \Big(\frac{\partial^2 U_{bm}}{\partial x^2} \Big)^2 + \frac{1}{2} K_{bm} U_{bm}^2 - D_{xy} \frac{\pi^2}{2b} U_{bm} \frac{\partial^2 U_{bm}}{\partial x^2} + D_s \frac{\pi^2}{4b} \Big(\frac{\partial U_{bm}}{\partial x} \Big)^2 \\ + \frac{1}{2} K_{tm}^{LC} \Bigg(\Big(\frac{\partial u_{tms}}{\partial x} \Big)^2 + \delta_m \Big(\frac{\partial u_{tmb}}{\partial x} \Big)^2 \Bigg) + \frac{1}{2} K_{tms} u_{tms}^2 + \frac{1}{2} K_{tmb} u_{tmb}^2 \\ + \frac{1}{2} K_{hb} \Bigg(\Big(u_{hb_1} + u_{rl_1} \frac{L_{st}}{L_{ro} - L_1} \Big)^2 + \Big(u_{hb_2} + u_{rl_2} \frac{L_{st}}{L_{ro}} \Big)^2 + \Big(u_{hb_3} + u_{rl_3} \frac{L_{hb}}{L_{ro} + L_1} \Big)^2 \Bigg) \\ + \frac{1}{2} K_{rl} \Big(u_{rl} + u_{ap} \frac{L_{ro}}{L_{pc}} \Big)^2 + \frac{1}{2} \sum_{j=1}^{3} K_{ohc} \big(u_{ohc_j}^{comp} \big)^2 \Bigg] dx \tag{2.21}$$

$$Q = \int_0^L \Bigg[-\left(C_{bm}\dot{U}_{bm}\right)U_{bm} - \sum_{m=0}^{M}\left(P_{sv}^{(m)} - P_{st}^{(m)}\right)\mu_m U_{bm} \\ - \left(C_{tm}^{LC}\frac{\partial \dot{u}_{tms}}{\partial x}\right)\frac{\partial u_{tms}}{\partial x} - \left(\delta_m C_{tm}^{LC}\frac{\partial \dot{u}_{tmb}}{\partial x}\right)\frac{\partial u_{tmb}}{\partial x} \\ - \left(C_{tms}\dot{u}_{tms}\right)u_{tms} - \left(C_{tmb}\dot{u}_{tmb}\right)u_{tmb} - \left(C_f\dot{u}_{hb/rl}\right)u_{hb/rl} - \sum_{j=1}^{3} f_{ohc_j}u_{ohc_j}^{comp}\Bigg] dx \tag{2.22}$$

where the transverse stiffness of the BM per unit length, K_{bm}, is defined as

$$K_{bm} = D_{yy}\frac{\pi^4}{2b^3}, \tag{2.23}$$

the coupling stiffness and damping of the TM are

$$\begin{aligned} K_{tm}^{LC} &= G_{tm}A_{tm} \\ C_{tm}^{LC} &= \eta_{tm}A_{tm}, \end{aligned} \tag{2.24}$$

and μ_m is the coupling coefficient between the m-th fluid pressure mode and BM displacement:

$$\mu_m = \int_{-b/2}^{b/2} \phi_m(y)\psi(y)dy. \tag{2.25}$$

The governing equations for the mechanical model are found using Hamilton's principle by taking the variation with respect to each of the mechanical DOFs (U_{bm}, u_{tms}, and u_{tmb})[91].

2.2.3 Electrical domain and mechanical-electrical coupling

The model uses an electrical domain model formulation very similar to that developed by Meaud and Lemons[82]. A circuit diagram of the model is shown in Figure 2.5.

New to this work, a current path was added from the scala media potential, ϕ_{sm}, to ground (with resistance R_{mg}). Such a current path is physically realistic and has been included in previous models[92,93]. In a model with three rows of OHCs (Figure 2.5A), cochlear nonlinearity is the consequence of the nonlinearity of the hair bundle mechano-

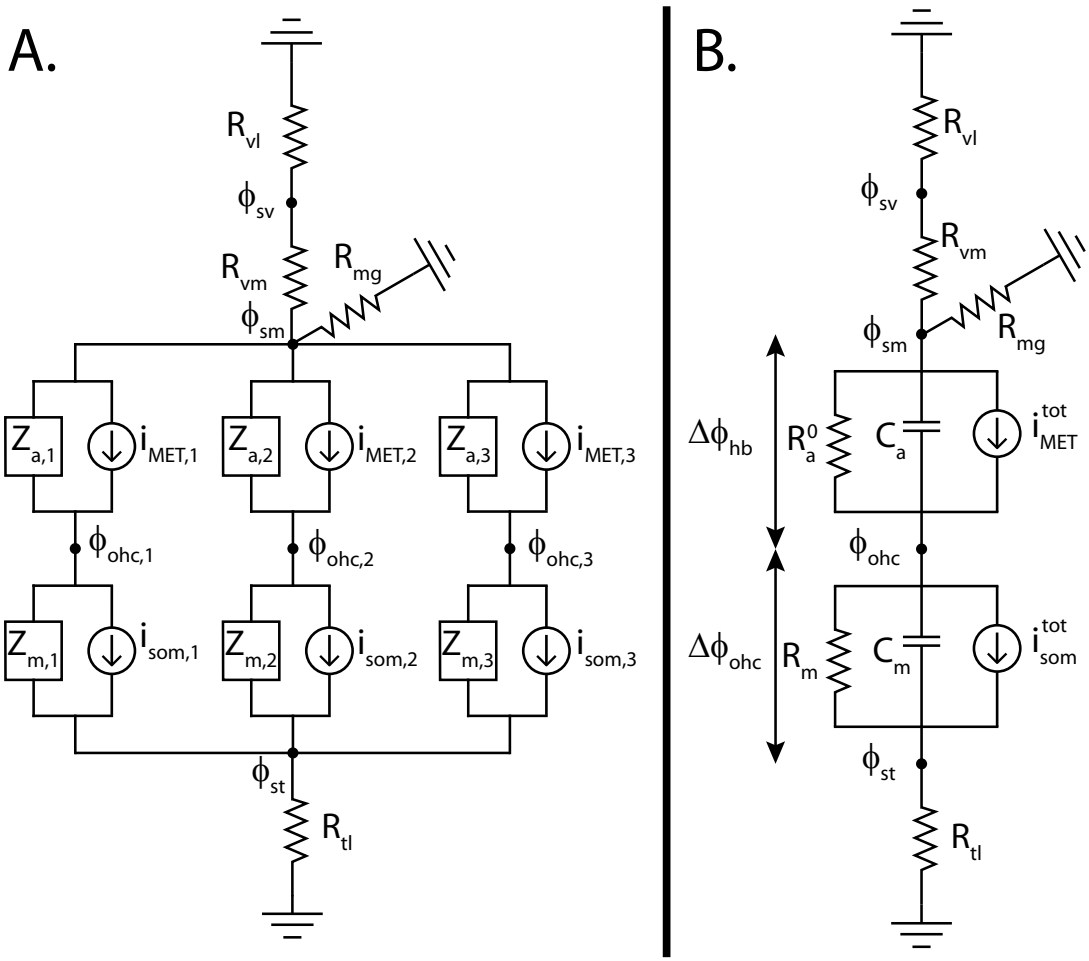

FIGURE 2.5. Circuit diagram of the electrical model. (A.) Model with three independent rows of OHCs. (B.) Equivalent model that was actually implemented. The model was obtained when the approximations in Equations 2.32 and 2.33 are applied to the model shown in panel A.

electrical transduction (MET) current, $i_{MET,j}$ where $j = 1,2,3$ for each of the three hair bundles. The MET current for the j-th hair bundle is given by:

$$i_{MET_j}(u_{hb/rl_j}) = G_{hb}^{max}\Delta V_{hb}^{0}\Big(P_0(u_{hb/rl_j}) - P_0^s\Big) \tag{2.26}$$

where G_{hb}^{max} is the saturating hair bundle MET conductance; P_0^s is the resting open probability of the MET channel (assumed to be equal to 0.4); ΔV_{hb}^{0} is the resting value of the difference between the scala media potential and intracellular OHC potential; P_0 is the open probability of the MET channel. The open probability of the MET channel is a Boltzmann

equation:

$$P_0(u_{hb/rl_j}) = \frac{1}{1+\exp\left[-\frac{u_{hb/rl_j}-X_0}{\Delta X}\right]} \tag{2.27}$$

where ΔX and X_0 are displacements given by

$$\Delta X = \frac{f_{gs}\gamma}{k_B T} \tag{2.28}$$

$$X_0 = \Delta X \log\left(\frac{1}{P_0^s} - 1\right) \tag{2.29}$$

where f_{gs} is the single channel gating force in the tip link direction; γ is the geometric gain factor; k_B is the Boltzmann constant; T is the temperature.

Somatic electromotility (i.e. the piezoelectric-like nature of the OHCs) is modeled by the following linear equations (that maintain reciprocity):

$$i_{som_j}(t) = -\varepsilon_3 \dot{u}^{comp}_{ohc_j}(t) \tag{2.30}$$

$$f_{ohc_j}(t) = \varepsilon_3 \Delta\phi_{ohc_j}(t) \tag{2.31}$$

where $j = 1,2,3$ for the j-th OHC; $\Delta\phi_{ohc_j} = \phi_{ohc,j} - \phi_{st}$, and f_{ohc_j} are the perturbations in the somatic current and electromechanical force from their resting values, respectively for the j-th OHC; ε_3 is the electromechanical coupling coefficient.

The model represented in Figure 2.5A includes six degrees of freedom (ϕ_{sv}, ϕ_{sm}, $\phi_{ohc,1}$, $\phi_{ohc,2}$, $\phi_{ohc,3}$, and ϕ_{st}). In the model that was actually implemented (Figure 2.5B), two approximations were made:

$$u_{hb/rl_j} = u^{avg}_{hb/rl} \tag{2.32}$$

$$u^{comp}_{ohc_j} = u^{comp}_{ohc}|_{avg} \tag{2.33}$$

where $u^{avg}_{hb/rl}$ and $u^{comp}_{ohc}|_{avg}$ are defined in Equations 2.15 and 2.16. As a consequence of

these approximations:

$$i_{MET}^{tot}(u_{hb/rl}^{avg}) = \sum_{j=1}^{3} i_{MET,j}(u_{hb/rl}^{avg}) \tag{2.34}$$

$$i_{som}^{tot}(t) = \sum_{j=1}^{3} i_{som,j}(t) \tag{2.35}$$

$$f_{ohc}(t) = \sum_{j=1}^{3} f_{ohc,j}(t) \tag{2.36}$$

$$\phi_{ohc} = \phi_{ohc,1} = \phi_{ohc,2} = \phi_{ohc,3} \tag{2.37}$$

The electrical impedances $Z_{a,j}$ and $Z_{m,j}$ shown in Figure 2.5A are related to the resistors and capacitors shown in Figure 2.5B if a harmonic response (with angular frequency ω) is assumed:

$$Z_a = R_a^0 + \frac{1}{i\omega C_a} = \frac{1}{3} Z_{a_j} \tag{2.38}$$

$$Z_m = R_m + \frac{1}{i\omega C_m} = \frac{1}{3} Z_{m_j} \tag{2.39}$$

where i is the unit imaginary number; R_a^0 and C_a are the apical resistance and capacitance, respectively, of the OHC; R_m and C_m are the basolateral resistance and capacitance of the OHC. Because the resistances and capacitances are the same for all three OHCs; as a result $Z_{a,1} = Z_{a,2} = Z_{a,3}$ and $Z_{m,1} = Z_{m,2} = Z_{m,3}$.

In the active linear formulation of model, the MET current (Equation 2.34) is linearized by taking a Taylor series expansion about $u_{hb/rl}^{avg} = 0$:

$$i_{MET}^{tot,lin}(u_{hb/rl}^{avg}) = \left.\frac{di_{MET}^{tot}}{du_{hb/rl}^{avg}}\right|_{u_{hb/rl}^{avg}=0} u_{hb/rl}^{avg} = G_{hb}^{max} \Delta V_{hb}^0 \frac{1}{\Delta X} P_0^s (1 - P_0^s) u_{hb/rl}^{avg} \tag{2.40}$$

This active model represents the response at a low stimulus level. A linear passive model is also considered and is analogous to the response at high stimulus levels (because the feedback from the OHCs saturates such that it has almost no effect on the acoustic response

of the system at high sound pressure levels). The passive model is obtained by setting $i_{MET} = 0$.

The DOFs of the electrical model at each cross section are: the potential in the SV, ϕ_{sv}; the potential in the SM, ϕ_{sm}; the potential at the OHCs, ϕ_{ohc}; and the potential in the ST, ϕ_{st} for the model shown in Figure 2.5B. The governing electrical domain equations are determined using Kirchhoff's law:

$$\mathbf{c_e}\dot{\phi} + \mathbf{k_e}\phi + \mathbf{i_s}(\mathbf{u_c}) = \mathbf{0} \tag{2.41}$$

where

$$\mathbf{c_e} = \begin{pmatrix} 0 & 0 & 0 & 0 \\ 0 & -C_a & C_a & 0 \\ 0 & C_a & -C_a - C_m & C_m \\ 0 & 0 & C_m & -C_m \end{pmatrix} \tag{2.42}$$

$$\mathbf{k_e} = \begin{pmatrix} -\frac{1}{R_{vl}} - \frac{1}{R_{vm}} & \frac{1}{R_{vm}} & 0 & 0 \\ \frac{1}{R_{vm}} & -\frac{1}{R_{vm}} - \frac{1}{R_a^0} - \frac{1}{R_{mg}} & \frac{1}{R_a^0} & 0 \\ 0 & \frac{1}{R_a^0} & -\frac{1}{R_a^0} - \frac{1}{R_m} & \frac{1}{R_m} \\ 0 & 0 & \frac{1}{R_m} & -\frac{1}{R_{tl}} - \frac{1}{R_m} \end{pmatrix} \tag{2.43}$$

$$\mathbf{i_s}(\mathbf{u_c}) = \begin{pmatrix} 0 \\ -i_{MET}^{tot} \\ i_{MET}^{tot} - i_{som}^{tot} \\ i_{som}^{tot} \end{pmatrix} \tag{2.44}$$

where $\phi = [\phi_{sv}, \phi_{sm}, \phi_{ohc}, \phi_{st}]^T$; C_a and R_a^0 represent the apical capacitance and resistance of the OHCs; C_m and R_m represent the basolateral capacitance and resistance of the OHCs; R_{vl} is the resistance seen by the current flowing from the SV to ground; R_{vm} is the resistance seen by the current flowing from the SV to the SM; R_{mg} is the resistance seen by the

current flowing from the SM to ground; R_{tl} is the resistance seen by the current flowing from the ST to ground. Closer inspection of $\mathbf{c_e}$ (Equation 2.42) reveals that it is a singular matrix of rank 2, such that Equation 2.41 is not a system of ordinary differential equations (ODEs), but is rather a system of differential algebraic equations (DAEs). This system can be transformed into a system of ODEs of the same form as Equation 2.41 where $\phi = [\Delta\phi_{hb} = \phi_{sm} - \phi_{ohc}, \Delta\phi_{ohc} = \phi_{ohc} - \phi_{st}]^T$:

$$\mathbf{c_e} = \begin{pmatrix} C_a & -C_m \\ C_a & 0 \end{pmatrix} \tag{2.45}$$

$$\mathbf{k_e} = \begin{pmatrix} \frac{1}{R_a^0} & -\frac{1}{R_m} \\ \frac{1}{R_a^0} + \frac{1}{R_{eq}} & \frac{1}{R_{eq}} \end{pmatrix} \tag{2.46}$$

$$\mathbf{i_s}(\mathbf{u_c}) = \begin{pmatrix} i_{MET}^{tot}(\mathbf{u_c}) - i_{som}^{tot}(\mathbf{u_c}) \\ i_{MET}^{tot}(\mathbf{u_c}) \end{pmatrix} \tag{2.47}$$

where

$$R_{eq} = R_{tl} + \left(\frac{1}{R_{vl} + R_{vm}} + \frac{1}{R_{mg}}\right)^{-1} \tag{2.48}$$

In this form, the matrix $\mathbf{c_e}$ (Equation 2.45) is of full rank. In previous versions of the model[82,94,95], the resistance from the SM to ground (R_{mg}) was infinite.

2.3 Middle ear model

For this work, a one DOF model of the middle ear was developed to enable easy modification of the boundary conditions at the stapes (Figure 2.6). In this model, the displacement of the stapes, u_s, is the DOF and its equation of motion is:

$$M_s\ddot{u}_s + C_s\dot{u}_s + K_s u_s = -f_s(t) + f(t) \tag{2.49}$$

where M_s, C_s, and K_s are the mass, damping, and resistance of the stapes; $f(t)$ is the stimulus force applied on the stapes; f_s is the force of the fluid in the scala vestibuli applied on the stapes:

$$f_s(t) = W \int_0^H P^{(0)}(0,z,t)dz \tag{2.50}$$

Because the stapes is modeled as a rigid body covering the entire cross section of the scala vestibuli, only the plane wave mode of the pressure ($P^{(0)}$) is coupled to the stapes. To convert the stimulus force magnitude to an ear canal pressure in dB SPL (with reference pressure of 20 μPa), the magnitude of the pressure in the SV at the stapes in response to a pure tone was examined; the ear canal pressure was assumed to be 30 dB lower than the pressure in the SV, based on measurements of the forward middle ear pressure transfer function in the gerbil[96,97]. To account for the reverse propagation of sound through the gerbil middle ear[97], a gain of -35 dB was added to convert the pressure at the stapes into the ear canal pressure.

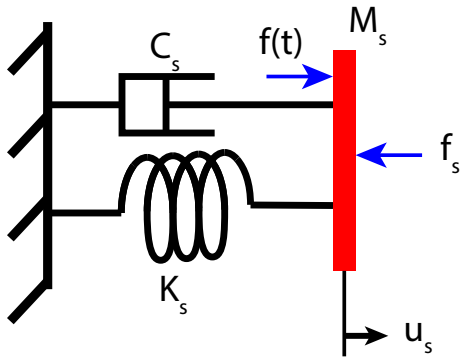

FIGURE 2.6. Free body diagram of the stapes.

2.4 Finite element and state space formulations

2.4.1 Finite element formulation

Applying the finite element method[98] to the governing equations results in the following equation for the acoustic, mechanical, and electrical domains:

$$\begin{pmatrix} \mathbf{M_s} & \mathbf{0} & \mathbf{0} \\ \mathbf{M_{sf}} & \mathbf{0} & \mathbf{0} \\ \mathbf{0} & \mathbf{0} & \mathbf{0} \end{pmatrix} \begin{pmatrix} \ddot{\mathbf{u}} \\ \ddot{\mathbf{p}} \\ \ddot{\phi} \end{pmatrix} + \begin{pmatrix} \mathbf{C_s} & \mathbf{0} & \mathbf{0} \\ \mathbf{0} & \mathbf{0} & \mathbf{0} \\ \mathbf{C_{es}} & \mathbf{0} & \mathbf{C_e} \end{pmatrix} \begin{pmatrix} \dot{\mathbf{u}} \\ \dot{\mathbf{p}} \\ \dot{\phi} \end{pmatrix} + \begin{pmatrix} \mathbf{K_s} & \mathbf{K_{fs}} & \mathbf{K_{se}} \\ \mathbf{0} & \mathbf{K_f} & \mathbf{0} \\ \mathbf{K_{es}^{lin}} & \mathbf{0} & \mathbf{K_e} \end{pmatrix} \begin{pmatrix} \mathbf{u} \\ \mathbf{p} \\ \phi \end{pmatrix} + \begin{pmatrix} \mathbf{0} \\ \mathbf{0} \\ \mathbf{F_{es}^{NL}}(\mathbf{u}) \end{pmatrix} = \begin{pmatrix} \mathbf{F_u} \\ \mathbf{0} \\ \mathbf{0} \end{pmatrix} \tag{2.51}$$

where $\mathbf{F_u} = [f_s, 0, ..., 0]^T$ where f_s is the stimulus force applied on the stapes; $\mathbf{u}$ a vector of the displacements of all the mechanical DOFs; $\mathbf{p}$ is a vector of all the cochlear fluid pressure DOFs; ϕ is a vector of the potentials of all the electrical DOFs.

2.4.2 State space formulation

Equation 2.51 is a system of differential algebraic equations. Recognizing that the second row of the matrices on Equation 2.51 only depend in $\ddot{u}$ and p, the pressure degrees of freedom can be eliminated:

$$\mathbf{p} = -\mathbf{K_f}^{-1}\mathbf{M_{sf}}\ddot{\mathbf{u}}. \tag{2.52}$$

Equation 2.51 may then be rewritten as a system of ordinary differential equations (ODEs) if the matrix $\mathbf{C_e}$ is non-singular:

$$\begin{pmatrix} \mathbf{M_{eff}} & \mathbf{0} \\ \mathbf{0} & \mathbf{0} \end{pmatrix} \begin{pmatrix} \ddot{\mathbf{u}} \\ \ddot{\phi} \end{pmatrix} + \begin{pmatrix} \mathbf{C_s} & \mathbf{0} \\ \mathbf{C_{es}} & \mathbf{C_e} \end{pmatrix} \begin{pmatrix} \dot{\mathbf{u}} \\ \dot{\phi} \end{pmatrix} + \begin{pmatrix} \mathbf{K_s} & \mathbf{K_{se}} \\ \mathbf{K_{es}} & \mathbf{K_e} \end{pmatrix} \begin{pmatrix} \mathbf{u} \\ \phi \end{pmatrix} + \begin{pmatrix} \mathbf{0} \\ \mathbf{F_{es}^{NL}}(\mathbf{u}) \end{pmatrix} = \begin{pmatrix} \mathbf{F_u} \\ \mathbf{0} \end{pmatrix} \tag{2.53}$$

where the effective structural mass matrix, $\mathbf{M_{eff}}$ is given by:

$$\mathbf{M_{eff}} = \mathbf{M_s} - \mathbf{K_{fs}}\mathbf{K_f}^{-1}\mathbf{M_{sf}}. \tag{2.54}$$

Elliott *et al.*[99] proposed using a state space formulation for determining cochlear model responses in the time domain. Using the state variables $\mathbf{v} = [\dot{\mathbf{u}}, \mathbf{u}, \phi]^T$, the system (Equation 2.53) can be rewritten[82]:

$$\mathbf{M}\dot{\mathbf{v}} = \mathbf{A_{lin}}\mathbf{v} + \mathbf{NL}(\mathbf{v}) + \mathbf{F} \tag{2.55}$$

where:

$$\mathbf{M} = \begin{pmatrix} \mathbf{M_{eff}} & \mathbf{0} & \mathbf{0} \\ \mathbf{0} & \mathbf{I} & \mathbf{0} \\ \mathbf{0} & \mathbf{0} & \mathbf{C_e} \end{pmatrix} \tag{2.56}$$

$$\mathbf{A_{lin}} = -\begin{pmatrix} \mathbf{C_s} & \mathbf{K_s} & \mathbf{K_{se}} \\ -\mathbf{I} & \mathbf{0} & \mathbf{0} \\ \mathbf{C_{es}} & \mathbf{K_{es}^{lin}} & \mathbf{K_e} \end{pmatrix} \tag{2.57}$$

$$\mathbf{NL}(\mathbf{v}) = -\begin{pmatrix} \mathbf{0} \\ \mathbf{0} \\ \mathbf{F_{es}^{NL}}(\mathbf{u}) \end{pmatrix} \tag{2.58}$$

$$\mathbf{F} = \begin{pmatrix} \mathbf{F_u} \\ \mathbf{0} \\ \mathbf{0} \end{pmatrix} \tag{2.59}$$

The matrix **M** is called the mass matrix in numerical methods literature, but should not be confused with a structural mass matrix.

Using this state space formulation gives flexibility to the model in terms of the types of simulations and analyses that may be performed[99]. Equation 2.55 can be solved using an ODE solver to give the time domain response. For this work, the ODE solver used was MATLAB's (The MathWorks, Natick, MA) *ode45*, which is based on an explicit Runge-Kutta (4,5) formula. Effort was made to improve the runtime performance of the time domain simulations by reducing the number of operations performed at each time step and making better use of MATLAB's built-in matrix functionality. This effort ultimately resulted in a more than 5x speedup so that the simulations will complete approximately 460 ms per day (Appendix D). Assuming a harmonic response ($f(t) = Fe^{i\omega t}$) and setting $\mathbf{NL}(\mathbf{v}) = \mathbf{0}$, Equation 2.55 may be rewritten to give the linear response of the model in the

frequency domain:

$$(i\omega\mathbf{M} - \mathbf{A_{lin}})\mathbf{v} = \mathbf{F} \tag{2.60}$$

where i is the unit imaginary number; ω is the angular frequency of the stimulus and response. Setting $\mathbf{F} = \mathbf{0}$ and $\mathbf{NL}(\mathbf{v}) = \mathbf{0}$ in Equation 2.55 results in a generalized eigenvalue problem:

$$\mathbf{A_{lin}}\mathbf{x} = \lambda\mathbf{M}\mathbf{x} \tag{2.61}$$

where $\mathbf{x}$ are the eigenvectors and the eigenvalues, λ, are the poles of the system and can be written in the form:

$$\lambda = \sigma + i2\pi F \tag{2.62}$$

where σ is the real part and ω is the imaginary part. A positive value for σ indicates that the model has a linearly unstable mode that grows exponentially and oscillates at the frequency F[99]. The poles of the model are used in Chapter 6 to evaluate the linear stability of the model when the TM viscoelastic longitudinal coupling is reduced.

2.5 Summary of contributions and conclusions

This chapter provided a complete description of the current model formulation and discussed many of the key assumptions made for the current model. Descriptions of the acoustic, mechanical, and electrical models, as well as finite element and state space formulations were provided. The interested reader may also refer to Appendix A, which describes the kinematic relationships of the cochlear model. This chapter will provide a useful reference for future researchers needing a complete description of the model.

CHAPTER 3

MODEL CALIBRATION, VALIDATION, AND PARAMETER SENSITIVITY ANALYSIS

3.1 Chapter overview

Previous versions of the model had parameters to so that the geometry and model responses approximated those of the guinea pig. Because one of the goals of this work was to compare model responses to measurements made in the gerbil, it was necessary to first adjust the model parameters so that the model responses approximated those of the gerbil. Several times throughout this work, aspects of the model response were examined and weaknesses were identified. At each time, a successive iteration of the model was used as an attempt to addressed the identified weaknesses. The first of these model iterations (from here on referred to as the Bowling 2018 model) was used primarily for the study of DP propagation (Chapter 4). The second model (referred to as the Bowling 2019 model) was primarily used for the study of the effects on longitudinal TM coupling on cochlear stability (Chapter 6). The most recent model (referred to as the current model) was used to study the generation locations of DPs (Chapter 5). The relatively minor modifications made to the later two models will be discussed in the related chapter. A brief model convergence study is provided in Section 3.2. Section 3.4 describes the process used for calibrating the Bowling 2018 model and also includes a parameter sensitivity analysis performed before calibration to determine how the structural parameters affect model response. The results of this analysis provided guidance in determining which model parameters should be the focus of

calibration. After calibration, the model is validated by comparing its response to other experimental data in Section 3.5.

3.2 Model convergence

It is necessary for the model to have a fine enough mesh for the finite element method to provide accurate results. Two convergence studies were performed using the linear model before its calibration. The first convergence study (Figure 3.2) was performed to determine the number of longitudinal elements needed to accurately capture the BM velocity response. The spatial response of the BM velocity for three meshes with different number of longitudinal elements are shown in Figure 3.1. The differences between the models are most visible around the peak (Figure 3.1B and 3.1D). Increasing the number of longitudinal elements results in an increase in the magnitude of the peak (Figure 3.1B) and the slope of the phase to become steeper (Figure 3.1D). Additionally, the peak position changes very slightly depending on the mesh (Figure 3.1B).

For this convergence study, the results from a model with N_x=1,345 nodes was used as the reference. The error at the peak of the traveling wave was evaluated in response to a 20 kHz tone:

$$E_i = 20\log_{10}\left|\frac{|V_{bm}^{ref}| - |V_{bm,i}|}{|V_{bm}^{ref}|}\right| \tag{3.1}$$

where V_{bm}^{ref} is the complex value of the BM velocity at the peak position for the N_x=1,345 model and $v_{bm,i}$ is the complex value of the BM velocity at the peak position with $N_x = i$. Similarly, the error of the phase at the peak is given by:

$$E_i = |\angle V_{bm}^{ref} - \angle V_{bm,i}|. \tag{3.2}$$

The error in the magnitude and phase of the peak BM velocity in response to a 20 kHz pure tone decreases as the number of longitudinal elements decreases (Figure 3.2). For the

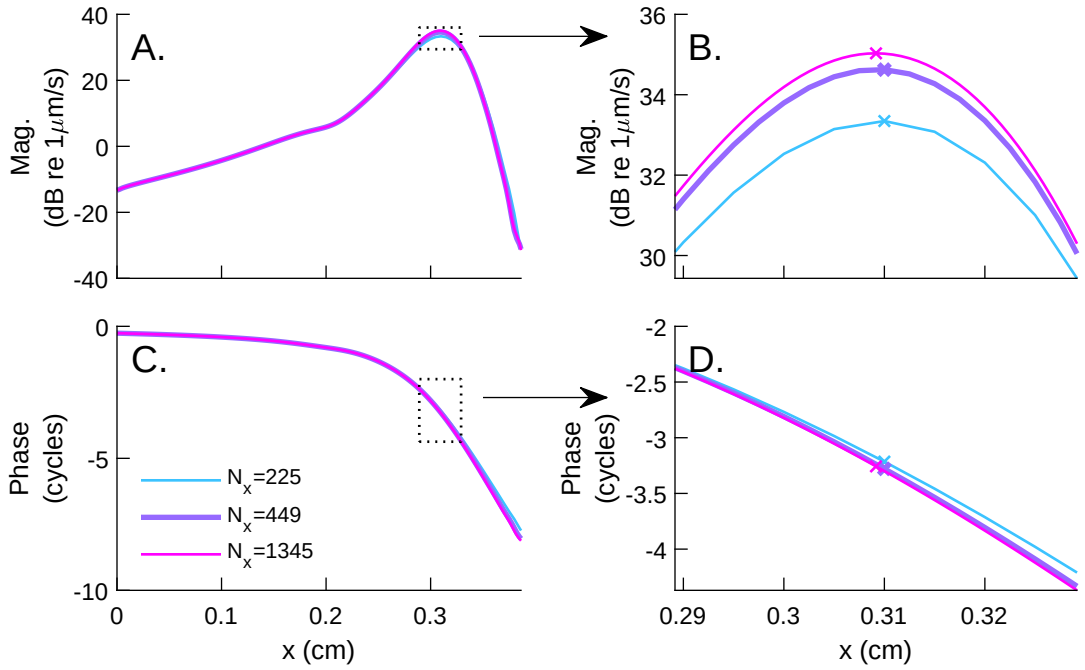

FIGURE 3.1. BM velocity in response to a pure tone at 20 kHz for models with different numbers of longitudinal elements. (A.) Magnitude. (C.) Phase. (B. and D.) Zoomed views around the peak indicated by the boxes in panels A. and C. The peak positions for each model are indicated with the x's.

baseline mesh used throughout this work (N_x=449 nodes, which corresponds to element lengths of 25 micron), the relative error in the magnitude is -27 dB and the relative error in the phase is 0.022 cycles. The computational time required to run a time domain simulation increases at $O((N_x)^4)$ (Appendix D), which makes running many simulations with a large number of nodes infeasible. Using N_x=449 strikes a good balance between mesh accuracy and computational time.

A second study was performed to determine the number of fluid modes needed to accurately capture the 3D nature of the fluid. The effect of the number of modes included on the pressure magnitude at the 20 kHz BP (Equation 2.6) is shown in Figure 3.3. For this convergence study, the results for the model with 75 fluid modes was used as the reference. In Figure 3.3A, while there is significant variation in the magnitude for 1, 3, and 8 modes at $y = 0$, for 25 modes the results matches very closely with the results for 75 modes. The

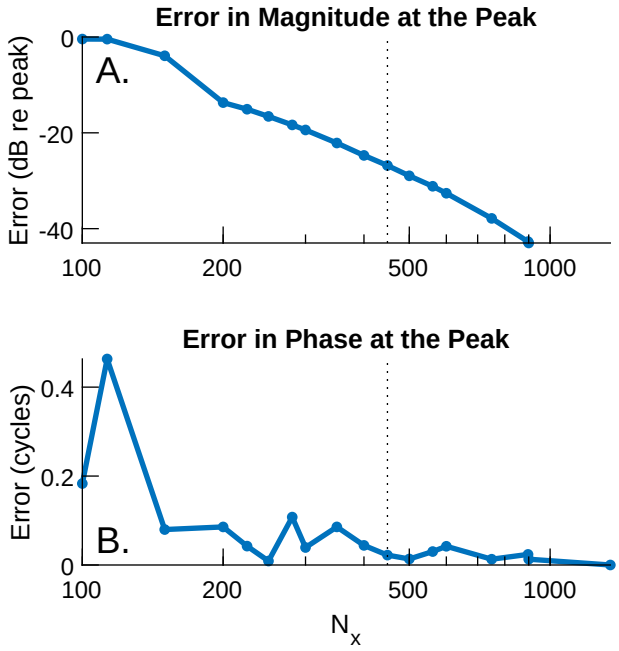

FIGURE 3.2. Error of the BM velocity at the peak for varied numbers of elements. The vertical dashed line denotes the baseline mesh (N_x=449).

relative percent error of the fluid pressure shown in Figure 3.3B is given by:

$$E_i = \left| \frac{P_{75} - P_i}{P_{75}} \right| \times 100\% \tag{3.3}$$

where P_{75} is the complex value of the pressure at $y = 0$ for the model with 75 fluid modes, and P_i is the complex value of the pressure for the model with i fluid modes. While the magnitude difference is fairly large for a model with only 1 mode, i.e. a 2D model, by 9 modes the pressure magnitude is within 0.1 dB of the 75 mode pressure magnitude and relative error of 1.2 percent. Although fewer modes (but more than 9) could have been used to accurately model the pressure, in this work 25 modes were used. Using the original[82] matrix assembly formulation, there is a significant increase in computational cost when using more fluid modes (see Appendix D for performance characterization and improvements made). The increase in computational cost was mitigated by assembling the finite element matrices only once and then loading them from a file for each subsequent simulation. Once the matrices are assembled, the number of modes has no influence on the computational

time needed to solve Equation 2.55.

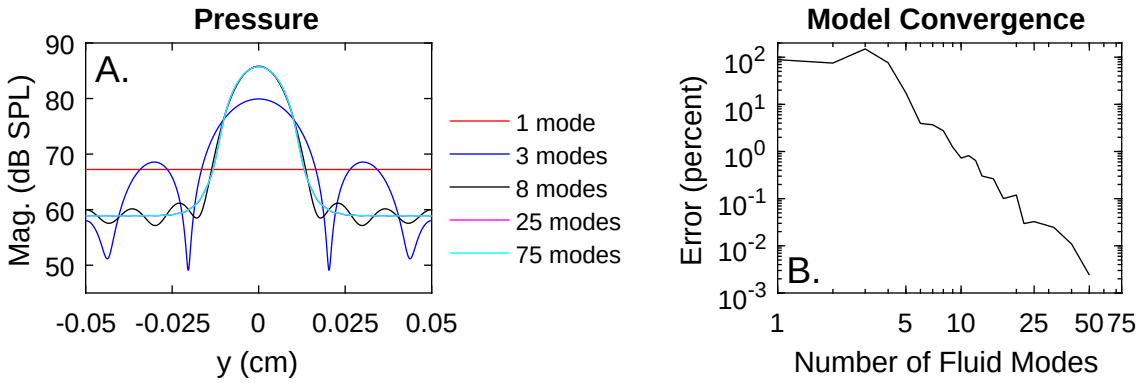

FIGURE 3.3. Convergence study for the number of fluid modes at z=0 in the SV at 20 kHz and its BP. A. Radial variations of the pressure magnitude. B. Relative percent error of the fluid pressure at y=0 relative to model with 75 pressure modes. Figure source: Ref.[94].

3.3 Middle ear model

When reverse traveling waves in the fluid reach the stapes, part of the energy is transmitted through the middle ear and into the ear canal while the rest is reflected by the stapes back towards the apex as a forward traveling wave. The stapes reflection coefficient is given as[100]:

$$R_{st} = \frac{Z_{meR}/Z_c^* - 1}{Z_{meR}/Z_c + 1} \tag{3.4}$$

where Z_{meR} is the reverse middle ear impedance (*i.e,* the impedance looking out from the stapes in the reverse direction[101]); Z_c is the input impedance of the cochlea. The reverse middle ear impedance is given in the frequency domain by:

$$Z_{meR} = \frac{1}{A_s^2}\left[M_s i\omega + C_s + \frac{K_s}{i\omega}\right] \tag{3.5}$$

where $A_s = WH$ is the area of the stapes. The input impedance of the cochlea (if the cochlea is stimulated from the middle ear side at the stapes) is

$$Z_c = \frac{P_s}{i\omega u_s A_s} \tag{3.6}$$

The model calibration process primarily focused on the cochlear model and tuning its parameters. In parallel to this effort, several different sets of parameters were determined for the middle ear model to yield different stapes reflection coefficients (Equation 3.4): (1) a baseline model where the stapes reflection coefficient is similar to that in human cadavers reported by Puria[101]; (2) a model with $|R_{st}| \approx 1$; (3) a model with $|R_{st}|$ minimized at 16 kHz. Having several models with different stapes reflection coefficients enables studying the effect of stapes condition on the interaction of forward and reverse travelling waves within the cochlea. The reverse impedance of the middle ear and stapes reflection coefficient of these models are shown in Figure 3.4 and the parameters are provided in Appendix C. The stapes reflection coefficient also depends on the cochlear input impedance (Equation 3.4); the cochlear input impedance predicted by the Bowling 2018 model is similar to (but slightly higher than) the impedance calculated from experimental measurements in the gerbil[102,103] (Figure 3.4A, D).

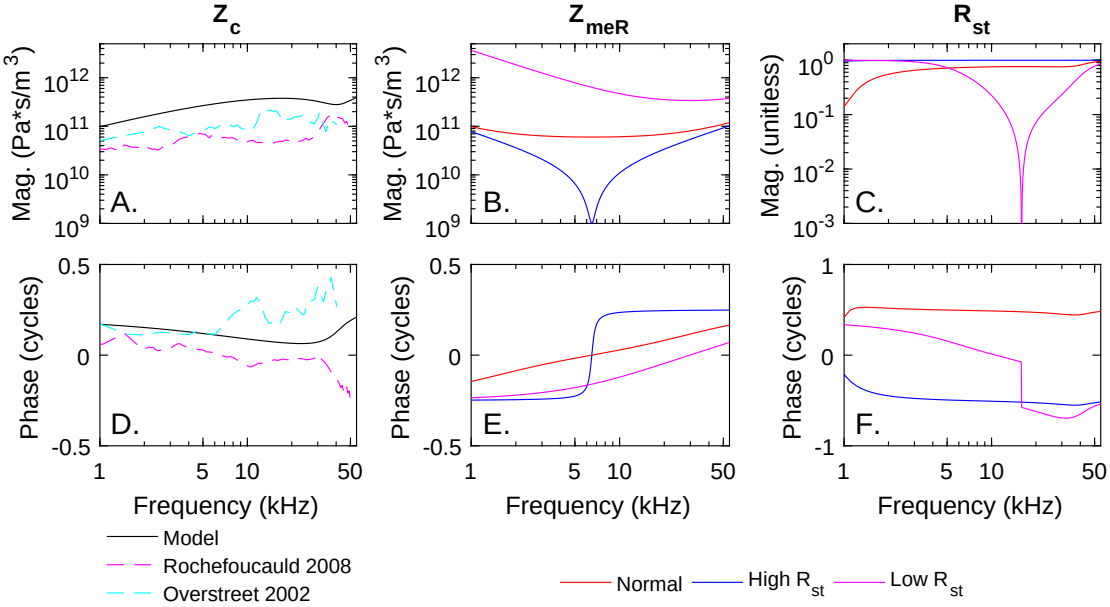

FIGURE 3.4. Different middle ear models. A. and D. Magnitude and phase of the cochlear input impedance of the Bowling 2018 model, compared to data from[102,103]. B.,E. Magnitude and phase of the reverse impedance of the middle ear model. C.,F. Magnitude and phase of the stapes reflection coefficient.

3.4 Model calibration

The cochlear model includes a large number of parameters. Although some parameters have been directly measured experimentally or can be estimated based on available data, there remains a significant number of parameters (more than a dozen) that needed to be adjusted manually. Where possible, parameter values were taken from values reported in the literature (e.g. many of the electrical model parameters). To determine the remaining parameters, an iterative process was used so that the model response would be analogous to experimental measurements made in the gerbil (Figure 3.5). Linear frequency domain simulations were used the model calibration because they are much faster than a nonlinear simulation and including nonlinearity was not required for calibration. Two types of linear models are used: (1) an active model that represents the model response at low stimulus level and (2) a passive model that represents the model response at high stimulus levels that is obtained by setting i_{MET}=0. The first step in model calibration was adjusting the geometric parameters so that the geometry of the model approximates the geometry observed by Edge *et. al*[90]; after this step the geometric parameters were fixed for all models. The remaining model parameters were then fit by alternatively matching the active and passive models to available measurements. A parameter sensitivity study was performed to determine how the model parameters affected the active and passive model responses. The results of this sensitivity study and an understanding of the concepts from dynamics and vibrations were lodestars for the calibration process. Although the model response is very sensitive to small changes in some of the parameters (e.g. the HB saturating conductance, G_{hb}^{max}, or the TM-bending mass, M_{tmb}), there are also some parameters that require very large changes to have meaningful effects on the model response (e.g. the RL and OHC stiffness, K_{rl} and K_{ohc}, respectively).

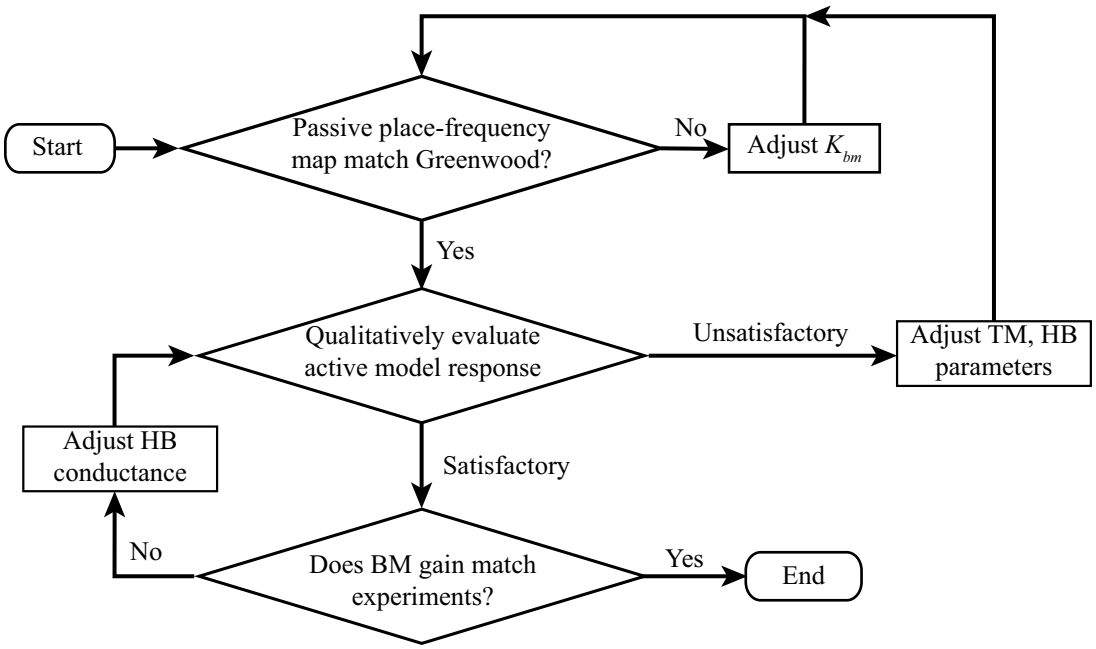

FIGURE 3.5. Flow chart of the model calibration process.

3.4.1 Passive model

Before discussing the process for calibrating the passive model, it is useful to discuss the relation between position and frequency in the cochlea. In Figure 3.6A, the BM velocity of the passive model is shown at three frequencies (3, 16, and 40 kHz). Each of these frequencies peaks at a specific position (the place-frequency map, Figure 3.6C). When the velocity is plotted against frequency (Figure 3.6B) at the positions of the peaks from Figure 3.6A, the peaks occur at the frequencies 3, 16, and 40 kHz. In Figure 3.6A and B, vertical dashed lines are used to denote the peak positions and frequencies, respectively; these lines are useful, especially when responses other than the BM velocity, and are used throughout this work.

A parameter sensitivity study was performed to determine which model parameters most significantly affect the BM response of the passive model (Figure 3.7). The passive model peak position is most sensitive to changes in either the BM stiffness, K_{bm} (Figure 3.7A), or the density of the cochlear fluid, ρ_f (Figure 3.7B). Varying the BM mass, M_{bm}, has little effect because the effective masses of the cochlear fluid and TM are significantly

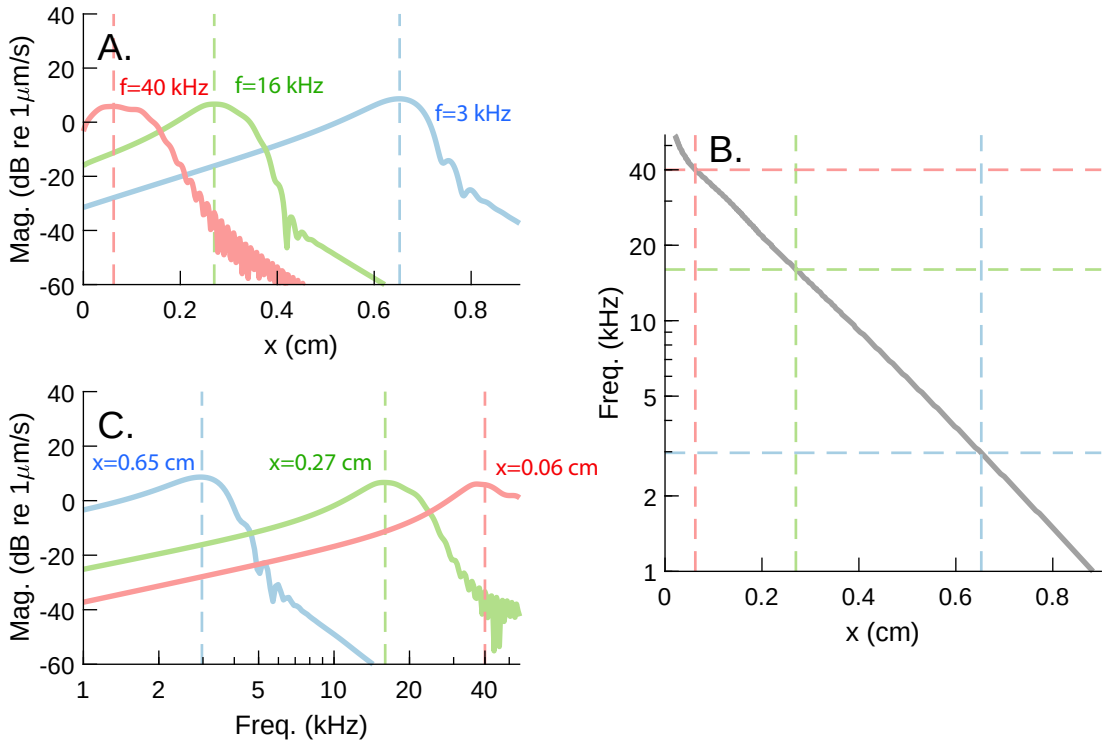

FIGURE 3.6. Passive Bowling 2018 model BM velocity response and place-frequency map. A. Velocity vs. position for the frequencies. B. Velocity vs. frequency taken at the peak positions of the frequencies shown in A. C. Passive model place-frequency map. The dashed lines denote the peak positions and frequencies.

larger. The dominant inertial term affecting the organ of Corti is the effective mass of the fluid (see Appendix B). For the baseline model at the 20 kHz peak position, the fluid has an effective mass 2 and 6 times larger than the mass of the TM in shear and bending, respectively. However, from an acoustics perspective the cochlear fluid is essentially water so the fluid density was not considered a free parameter during calibration. Unlike the BM stiffness, the passive model is relatively insensitive to changes in the stiffness of the RL, OHCs, and TM-bending mode.

As indicated by the parameter sensitivity study (Figure 3.7), very few of the model parameters significantly affect the passive model response, making calibrating the passive model a fairly straight-forward process. The main goal of calibrating the passive model was to insure that the passive model place-frequency map matches Greenwood's[4] place-

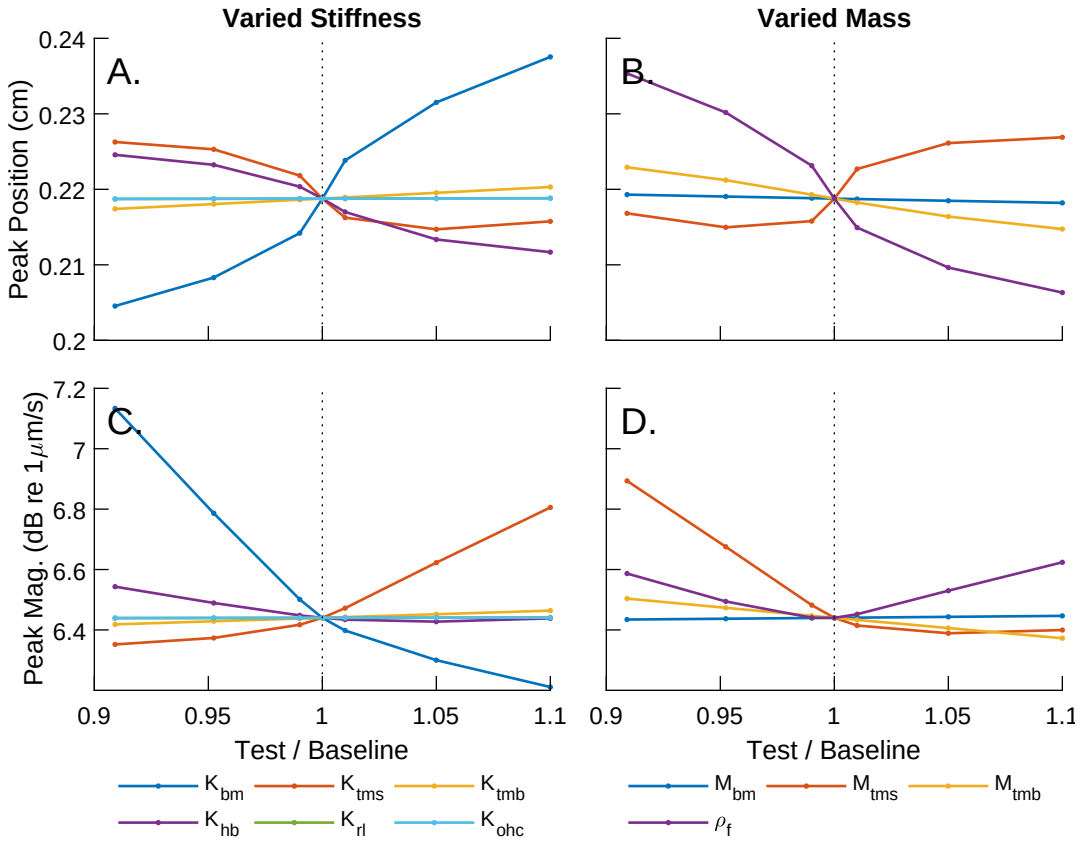

FIGURE 3.7. Effect of varying mechanical properties on passive 2018 model BM velocity peak position and magnitude in response to a 20 kHz pure tone. The abscissa is the change in the parameter relative to the baseline value. A. and B. Effect of varying parameters on the peak position. C. and D. Effect of varying parameters on the peak magnitude. A. and C. Effect of varying individual stiffness parameters. B. and D. Effect of varying individual mass parameters.

frequency map of the gerbil, which is given by:

$$CF = A(10^{a(L-x)/L} - k) \tag{3.7}$$

where CF is the characteristic frequency in kHz; A = 0.4 kHz; a=2.1; x is the longitudinal distance along the cochlear from the stapes; L is the length of the BM; k=0.35.

The stiffness of the BM decreases with increasing distance from the stapes[6] and is assumed to have the following form in the model:

$$K_{bm}(x) = K_{bm}(0)e^{\alpha_{Kbm}x}. \tag{3.8}$$

Just like increasing the stiffness of a simple harmonic oscillator increases its resonant frequency, increasing $K_{bm}(0)$ causes the CF for a given position to increase in frequency (e.g. at x=20%, a 25% increase in $K_{bm}(0)$ increases CF 16% from 19.4 kHz to 22.6 kHz, Figure 3.8A). Decreasing $K_{bm}(0)$ causes a similar reduction in CF for a given position. Varying the gradient of the BM stiffness, α_{Kbm}, has similar effects on the place-frequency map (Figure 3.8B): increasing the gradient (making α_{Kbm} more negative) causes the place-frequency map to have a steeper slope, while decreasing the gradient has the opposite effect. Matching Greenwood's place-frequency map (except at very basal and apical positions) is then easily accomplished by adjusting $K_{bm}(0)$ and α_{Kbm}.

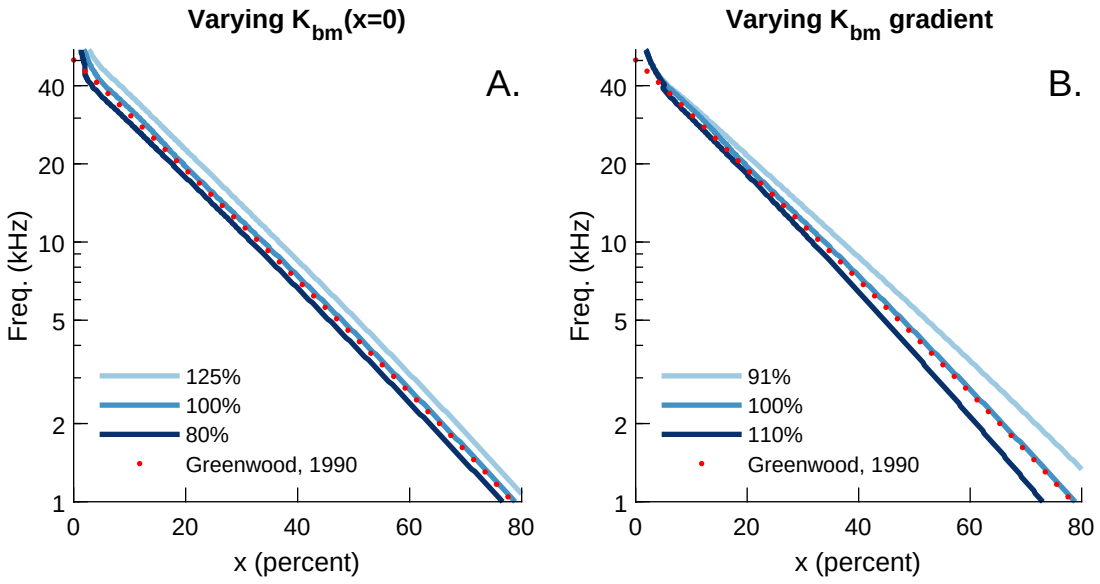

FIGURE 3.8. Effect of varying the BM stiffness on the passive model place-frequency map. The baseline model corresponds to 100%. A. Effect of making $K_{bm}(0)$ either 125% or 80% of the baseline value. B. Effect of making the BM stiffness gradient, α_{Kbm} either 91% or 110% of the baseline value. Greenwood's[4] gerbil place-frequency map is shown for reference.

3.4.2 Active model

Before discussing the process for calibrating the active model, it is beneficial to discuss the differences between the active and passive model responses. For a given frequency, the active model peaks at a more apical position and has a larger peak magnitude than the

passive model (Figure 3.9A). Similarly, for a given position, the active model peaks at a higher frequency and magnitude than the passive model (Figure 3.9C). This increase in magnitude is due to an active force (somatic electromotility) applied by the OHCs. Due to this difference in peak position and frequency, the active model place-frequency map is shifted up and/or to the right compared to the passive place-frequency map (Figure 3.9B). These changes in the response from passive to active are similar to what is observed in experiments when the stimulus level is varied (as discussed when the model is compared to experiments in subsequent figures).

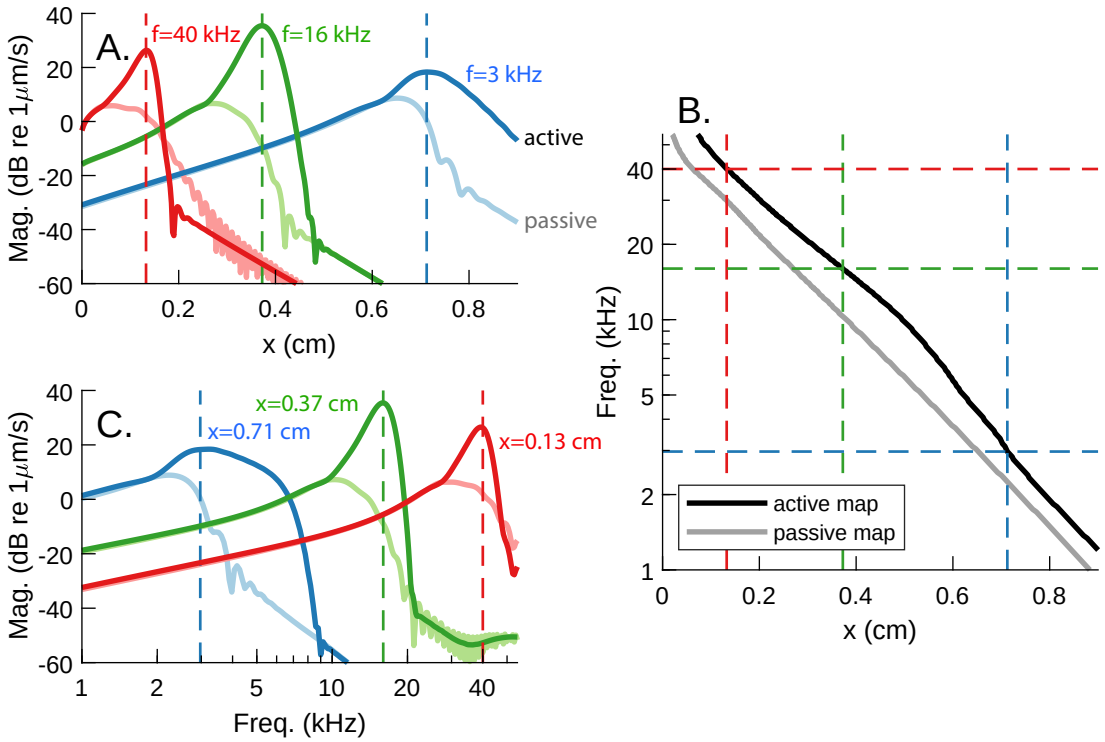

FIGURE 3.9. Passive and active Bowling 2018 model BM velocity responses and place-frequency maps. All other details are the same as Figure 3.6.

Due to the active force applied by the OHCs, changes in the model parameters have different effects on the passive model (Figure 3.7) and active model (Figure 3.10). For example, while varying the BM stiffness changes the peak position of the passive model, the peak position of the active model is relatively insensitive to any changes in the stiffness parameters. It is for this reason that the place-frequency map of the passive model was fit

before considering the active model. While the changes to the stiffness parameters changed the peak magnitude of the passive model by less than 1 dB (Figure 3.7C), similar changes to the active model result in a change of more than 3 dB in the peak magnitude (Figure 3.10C). Of all the model parameters considered, the model is most sensitive to changes in the mass of the TM-bending mode, M_{tmb}.

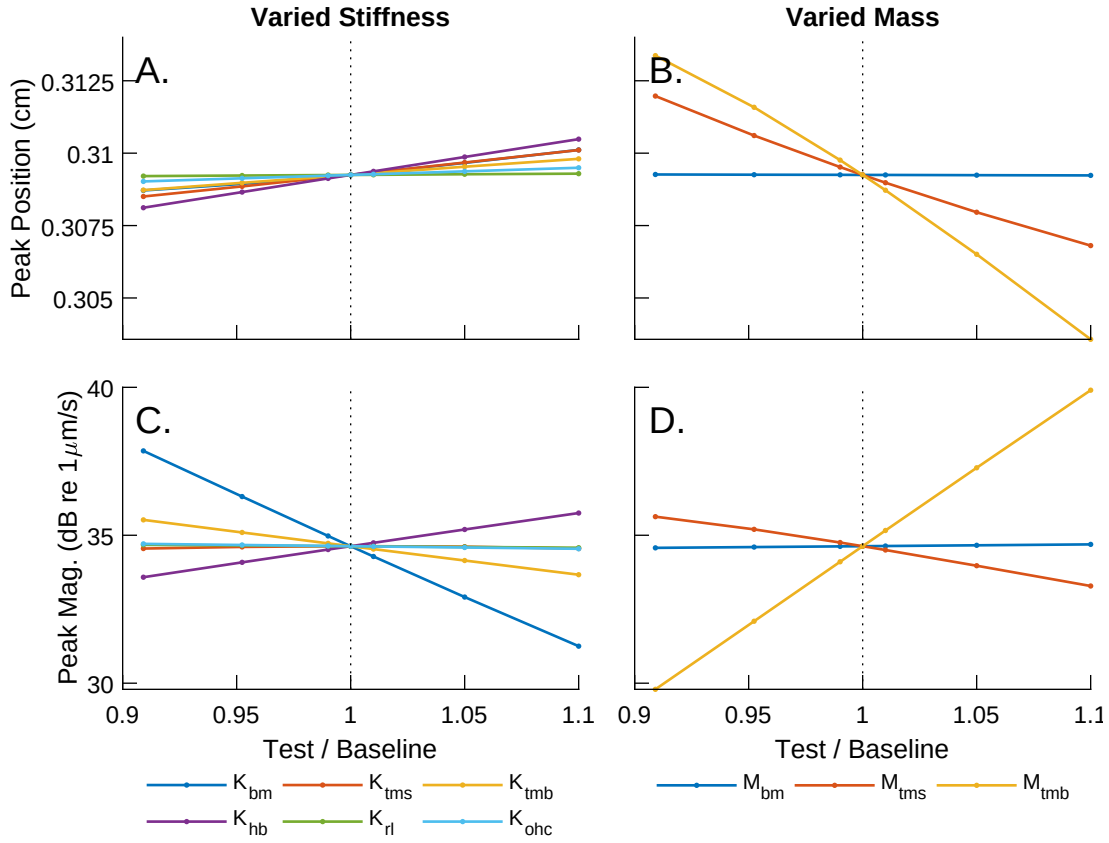

FIGURE 3.10. Effect of varying mechanical properties on the 2018 active model BM velocity peak position and magnitude in response to a 20 kHz pure tone. The abscissa is the change in the parameter relative to the baseline value. A. and B. Effect of varying parameters on the peak position. C. and D. Effect of varying parameters on the peak magnitude. A. and C. Effect of varying individual stiffness parameters. B. and D. Effect of varying individual mass parameters.

While fitting the passive model place-frequency map to the Greenwood place-frequency map is a straight-forward process and yields a near-exact match, evaluating if an active model is "good" is a much more subjective process. Multiple characteristics were considered when judging the active model response: the amount of BM gain; the sharpness

of tuning (measured by Q_{10dB}); the place-frequency map; the comparison of the model BM velocity response to experimental data at two longitudinal positions[85,86]; and does any parts of the model response appear non-physical or exhibit features that are not expected based on available experimental data. Although somewhat subjective, this last point is important because a model response may, by visual inspection, be clearly wrong even if all the chosen quantitative measures (e.g. gain and tuning) indicate that the model matches the experimental data well. The calibration process focused almost exclusively on the cochlear model; taking the response relative to the stapes eliminates the influence of the middle ear. At a longitudinal position x and frequency ω, the gain of the BM velocity relative to the stapes velocity is defined as:

$$G_{bm}(x,\omega) = \frac{V_{bm}(x,\omega)}{v_s(\omega)} \tag{3.9}$$

where V_{bm} and v_s are the velocities of the BM and stapes, respectively. The gain of the BM relative to the passive model is calculated as:

$$G_{bm}^{active/passive}(x) = \frac{\max_{\omega} |G_{bm}^{active}(x,\omega)|}{\max_{\omega} |G_{bm}^{passive}(x,\omega)|} \tag{3.10}$$

where G_{bm}^{active} is the gain of the BM velocity relative to the stapes for the active model, $G_{bm}^{passive}$ is the gain of the BM velocity relative to the stapes for the passive model, and the maximum amplitude is taken across frequency for a given position. Throughout this dissertation, "BM gain" refers to the gain of the BM relative to the passive model, $G_{bm}^{active/passive}$. The quality factor, Q_{10dB} is defined as:

$$Q_{10dB} = \frac{CF}{\Delta f} \tag{3.11}$$

where CF is the characteristic frequency at the considered position and Δf is the bandwidth where the response is 10 dB below the peak. Figure 3.11 provides an example of how both the BM gain and quality factor are calculated.

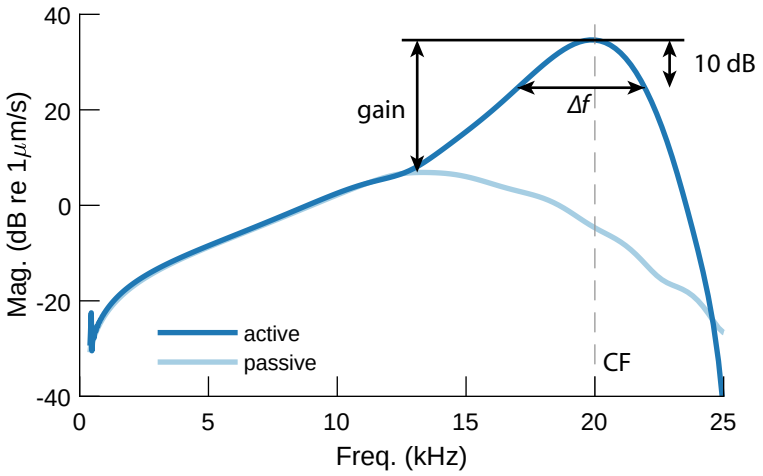

FIGURE 3.11. Example of determining the gain and tuning of the active model. The BM response of the active and passive model are shown at the 20 kHz best place.

Of all the model stiffness parameters, the HB stiffness is the only parameter for which increasing the stiffness results in an increase in the peak magnitude (Figure 3.10C). As a result, much of the calibration process focused on adjusting the HB stiffness. Like the BM stiffness, K_{bm} (Equation 3.8), the HB stiffness is assumed to have the following form in the model:

$$K_{hb}(x) = K_{hb}(0)e^{\alpha_{Khb}x}. \tag{3.12}$$

Increasing the HB stiffness results in an increase in the BM velocity and gain (Figure 3.12A-B), but has minimal effect on the BM phase (Figure 3.12C) compared to the baseline. Increasing the HB stiffness also results in sharper BM tuning (Figure 3.12D). Decreasing the HB stiffness has the opposite effect: low BM velocity and broader tuning. Unlike the active model, the passive model is relatively insensitive to changes in the HB stiffness (Figures 3.7, 3.12A, and 3.12C).

During calibration, the saturating HB conductance, G_{hb}^{max}, was adjusted so that the model BM gain would match the BM gain of the low level response relative to the high level response reported experimentally. Changing the HB conductance, however, affected more of the response than just the BM gain. Increasing the HB conductance by 10% not only increases the BM velocity and gain relative to the passive model, but also sharpens

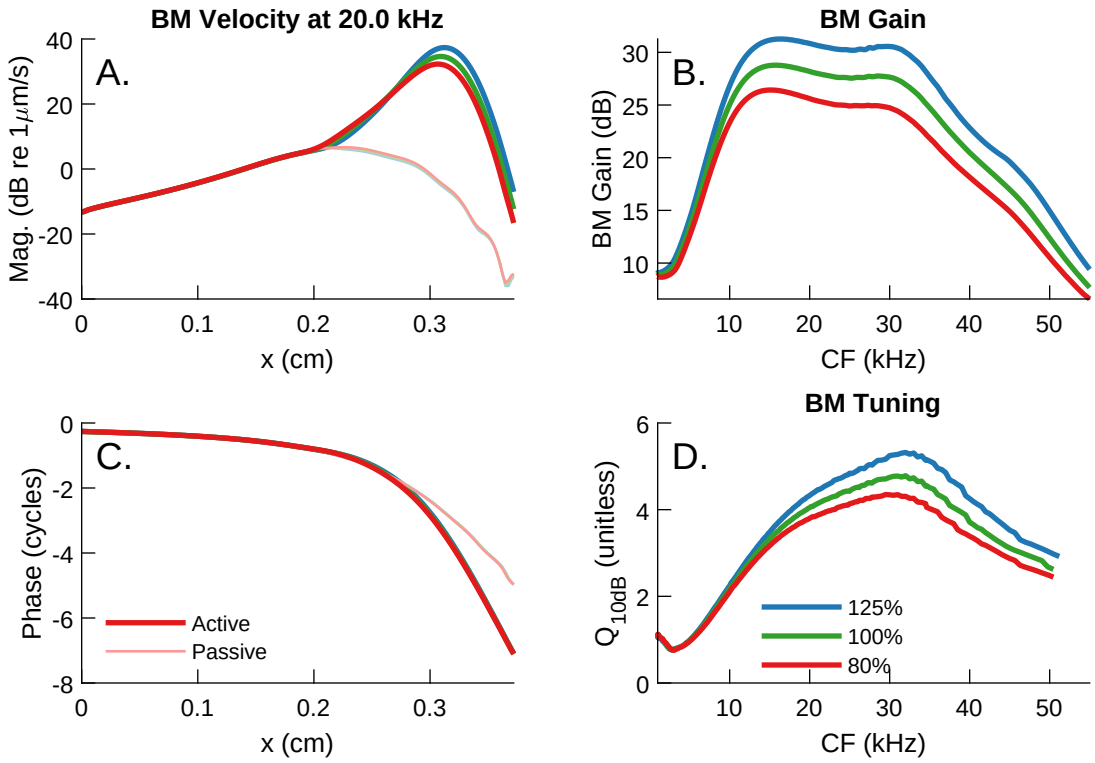

FIGURE 3.12. Effect of varying the HB stiffness on model response. The baseline model is shown as 100%. The HB stiffness, $K_{hb}(0)$, was either increased to 125% of the baseline value or decreased to 80% of the baseline value. A. and C. Magnitude and phase, respectively, of the BM velocity response at 20 kHz. B. Gain of the BM velocity relative to the passive model. D. Quality factor, Q_{10dB}, of the tuning of the BM.

the tuning (as quantified with Q_{10dB}, Figure 3.13D) and causes the BM velocity phase to decrease more (Figure 3.13C). Because changing a single parameter can change multiple aspects of the model response (sometimes for the worse), the calibration was achieved through hundreds of iterations of the trial-and-error process described earlier.

3.4.3 Pure tone response

The discussion thus far has focused on the process of model calibration, without describing what kinds of experimental data were used during calibration. The majority of the calibration process for the Bowling 2018 model relied on intracochlear measurements of the response of the BM to pure tones in the gerbil cochlea by Overstreet et al.[86] and Ren et al.[85]. In response to a 30 dB SPL stimulus (lowest stimulus level considered from exper-

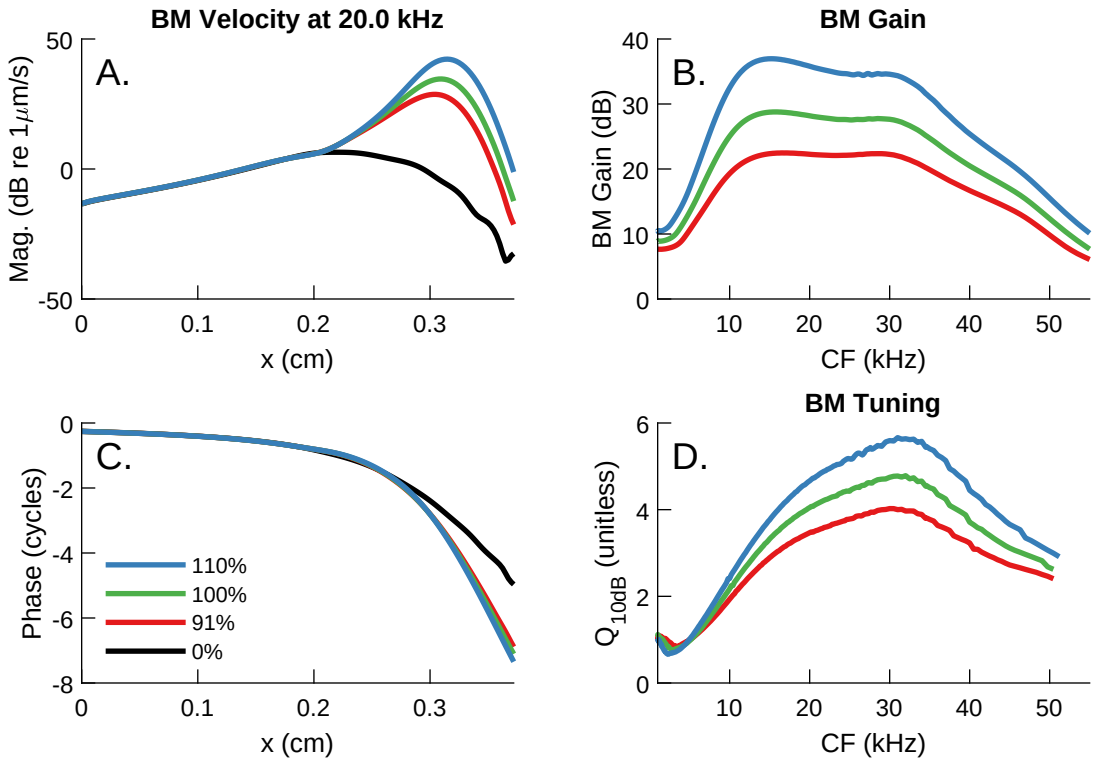

FIGURE 3.13. Effect of varying the saturating HB conductance, G_{hb}^{max}, on model response. The baseline active model is shown as =100% and the passive model is shown as 0%. Two additional cases are shown, for which the HB conductance was either increased or decreased by 10% from the baseline active model. Other details are the same as Figure 3.12.

imental data), the nonlinear model response and active linear model response are nearly identical. The passive model is analogous to the response to high stimulus levels when the MET current is completely saturated. However, at 90 dB SPL (one of the highest stimulus levels reported in the experimental data) the MET current is not completely saturated so that the passive model does not provide the most useful comparison. As a result, although the linear model was used for the calibration process, the model results in Figure 3.14 were obtained from the nonlinear time domain model to provide the most accurate comparison between model and experiment.

In Figures 3.14A and 3.14B, the magnitude of the BM gain relative to the stapes is normalized by the low SPL value of the gain at CF (to aid in comparison with experimental data) and is plotted as a function of frequency at two longitudinal positions (chosen to

match the positions of measurements of the BM response in from the experimental measurements[85,86]). At both positions, the sharpness of tuning seen in the low SPL results is similar to what is seen in the experimental data; furthermore, the gain of the low SPL to high SPL model results (22.6 dB for CF=34.6 kHz and 28.5 dB for CF = 13.4 kHz) is similar to what is seen in the experimental data (22.2 dB for CF=34.6 kHz and 27.5 dB for CF=13.4 kHz). This is a result of an effort during the calibration process to match the experimental gain and tuning sharpness seen in those experiments by tuning the value of the saturating HB conductance, G_a^{max}. At the more basal position (CF=34.6 kHz), the model high SPL results peak at 26 kHz and the experiment high SPL data peak at 24-25 kHz, whereas, at the more apical position (CF=13.4 kHz) both model and experimental high SPL results peak at 8-9 kHz. In Figure 3.14C, the model phase decreases at almost the same rate as the experimental results. In Figure 3.14D, both the low and high SPL model phases decrease at a faster rate than the experimental data. Having a model phase that rolls-off or decreases slightly more rapidly than what is observed experimentally is a common problem with cochlear models[104,105] and is an issue to varying degrees for all three iterations of the model presented in the dissertation.

3.4.4 Response at all longitudinal positions

The place-frequency map, BM gain at CF, and quality factor, Q_{10dB} are used to quantify the pure tone response of the model at all longitudinal positions (Figure 3.15). These results were obtained using the linear formulation of the model solved in the frequency domain. In Figure 3.15A, the passive and active model place-frequency maps are compared with experimental data from Refs. 85, 86 and Greenwood's place frequency map[4] for the gerbil cochlea. The passive model place-frequency map is in good agreement with Greenwood's map at all positions. At more basal positions, the relative frequency spacing between passive and active models for a given position matches the experimental results[86]. At the more apical position, the frequency difference between passive and active models

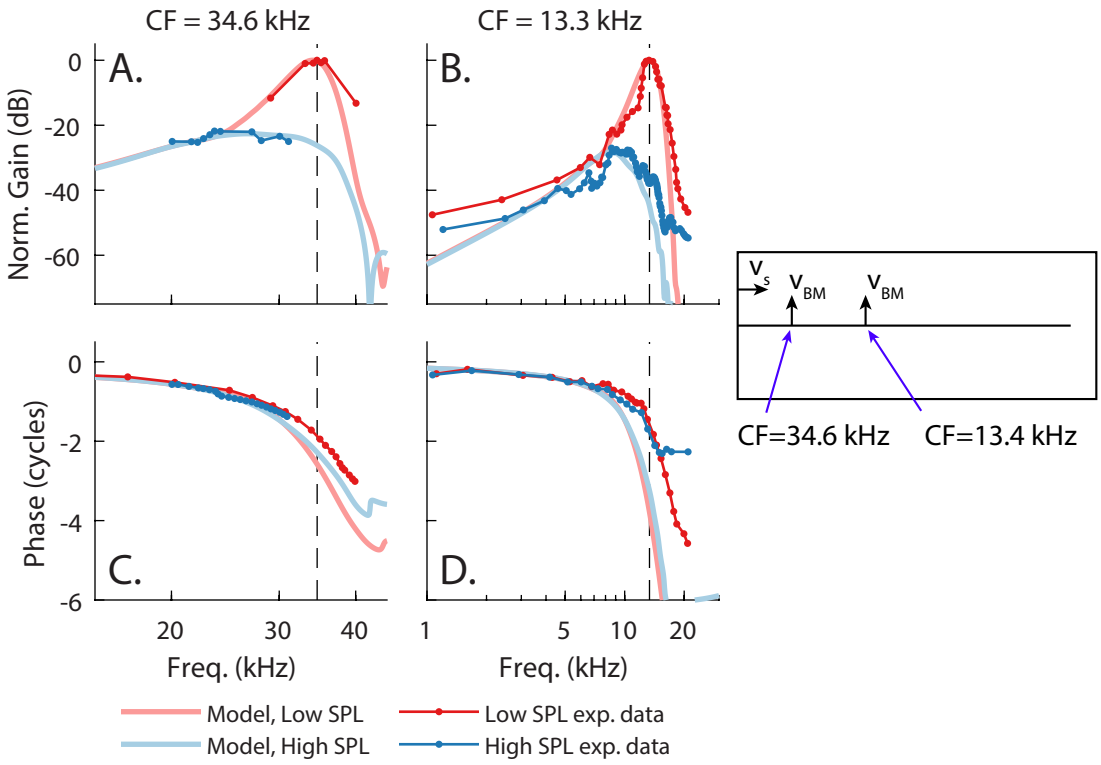

FIGURE 3.14. Comparison of BM pure tone response for the nonlinear model and experimental data[85,86]. (*A* and *B*) Gain of the BM velocity relative to the stapes velocity. The model gain was normalized by the gain predicted by the model at low SPL at CF (55 dB in *A* and 60 dB in *B*); the experimental data was normalized by the gain seen at CF in the low SPL experiments (53 dB in *A* and 49 dB in *B*). (*C* and *D*) Phase of the BM velocity relative to the stapes velocity. (*A* and *C*) Experimental data from Ref.[86] is given. (*B* and *D*) Experimental data from Ref.[85] is given. (*A* and *C*) Results for 30- and 90 dB SPL and 50- and 90 dB SPL stimuli, respectively. (*B* and *D*) Results for 30- and 100 dB SPL stimuli. The vertical black dashed lines denote CF. Figure modified from Bowling and Meaud, 2018[94].

for a given position is larger than that of the experimental results[85].

In Figure 3.15B, the BM gain is plotted as a function of the CF of each location and is compared with the gain calculated from the measurements from Refs. 85, 86. Across the range of frequencies of interest for this work, the model has at least 20 dB of gain from 7 to 40 kHz. Effort was made during the calibration process to match the experimental gain from 85, 86. The tuning sharpness of the active model, evaluated using the quality factor, Q_{10dB}, is shown in Figure 3.15C. As shown in Figures 3A and 3B, the model matches the tuning sharpness around 13 and 34 kHz best places from Refs. 85, 86. The model has fairly

broad tuning across frequency and becomes more broadly tuned towards the apex. Recent OCT measurements in the gerbil have indicated that the response in apical regions is more broadly tuned and fundamentally different from the response at more basal positions[106]. However, the focus of work in this dissertation is on basal regions and the response at the apex was not considered during model calibration.

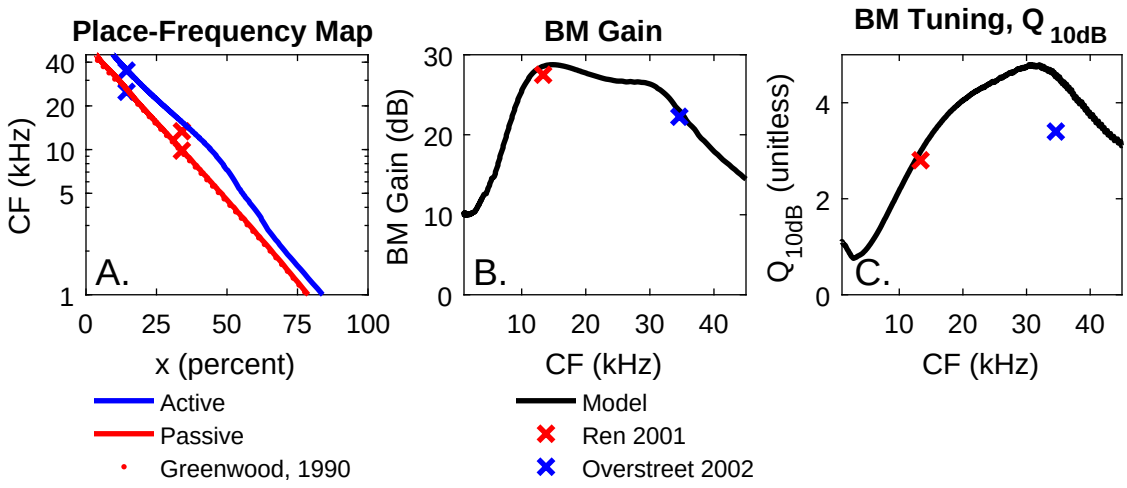

FIGURE 3.15. Comparison of BM pure tone response for model and experimental data from Refs.[4,85,86]. (*A*) Place-frequency map of the passive and active models with experimental data[4,85,86]. (*B*) Amplification of active model relative to passive model. (*C*) Quality factor, Q10dB, of the tuning of the BM. Model results are compared with measurements from the 13 kHz[85] and 34 kHz[86] best places. The stimulus levels used for computing the gain from the experimental data at the 13 and 34 kHz positions were 30 and 100; 30 and 90 dB SPL, respectively. The quality factors for the experiments were computed from the responses to a 30 dB SPL stimulus. Figure source: Bowling and Meaud, 2018[94].

3.5 Model validation

3.5.1 BM response to a pure tone

Once calibration of the model was complete, it was validated against other experimental pure tone data that was not used in model calibration. The nonlinear model was used for validation (and all results in this dissertation except for model calibration) against other sets of experimental data over the full dynamic range most commonly used in hearing studies (30-80 dB SPL). The model BM displacement is compared to BM displacement

data recently obtained with OCT at another location (CF=26.6 kHz) by He *et al.*[75]. The magnitude of the displacement is very similar to the experimental data in terms of the peak value at three sound pressure levels, tuning, and overall shape (Figure 3.16A). As was observed in Figure 3.14, the phase of the model BM displacement decreases quicker than is observed experimentally (Figure 3.16B).

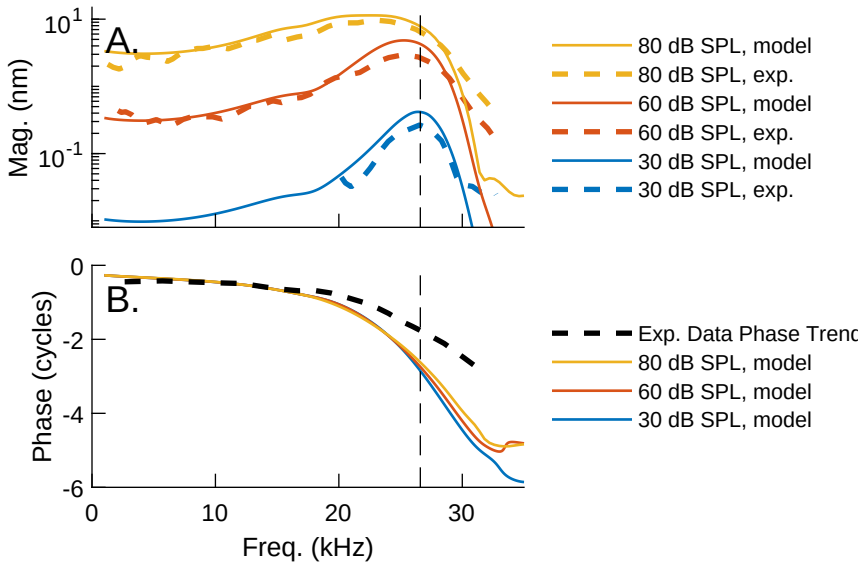

FIGURE 3.16. Comparison of model and experiment[75] BM displacement at the 26.6 kHz best place. (A) Magnitude. (B) Phase. The black vertical dashed line denotes the CF (26.6 kHz).

3.5.2 Pressure response to a pure tone

While many experimental and theoretical studies focus on the mechanical response of cochlear structures to sound, the cochlear fluid plays an essential role in cochlear mechanics. Hence, the response of the fluid pressure in the model was compared to measurements of the pressure to provide additional evaluation of cochlear mechanics and model validation. Throughout this work, pressure magnitudes presented in dB SPL have a reference pressure of 20 μPa. Before comparing the pure tone pressure response of the model to experiments, the spatial variations of the model pressure within the cochlear ducts are discussed (Figure 3.17). The fluid pressure varies not only in the longitudinal direction, but

also in the transverse and radial directions. Additionally, the pressure contains both the slow and fast waves, which can interact to complicate the response. The pressure can be decomposed into two components (a slow wave and a fast wave): an antisymmetric component, P_{as}, and a symmetric component, P_s (Figure 3.17A and C)[107]:

$$P_{as}(x,y,z,t) = \frac{1}{2}\left[P(x,y,z,t) - P(x,y,-z,t)\right] \tag{3.13}$$

$$P_s(x,y,z,t) = \frac{1}{2}\left[P(x,y,z,t) + P(x,y,-z,t)\right] \tag{3.14}$$

Because the round window is modeled as a pressure release, the symmetric and antisymmetric components must be equal at $x = 0$. Only the antisymmetric component interacts with the BM because the SV and ST dimensions are identical in the model (Figure 2.2) and the fluid is only coupled to the BM. Hence, the antisymmetric and symmetric components correspond to the slow traveling wave and fast compression wave, respectively[107,108]. Previously (e.g.[78,82]), only the antisymmetric component was included in the model. Because including both the slow and fast waves in the model was critical for studying DP propagation and generation (Chapters 4 and 5), the scala tympani was added to the model for this work to provide the symmetric component.

The symmetric pressure is essentially uniform while the antisymmetric pressure (which is coupled to the BM displacement) depends on position and is qualitatively similar to the BM velocity response. The spatial variations of the fluid pressure (Figure 3.17C) are similar to what has been previously observed in 3D two-duct cochlear models[109,104,110]. The lobes seen in the total pressure close to the BM from $x = 0.2$ to 0.5 cm are due to wave interference between the antisymmetric and symmetric components (Figure 3.17A). Similar notches in the pressure have been observed experimentally[30,31]. At the base, in the long-wave region (when the wavelength is large compared to the height of the duct), the antisymmetric pressure is approximately 1D while it becomes more localized and 3D around the BM closer to the 16 kHz best place, in the short-wave region. Due to the pressure-release

boundary condition at the round window, the pressure goes to zero and the symmetric and antisymmetric pressure components are exactly equal. Beyond the best place, the total pressure approaches the symmetric pressure component and the antisymmetric pressure component becomes evanescent.

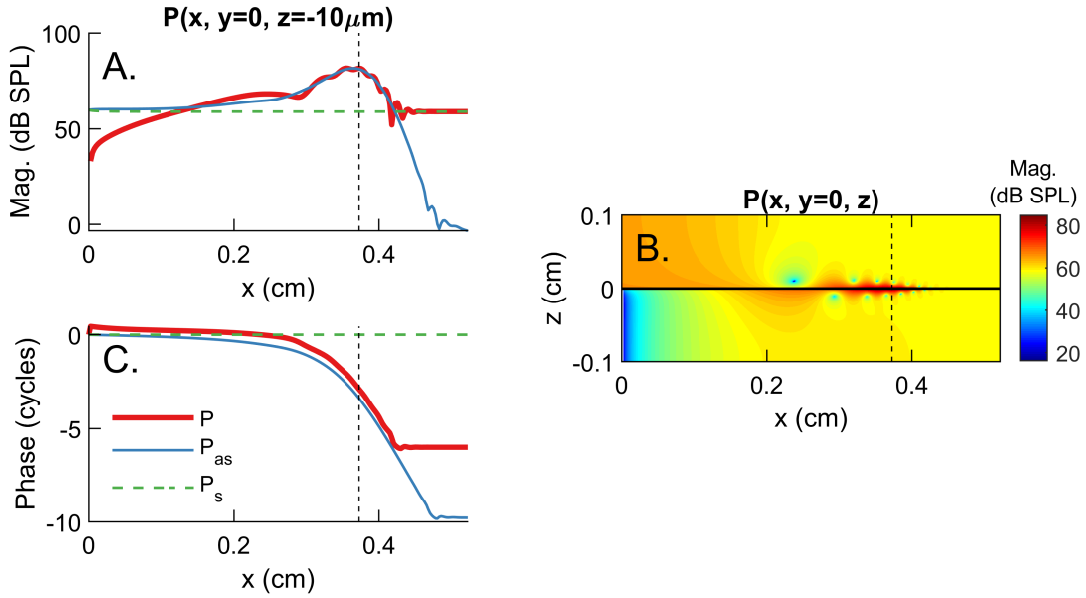

FIGURE 3.17. Spatial variations of the fluid pressure in response to a pure tone at 16 kHz. (A,C) Pressure response vs longitudinal position in the scala tympani close to the BM. (B) Spatial variations of the pressure. All results are taken at $y = 0$. The vertical dashed lines denote the 16 kHz best place. The solid horizontal line in (B) denotes the cochlear partition.

The pure tone pressure response of the model is compared with experimental pressure measurements in two different animals[74] in Figure 3.18. In Figure 3.18A for the pressure 15 μm away from the BM, the model peaks in magnitude 2 dB higher than the experimental results, while in Figure 3.18B, the model pressure peaks in magnitude nearly 16 dB lower than the experimental results for a 60 dB SPL stimulus. Although the experimental measurements were taken at two different longitudinal positions, the difference in CFs is not expected to result in a significant difference in the response. The difference in experimental magnitudes between Figures 3.18A and 3.18B ($\approx$ 10 dB at the peaks) are not unexpected given that the measurements were taken in different animals. Given the variability in the experimental magnitudes, the model results for the peak magnitude are not unrealistic. In

Figure 3.18, a high frequency plateau is observed in the magnitude, both for the model and the experiments; this plateau corresponds to the symmetric pressure components (see Figure 3.17). The notches for the model results at 115 μm in Figure 3.18A are due to interference between the symmetric and antisymmetric pressure components. As with the BM velocity results, the model pressure phase decreases at a faster rate than the experimental results.

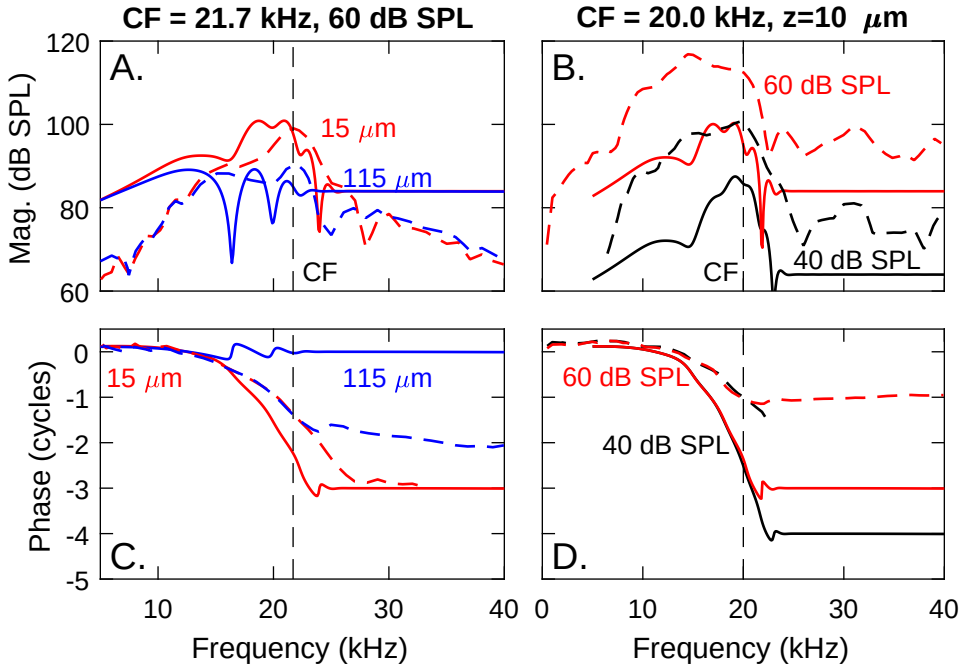

FIGURE 3.18. Comparison of fluid pressure pure tone responses for model and experimental data from two different animals[74] for 40 and 60 dB SPL stimuli. Experimental results in (A,C) and (B,D) were taken from Figs. 4 and 6, respectively, of Dong, 2017[74]. (A-B) Magnitude. (C-D) Phase. All model phases and the experimental phases in D. are taken relative to the pressure at the stapes, while the experimental phases in C. are taken relative to the ear canal pressure. Pressures were taken at 15 and 115 μm from the BM in the ST for a 60 dB SPL stimuli (A,C) and 10 μm from the BM in the ST for 40 and 60 dB SPL stimuli (B,D). Model results are drawn with solid lines and experimental results with dashed lines. Figure source: Bowling and Meaud, 2018[94].

3.6 Summary of contributions and conclusions

This chapter describes the process used for calibration and validation of the computational model. A parameter sensitive study was used to determine which model parameters should

be the focus of the calibration process. The calibration process included steps for matching the passive model place-frequency map and active model response with available experimental data. Following calibration, the model was validated against other experiment data that was not used during calibration. The validation results indicate that the model is able to match several key features in the experimental data (such as the magnitude values, broadness of the peaks as quantified by the quality factor, and amount of gain between the response to low and high stimulus levels). The calibration and validation processes did, however, indicate that the model phase decreases faster than that of the experimental data. This issue, though common to many cochlear models, should be considered when analyzing the phase of the model throughout this dissertation.

CHAPTER 4

DISTORTION PRODUCT PROPAGATION

4.1 Chapter overview

The aim of this study is to determine how distortion products propagate from their generation locations to the middle ear. The contributions of the slow reverse wave and fast compression wave to the propagation of intracochlear distortion products is evaluated using a physiologically based nonlinear model of the gerbil cochlea (the Bowling 2018 model). The $2f_1 - f_2$ DP response of the BM and cochlear fluid is compared to experimental results and the pure tone response. The DP is decomposed into forward and reverse wave components to determine their relative contributions to the total intracochlear response.

4.2 Introduction

As described previously in Chapter 1, a wave propagates on the BM in the forward direction (in the $+x$ direction, see Figure 4.1) in response to an acoustic stimulus in the ear canal. Despite the common use of DPOAEs both clinically and in the laboratory[73,111,112], questions still remain as to how DPs propagate in the reverse direction ($-x$ direction) from their generation sites to the ear canal. Two main hypotheses, shown in Figures 4.1B and C, have been proposed for how DPs propagate: (1) as a slow reverse traveling wave along the BM[26,22] or (2) as a fast compression wave through the cochlear fluid[113,114]. The fast compression wave is a longitudinal pressure wave that travels at the speed of sound in water (1500m/s).

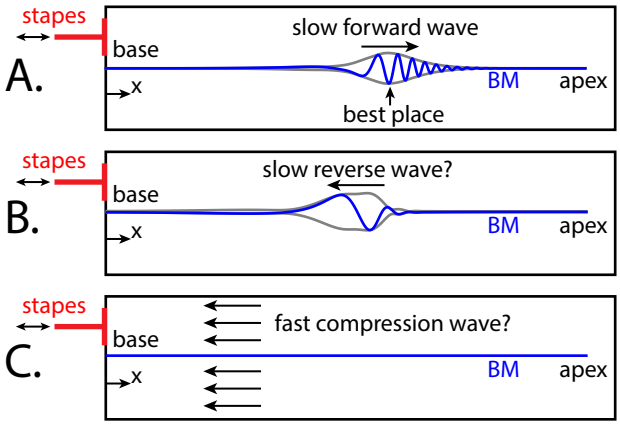

FIGURE 4.1. Schematics of wave propagation in the cochlea. (A) In response to an acoustic stimulus. Proposed hypotheses for DP propagation as (B) slow reverse wave and (C) fast compression wave. Figure source: Bowling and Meaud, 2018[94].

In the slow wave theory, once the reverse DP traveling wave reaches the stapes, part of this wave is transmitted through the middle ear and into the ear canal where it can be measured as a DPOAE; the other part is reflected at the stapes and propagates as a slow forward wave. Early models (e.g.[115]) have shown that DPs are expected to propagate back to the stapes as slow traveling waves. However, measurements of the BM velocity at the DP frequency have not provided any direct evidence for slow reverse propagation. Ren[113] measured the DP in the BM velocity at multiple positions and found that the phase is consistent with a forward propagating wave even though the locations were hypothesized to be basal to the DP generation site (such that a slow reverse traveling wave was expected to be observed). These results were interpreted as evidence that the DP propagates as a fast compression wave in the cochlear fluid; according to this theory, the fast compression wave would be reflected at the stapes, which would launch a slow forward traveling wave. Simultaneous measurements of the DP at the stapes and two longitudinal BM positions in a subsequent paper[114], and of the phase of the stapes vibrations relative to the BM vibrations at the DP frequency[116] were interpreted as further supporting the theory of fast compression waves.

However, it has been argued that the BM measurements of Ren and coworkers[113,114,116]

might be within the region in which DPs are generated, which might complicate the interpretation[117]. Indeed, theoretical efforts using one-duct models that only allow slow wave components[118,119,120,121,122] have demonstrated that these measurements are not necessarily inconsistent with the reverse traveling wave theory. Analysis using one-dimensional (1D) nonlinear cochlear models have shown that DP generation extends over a wide region that extends toward the base for low f_2/f_1 ratios and moderate to high stimulus levels[119,121]. Similarly, Sisto *et al.*[120] found that a region dominated by a forward traveling wave is expected whenever DP generation occurs over a wide region and/or the stapes has high reflectivity. Using a more realistic 2D one-duct cochlear model, Vetešník and Gummer[122] also explained the observation of forward traveling waves[113,114,116] by the fact that the measurement locations might be located at or apical to the DP generation sites. In Ref. 123, DP propagation was studied using a nonlinear three-dimensional (3D) cochlear model with the stimulus applied from within the cochlea instead of from the stapes; decomposition of the DP response into forward and reverse traveling waves showed that the response is dominated by a slow reverse traveling wave from around the f_2 best place to the stapes. de Boer *et al.*[124] measured DPs with a frequency well below the CF of the measurement location and observed that while a forward traveling wave is observed when f_2 is near CF, a slow reverse traveling wave is observed when f_2 is lower than CF.

It is more advantageous to investigate DP propagation by measuring the intracochlear pressure instead of the BM response because pressure measurements can identify both the compression and slow traveling wave modes[31]. Many theoretical papers have investigated intracochlear fluid mechanics in response to a pure tone[107,109,104]. It is well understood that the fluid pressure is truly 3D close to the peak of the traveling wave in the short-wave region (*i.e.*, in the region where the wavelength of the slow wave is small compared to the height of the cochlear ducts), while it is approximately 1D closer to the base, in the long wavelength region (*i.e.*, in the region where the wavelength is large compared to the duct height)[125]. Using novel pressure sensors[126], Olson characterized the *in vivo* response of

the intracochlear fluid pressure to a pure tone[77,96]. More recently, Dong and Olson[30,31] and Dong[74] measured the intracochlear pressure DP in response to a two-tone stimulus. When the CF of the measurement location is near the f_2 and f_{DP} best places, it was found that the DP pressure in the scala tympani (ST) is localized around the BM[30]. In these measurements, the amplitude of the DP decreases at a similar rate as a pure tone of the same frequency with increasing distance from the BM; such a decay of the amplitude is at odds with the compression wave theory. Subsequent measurements[31] provided strong evidence for the reverse traveling wave hypothesis, since the ear canal pressure is delayed relative to the intracochlear DP for f_2 frequencies that are significantly lower than the CF of the measurement location. Recent measurements of the pressure at two basal intracochlear locations by Dong[74] confirmed that the DPs are generated near the f_2 best place and have both forward and reverse traveling wave components.

Despite the critical role of the intracochlear fluid in the propagation of the DP from its generation site to the stapes, no model has investigated the DP intracochlear pressure. It is challenging to measure the fluid pressure at multiple longitudinal locations *in vivo*. Because of the presence of multiple waves (slow reverse wave, slow forward wave and fast wave), measurements at one or two longitudinal location(s) are difficult to interpret. Furthermore, while the ST fluid pressure has been measured in active cochleae[96], measurements of the fluid pressure in the scala media have only been possible in passive cochleae[108]. Hence, a model is needed to clarify how DPs vary spatially within the cochlear fluid pressure. The objective of this work is to analyze the generation of DPs and to quantify the relative contributions of slow reverse waves and fast compression waves to DP propagation. The hypothesis of this study is that DPs propagate from their generation locations to the stapes as a slow reverse traveling wave. Since cochlear fluid mechanics is 3D and includes fast and slow modes, these questions are addressed using a physiological two-duct 3D model of the cochlea. Spatial variations of the total fluid pressure and of the different pressure modes are analyzed to gain a more complete understanding of how DPs propagate from

their generation location out of the cochlea.

4.3 Results

Distortion product simulations are run in the time-domain using the nonlinear model. A two-tone stimulus with frequencies f_1 and f_2 ($f_2 > f_1$) is applied as a force on the stapes. Once the simulation is complete, the fast Fourier transform (FFT, MATLAB's `fft` function) of the response (such as the BM velocity or cochlear fluid pressure) is computed to provide the steady state responses of the primaries and DPs.

4.3.1 Response on the basilar membrane to a two-tone stimulus

The spatial response of the BM to a two-tone stimulus is shown in Figure 4.2 for two primary frequency ratios ($f_2/f_1 = 1.05$ in Figures 4.2A and C; $f_2/f_1 = 1.35$ in Figures 4.2B and D). As in most of the intracochlear DP pressure measurements[30,74], the level of the primaries was chosen to be 80 dB SPL. At a narrow primary frequency ratio (e.g. $f_2/f_1 = 1.05$), f_1, f_2, and f_{DP} are all relatively close in frequency (22.9, 24.0, and 21.7 kHz, respectively, for the case shown in Figures 4.2A and C). Due to this closeness in frequency and the tonotopic organization of the cochlea, all three frequencies peak relatively close to each other. At wider primary frequencies, the two primaries and DP are more separated in both frequency and peak position. For both primary ratios, the f_1 and f_2 responses have peaks of similar amplitude (Figures 4.2A-B) and the primaries peak at a location basal to their best places due to the relatively high stimulus level of the two primaries. The DP peaks slightly basal to its best place for $f_2/f_1 = 1.05$ and at its best place for $f_2/f_1 = 1.35$. When analyzing the response of the DP, it is useful to know the positions of the f_1, f_2, and f_{DP} peaks on the BM. For example, it is useful to know the positions of the two primary peaks when examining the phase of the DP (Figures 4.2C and D). Throughout this work, these peak positions will be indicated with vertical dashed lines.

Two different regions can be identified in the plot of the phase at the DP frequency

(Figures 4.2C and D): in the basal-most red-shaded region, the slope of the phase is positive, such that DP propagation is dominated by a slow reverse traveling wave; in the blue-shaded region, the phase slope is negative, which indicates that DP propagation is dominated by a slow forward traveling wave. For $f_2/f_1 = 1.05$, this transition from reverse to forward wave propagation occurs basal to the f_2 best place, while for $f_2/f_1 = 1.35$, this transition occurs approximately at the f_2 best place.

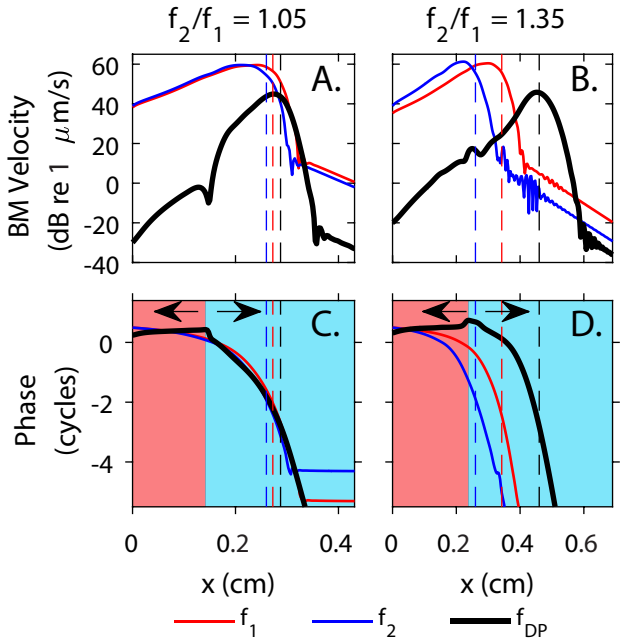

FIGURE 4.2. BM velocity of the DP and primaries as a function of longitudinal position for primary frequency ratios, f_2/f_1, of 1.05 and 1.35, f_2 = 24 kHz, and primary stimuli levels of 80 dB SPL. The vertical dashed lines from left to right indicate the f_2, f_1, and f_{DP} best places, respectively. The red shading indicates where when the phase has a positive slope and the cyan shading indicates when the phase has a negative slope. Figure source: Bowling and Meaud, 2018[94].

4.3.2 Spatial variations in intracochlear pressure

Because the cochlear fluid plays a critical role in the propagation of both slow and fast waves, the spatial variations of the pressure were analyzed (Figure 4.3). In Figures 4.3C-F, the pressure magnitude is plotted as a function of x and z for positions within the plane shown in Figure 4.3A. To help understand the DP response in response to a two-tone stim-

ulus, the pure tone response is first presented in Figures 4.3C-D; the stimulus frequency was chosen to match the frequency of the DP (16 kHz) seen in the two-tone results. The total pressure was decomposed into its symmetric and antisymmetric components (Equations 3.13 and 3.14), which correspond to the fast and slow waves, respectively. For brevity and because it is nearly uniform throughout both cochlear ducts, the symmetric pressure is not shown; the amplitude of the symmetric component corresponds to the total pressure amplitude in the most apical region near the helicotrema where the antisymmetric pressure has a low amplitude.

The fluid pressure at the DP frequency in response to a two-tone stimulus shares some similarities with the pure tone response. In addition to the pressure as a function of x and z (Figures 4.3E-F), the DP results include the pressure as function of y and z (Figures 4.3G-I) at three longitudinal locations identified by the three planes shown in Figure 4.3B. The DP antisymmetric pressure is 1D in the long wave region and 3D in the short wave region (Figure 4.3F). As with the pure tone, the DP symmetric pressure is nearly uniform throughout the cochlear ducts and the amplitude of the symmetric component corresponds to the total pressure in the apical regions. However, some notable differences between the pure tone and DP responses can be observed. The magnitude of the pure-tone symmetric pressure is much higher than the DP symmetric pressure, such that lobes of minimum pressure close the BM are not observed in the total DP response in Figure 4.3E. Furthermore, a region of minimum magnitude is observed both in the total and antisymmetric DP pressure around $x = 0.20$ cm; this minimum, not observed in the pure tone response, relates to the minimum or notch in the BM response in Figure 4.2 and will be discussed further below.

The spatial variations of the fluid pressure of the primary tones and DP obtained with the model are compared with pressure measurements by Dong and Olson[30] in Figure 4.4. For these measurements, the primary frequencies were varied so that f_2, f_1, and f_{DP} were alternatively set to CF = 21 kHz. In all three cases, both model and experimental primaries show very little spatial variation. The DP decreases at a fast rate as the distance from

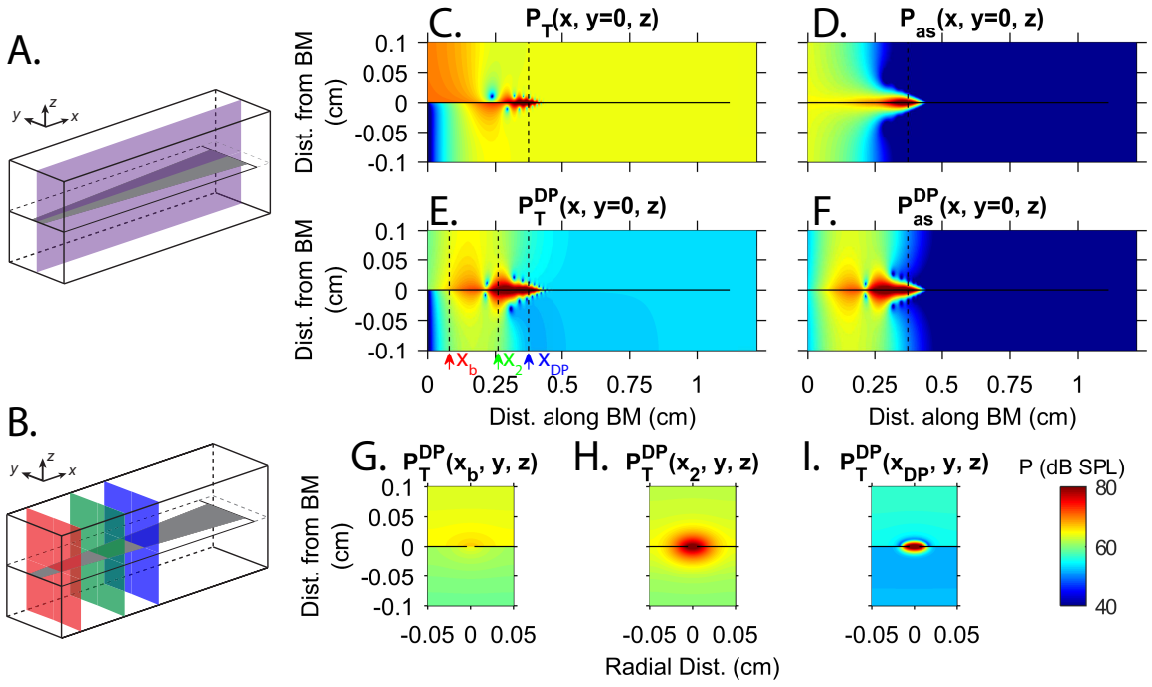

FIGURE 4.3. A,B. Box models with planes indicating where the pressure is shown in (C-F) and (G-I), respectively. Total and antisymmetric pressure component magnitudes for pure-tone (C-D) and two-tone stimuli (E-F). Cross-sections of pressure magnitude at several positions (G-I). The pure-tone stimuli (C-D) was at 16 kHz and 40 dB SPL and the two-tone stimuli (E-I) has $2f_1 - f_2$ = 16 kHz, primary frequency ratio f_2/f_1 = 1.20, and primary stimulus level of 80 dB SPL. The horizontal black line represents the cochlear partition. The vertical dashed line in (C, D, F) denotes the 16 kHz best place. The arrows and vertical dashed lines on panel E from left to right denote the positions shown in panels (G-I), respectively. The three positions shown in panels (G-I) are an arbitrarily chosen basal position, x_b = 0.08 cm, the f_2 best place (x_2 = 0.26 cm), and the DP best place (x_{DP} = 0.37 cm), respectively. Figure source: Bowling and Meaud, 2018[94].

the BM increases, both in the model simulations and the experiments; however, the slope seen in the model simulations is steeper than in the measurements. When the DPs from Figure 4.4A-C are compared to a low intensity pure tone of the same frequency (Figures 4.4D-F), similar decreases in magnitude with distance from the BM are found, which has also been observed experimentally (see Figure 4B in 74). However, the pure tone pressure converges to a higher value than the DP pressure at large distances from the BM because the pure tone symmetric pressure is higher than the DP symmetric pressure (Figures 4.4G-I). The pure tone and DP antisymmetric pressure decrease at nearly the same rate and

converge to approximately the same value. For all three cases, the antisymmetric pressure is much higher than the symmetric pressure close to the BM and decreases exponentially with increasing distance from the BM. Close to the BM, the antisymmetric pressure dominates the symmetric pressure, while farther from the BM the symmetric pressure dominates the antisymmetric pressure, at which point the total pressure varies little with distance from the BM.

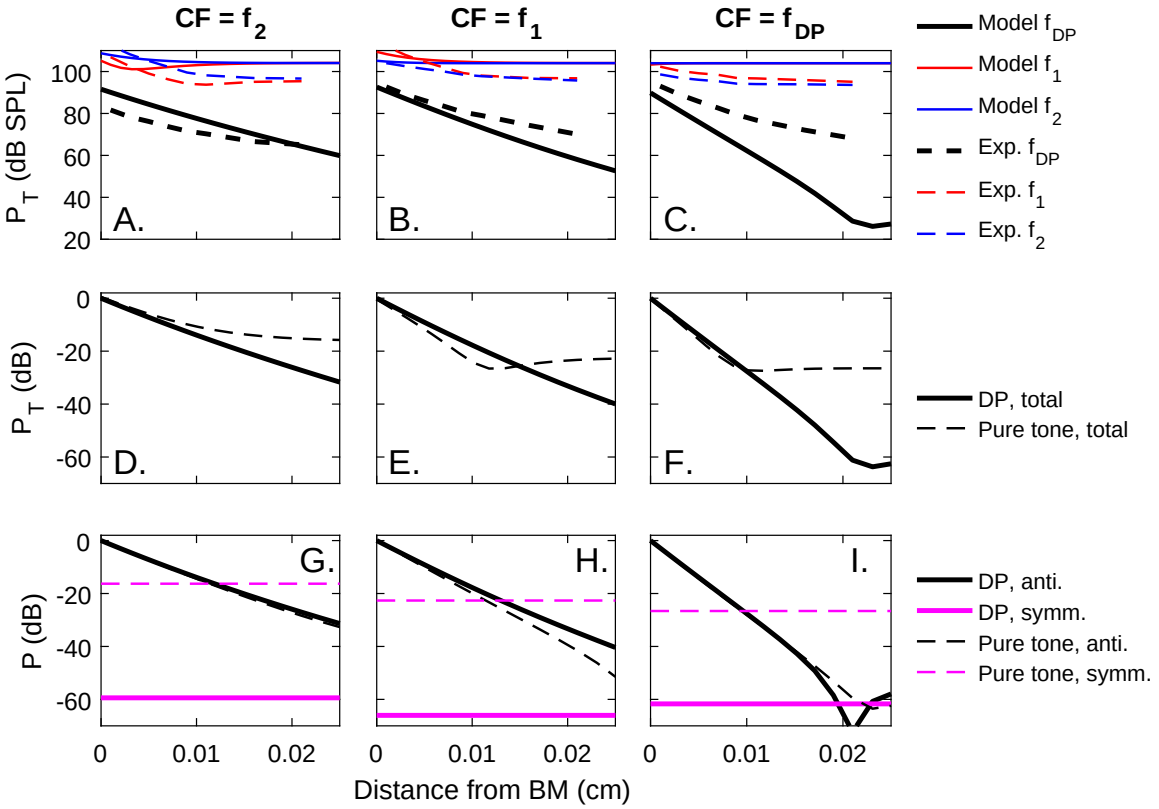

FIGURE 4.4. A-C. Comparison of pressure magnitude vs distance from BM in ST with experimental data[30]. D-F. Comparison of total pressure magnitude vs distance from BM in ST for DP and pure tone of the same frequency. G-I. Decomposition of the pressure from D-F into symmetric and antisymmetric components. Horizontal lines in G-I are the symmetric pressures. All model and experimental data were taken at the 21 kHz best place with primary stimuli of 80 dB SPL and f_2/f_1=1.10. The pure tone model results in D-I were obtained from the nonlinear model with a stimulus at 30 dB SPL. Magnitudes in D-I were normalized by the magnitude of the antisymmetric pressure at the BM, $P_{as}(z=0)$. Figure source: Bowling and Meaud, 2018[94].

4.3.3 Effects of varying f_2 on DP propagation at fixed location

While cochlear models easily provide the response for a given frequency at all positions, it is much easier to measure the response at a fixed position and sweep frequency in an experiment. In a scale invariant cochlea, these two methods should be equivalent[124]. In Figure 4.5, the effects of varying f_2 at a fixed position (20 kHz best place) for different f_2/f_1 ratios are shown. This scheme is commonly used in experiments (e.g. Refs. 124, 31, 114, 116, 74) to investigate intracochlear DP response and propagation. The magnitude and phase of the ratio of the pressure in the ST close to the BM to the pressure in the SV close to the stapes are compared with recent measurements from Dong[74]. Due to variability in the absolute magnitudes of the pressure from individual animal to individual animal, only the pressure ratios are compared here.

As in the measurements (Figure 4.5B), the peak of the DP response shifts to higher frequency as the frequency ratio is increased (Figure 4.5A); this is because the DP is approximately tuned to its own CF and the x-axis is f_2. While the magnitude of the pressure ratio agrees well with experiments for f_2/f_1=1.25 and 1.35, it is about 10dB higher than in the experiments for f_2/f_1=1.05 and 13dB lower than in the experiments for the pure tone results. Both in the model and the experiments, the DP response for f_2/f_1=1.05 has similar tuning as the pure tone response, while it has broader tuning at higher ratios. In contrast to the experimental results, the curves obtained with the model are smooth, possibly because the reflection from the DP best place due to cochlear roughness is not taken into account in the model. Similar to the lobes in Figure 4.3C, the pure tone shows notches in amplitude around 14 and 23 kHz that are due to interactions between the symmetric and antisymmetric pressure. For f_2 above 30 kHz, the magnitudes of the f_2/f_1 = 1.05 DP and pure tone are almost constant, indicating that the total pressure is converging to the symmetric pressure.

The phase of the ST pressure at the 20 kHz best place relative to the SV phase at the stapes, shown in Figures 4.5C and 4.5D, is particularly important for determining how DPs propagate. Two frequency regions can be identified, both in the case of the model simula-

tions (Figure 4.3C) and the experiments (Figure 4.3D). At low frequency, the slope of the phase is positive but shallow (indicating a "slow" reverse traveling wave with a relatively high phase velocity) for f_2/f_1=1.25 and 1.35 while both positive and negative slopes are observed for f_2/f_1=1.05 (indicating wave interference). At higher frequencies, a negative slope that progressively becomes steeper (indicating a forward traveling wave that slows down) is observed. For f_2/f_1=1.05 and 1.25 the region dominated by the forward wave starts at frequency f_2 below the CF of the location; for f_2/f_1=1.35, this frequency region starts approximately when $f_2 = CF$ in the model simulations while a forward traveling wave is not clearly observed for the frequencies that were measured in the experiment. As in the pure tone response, the phase predicted by the model has a steeper slope when $f_{dp} \approx$ CF than in the experiment.

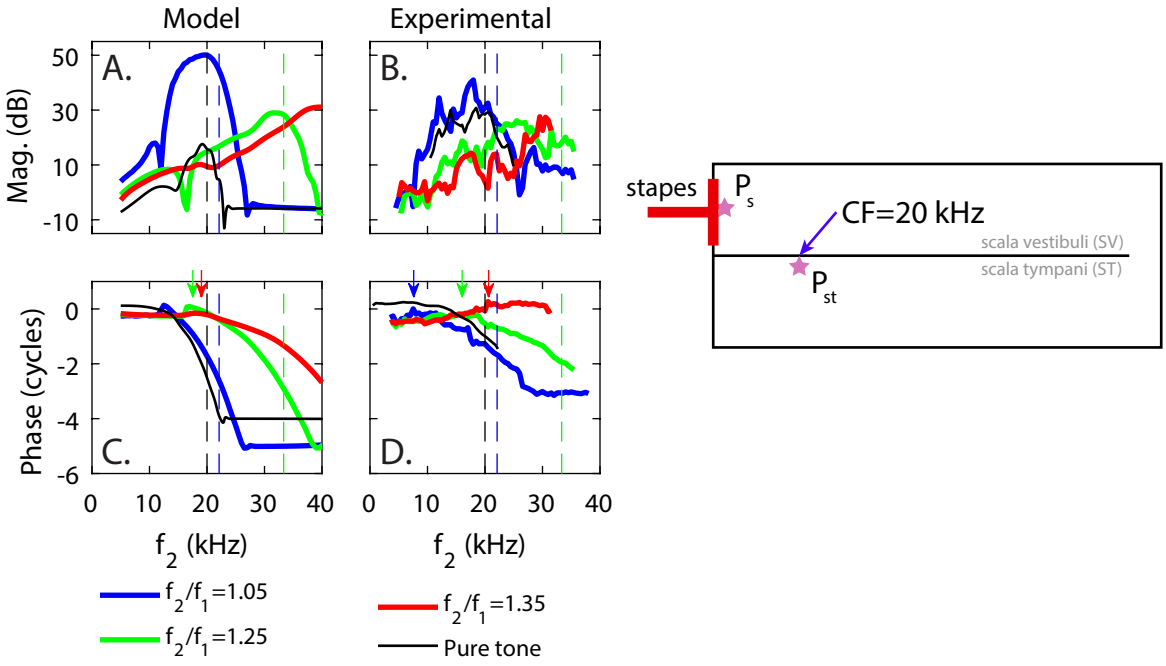

FIGURE 4.5. Magnitude (A and B) and phase (C and D) of the ratio of the DP pressure in the ST, 10μm from the BM, to the DP pressure in the SV next to the stapes (halfway between the BM and the top of the SV) as a function of f_2. (A.,C.) Model results. (B.,D.) Measurements from Dong[74]. All results at the 20 kHz best place. Model and experimental DPs had primary stimuli levels of 80 dB SPL. For reference, the response to a pure tone with a 40 dB SPL stimulus is also shown. The vertical dashed lines indicate f_2 when f_{DP} (or f for the pure tone) corresponds to the CF of 20 kHz. Vertical arrows mark the transition from reverse to forward waves. Figure source: Bowling and Meaud, 2018[94].

4.3.4 Effect of varying primary stimulus level

Two-tone simulations for different primary stimuli levels are compared with experimental measurements taken by Dong[74] (see Figure 4.6). For both the 50 dB SPL model and experimental results the magnitude peaks near f_{DP}=CF, while for 80 dB SPL the model peaks near f_{DP}=CF and the experimental results peak at a slightly lower frequency (f_2=27 kHz). Both 50 and 80 dB SPL model results show a notch in magnitude and corresponding phase shift below 20 kHz; the notch and phase shift are due to the interference between the forward and reverse waves. Below this phase shift, the phase is either nearly flat or has a slight positive slope indicating a reverse wave.

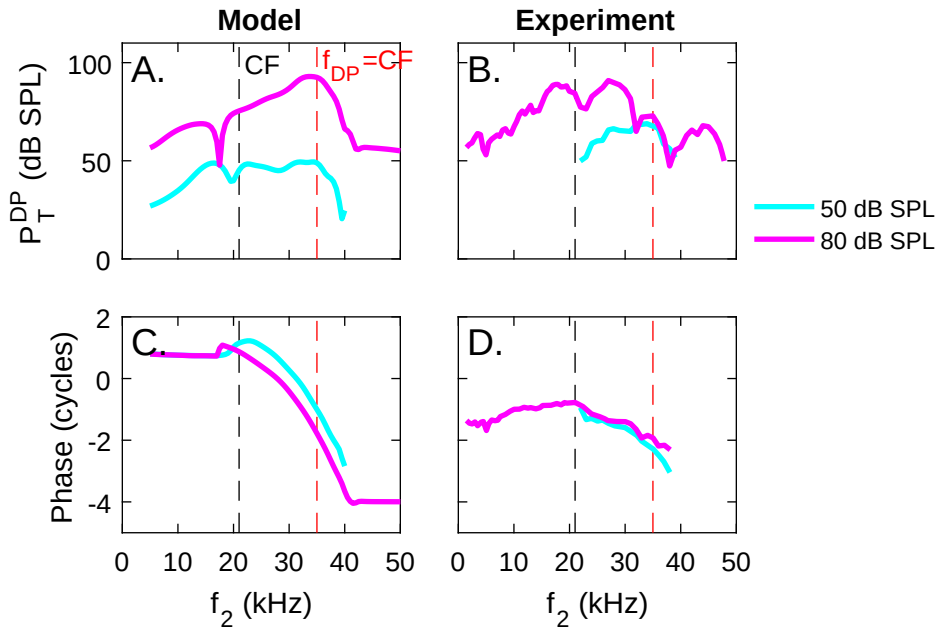

FIGURE 4.6. DP model and experimental measurements from Dong[74] of fluid pressure for varied stimulus levels. Model results and experimental measurements were taken at 21 kHz BP in ST 10 μm from BM for f_2/f_1=1.25. The model phase is referenced to the pressure in the SV at the stapes and the experimental phase is taken relative to the ear canal pressure. (A-B). Magnitude of fluid pressure. (C-D). phase of fluid pressure. Figure source: Bowling and Meaud, 2018[94].

4.3.5 Forward and reverse wave components

The DP results presented thus far have contained both forward and reverse wave components; however, the objective of this work is the determine the relative contributions from the forward and reverse waves. First, the DP fluid pressure was decomposed into its symmetric and antisymmetric components (Equations 3.14 and 3.13, respectively) and then the antisymmetric pressure was decomposed into forward and reverse components. Following the approach from de Boer *et al.* [123], the model response at the DP frequency is decomposed into approximate forward and reverse traveling wave components. The procedure involves taking the spatial Fourier transform of the antisymmetric pressure at the DP frequency, $P_{as}^{DP}(x,y,z)$, into the wavenumber domain:

$$\tilde{P}_{as}^{DP}(k,y,z) = \int_{-\infty}^{\infty} P_{as}^{DP}(x,y,z)e^{-ikx}dx \tag{4.1}$$

where k is the wavenumber and $\tilde{P}_{as}^{DP}$ is the wavenumber spectrum of P_{as}^{DP}. The wavenumber spectrum is then separated into a forward wave component, $\tilde{P}_{as}^{DP,f}$, and a reverse wave component, $\tilde{P}_{as}^{DP,r}$ by assuming that for $k \neq 0$:

$$\begin{aligned}
\tilde{P}_{as}^{DP,f}(k,y,z) &= \tilde{P}_{as}^{DP}(k,y,z) \text{ if } k > 0 \\
\tilde{P}_{as}^{DP,r}(k,y,z) &= \tilde{P}_{as}^{DP}(k,y,z) \text{ if } k < 0 \\
\tilde{P}_{as}^{DP}(k,y,z) &= \tilde{P}_{as}^{DP,f}(k,y,z) + \tilde{P}_{as}^{DP,r}(k,y,z) \text{ for any } k \neq 0
\end{aligned} \tag{4.2}$$

For $k = 0$, $\tilde{P}_{as}^{DP,f}(k=0)$ and $\tilde{P}_{as}^{DP,r}(k=0)$ are assumed to be given by:

$$\tilde{P}_{as}^{DP,f}(k=0) = \alpha_P \tilde{P}_{as}^{DP}(k=0) \tag{4.3}$$

$$\tilde{P}_{as}^{DP,r}(k=0) = (1-\alpha_P)\tilde{P}_{as}^{DP}(k=0) \tag{4.4}$$

where α_P is a complex number. At the stapes, the forward and reverse waves should satisfy:

$$R_{st} = \frac{P_{as}^{DP,f}(x=0)}{P_{as}^{DP,r}(x=0)} \tag{4.5}$$

Using the definition for the discrete Fourier transform[127]:

$$\begin{aligned} P_{as}^{DP,f}(x=0) &= \frac{1}{N}\sum_{I=1}^{N}\tilde{P}_{as}^{DP,f}(k_I) \\ &= \frac{1}{N}\Big[\alpha\tilde{P}_{as}^{DP}(k=0) + \sum_{k>0}\tilde{P}_{as}^{DP,f}(k)\Big] \end{aligned} \tag{4.6}$$

and

$$\begin{aligned} P_{as}^{DP,r}(x=0) &= \frac{1}{N}\sum_{I=1}^{N}\tilde{P}_{as}^{DP,r}(k_I) \\ &= \frac{1}{N}\Big[(1-\alpha_P)\tilde{P}_{as}^{DP}(k=0) + \sum_{k<0}\tilde{P}_{as}^{DP,r}(k)\Big], \end{aligned} \tag{4.7}$$

where N is the number of samples. Equation 4.5 is solved for α_P to yield:

$$\alpha_P = \frac{\Big[\tilde{P}_{as}^{DP}(k=0) + \sum_{k<0}\tilde{P}_{as}^{DP}(k)\Big]R_{st} - \sum_{k>0}\tilde{P}_{as}^{DP}(k)}{(1+R_{st})\tilde{P}_{as}^{DP}(k=0)}. \tag{4.8}$$

From here, all parameters are known and the forward and reverse waves are transformed back by into the spatial domain using the inverse Fourier transform:

$$P_{as}^{DP,f}(x,y,z) = \int_{-\infty}^{\infty}\tilde{P}_{as}^{DP,f}(k,y,z)e^{ikx}dk \tag{4.9}$$

$$P_{as}^{DP,r}(x,y,z) = \int_{-\infty}^{\infty}\tilde{P}_{as}^{DP,r}(k,y,z)e^{ikx}dk. \tag{4.10}$$

where $P_{as}^{DP,f}$ and $P_{as}^{DP,r}$ are the forward and reverse wave components, respectively, in the spatial domain.

As required by the pressure release boundary condition at the round window, the sym-

metric pressure equals the antisymmetric pressure at x=0 (Figure 4.7A); furthermore, the symmetric pressure is nearly constant. As expected, the phase lag of the forward waves increases as it propagates forward while the phase lag of the reverse wave increases as it propagates toward the stapes (Figure 4.7B). This confirms that the wave decomposition method is able to separate the total response into forward and reverse wave components. At $x = 0$, the only location that matters for emissions out of the cochlea, the reverse traveling wave is more than 10 dB higher than the symmetric pressure, implying that emissions are dominated by the slow reverse traveling wave. The decomposition is particularly useful in interpreting the magnitude and phase of the total response. For example, the reverse wave has a higher magnitude than the forward wave basal to $x = 0.20$ cm in Figure 4.7A; hence the total response is dominated by the reverse wave at the base and the phase of the total response has a positive slope (Figure 4.7B). Near $x = 0.20$cm, both forward and reverse waves have similar magnitudes but phases that differ by nearly half a cycle. This results in wave interference and a minimum in the total and antisymmetric pressure (Figures 4.7A and C). Apical to $x = 0.20$ cm, the magnitude of the reverse wave decreases and the magnitude of the forward wave matches the total response almost exactly (Figure 4.7A); this is expected because no reverse traveling waves are expected to be generated near or apical to the DP best place and thus the response should be dominated by the forward traveling wave. Because the response is dominated by a forward wave, the phase of the total response has a negative slope. Because the DP reverse traveling wave originates basal to the region of amplification, the reverse wave is similar to the pure tone response (if the phase is negated). Furthermore, the phase accumulation of the reverse wave from the generation site to the stapes is very limited since the wavelength of a slow wave (both in the case of a forward or reverse wave) is large at locations basal to the best place.

For the case shown in Figure 4.7B, the phase delay of the forward and reverse waves

relative to the position of maximum phase ($x = 0.16$cm) can be calculated as:

$$\tau_\phi(x) = \frac{\phi_{DP}(x = 0.16) - \phi_{DP}(x)}{f_{DP}}. \tag{4.11}$$

where τ_ϕ is the phase delay and ϕ_{DP} is the phase of the antisymmetric pressure at f_{DP}. The phase delay for the forward wave between x=0.16 cm and the DP best place (x=0.37 cm) is 0.22 ms, corresponding to an average phase velocity of about 9 m/s. The phase delay for the reverse wave between x=0.16 cm and x=0 is 0.014 ms, corresponding to an average phase velocity of about 112 m/s. Thus the reverse wave propagates back to the base from the generation region $\approx$ 12 times faster than the forward wave propagates from the generation region to the DP best place. Examining the spatial variations of the pressure in x and z (Figures 4.7C-E) yields similar findings to Figure 4.7A. Like the antisymmetric pressure, the forward wave pressure is localized around the BM near the primary and DP best places. The reverse wave appears less localized around the BM and the pressure is nearly 1D because the reverse wave has a maximum amplitude in the long wave region for the DP frequency. Furthermore, the zone of low pressure in the antisymmetric pressure close to the BM around $x \approx 0.22$cm is due to wave interference between the forward and reverse waves. The effect of varying the primary frequency ratio on the forward and reverse waves is shown in Figure 4.8. At f_2/f_1=1.05 (Figure 4.8A), the reverse wave is larger than the forward wave from the base to approximately x=0.23 cm, while apical to this position the forward wave is larger than the reverse wave. At f_2/f_1=1.35 (Figure 4.8B), the reverse wave is larger than the forward wave from the base to approximately x=0.17 cm, while apical to this position the forward wave is larger than the reverse wave. Although the transition point from the reverse wave dominating to the forward wave dominating occurs at similar positions for the two primary frequency ratios, this transition occurs very far towards the base from the f_2 best place for f_2/f_1=1.05 while it occurs very close to the f_2 best place for f_2/f_1=1.35.

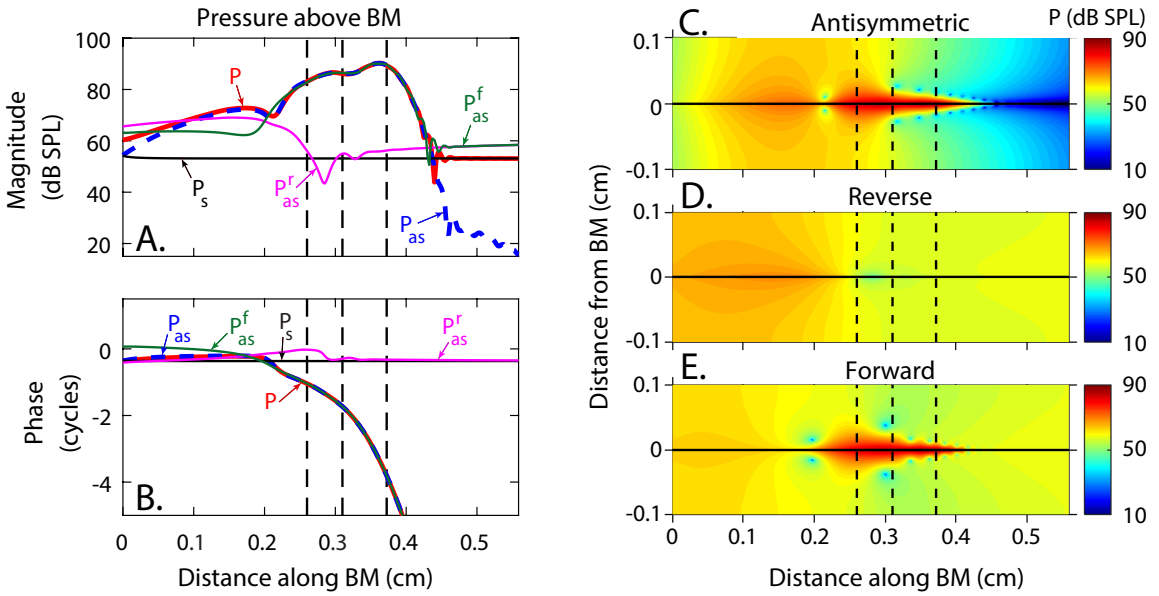

FIGURE 4.7. Decomposition of the DP pressure for equi-level primaries of 80 dB SPL with $f_2/f_1 = 1.20$ and $f_2 = 24$ kHz. (A-B). Magnitude and phase of the total pressure, P_T; symmetric pressure, P_s; antisymmetric pressure P_{as}; forward wave component of the antisymmetric pressure, P_{as}^f; and reverse wave component of the antisymmetric pressure, P_{as}^r; all taken directly above the BM in the SV. C-E. Magnitude of the antisymmetric pressure (C), reverse wave component of antisymmetric pressure (D), and forward wave component of antisymmetric pressure (E). The vertical dashed lines indicate, from left to right, the f_2, f_1, and f_{DP} best places. Figure source: Bowling and Meaud, 2018[94].

4.3.6 Effect of stapes reflection on forward and reverse waves

To investigate the role of the middle ear on DP propagation, two additional middle ear models were considered (see Table C.2 and Figure 3.4): (1) with a stapes reflection coefficient, R_{st}, of high magnitude across frequency and (2) with a stapes reflection coefficient of small magnitude at 16 kHz. The high $|R_{st}|$ is the case when most energy propagating in the reverse direction is reflected back into the cochlea, while for the low $|R_{st}|$ case very little of the reverse wave for f_{DP} is reflected back into the cochlea (Equation 3.4).

The effect of varying the stapes reflection coefficient is investigated in Figure 4.9. The most predominant changes in varying the stapes occur in the most basal regions, while closer to the DP best place the effect of the stapes variations appears negligible. For the high $|R_{st}|$ model, the forward and reverse waves have approximately the same magnitude

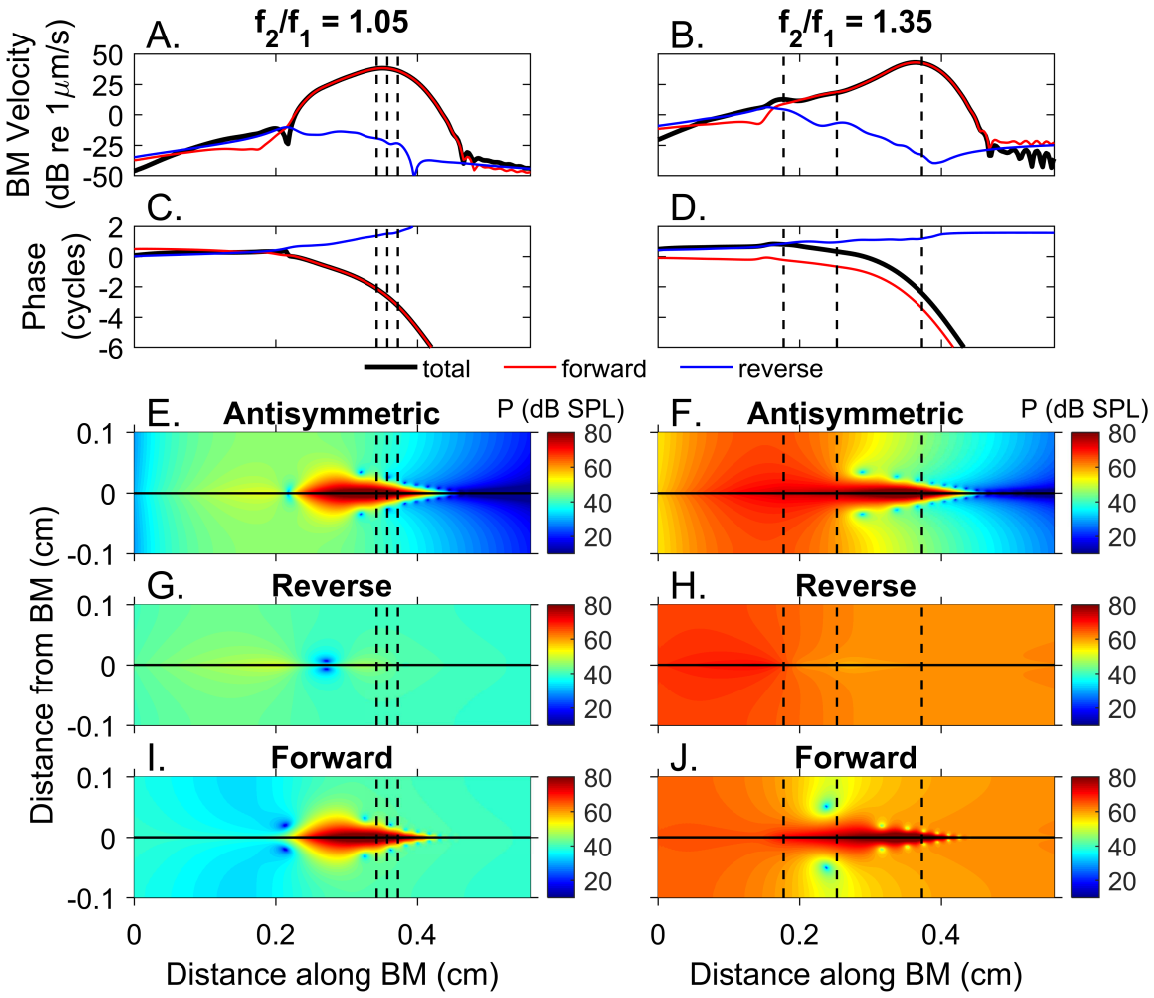

FIGURE 4.8. Decomposition of BM velocity and antisymmetric pressure at f_{DP} into forward and reverse waves for equi-level primaries of 80 dB SPL for f_2/f_1 = 1.05 and 1.35, and f_{DP}=16 kHz. A.,B. Magnitude of BM velocity. C.,D. Phase of BM velocity. E.,F. Magnitude of antisymmetric pressure. G.,H. Magnitude of reverse wave component of antisymmetric pressure. I.,J. Magnitude of forward wave component of antisymmetric pressure. The vertical dashed lines indicate, from left to right, the f_2, f_1, and f_{DP} best places. Figure source: Bowling and Meaud, 2018[94].

while the phase differs by half a cycle (due to the phase of R_{st}). As a result of this phase difference, the total BM velocity and antisymmetric pressure close to the stapes is relatively small. For the low $|R_{st}|$ case, very little of the reverse wave is reflected at the stapes and thus the forward wave is very small at the stapes.

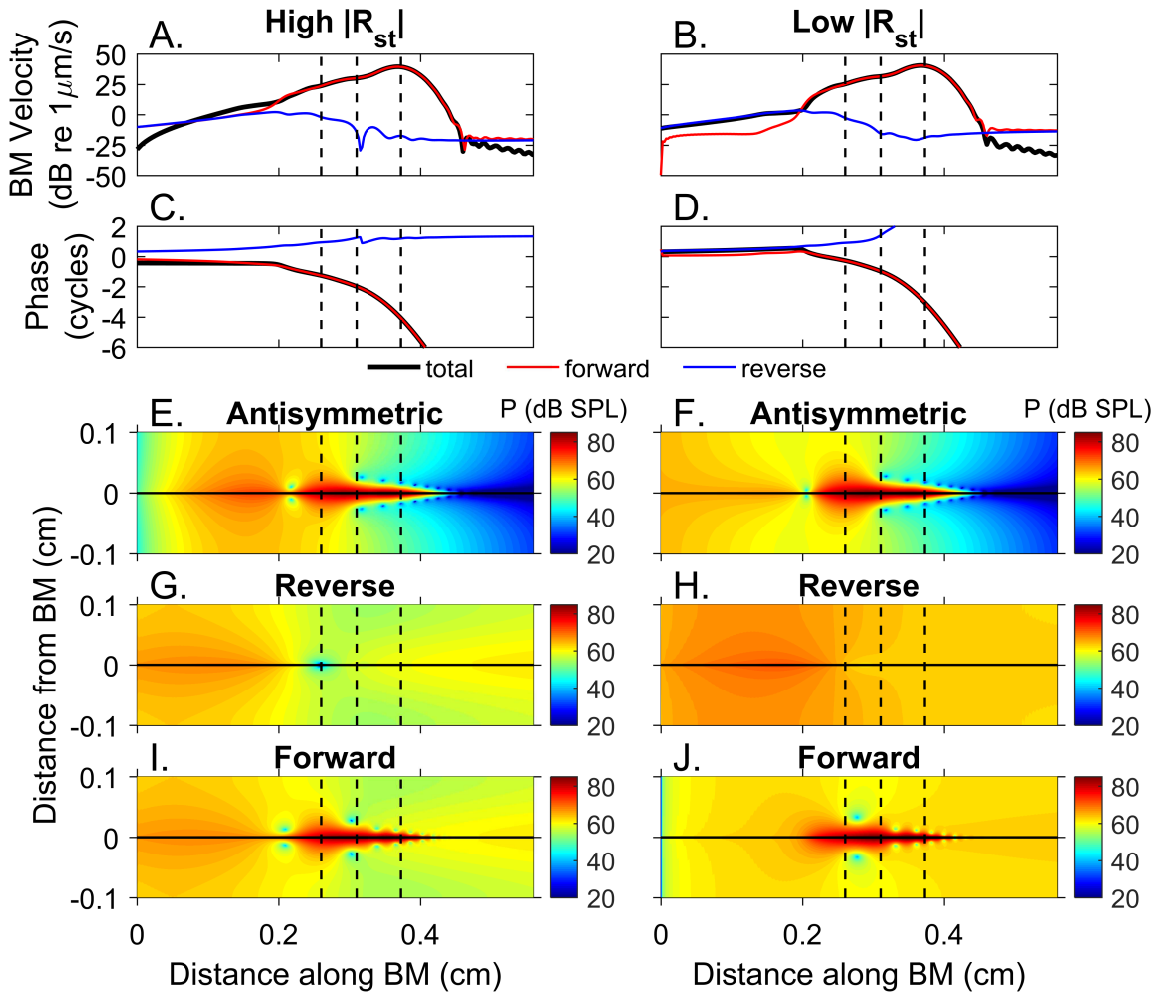

FIGURE 4.9. Decomposition of BM velocity and antisymmetric pressure at f_{DP} into forward and reverse waves for equi-level primaries of 80 dB SPL with f_2/f_1 = 1.20 and f_{DP}=16 kHz for different middle ear models. A.,B. Magnitude of BM velocity. C.,D. Phase of BM velocity. E.,F. Magnitude of antisymmetric pressure. G.,H. Magnitude of reverse wave component of antisymmetric pressure. I.,J. Magnitude of forward wave component of antisymmetric pressure. The vertical dashed lines indicate, from left to right, the f_2, f_1, and f_{DP} best places. Figure source: Bowling and Meaud, 2018[94].

4.4 Discussion

4.4.1 Strengths and limitations of modeling approach

The propagation of DPs is examined in this study using a physiologically-based model that is more realistic than in previous theoretical studies[123,119,120,121,122]: this model includes

a detailed representation of OHC biophysics, with nonlinear MET channels and linearized somatic electromotility; furthermore, the fluid model is based on a two-duct 3D model. In a one duct model, only the slow traveling wave is included; by using a two-duct model to represent both the scala vestibuli and scala tympani, the slow and fast waves can both be investigated and the model pressure response may be compared with experimental measurements of the pressure. While the fluid pressure only varies only with longitudinal at the base in response to a pure tone, around the best place the pressure is 3D[125]. To accurately represent the 3D nature of the fluid pressure, a 3D fluid model is required. While 3D cochlear models have previously examined intracochlear fluid mechanics in response to a pure tone[107,109,104], intracochlear fluid mechanics is analyzed for the first time in response to two tone stimuli in this work. Note, however, that the fluid is only coupled to the BM in this model. Direct coupling of the ST fluid to the TM, as in some recent models[128,129,130], might better represent intracochlear fluid mechanics; however, the coupling considered in this paper is simpler to analyze, since decomposition of the pressure into symmetric and antisymmetric components makes it possible to identify the slow and fast waves. In order to get insight into how DPs propagate, the slow wave component of the fluid pressure was decomposed into forward and reverse waves using the method previously proposed for the decomposition of the BM velocity by de Boer and Shera[123].

Due to the discrepancy between model and experiments in the phase of the pure tone response (Chapter 3), the slope of the phase of the DP response when $f_{dp} \approx$ CF is steeper than in the measurements; furthermore the magnitude of the DP pressure decays at a faster rate as the location moves away from the BM than in experiments (Figure 4.4A-C).

4.4.2 Analysis of the spatial variations of the DP fluid pressure

In a two-duct model, the response of the fluid pressure is the superposition of a symmetric, fast wave mode and of an antisymmetric, slow wave mode that propagates on the BM due to the fluid/structure interaction between the BM and the fluid. The presence of both

modes is predicted both in the case of the pure tone response and of the DP response; furthermore, the main properties of the two modes are the same in the pure tone and DP responses. Because a rectangular geometry is used for the two ducts, the fast compression mode is nearly uniform throughout the cochlear ducts[125] (Figures 4.3, 4.7, and 4.4). The properties of the slow wave mode depend on the local wavelength of the traveling wave. Close to the stapes, the wavelength is long, such that the pressure is 1D and varies only with longitudinal position with little phase accumulation. As the wave approaches its best place, the wavelength becomes shorter and the wave slows down, resulting in more phase accumulation. In this short wave region, the pressure becomes more 3D and localized around the BM. Both in model simulations and in experiments[30,74], the fluid pressure in the ST decays exponentially as the measurement location is moved away from the BM when f_{dp} ≈CF. This is because the symmetric pressure (which is nearly uniform) has a much smaller amplitude than the antisymmetric pressure (Figure 4.3). Furthermore, the DP pressure decays at a similar rate as a pure tone pressure of the same frequency because the DP and pure tone waves of the same frequency have approximately the same wavelength (Figure 4.4), as observed experimentally[30].

The propagation of DPs can be represented by the schematics of Fig. 4.10 (which is an extension of Figure 12 from Shera and Guinan[22]). In response to a two-tone stimulus, the two primaries propagate along the BM. A DP is generated due to nonlinear distortion in the region where the response to both primaries has a sufficiently high amplitude. According to the results presented here, this DP propagates as a slow reverse wave toward the stapes and as a slow forward wave towards the helicotrema. As the forward wave approaches the DP best place, the forward wave is amplified and slows down (such that the wavelength becomes shorter); because of the short wavelength, the pressure is highly 3D and localized to the BM. The reverse wave propagates back to the base with little phase accumulation (since the wavelength is very long basal to the DP generation site); furthermore, because of the long wavelength, the pressure is approximately 1D. When this reverse wave reaches

the stapes, part of this wave is transmitted by the middle ear (hence, a DPOAE is measured in the ear canal) while the other part is reflected by the stapes such that a slow forward traveling wave is generated. Simultaneously satisfying the boundary conditions at the stapes and round window requires the pressure to have a symmetric component, such that a DP fast wave is also generated. The DP fast mode is not directly generated by the OHCs since excitation of the fast wave by OHCs would require them to change volume. The fast wave instantly fills the cochlear ducts (since the fluid is assumed to be incompressible in the model), while the slow wave propagates forward with increasing phase accumulation as it approaches its best place.

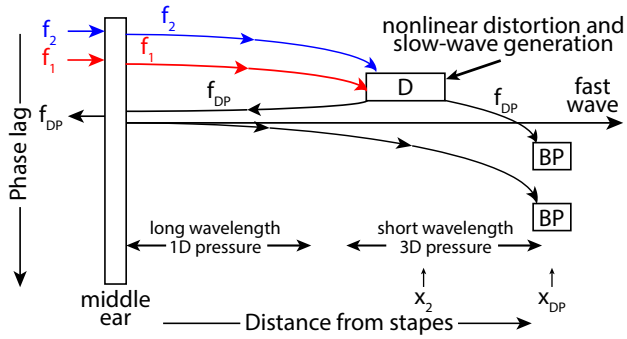

FIGURE 4.10. Schematic of DP propagation adapted from[22]. D denotes the distortion source, BP indicates the DP best place, x_{DP}, and x_2 indicates the f_2 best place. Figure source: Bowling and Meaud, 2018[94].

Due to the presence of slow reverse and forward waves, a zone of wave interference is observed in the DP response of the BM velocity and fluid pressure. As found in previous BM DP modeling work[123,119,120,121,122] and experiments[113,114,116,74], varying the stimulus parameters, the longitudinal position and the stapes reflectivity affects where and whether the forward or reverse wave dominates. Determining whether DPs propagate as a slow wave or a fast wave using only measurements at a couple of longitudinal locations is particularly challenging due to the complicated influence of the stimulus parameters (such as the levels or frequency ratio of the primaries) and to the wave interference between the forward and reverse waves.

4.5 Summary of contributions and conclusions

In this study, a two-duct 3D model with a realistic model of OHC biophysics was used to investigate how DPs vary spatially in the intracochlear fluid pressure. Some similarities with the pressure obtained in response to a pure tone are observed in the DP pressure. At positions at which the wavelength of the traveling wave is short, the DP pressure is 3D while it is approximately 1D closer to the base where the wavelength is long. The DP pressure from the model exhibits several similarities with experimental data, including a shift in the peak frequency of the DP with increasing f_2/f_1 ratio and transition from reverse-dominated traveling waves to forward-dominated traveling waves around the f_2 peak when f_2/f_1=1.25. Simulations demonstrate the presence of a fast compression wave, and a slow traveling wave that could be decomposed into forward and reverse traveling waves to help clarify DP propagation. Within the cochlea the fast wave has an amplitude much lower than that of the slow wave. The presence of wave interference between forward and reverse components affects the amplitude and phase response of the DP on the BM and cochlear pressure. At the base ($x = 0$), the fast compression and slow traveling waves were equal in amplitude, but the reverse traveling wave was substantially larger than the fast compression wave. Thus, emissions are dominated by the slow traveling wave mode.

CHAPTER 5

LOCATIONS OF DISTORTION PRODUCT GENERATION

5.1 Chapter overview

DP generation does not occur at a single position along the length of the cochlea, but is instead distributed over a range of positions. For proper analysis of DPOAE measurements, it is crucial to understand the locations of DP generation. In this chapter, the term "DPOAE" will be used to refer to distortion products measured in the ear canal pressure, while distortion products in the cochlea will be referred to as intracochlear distortion products (iDPs). The term "DPOAE generation" refers to the generation of iDPs that contribute to the DPOAE. Acoustic trauma or applying a third stimulus tone have been used experimentally to probe how DPOAE generation extends towards the base in the pristine cochlea, but the experiments yielded conflicting results. The aim of this study is to determine the locations of DP generation, specifically how far DPOAE generation extends towards the base. Model results of DPOAE and iDP in response to 2- and 3-tone stimuli are compared to experimental measurements to validate the model response and determine how well the model predicts the iDP OHC response. The effects of adding a third stimulus tone or mimicking the effect of acoustic trauma (OHC loss) on DPOAE and iDP are investigated with the model.

5.2 Introduction

Distortion products are generated in the cochlea in response to a two-tone stimulus of frequencies f_1 and f_2 ($f_2 > f_1$). It is broadly accepted that iDP generation from nonlinear distortion occurs not at a single location, but is, rather, distributed over a range of longitudinal positions along the cochlea around the f_1 and f_2 best places where the envelopes overlap and OHCs respond to both frequencies[131,121,132,133] (see Figure 5.1). However, due to the distributed nature of iDP generation, and to the phase variations of the iDP, phase cancellations occur when the iDP propagates toward the middle ear. Where the DPOAEs measured in the ear canal primarily originate from is currently debated[134,135].

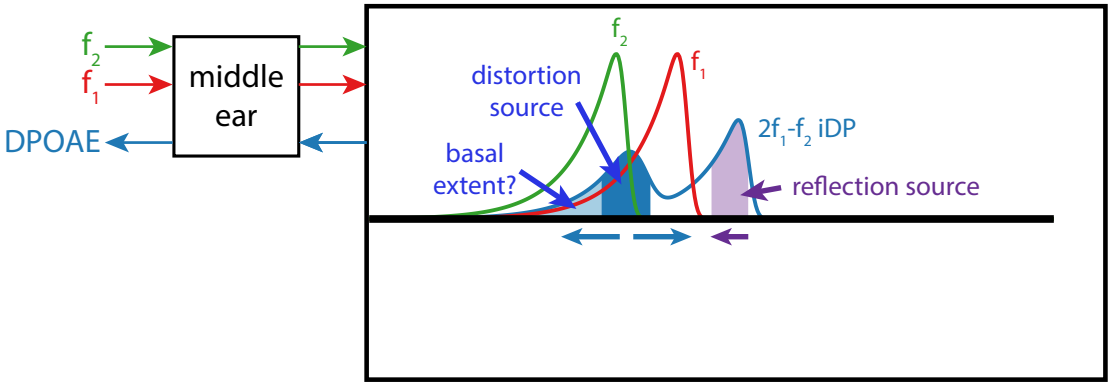

FIGURE 5.1. Schematic of the distortion and reflection sources for the $2f_1 - f_2$ iDP.

The reflection source DPOAE is expected to be generated in the region around the DP best place[22]. The reflection source is caused by mechanical impedance perturbations around the DP best place that cause reflections of the DP wave; these reflected waves then propagate backwards through the cochlea and middle ear and into the ear canal[22,32]. Multiple stimuli parameters (e.g. primary frequency ratio, f_2/f_1, and stimulus level of the primaries) are known to affect the locations of DP generation[25,119,121]. DPOAEs provide information about the functional health of the OHCs located in the region where they are generated[133]. Hence, knowing where the DPOAE is generated is needed to estimate the location of OHC damage. Due to the importance of knowing the exact locations of DPOAE

generation on the correct interpretation of DPOAEs[133], there has been extensive work, both experimental and theoretical, to determine the locations of DPOAE generation. Of particular interest has been the extent to which DPOAE generation extends towards the base from the f_2 best place (see Figure 5.1).

Withnell and Lodde[134] studied the effect of acoustic trauma in the base of the cochlea on DPOAEs. Their hypothesis was that causing acoustic trauma (achieved by exposure to a high sound pressure level tone: 100-105 dB SPL at 12 kHz) at the base would eliminate any DPOAE generators located basal to the f_2 peak and therefore have a measurable affect on the DPOAE. However, they did not find significant changes in the DPOAE for f_2<9 kHz and interpreted the lack of a change in the DPOAE as evidence that there are no basal iDP generators that contribute to the DPOAE. Several studies using a third stimulus (interference) tone, however, have suggested that some of the DPOAE is generated basal to the f_2 peak[136,135].

Suppression is one of the characteristics of nonlinearity in the cochlea; for example, the intracochlear response to a pure tone (called the probe tone) will be reduced when a second tone (called the suppressor) is simultaneously applied[137]. This reduction in the response to the probe is closely linked to the saturation of the MET current[138]. In the studies of DPOAE generation with the third stimulus tone, the third tone can suppress the response of the primaries and generation of DPOAEs over the region in which the response of the third tone is large[136,135]. Suppression and enhancement of the DPOAE was reported when a third tone of frequency $f_3 > f_2$ was introduced, suggesting that there are some iDP generators that contribute to the DPOAE basal to the f_2 peak[136]. A later study comparing the effects of applying a third stimulus tone 1/3-octave above f_2 in healthy and damaged rabbit ears suggested that some DPOAE components are significantly generated basal to the f_2 region[135].

Later measurements of DPOAEs determined that iDP waves traveling in the forward and reverse directions with different phases can interact, resulting in varying levels of

cancellation and enhancement[139]. These phase cancellations make interpretation of the DPOAEs challenging due to the complex relationship between DPOAEs and iDPs[32].

In addition to experimental studies aimed at determining the location of DPOAE generation, there have also been several theoretical studies. Young et al. found that the distortion source region spans either side of the f_2 best place by isolating individual distortion source elements and determining when the DPOAE resulting from that element contributed to within 10 dB of the overall DPOAE level[121]. Further, they found that the effective length of the distortion source increases as the f_2/f_1 ratio decreases and when the stimulus level is increased[121]. Some of the most closely related studies to that proposed here is by Vencovskỳ et al.[140,141], in which a nonlinear 2D cochlear model of the human cochlea was used to investigate how the region of iDP and DPOAE generation vary with primary stimulus level. Their results (mostly for f_2/f_1=1.20) indicate that as the primary stimulus level increases, the region of large iDP and DPOAE generation force broadens and shifts towards the base. Because their model represents the human cochlea, there is limited calibration of the model (although they tried to calibrate their model using DPOAE measurements from humans) and model results cannot be compared to direct *in vivo* measurements.

The objective of this work is to determine the extent of DPOAE generation basal to the f_2 best place using a computational model of the gerbil cochlea. It is expected that iDP generators may extend basal to the f_2 best place for larger stimulus levels and narrower primary frequency ratios and that some of these generators might contribute to the DPOAE. The distortion source component is the focus of this work; additional work investigating the reflection source component is on-going in the Meaud lab group[43]. In this study, the model response of the acoustic, mechanical, and electrical domains is examined and compared with experimental data to validate the model and determine its strengths and limitations. A novel aspect of this work is that the model response is compared to experimental measurements of not just the BM, but also the cochlear fluid pressure and extracellular OHC potential. Examining the OHC extracellular potential, which is closely

related to OHC force generation, gives considerable insight into iDP generation. The previously mentioned conflicting experimental results were obtained with different approaches for affecting iDP generation: causing acoustic trauma or adding a third stimulus tone. Using the model, both approaches are tested to determine the effect not only on the DPOAE, but also on the iDP to probe the origins of the conflicting results.

5.3 Revisiting the pure-tone response

Due to the nonlinearity of the MET channels and somatic electromotility, the OHCs are believed to generate iDPs and cause vibrations at the DP frequency by applying a force on the neighboring structures[27]. Knowing how the electromotile OHC force varies with position and frequency is critical to determining the locations of DPOAE generation. However, measuring the electromotile OHC force experimentally *in vivo* is unfeasible. In the model, the force applied by the OHCs on the surrounding structures (i.e. the BM and RL) is proportional to the voltage difference across the OHC (Equation 2.36, shown here for convenience):

$$f_{ohc}(t) = \varepsilon_3 \Delta\phi_{ohc}(t). \tag{5.1}$$

Measuring the voltage difference across the OHCs ($\Delta\phi_{ohc}$, which is called the transmembrane potential in the literature) *in vivo* while maintaining cochlear sensitivity is extremely challenging (but see Ref. 142). Another method to estimate the electrical output of the OHCs is to measure the OHC extracellular potential (i.e. potential in the scala tympani near the BM, ϕ_{st}). In the model, the potential, ϕ_{st} is directly related to the voltage difference across the OHC (Equation 2.41):

$$\frac{1}{R_{tl}}\phi_{st} = \frac{1}{R_m}\Delta\phi_{ohc} + C_m\Delta\dot{\phi}_{ohc} + i_{som} \tag{5.2}$$

Because the ST potential, ϕ_{st}, is much smaller than the voltage difference across the OHCs, $\Delta\phi_{ohc}$, varying R_{tl} has a limited effect on $\Delta\phi_{ohc}$ and thus cochlear amplification. While

slightly less informative than the voltage difference across the OHCs, the extracellular OHC potential near the BM has been reported experimentally by Dong and Olson in response to a pure-tone[143] and more recently by Dr. Dong in response to a 2-tone stimulus. Comparing the model extracellular potential with the available experimental data provides a useful means for estimating whether the force produced by the OHCs is realistic in the model.

5.3.1 Model recalibration motivated by electrical OHC measurements

Although this chapter appears before Chapter 6, chronologically this study occurred after the work in Chapter 6, which used the 2019 model; see Section 6.3.1 for a discussion of the differences between the 2018 and 2019 iterations of the model. Early results with the 2019 model indicated that the model response for the OHC extracellular potential was significantly different from what has been reported experimentally by Dong and Olson[143] (Figure 5.2). At 30 dB SPL, the peak voltage for the model is 180 times (45 dB) larger than the experimental data, while at 90 dB SPL the model is 360 times (51 dB) larger. Given this large discrepancy, it was determined that the model electrical parameters needed to be recalibrated.

Analysis of the electrical model (Figure 2.5, Equation 5.2) indicated that the ST-ground resistance, R_{tl}, had a direct influence on the ST potential and could thus be adjusted to lower the peak magnitude. After applying the adjustment, the peak voltage of the model for the 30 dB SPL stimulus is nearly identical to the peak voltage in the experimental data (Figure 5.3). It should be noted that the electrode sensor used by Dong and Olson has an outer diameter of 28 μm[143], which is larger than the width of a single OHC (10 μm[6]) but is very similar to the length of the elements in the model (25 μm). At CF, the traveling wave has a wavelength of 300 μm, and therefore the diameter of the electrode sensor is less than one-tenth a wavelength[143]. Dong and Olson concluded that the voltage response for low stimulus levels at CF originates from the local OHCs with little interference from more distant OHCs[143]. Therefore, matching the experiment voltage at CF by varying the

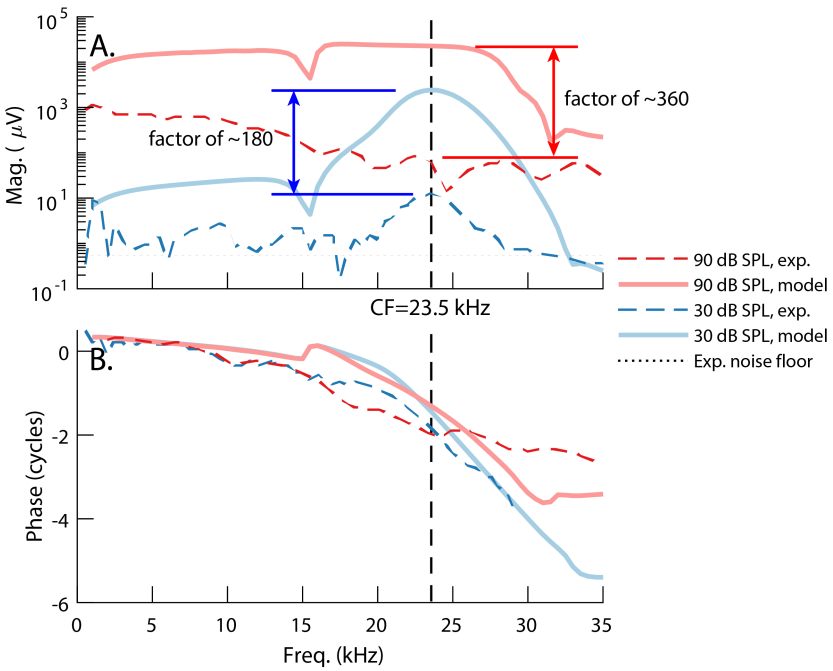

FIGURE 5.2. Comparison of ST potential from the Bowling 2019 model to experimental data by Dong and Olson[143] taken at the 23.5 kHz best place. (A.) Magnitude. (B.) Phase relative to the ear canal pressure.

model parameters can be done with confidence that the experiment data is robust against interference.

In the previous iterations of the model, the electrical parameters of the cochlear ducts were set to values determined by Strelioff in the early 1970s using earlier measurements of electrical resistances within the cochlea[92]. Except for the ST-ground and SM-ground resistances, R_{tl} and R_{mg} respectively, the current model uses parameter values determined by Teal and Ni[93] with an electrical finite element model of the cochlear ducts (see Table C.3). The value of the ST-ground resistance in the current model (0.273 Ω·m) is, however, within one order of magnitude of the value reported by Teal and Ni (which varied from 0.028 Ω·m at the base to 0.098 Ω·m at the apex)[93]. The SM-ground resistance is set to the value of 27 Ω·m reported by Strelioff[92]; though this value is about one order of magnitude larger than the value reported by Teal and Ni at the base (3 Ω·m)[93], it is significantly closer than the previous model which assumed the resistance was infinite.

After calibration, the model ST potential for a 30 dB SPL stimulus has nearly the same

peak magnitude as the experiment data (relative difference of <2 percent). Additionally, at 30 dB SPL the broadness of the model voltage peak ($Q_{10dB} = 3.8$) is somewhat similar to that of the experiment data (Q_{10dB}=5.09). However, the magnitude of the 30 dB SPL model response at low frequency compared to CF (below 16 kHz) is approximately an order of magnitude smaller than the experiment data. While the experiment data below 16 kHz is near the noise floor, the 30 dB SPL response normalized by the ear canal pressure is nearly identical to that at 40-60 dB SPL (Figure 2B of Ref. 143), suggesting that the experiment responses at 30 dB SPL are sufficiently above the noise floor (if there was an issue at 30 dB SPL, the normalized responses would likely be different from the 40-60 dB SPL responses, which are well above the noise floor). At 90 dB SPL, the magnitude of the model ST potential is higher than the experiment data at CF (by a factor 2.3) and lower than the data below CF (by a factor 7.2 at 5 kHz).

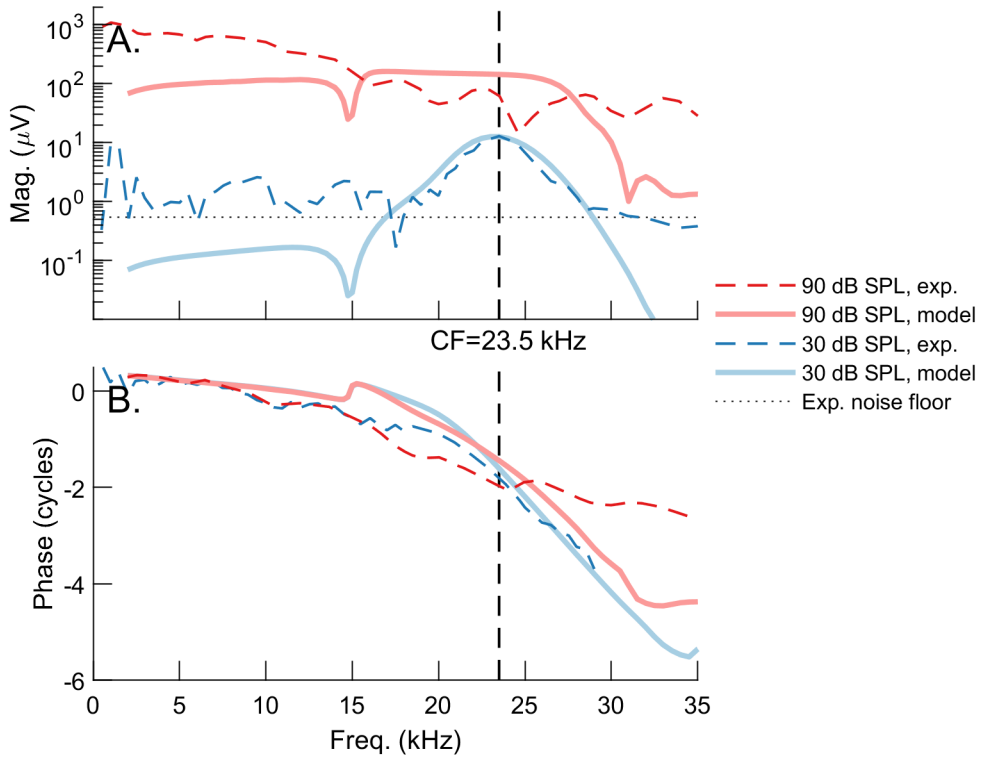

FIGURE 5.3. Comparison of ST potential from the current model to experimental data by Dong and Olson[143] taken at the 23.5 kHz best place. (A.) Magnitude. (B.) Phase relative to the ear canal pressure.

Both the model and experimental 30 dB SPL data show a noticeable notch (at 14.8 kHz and 17.5 kHz, respectively) below CF . Dong and Olson reported that this notch (and an accompanying phase shift) corresponds to the onset of nonlinearity in the BM response[143]. In the model, this notch corresponds to the resonance of the TM-shear mode mass, f_{tms}[81]:

$$f_{tms}(x) = \frac{1}{2\pi}\sqrt{\frac{K_{tms}(x)}{M_{tms}(x)}}. \tag{5.3}$$

At this frequency, the TM and RL move in phase in the shear direction, resulting in reduced HB deflection[81,144]. The reduced HB deflection in turn reduces the MET current, which results in a notch in the voltage. Increasing the TM-shear stiffness, K_{tms} or decreasing the TM-shear mass, M_{tms}, therefore, increases the value of f_{tms} and notch in the voltage. However, increasing K_{tms} also causes several issues with the qualitative response of the model such that despite efforts during calibration, the notch frequency in the model is still below the notch frequency observed in the experimental data. Because the TM-shear mass was considered a fixed parameter during calibration, decreasing the TM-shear mass was not considered.

The pure tone BM response of the current model is compared to experimental data taken at two longitudinal positions in Figure 5.4. Because none of the structural parameters were changed from the 2019 model values, there are only minor differences in the BM response of the 2019 and current models. The most noticeable difference is in the phase (Figures 5.4C-D): the current model phase decreases slightly faster than the 2019 model.

The place-frequency map, BM gain at CF, and quality factor, Q_{10dB} are used to quantify the pure tone response of the model at all longitudinal positions (Figure 5.5). These model results were obtained using the linear frequency domain model. At positions in the basal half of the cochlea, the current active model response peaks at a slightly higher frequency than the 2019 model (Figure 5.5A). The current model has slightly lower BM gain above 12 kHz and slightly more gain below 12 kHz (Figure 5.5B). Related to the decrease in gain,

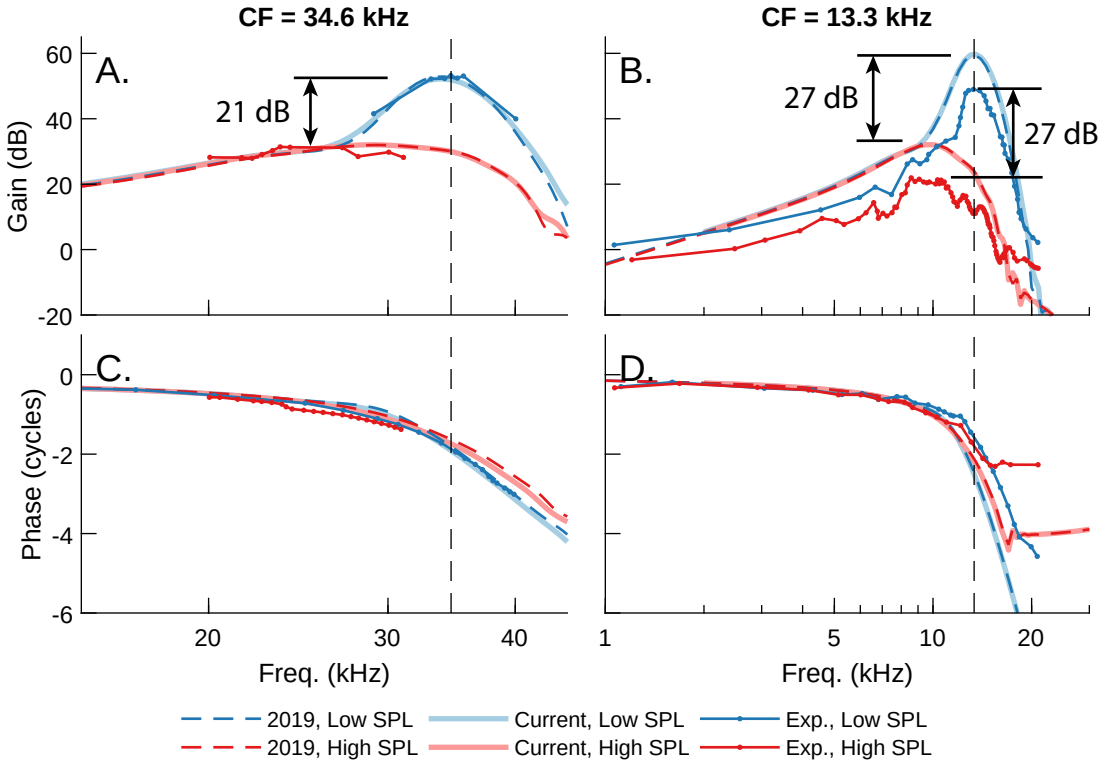

FIGURE 5.4. Comparison of BM pure tone response for the Bowling 2019 and current models at two longitudinal positions with experimental data taken from Refs.[85] and[86]. A. and B. Gain of the BM velocity relative to the stapes velocity. C. and D. Phase of the BM velocity relative to the stapes velocity. A. and C. Experimental data from Ref.[86] is given for 30- and 90 dB SPL and 50- and 90 dB SPL stimuli, respectively. B. and D. Experimental data from Ref.[85] is given for 30 and 100 dB SPL stimuli. The vertical dashed lines denote CF.

the current model is slightly more broadly tuned above 12 kHz (Figure 5.5).

5.3.2 OHC Transmembrane potential and force

As described earlier, it is difficult to measure the voltage difference across the OHCs; as a result the potential in the ST near the OHCs has been used experimentally to provide an indirect estimate of the electrical response of the OHCs. The model, however, gives a prediction of both the voltage difference across the OHCs and the potential in the ST near the OHCs (Figure 5.6). Near the peak frequency, the voltage across the OHCs is approximately 210 times larger than the ST potential at 30 dB SPL and 330 times larger at 90 dB SPL. The decrease in magnitude of the ST potential compared to the voltage

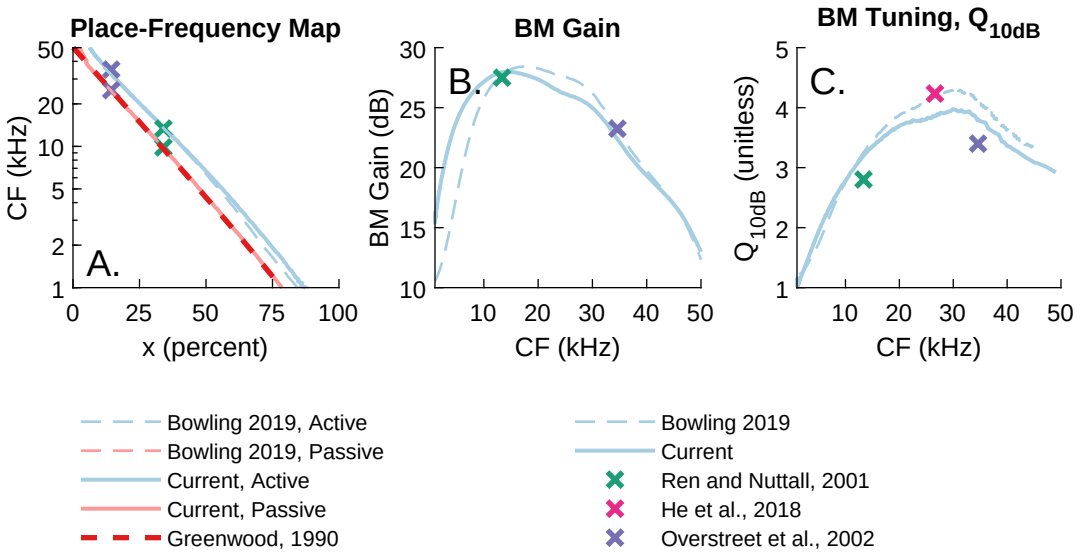

FIGURE 5.5. Comparison of BM pure tone response for the 2019 and current models and experimental data from[4,85,86,75]. A. Place-frequency map of the passive and active models with experimental data[4,85,86]. B. Amplification of active model relative to passive model. C. Quality factor, Q10dB, of the tuning of the BM. Model results are compared with measurements from the 13 kHz[85], 27 kHz[75], and 34 kHz[86] best places. The stimulus levels used for computing the gain from the experimental data at the 13 and 34 kHz positions were 30 and 100; 30 and 90 dB SPL, respectively. The quality factors for the experiments were computed from the responses to a 30 dB SPL stimulus.

across the OHCs is explained by the relatively small value of the ST-ground resistance (0.273 Ω·m) compared to the basolateral resistance of the OHC (21.4 Ω·m at the 23.5 kHz best place). At 90 dB SPL, the ST potential (Figure 5.6B) varies by less than an order of magnitude from low frequency to above CF. The voltage across the OHCs at 90 dB SPL, however, is more tuned and has slightly more variation with frequency (Figure 5.6A). At 90 dB SPL, the voltage across the OHCs has the same order of magnitude (but is slightly higher) as the saturation voltages reported from *in vitro* measurements of gerbil OHCs[145], suggesting that the model predicted values of the OHC voltage are not unreasonable.

The force applied by the OHCs on the surrounding structures in response to a pure tone is shown in Figure 5.7A-B. The electromechanical coupling coefficient, ε_3, specifies the amount of force applied based on the OHC transmembrane potential, $\Delta\phi_{ohc}$ (Equation 2.36, Figure 5.7C). The coupling coefficient ranges from 104 pN/mV at the base to 63

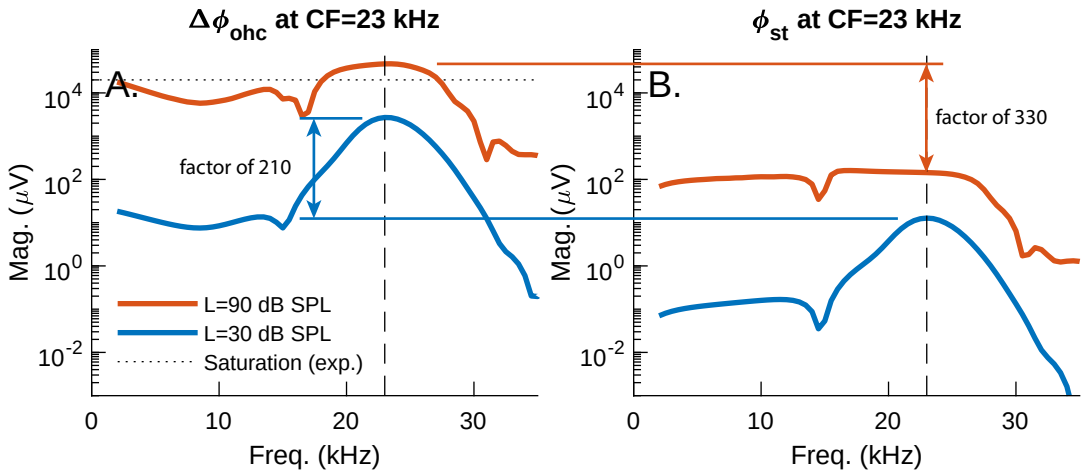

FIGURE 5.6. Comparison of transmembrane ($\Delta\phi_{ohc}$, A.) and extracellular (ϕ_{st}, B.) potentials in response to a pure tone at the 23 kHz best place. The vertical dashed lines denote the CF=23 kHz. A. The horizontal dashed line indicates the saturation transmembrane voltage reported from *in vitro* measurements [145].

pN/mV at the apex and is based on the values reported by Iwasa and Adachi: using *in vitro* measurements of the force applied by clamped OHCs and applying a voltage stimulus, they estimated the electromechanical coupling coefficient at 100 pN/mV with a standard deviation of 25-50 pN/mV [146]. Their estimated value is comparable to that of the model (Figure 5.7C).

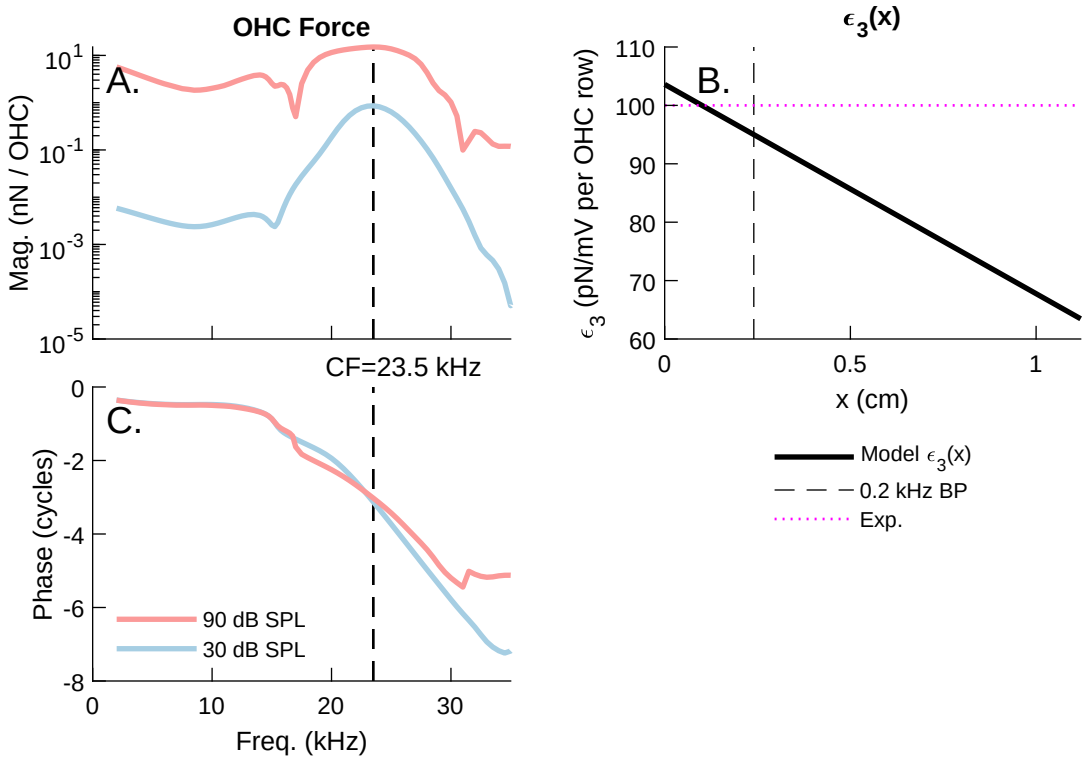

FIGURE 5.7. (A. and B.) Force applied by OHCs on surrounding structures at the 23.5 kHz best place in response to a pure tone stimulus. (C.) Spatial variations of the electromechanical coupling coefficient, ε_3. The vertical dashed line denotes the 23.5 kHz best place and the horizontal dotted line corresponds to the value of the electromechanical coupling coefficient estimated by Iwasa and Adachi[146].

5.4 Two-tone response

Before the model can be used to determine the locations of iDP and DPOAE generation, it must first be validated against other sets of experimental data. Because much of this work study focuses on the electrical response of the OHCs; model predictions for the response to a two-tone stimulus were validated against electrical measurements in addition to the mechanical/fluid pressure measurements. The two-tone response of the model ST pressure and potential is validated with experimental data provided by Dr. Wei Dong for three f_2/f_1 ratios: f_2/f_1=1.05 in Figures 5.8 and 5.11; f_2/f_1=1.25 in Figures 5.9 and 5.13; f_2/f_1=1.35 in Figures 5.10, and 5.13. In all of these comparison figures, the noise floor from the experiments is shown on the panels for both the model and experiment because experiment

and model results should only be compared when the experiments are above the noise floor.

5.4.1 ST pressure

At three primary frequency ratios, both model and experiment show similar variations in the peak magnitudes as the stimulus level is varied (Figures 5.8, 5.9, and 5.10). As the stimulus level of the primaries increases, the peaks become broader for both the primaries and iDP. Around the peaks for both model and experiment, the response at f_1 is slightly smaller than the response at f_2, indicating that f_2 response suppresses the f_1 response. If the two tones were played individually, the their responses would overlap; that the f_1 response is affected by f_2 is an example of two-tone suppression.

For f_2/f_1=1.05, the model iDP for L=80 dB SPL is significantly smaller than the experiment iDP (Figure 5.8E-F). Comparison of the iDP at low frequency is difficult for the wider ratios given that most of the experimental data is in the noise floor (Figures 5.9F and 5.10F). In the model iDP response for f_2/f_1=1.25 (Figure 5.9E) , there is a small peak that decreases from 15.3 kHz for the 40 dB SPL stimulus level to 13.2 kHz for the 80 dB SPL stimulus. A similar peak is observed for the iDP response for f_2/f_1=1.35 (Figure 5.10E) that decreases from 12.76 kHz for the 40 dB SPL stimulus level to 10.59 kHz for the 80 dB SPL stimulus level. Because the abscissa in Figures 5.9E and 5.10E is the $2f_1 - f_2$ frequency, these peaks correspond approximately (especially at the higher stimulus levels) to when f_2 peaks at CF ($2f_1 - f_2$=13.0 kHz for f_2/f_1=1.25 and $2f_1 - f_2$=10.45 kHz for f_2/f_1=1.35; see the green vertical dashed lines). For f_2/f_1=1.25, this peak also corresponds to the transition from forward wave dominated (negative phase slope) to reverse wave dominated (positive phase slope, Figure 5.9G). The iDP is expected to be generated around the f_2 peak position; the peak in the ST pressure at the iDP and fact that the forward and reverse waves seem to originate from this position may be evidence that the DPOAE originates from this region. It should be noted though, that the experimental data for f_2/f_1=1.25 does not show a peak, but instead shows a notch very near f_2=CF (notch

frequency = 13.9 kHz) and peak at a slightly higher frequency (17.6 kHz for the 80 dB SPL stimulus, Figure 5.9F).

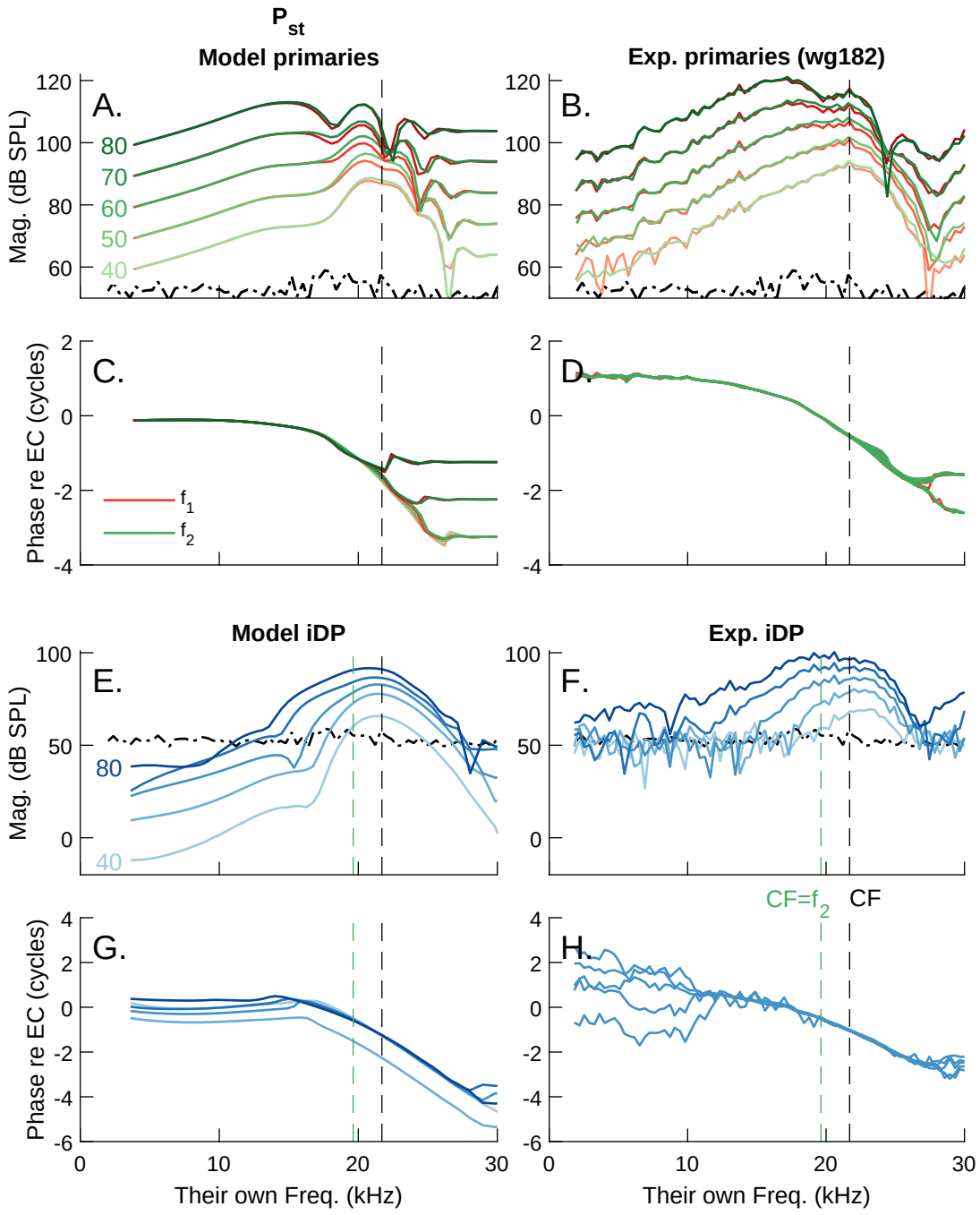

FIGURE 5.8. Comparison of the ST fluid pressure two-tone response for the model and experimental data from Dong[147] for f_2/f_1=1.05 taken at the 21.7 kHz best place for primary stimulus levels of 40 to 80 dB SPL in 10 dB steps. (A-D) Response of the primaries. (E-H) Response of the $2f_1 - f_2$ iDP. (A, C, E, G) Model results. (B, D, F, H) Experimental results from experiment wg182 taken in the ST 10 μm from the BM. The noise floor from the experiment is plotted as a black dash-dotted line on both the experiment and model panels.

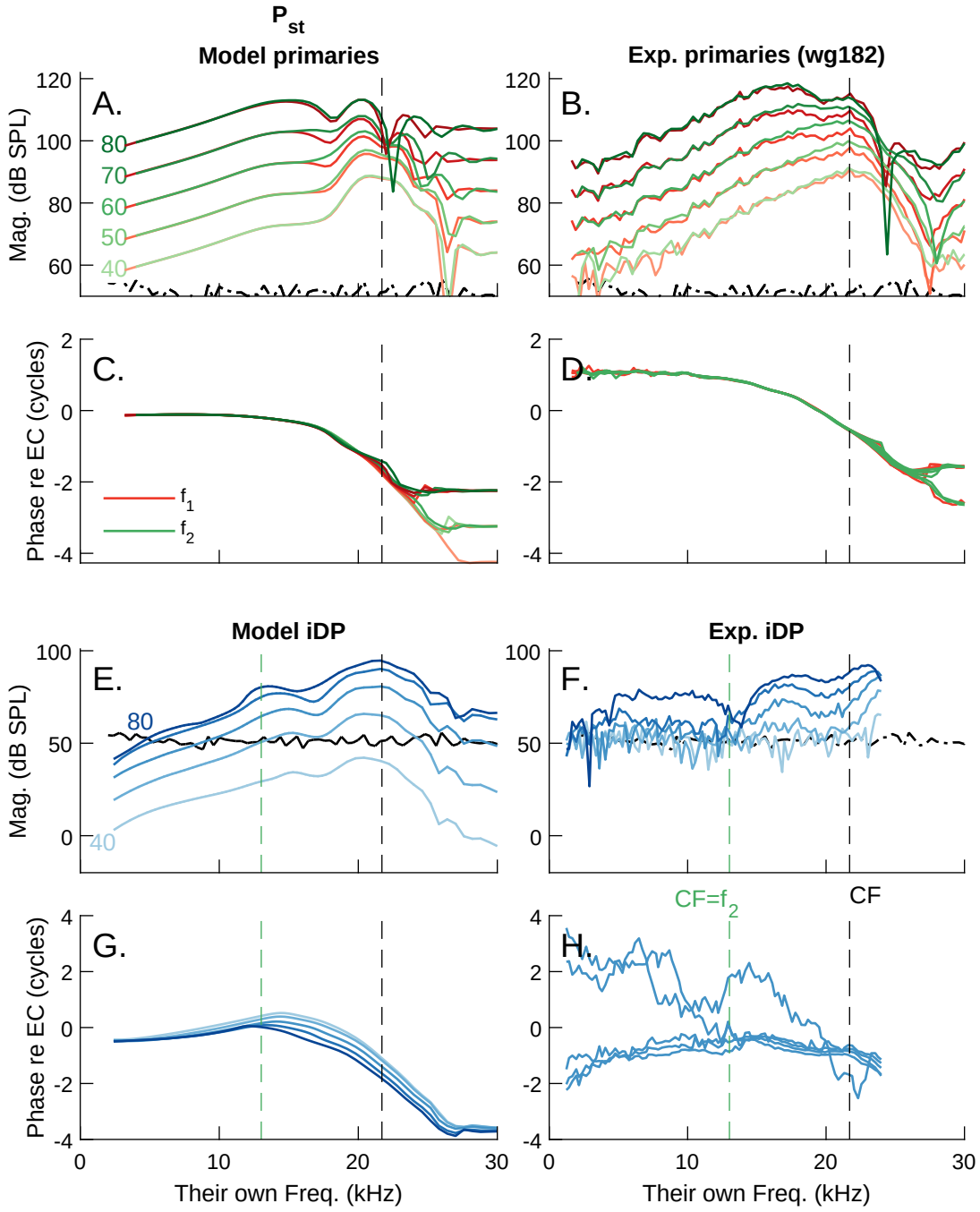

FIGURE 5.9. Comparison of the ST fluid pressure two-tone response for the model and experimental data from Dong[147] for f_2/f_1=1.25. All other details are the same as Figure 5.8.

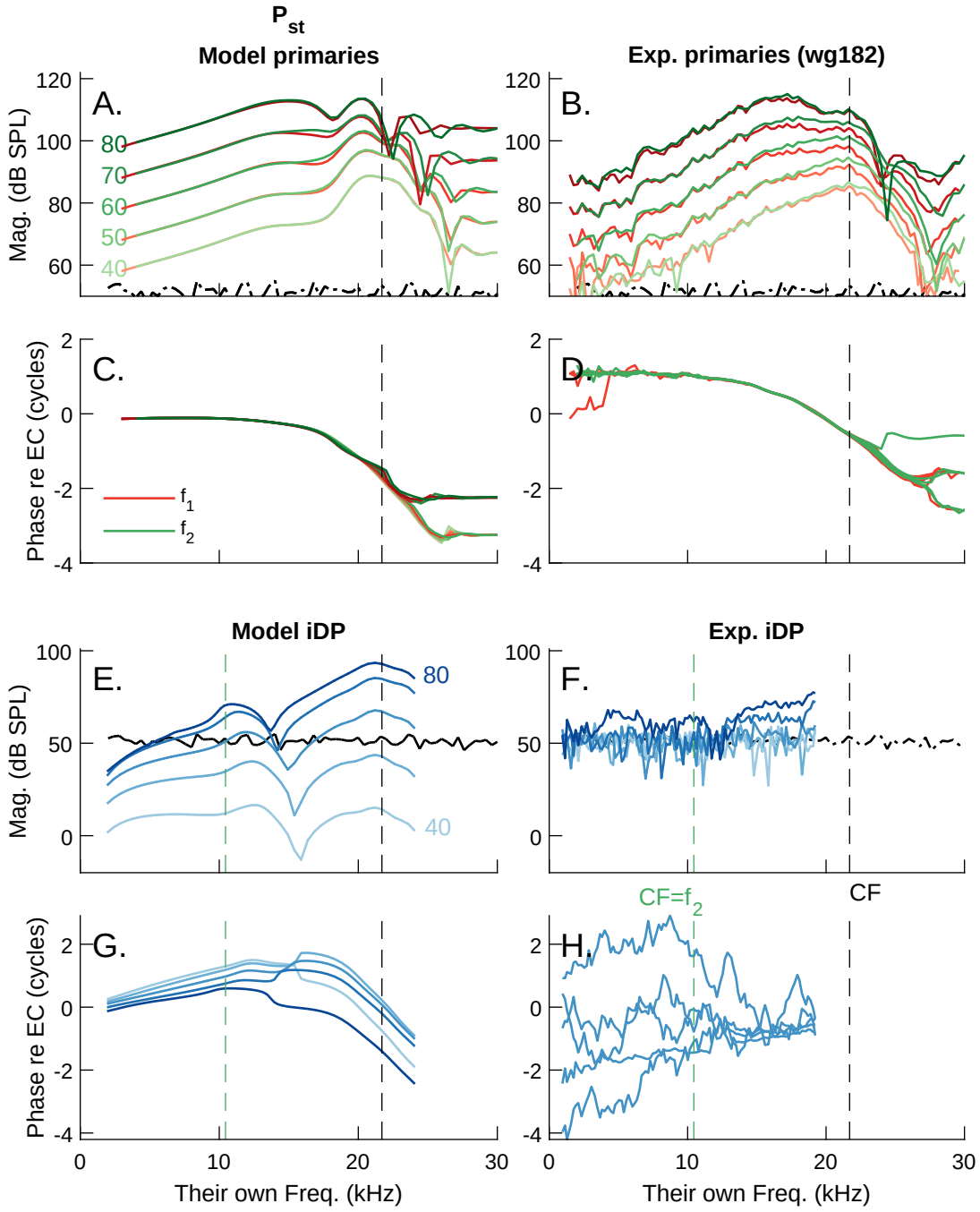

FIGURE 5.10. Comparison of the ST fluid pressure two-tone response for the model and experimental data from Dong[147] for f_2/f_1=1.35. All other details are the same as Figure 5.8.

5.4.2 ST potential

The iDP in the ST pressure is the consequence of both the passive mechanics of the cochlea and the nonlinear OHC response. Because of the influence of the passive mechanics, it is quite difficult to estimate where iDPs are generated from the ST pressure alone. The OHC extracellular potential, however, is much more directly linked to the nonlinear OHC function, which makes it particularly useful to study iDP generation.

The comparison of model and experimental pure tone ST potential response indicates that the model is unable to match the experimental voltage response at low frequencies relative to CF (Figure 5.3). It is therefore unsurprising that the model response of the two primaries at low frequencies relative to CF is also around 10 dB lower than the experimental data (Figures 5.11A-B, 5.12A-B, and 5.13A-B). However, the response close to the peak region of the primary responses is more important for iDP generation. For both the primaries and iDP, the peak voltage around CF is larger in the model than the experiment. This difference in magnitudes is likely related to the fact that the model tends to overestimate the response potential to a pure-tone at high sound pressure levels and low frequencies relative to CF (Figure 5.3).

At all three f_2/f_1 ratios and stimulus levels, the model responses of the primaries have a noticeable notch in magnitude near 13.3 kHz that corresponds to the resonance of the TM-shear mode (Equation 5.3). Even though a clear notch was observed in the pure-tone experimental results of Figure 5.3[143] (albeit at a higher frequency than in the model), no notch is apparent in the response of the primaries to a two-tone stimulus. The cause of this discrepancy in the experimental results in unknown, though it should be noted that these measurements were taken in different animals.

For f_2/f_1=1.05, the model and experiment iDPs have similarly shaped peaks around CF (Figure 5.11E-F). Comparison of the iDP response around CF is difficult for the wider ratios in part because the limited frequency range of the experimental data (Figures 5.12E-F and 5.13E-F). At the wider f_2/f_1 ratios, the model iDP response has a large peak around f_2=CF

(Figures 5.12E and 5.13E) that is more pronounced than the peaks of similar frequency in the model ST pressure (Figures 5.9E and 5.10E) that were discussed earlier. Like the peaks in the ST pressure, the peaks in the ST potential decrease in frequency as the primary stimulus level is increased (Figures 5.12E and 5.13E). For f_2/f_1=1.25 and the 80 dB SPL stimulus (Figure 5.12), the peak (of frequency 12.3 kHz) is below CF=f_2 (13.0 kHz). For f_2/f_1=1.35 and 80 dB SPL stimulus (Figure 5.13), the peak (of frequency 10.4 kHz) is nearly identical to CF=f_2 (10.5 kHz). These peaks in the magnitude also corresponds approximately to transition from forward to reverse traveling waves (Figures 5.12G and 5.13G). At lower stimulus levels and wider f_2/f_1 ratios, similar peaks of observed in the experiment results (Figures 5.12F and 5.13F). For f_2/f_1=1.25 and a 50 dB SPL stimulus (Figure 5.12F), there is a peak at 15.6 kHz (above CF=f_2=13.0 kHz) in the experiment iDP that decreases by less than 1 kHz as the stimulus level is increased (thus it remains above CF=f_2). For f_2/f_1=1.35, there is a peak around 12.5-13.0 kHz in the experiment iDP for 50-70 dB SPL stimuli that does not significantly change frequency with stimulus level (Figure 5.13F).

Although the model generally under-predicts the magnitude of the ST potential at low frequencies relative to CF, the magnitude of the potential at f_2=CF is similar for both model and experiment. The model and experiment are within 0.3 dB at f_2=CF for f_2/f_1=1.25 and 80 dB SPL stimulus (Figure 5.12E-F). For f_2/f_1=1.35 and 80 dB SPL stimulus, the model and experiment are within 5.5 dB (Figure 5.13E-F). However, there are several noticeable differences between the model and experiment iDP response. Like the response of the primaries, the experimental iDP is generally largest at low frequencies relative to CF and decreases slightly as frequency increases to CF (Figures 5.11F, 5.12F, and 5.13F) while the model iDP is largest at CF (Figures 5.11E, 5.12E, and 5.13E).

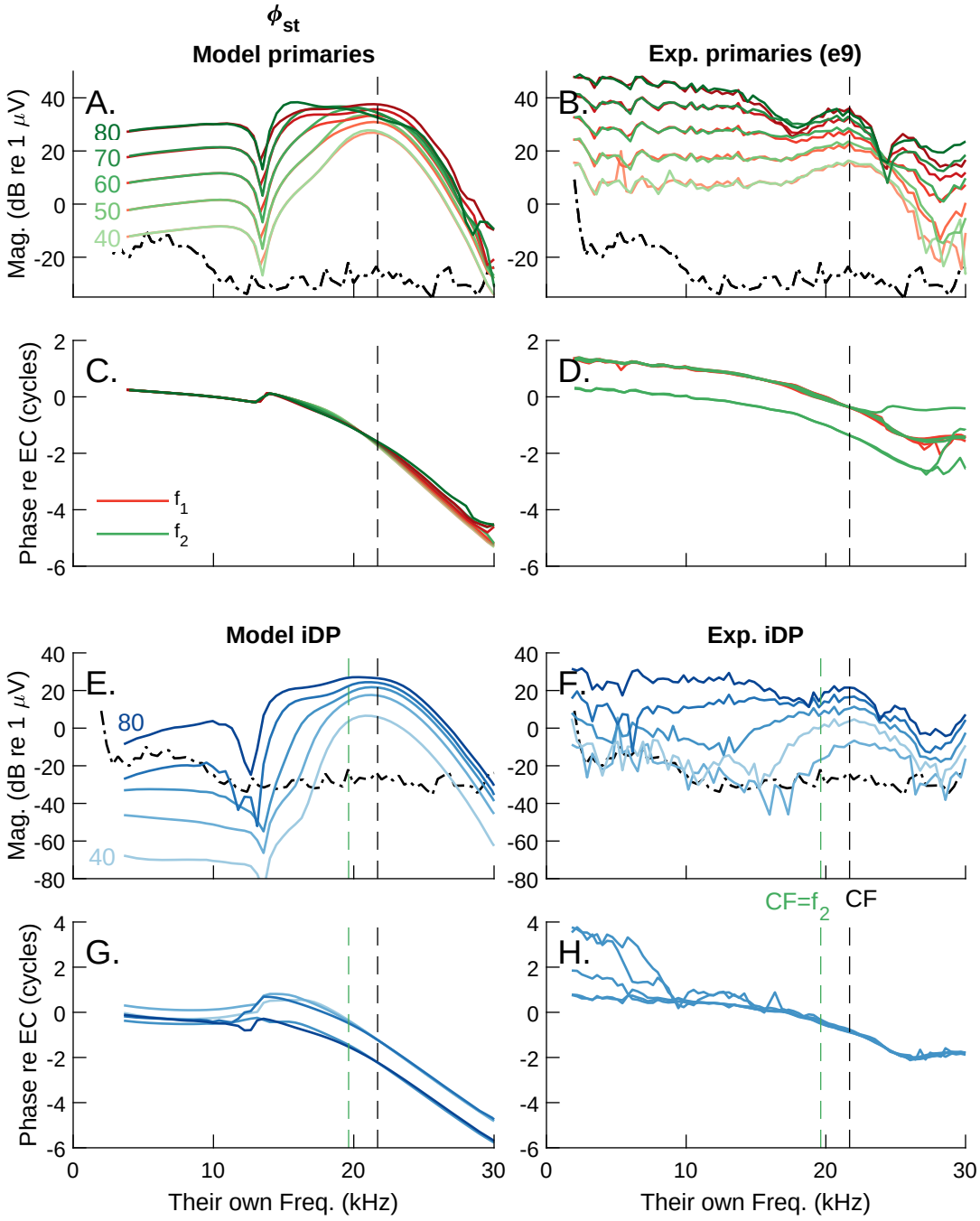

FIGURE 5.11. Comparison of the ST potential two-tone response for the model and experimental data from Dong[147] for f_2/f_1=1.05. All other details are the same as Figure 5.8.

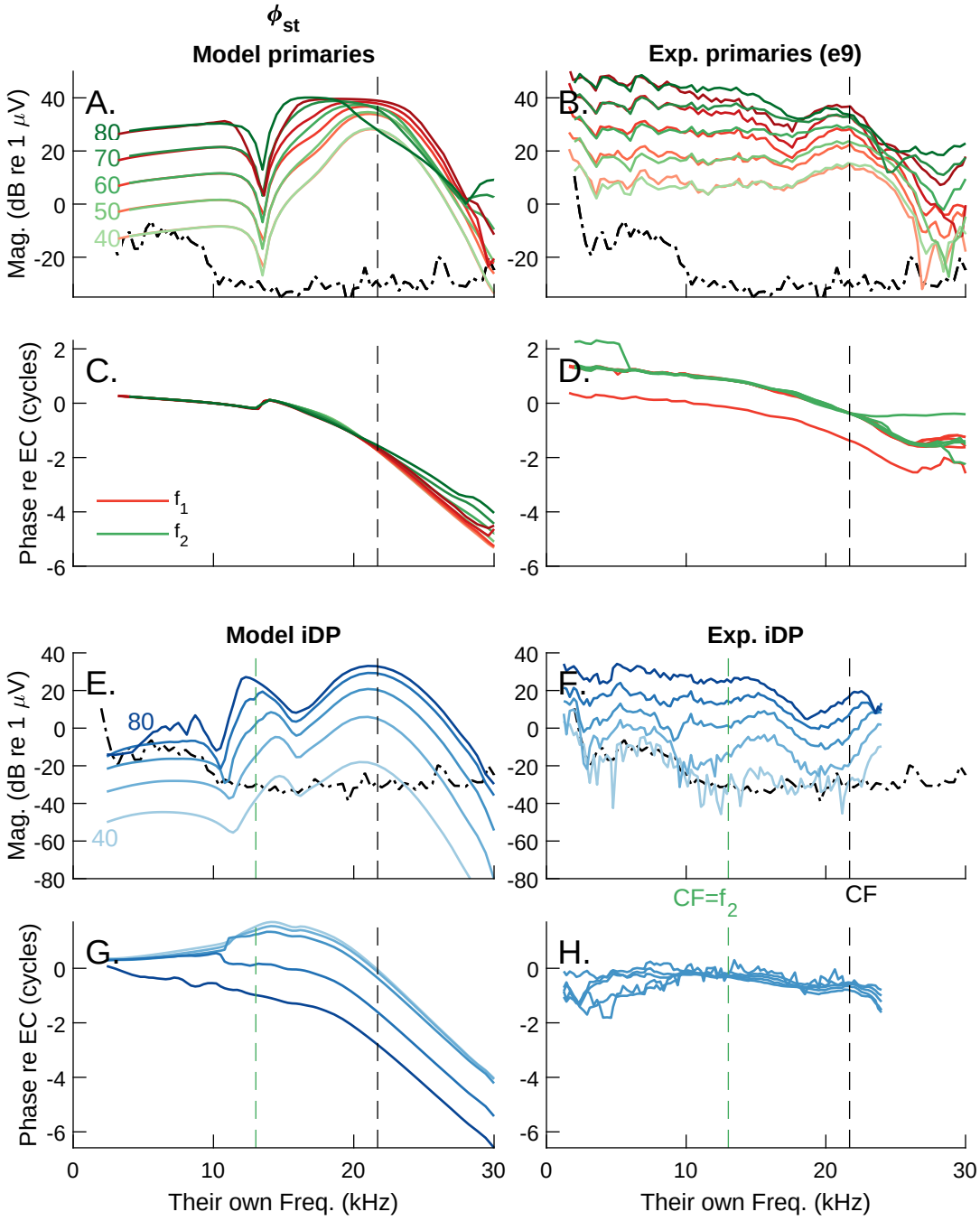

FIGURE 5.12. Comparison of the ST potential two-tone response for the model and experimental data from Dong[147] for f_2/f_1=1.25. All other details are the same as Figure 5.8.

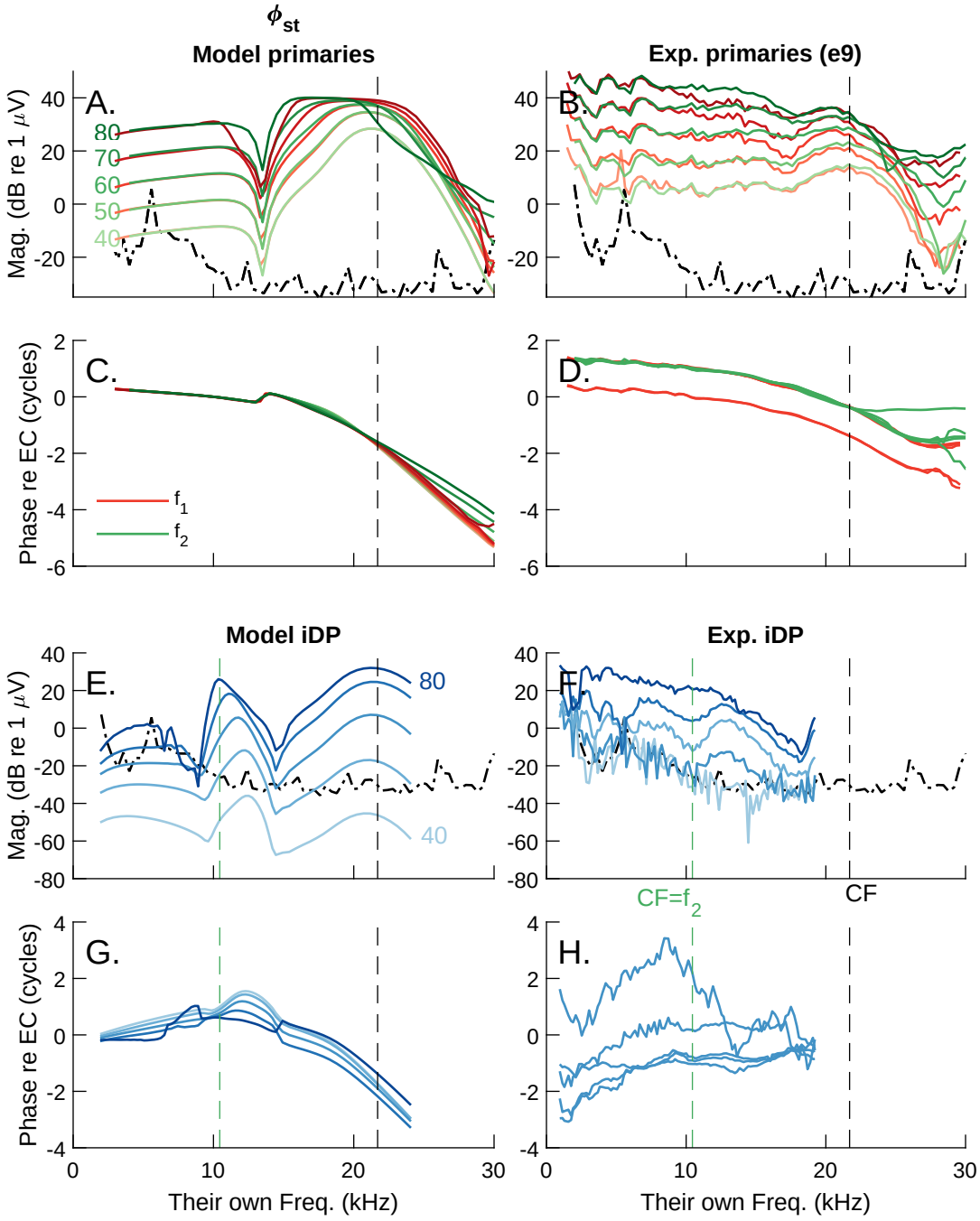

FIGURE 5.13. Comparison of the ST potential two-tone response for the model and experimental data from Dong[147] for f_2/f_1=1.35. All other details are the same as Figure 5.8.

5.4.3 Comparison of ST pressure and potential peak magnitudes for varied f_2/f_1

One surprising difference between the model predictions and the experiments in the previous figures pertains to the influence of f_2/f_1 on the f_2 primary response. In the model ST pressure, the magnitude of the f_2 primary response at its CF does not depend significantly on f_2/f_1, while it decreases as f_2/f_1 increases in the experiment (Figure 5.14A-B). Using the f_2 primary response at CF in the ST pressure with a 80 dB SPL stimulus as an example, the magnitude predicted by the model is around 108-109 dB SPL for varied f_2/f_1 while the magnitude from the experiment decreases from 116 dB SPL at f_2/f_1=1.05 to 110 dB SPL at f_2/f_1. This decrease in the f_2 response magnitude is unexpected because the same primary stimulus level was used for all f_2/f_1. Due to two-tone suppression, it could be expected that the magnitude of the f_2 response would decrease as f_2/f_1 decreases due to an increase in the overlap between the two primary responses (as observed in the model predictions). However, the opposite trend is observed in the experiments, suggesting that two-tone suppression is not the cause of the decrease in the f_2 primary response. Unlike the ST pressure,the experiment f_2 primary response in the ST potential does not significantly decrease in magnitude (Figure 5.14D), implying that the results for the ST pressure and potential are inconsistent.

Several explanations are possible regarding the surprising influence of varying f_2/f_1 on the ST pressure and potential: a reduction in cochlear amplification, a shift in the position of the pressure sensor during the measurement, or degradation of the pressure sensor during the measurement. The fact that the f_2 response in the ST pressure decreases by 6-7 dB with increasing f_2/f_1 while the ST potential varies by <2 dB implies that a reduction in cochlear amplification or OHC performance during the experiments is probably not the cause of the reduction in the ST pressure because the ST potential is more sensitive to the output of the OHCs than the pressure. If the longitudinal position of the pressure sensor was changed during the experiment, there would also be a shift in the peak frequency due to tonotopy (place-frequency map) of the cochlea; however, no such shift in frequency is observed.

The decrease in the peak magnitudes of the pressure could be explained by a change in the distance between the sensor and BM (the pressure would decrease as the sensor is moved away from the BM, Figure 4.4). Another possible explanation is that the pressure sensor is degraded during the measurements, possibly due to bone fragments (created by the drill used to access the cochlea) damaging the thin plastic diaphragm at the tip of the sensor.

It is difficult to assess the accuracy of the f_2 primary response predictions given the noted unexpected experiment results, but the model response does not appear to be unreasonable.

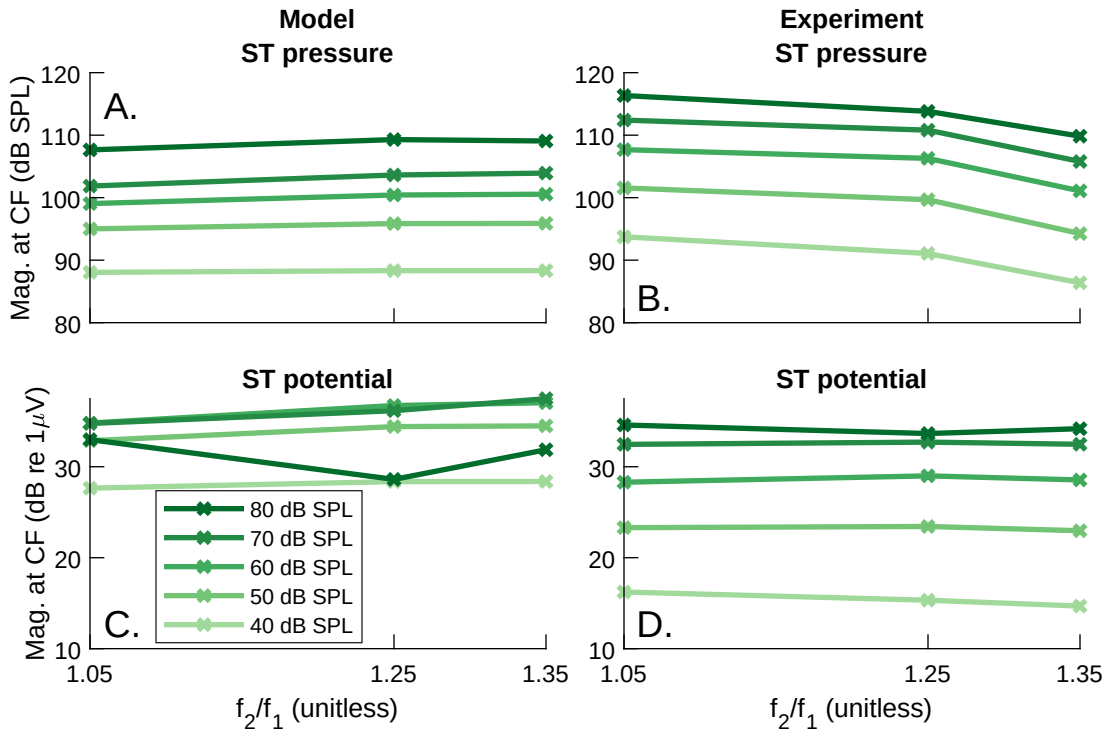

FIGURE 5.14. Magnitude of the f_2 response at CF for the model and experiment ST pressure and potential. (A.) Model ST pressure. (B.) Experiment ST pressure. (C.) Model ST potential. (D.) Experiment ST potential.

5.5 Three-tone response

5.5.1 Overview of 3-tone response

In experiments, applying a third stimulus tone has been effectively used to affect the region of iDP and DPOAE generation[136]. Adding a third tone with a relatively large stimulus level will cause saturation of the MET current. The amount of saturation is related to the HB deflection at f_3. Figure 5.15 shows the magnitude of the HB deflection in response to a high level tone (a third tone suppressor). In Figure 5.15 (and Figures 5.16, 5.22, 5.23, and 5.24), shading is used to indicate the spatial extent over which the magnitude of the HB deflection at f_3 is large.

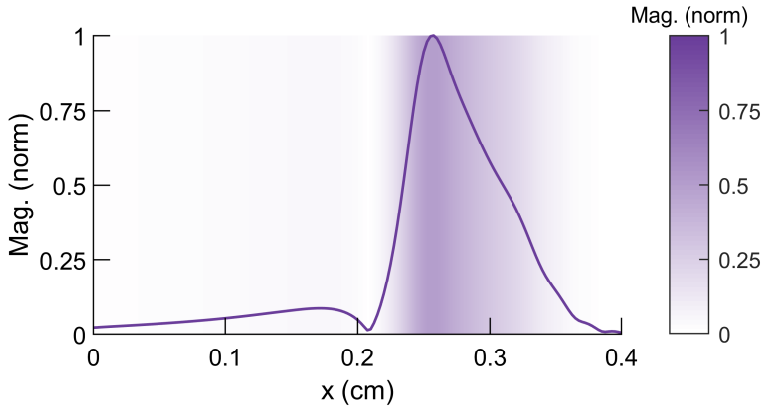

FIGURE 5.15. Magnitude of the HB deflection in response to a third tone at f_3=17.01 kHz at 90 dB SPL. The response is normalized by the peak magnitude. The shading denotes the region of large HB deflection at f_3.

The effect of applying a third stimulus tone of frequency f_3 near f_2 on the BM velocity response of the two primaries and iDP is examined in Figure 5.16. Due to the relatively high stimulus level of the two primaries (80 dB SPL), the MET current for the two primaries is nearly saturated such that the third tone only slightly suppresses the responses at f_1 and f_2 (adding f_3 reduces the peak magnitudes of f_1 and f_2 by 3.0 and 3.5 dB, respectively, Figure 5.16A). However, the response of the iDP in the 3-tone case is dramatically reduced from the 2-tone case (generally $\geq$20 dB) at all positions. In addition to the response on the BM,

the DPOAE (ear canal pressure at $2f_1 - f_2$, not shown in Figure 5.16) is reduced by 22 dB when the third tone is added. This reduction in the iDP and DPOAE response is due to the third tone saturating the MET current and thereby significantly decreasing iDP generation. These results also imply that in response to the two-tone stimulus, the DPOAE primarily originates from the shaded region where the f_3 HB response has a large magnitude.

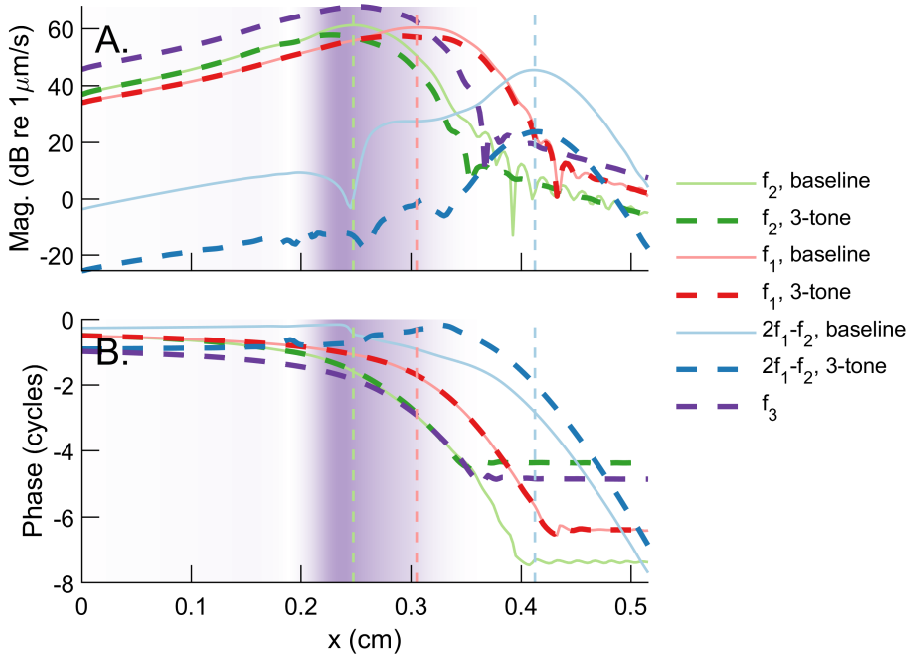

FIGURE 5.16. BM velocity response of the primaries and iDP for 2- and 3-tone stimuli for f_2/f_1=1.25 with f_1=16 kHz and f_2=20 kHz both at 80 dB SPL. The third tone was set to f_3=18.5 kHz at 90 dB SPL. (A.) Magnitude. (B.) Phase. The vertical dashed lines denote, from left to right, the f_2, f_1, and $2f_1 - f_2$ peak positions from the 2-tone response. The intensity of the shading denotes the normalized magnitude of the HB deflection at f_3.

5.5.2 Comparison of model and experiment responses

In the remainder of this section, the response of the model to a three-tone stimulus is compared to experimental data provided by Dr. Wei Dong. The purpose of this comparison is to validate the effects of suppression on the model response and to determine how varying the frequency of the third tone relative to the primaries affects iDP generation and DPOAEs. In contrast with Figure 5.16, the location of the measurement and ratios f_2/f_1 and f_3/f_2

are fixed while the frequencies f_1, f_2, and f_3 are varied continuously.

In Figure 5.17, the effect of applying a third tone at a frequency $f_3 > f_2$ is given. When the third tone is slightly above f_2 (f_3/f_2=1.15), the f_2 response is suppressed compared to the two-tone response (Figure 5.17A-B). Near CF, the magnitude of the model f_2 response is decreased by nearly 10 dB (f_3/f_2=1.15, Figure 5.17A) while the magnitude of the experiment f_2 response is decreased by more than 20 dB (Figure 5.17B). When the third tone is farther above f_2 (f_3/f_2=1.5), the f_2 response is not significantly affected: the model peak magnitude is essentially unchanged and the experiment peak magnitude decreases by less than 3 dB. The model f_1 responses for both f_3/f_2 ratios are not affected by the third tone due to the small amplitude of f_3 over the region where the f_1 response is large (Figure 5.17A). While the experiment f_1 response for f_3/f_2=1.5 is unaffected by the third tone, the f_1 response for f_3/f_2=1.15 is reduced by more than 20 dB (Figure 5.17B).

For the 2-tone stimulus, the peak magnitudes of the model primaries are within 2 dB of the peak magnitudes of the experiment primaries (Figure 5.17A-B). The peak magnitude of the model 2-tone iDP, however, is approximately 10 dB higher than the peak of the experiment iDP (Figure 5.17E-F). Applying the third tone slightly above f_2 (f_3/f_2=1.15) results in a $\approx$5 dB decrease in the model iDP response (Figure 5.17E) and much larger decrease of more than 20 dB for the experiment iDP (Figure 5.17F). The addition of the third tone also reduces the DPOAE (Figure 5.18A-B). Because f_3/f_2 is fixed, the third tone has a similar effect on the primaries and DPOAE regardless the frequency. As a result, for f_3/f_2=1.15 the third tone results in a fairly consistent decrease of 5-10 dB in the model (Figure 5.18A), similar to the decrease on the BM (Figure 5.17E). The experiment DPOAE for f_3/f_2=1.15 has a much larger decrease in magnitude (>10 dB) relative to the 2-tone data (Figure 5.18B). The decrease in the iDP BM response and DPOAE indicate that the f_3/f_2=1.15 third tone is able to reduce iDP generation in the region from where the DPOAEs originate.

Applying the third tone further above f_2 (f_3/f_2=1.5) has minimal effect on both the

model and experiment iDP (Figure 5.17E-F). Similarly, the third tone has only a very limited effect on the model and experiment DPOAE (Figure 5.18A-B). The fact that the iDP and DPOAE are unaffected when f_3/f_2=1.5 implies that there are no iDP generators in the region of the f_3 peak that contribute to the DPOAE.

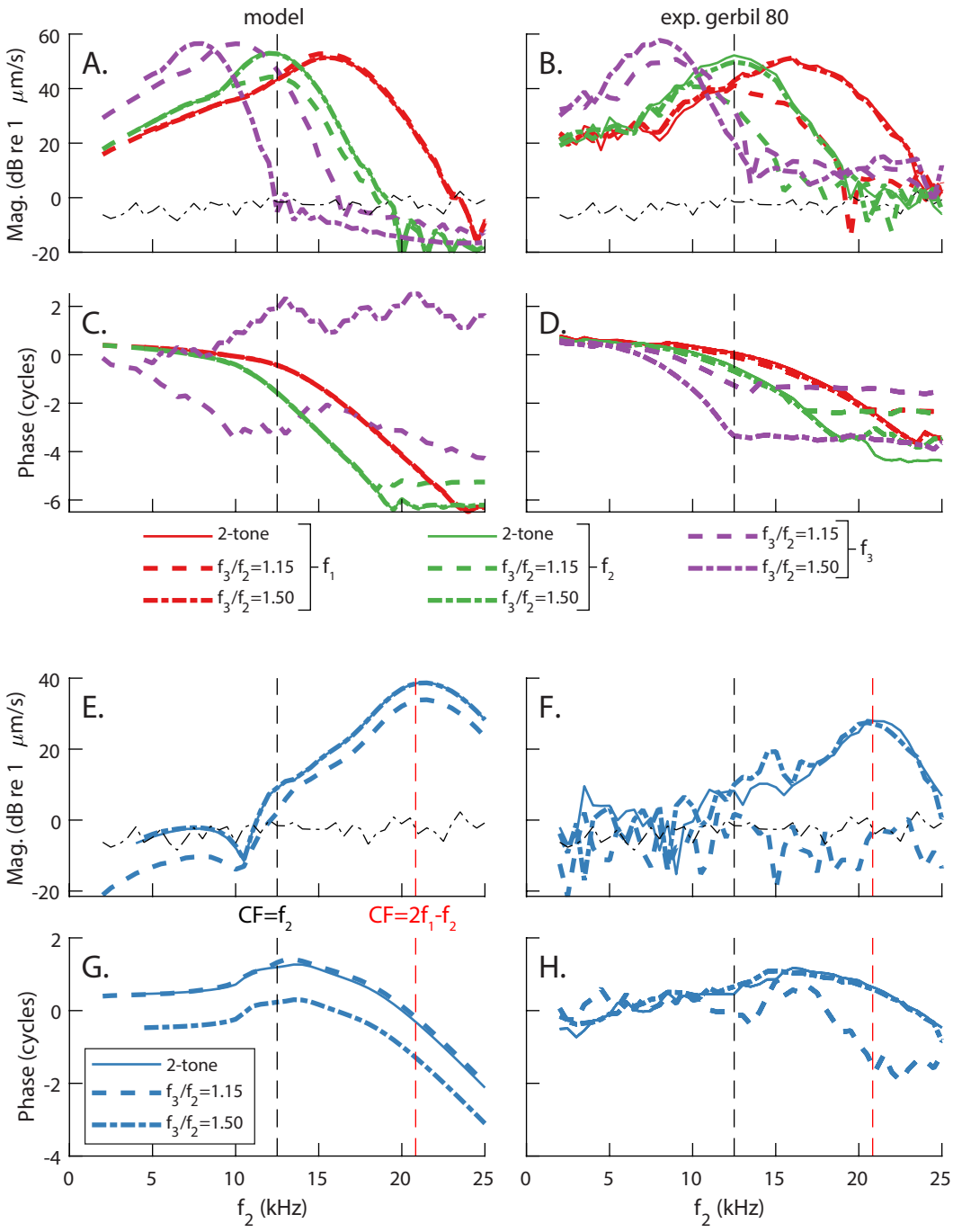

FIGURE 5.17. Comparison of the BM velocity response for two- and three-tone stimuli for the model and experimental data from Dong[147] for f_2/f_1=1.25 at the 12.5 kHz best place for primary stimulus levels of 60 dB SPL and a third tone of frequency f_3 above f_2 at 70 dB SPL. (A-D) Response of the primaries and third tone. (E-H) Response of the $2f_1 - f_2$ iDP. (A,C,E,G) Model results. (B,D,F,H) Experimental results from gerbil experiment 80. The noise floor from the experiment is plotted as a black dash-dotted line on both the experiment and model panels.

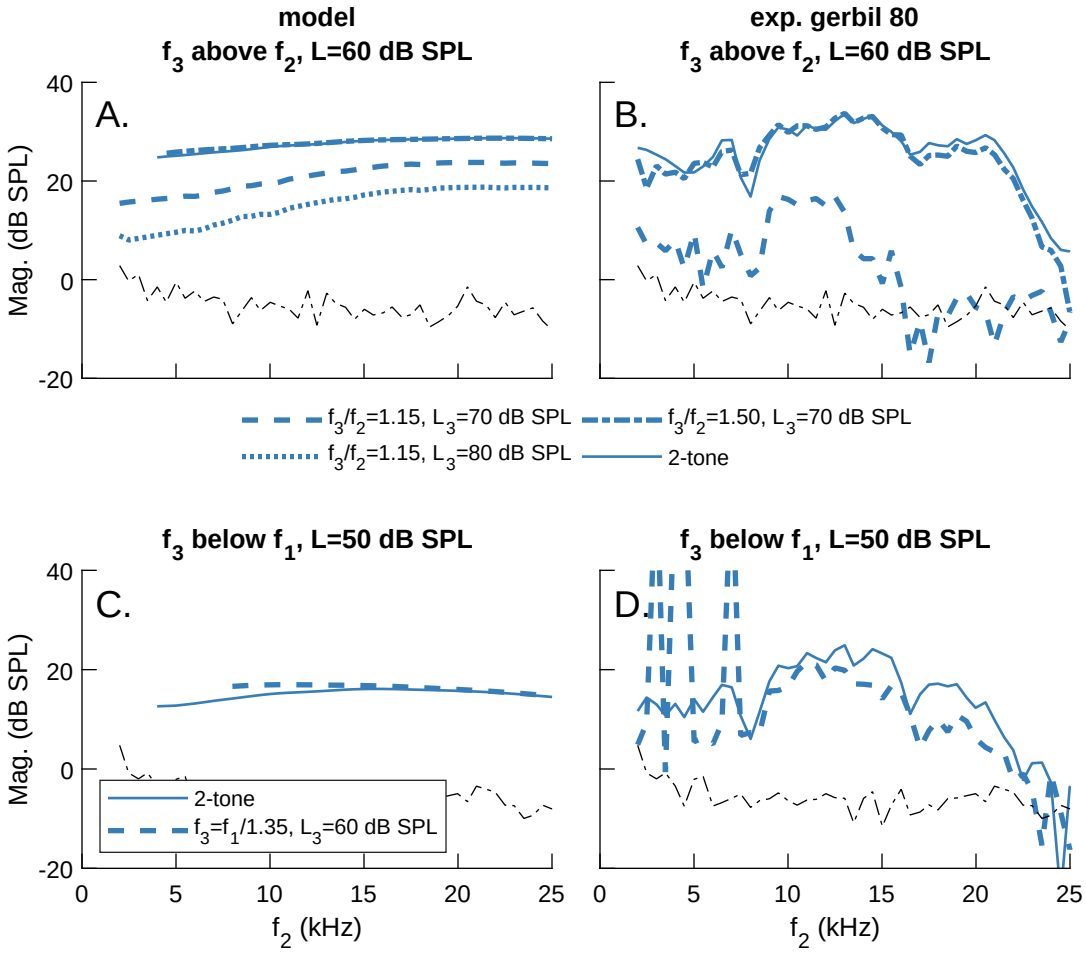

FIGURE 5.18. Comparison of the DPOAE (DP in the ear canal) for the model and experiment in response to a 2- or 3-tone stimulus. The noise floor from the experiment is plotted as a black dash-dotted line on both the experiment and model panels. (A. and C.) Model results. (B. and D.) Experiment results. (A. and B.) The primary stimulus level was 60 dB SPL and the third tone of frequency f_3 was at 70 dB SPL. (C. and D.) The primary stimulus level was 50 dB SPL and the third tone was at 60 dB SPL.

Applying a third tone with a frequency close to $2f_1 - f_2$ suppresses the iDP response around CF=$2f_1 - f_2$ (Figure 5.19). In this case, the third tone has minimal to no effect on the response of the primaries, both for the model and experiment (Figure 5.19A-D). The third tone has no effect on the primaries because the response of the third tone is very small at the peaks of the response to the primaries (Figure 5.19) and the primaries are already decreasing where the third tone peaks. Surprisingly, the experiment 2-tone iDP does not peak at $2f_1 - f_2$=CF (vertical red dashed line, Figure 5.19F). This is inconsistent with both

the model results (Figure 5.19E) and similar 2-tone experimental results in Figure 5.17F, which all show a peak in the iDP response when $2f_1 - f_2$=CF. The peak of the iDP response (at $2f_1 - f_2$=CF) is reduced by nearly 15 dB for the model when the third tone is added (Figure 5.19E). For the experiment, the decrease is at least 15 dB; it may be even more than that but the iDP for the 3-tone is in the noise so an exact value of the decrease cannot be determined (Figure 5.19F). These decreases in the iDP response, however, do not have an effect on the DPOAE for both model and experiment (Figure 5.18C-D), indicating that the DPOAE measured in the ear canal does not originate from the best place of the iDP.

In this section the model responses of the BM and DPOAE for 2- and 3-tone stimuli were compared to experimental data. Both model and experiment show suppression of the iDP and DPOAE when a third tone is added at $f_3 = 1.15f_2$; however, the model appears to underpredict the amount of suppression. When a third tone of frequency f_3 is applied either farther above f_2 (i.e. when $f_3 = 1.5f_2$) or below f_1 (i.e. when $f_3 = f_1/1.35$), both model and experiment show minimal change in the DPOAE.

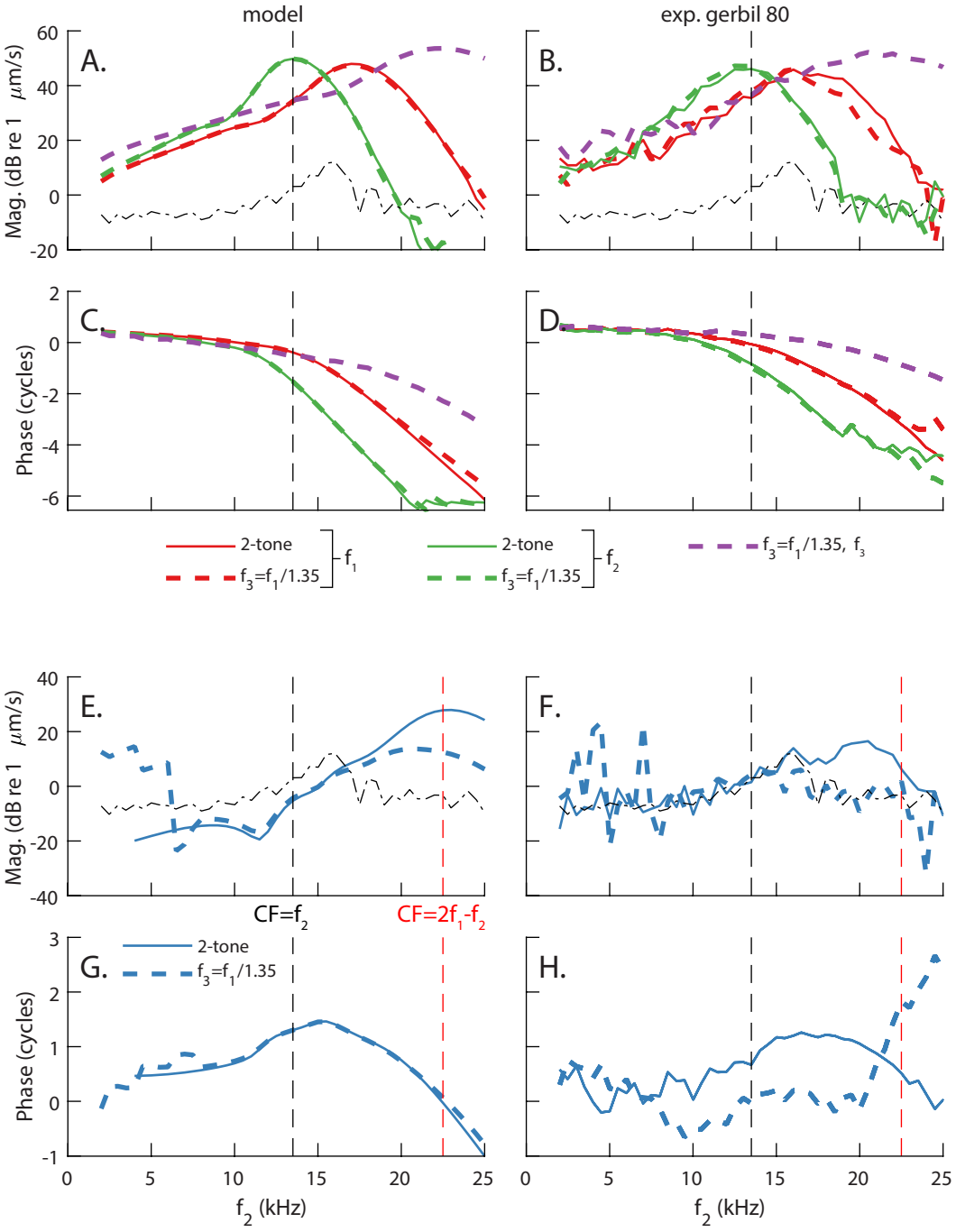

FIGURE 5.19. Comparison of the BM velocity response for two- and three-tone stimuli for the model and experimental data from Dong[147] for f_2/f_1=1.25 at the 12.5 kHz best place for primary stimulus levels of 50 dB SPL and a third tone below f_1 at 60 dB SPL. Other details are the same as Figure 5.17.

5.6 Estimating locations of iDP generation

5.6.1 Applying local damage

To mimic the effect of local OHC damage, one of the parameters closely associated with the OHCs, the MET current, i_{MET}, was set to zero over a small region (Figure 5.20):

$$i_{MET}(u_{hb/rl}) = w(x) i_{MET,baseline}(u_{hb/rl}) \tag{5.4}$$

where $i_{MET,baseline}$ is defined by Equation 2.34 and $w(x)$ is the local damage profile. Setting $w(x) = 1$ represents the baseline, healthy cochlea. Setting $w(x) = 0$ represents damage, where the MET current and nonlinearity are eliminated. While applying a third tone can cause saturation of the MET current over a relatively large extent of the cochlea, applying local damage in the model causes total elimination of the MET current over a well defined, and potentially narrow, spatial region. Any abrupt change in the spatially-dependent cochlear properties will cause reflections; to minimize these reflections there is a smooth transition (using a raised cosine, Figure 5.20) between the "undamaged" baseline regions to the "damaged" region.

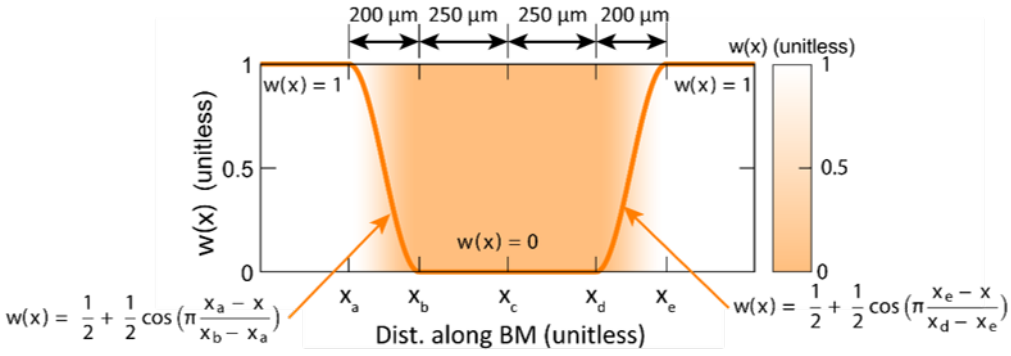

FIGURE 5.20. Weighting function for applying local damage. The intensity of the shading denotes the value of $w(x)$.

The effect of applying local damage near the f_2 peak on the BM velocity response of the two primaries and iDP is examined in Figure 5.21. Due to the relatively high stimulus

level (80 dB SPL), the MET current for the two primaries is nearly saturated such that the damage has minimal effect on the response of the primaries (although the peak of the f_1 response is reduced slightly). The response of the iDP from the damaged case is significantly reduced at nearly all positions from the base to beyond the iDP best place (Figure 5.21A). In addition to reducing the response on the BM, the local damage reduces the DPOAE (ear canal pressure at $2f_1 - f_2$) magnitude by more than 15 dB.

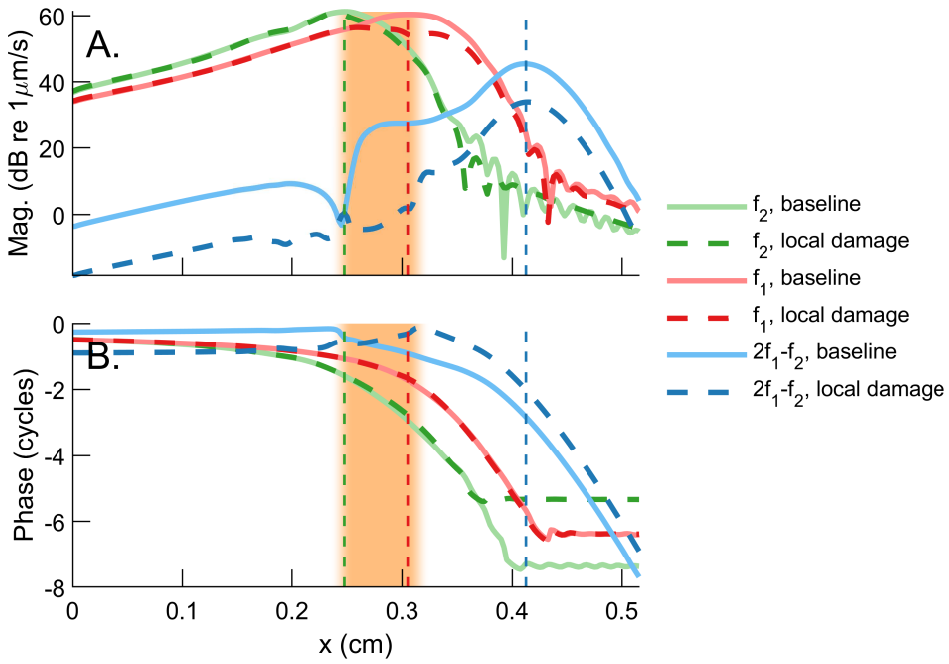

FIGURE 5.21. BM velocity response of primaries and iDP for baseline and local damage for f_2/f_1=1.25 with f_2=20 kHz at 80 dB SPL. The local damage was applied at x_c=0.28 cm. (A) Magnitude. (B) Phase. The vertical dashed lines denote, from left to right, the f_2, f_1, and $2f_1 - f_2$ peak positions for the baseline model. The intensity of the shading denotes the value of $w(x)$ for the locally damaged model.

5.6.2 Effect of local damage or third tone on BM and extracellular potential

In the next three figures, the effects of applying local damage or a third tone on the spatial responses of the BM and OHC extracellular potential iDPs are reported for three cases: (1) affecting a region very basal to the f_2 peak (Figure 5.22); (2) affecting the region between the f_2 and f_1 peaks (Figure 5.23); (3) affecting the region around the $2f_1 - f_2$ peak (Figure

5.24). In all three cases, the third tone frequency and local damage positions were chosen such that they affected similar longitudinal positions (i.e. the center of the local damage (x_c, Figure 5.20) was chosen to correspond approximately to the peak of the third tone response). It should be noted, however, that added a third tone or local damage are not equivalent; the third tone tapers off slower and affects a slightly larger region compared to the local damage (Figures 5.20 and 5.15).

For the case shown in Figure 5.22, applying damage or third tone at a frequency well above f_2 results in a change in the DPOAE of less than 0.1 dB. The response of the BM velocity is similarly unaffected by the damage or third tone (Figure 5.22). This also implies that iDP BM response is due to iDP generators located apical to the affected region. However, the iDP response on the voltage are reduced by the damage or third tone. This suggests that there is some local DiP generation at these positions, but because the DPOAE was unaffected, these generators do not significantly contribute to the DPOAE. The damage and third tone have minimal effect on the BM and voltage apical to x=0.2 cm. Combined with the fact that the DPOAE was unaffected, these results indicate that for the stimulus parameters considered here (f_2/f_1=1.25 and f_2=20 kHz at 80 dB SPL), all the iDP generators that contribute to the DPOAE are located apical to the affected region.

When the location of the local damage and frequency of the third tone are selected to affect the region between the f_2 and f_1 peaks (Figure 5.23), the DPOAE is significantly reduced. Additionally, the iDP BM velocity and extracellular voltage are reduced significantly at all longitudinal positions. Applying local damage resulted in a 15 dB decrease in the DPOAE while the third tone resulted in a 29 dB decrease. BM and voltage responses are significantly reduced between the f_2 and f_1 peaks. At the iDP best place, BM and voltage are reduced by similar amounts (approximately 10 dB). When local damage is applied, the iDP BM response is reduced at the base by nearly 15 dB while the voltage is reduced by 7 dB (Figure 5.23A). When a third tone is applied, the BM response at the base is reduced by 27 dB while the voltage is reduced by 13 dB (Figure 5.23B). For both the local damage

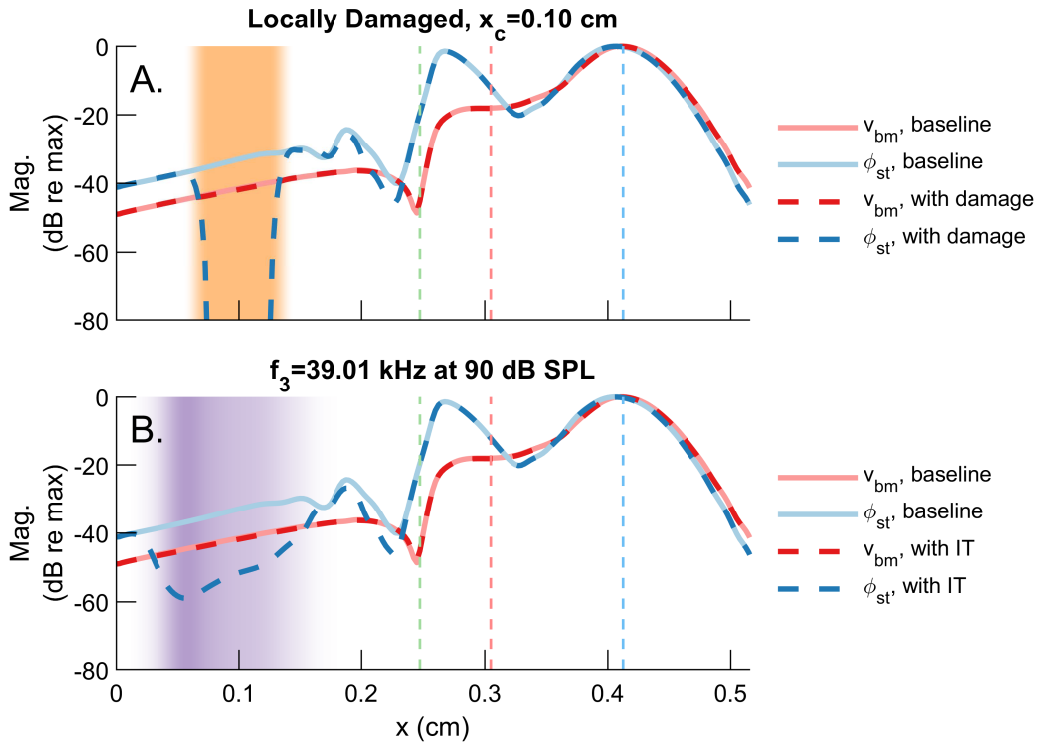

FIGURE 5.22. Comparison of the effects of adding either local damage or a third tone at a basal position on the spatial response of the iDP on the BM and extracellular voltage. The primary frequency ratio is f_2/f_1=1.25 with f_2=20 kHz at 80 dB SPL. A. Local damage applied at x_c=0.10 cm. B. A third tone added at f_3=39 kHz (f_3/f_2=1.95) at 90 dB SPL. The vertical dashed lines denote, from left to right, the f_2, f_1, and $2f_1 - f_2$ peak positions for the baseline model.

and third tone, the BM response at the base and DPOAE are reduced by similar amounts (15 dB for damage and 27-29 dB for third tone). Before the iDP makes it into the ear canal to appear as a DPOAE, it must first transit the base of the cochlea as a reverse traveling wave (Chapter 4). This fact (along with the model assumption that the middle ear is a linear system), explains why the iDP BM response at the base and DPOAE are reduced by similar amounts when local damage or a third tone are applied. The significant reduction in the DPOAE when either local damage or a third tone are applied to affect the region between the f_2 and f_1 peaks indicate that this region contains many of the iDP generators that contribute to the DPOAE.

When the location of the local damage and frequency of the third tone are selected to

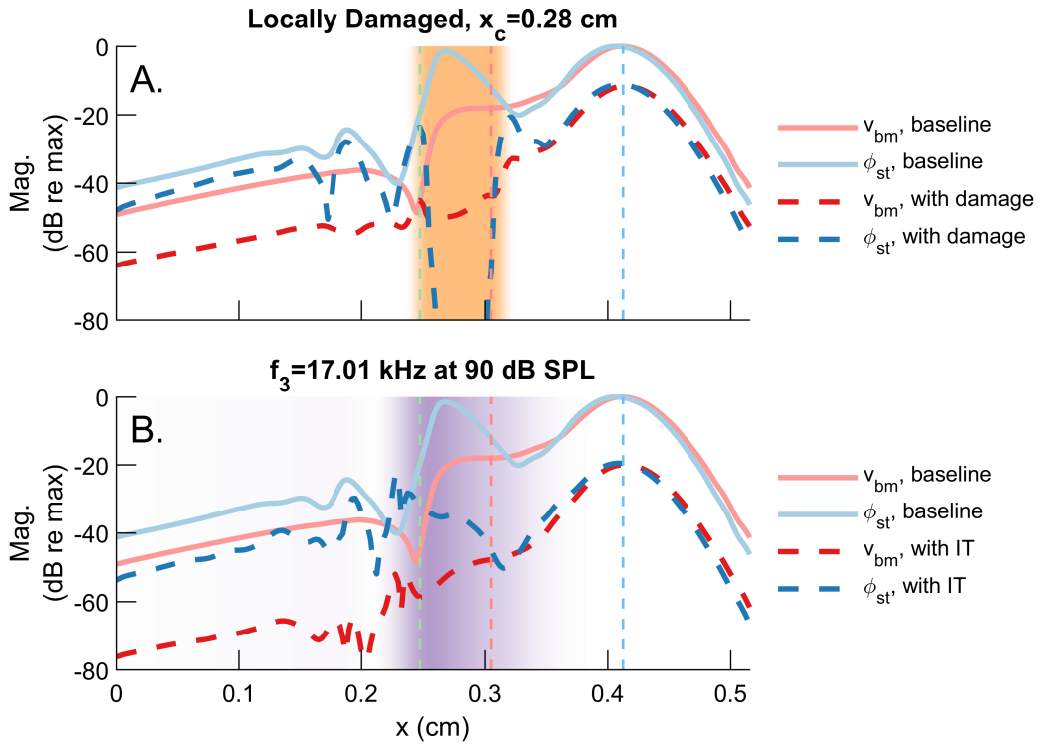

FIGURE 5.23. Comparison of the effects of adding either local damage or a third tone at a position between the f_2 and f_1 peak positions on the spatial response of the DP on the BM and extracellular voltage. The primary frequency ratio is f_2/f_1=1.25 with f_2=20 kHz at 80 dB SPL. A. Local damage applied at x_c=0.28 cm. B. A third tone added at f_3=17.01 kHz at 90 dB SPL. The vertical dashed lines denote, from left to right, the f_2, f_1, and $2f_1 - f_2$ peak positions for the baseline model.

affect the region around the iDP peak (Figure 5.24), the DPOAE is only minimally affected. Applying local damage resulted in a 2.54 dB increase in the DPOAE while the third tone resulted in a 0.81 dB decrease. Given the small changes in the DPOAE, the effects of the local damage or third tone were likely not limited to just the region around the iDP best place and may have extended towards the f_1 peak. The local damage and third tone most significantly affect the iDP response only around the iDP peak. Because the model does not include roughness, no iDPs are expected to be generated around the iDP best place, and so most iDP generation is basal to the f_1 peak. Since the local damage and third tone do not affect significantly affect the response basal to x=0.35 cm, none of the iDP generators that contribute to the DPOAE were affected and thus the DPOAE is relatively unaffected.

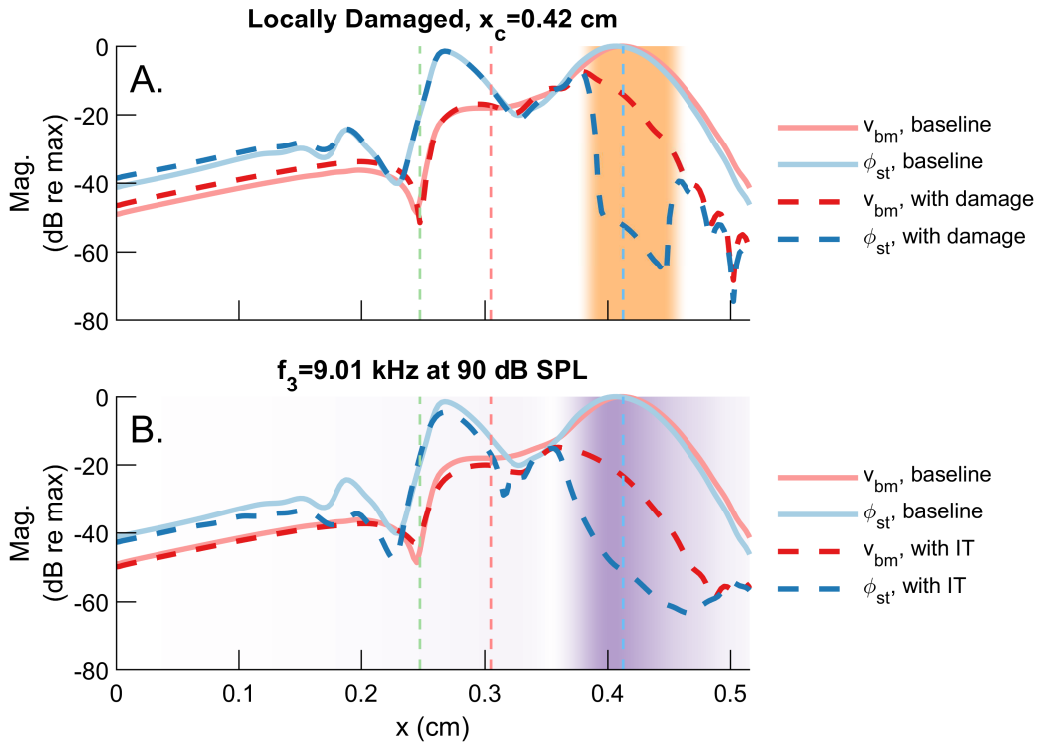

FIGURE 5.24. Comparison of the effects of adding either local damage or a third tone near the $2f_1 - f_2$ peak on the spatial response of the DP on the BM and extracellular voltage. The primary frequency ratio is f_2/f_1=1.25 with f_2=20 kHz at 80 dB SPL. A. Local damage applied at x_c=0.42 cm. B. A third tone added at f_3=9.01 kHz at 90 dB SPL. The vertical dashed lines denote, from left to right, the f_2, f_1, and $2f_1 - f_2$ peak positions for the baseline model.

5.6.3 Effect of varying f_3 and local damage on DPOAE for fixed f_1 and f_2

The comparison of model and experiment results with a three-tone stimulus (Figures 5.17, 5.19, and 5.18) fixed the ratio f_3/f_2 and varied f_2 (and thus f_3). Another common approach used experimentally is to fix f_1 and f_2 while varying f_3 [148]. This second approach enables determining when a third tone will have the most significant effect on iDP generation and the DPOAE and is considered in this section.

Applying local damage or adding a third stimulus tone have different effects on iDP generation, even when they affect similar positions. The effects of varying either the position of local damage or f_3 on the DPOAE are compared with the extracellular voltage in Figure 5.25 for three f_2/f_1 ratios with fixed f_2. The DPOAEs corresponding to the iDP

responses presented in Figures 5.22, 5.23, and 5.24 are indicated with arrows in Figure 5.25B. Applying local damage effectively disables the iDP generators over the affected area. By fixing f_2 and f_1 while varying the position of the local damage, the DPOAE in the locally damaged model will be affected when the damage is in the regions of iDP generation. Similarly, adding a third tone causes saturation of the MET current and a reduction in iDP generation.

Applying damage or a third tone at either very basal or very apical positions relative to the peak positions has minimal to no effect on the DPOAE, indicating that no DPOAEs originate from these regions. For f_2/f_1=1.05 (Figure 5.25A), local damage actually results in an increase in the DPOAE relative to the baseline undamaged 2-tone DPOAE. For the local damage, this region of increased DPOAE extends relatively far both basal to the f_2 best place and apical to the $2f_1 - f_2$ best place (x_C=0.16-0.36 cm for the damage to cause a >3 dB change in the DPOAE). Applying a third tone can result in either suppression or enhancement of the DPOAE, depending on f_2/f_1 and f_3. At narrow f_2/f_1 ratios and high stimulus levels, both primaries are large over a relatively wide region, providing a large region for iDP generation. The phase of the primaries (ϕ_1 and ϕ_2) and thus iDP (which varies with $2\phi_1 - \phi_2$) varies with position (Figure 5.21B). Distortion sources with opposite phase can cancel each other to reduce the overall emission. Applying a third tone with f_2/f_1=1.05 (Figure 5.25A) results in a >3 dB change in the DPOAE when the third tone peak position is between 0.17 cm and 0.36 cm (similar to the local damage). At a narrow ratio, some of this cancellation very like occurs in the baseline model; applying local damage or third tone can eliminate distortion sources that would otherwise interfere with other sources, resulting in an overall larger emission.

At wider f_2/f_1 ratios (Figures 5.25B-C), the damage and third tone reduce the DPOAE most significantly when the affected region occurs between the f_2 and f_1 peak positions, suggesting that the DPOAE primarily originates from this region. For f_2/f_1=1.25 (Figure 5.25B) and f_2/f_1=1.35 (Figure 5.25C), applying local damage between x_C=0.20-0.45 cm

and x_C=0.21-0.52 cm, respectively, results in a >3 dB change in the DPOAE. Applying a third tone when f_2/f_1=1.25 and 1.35 results in a >3 dB change in the DPOAE when the third tone peaks between 0.20 to 0.52 cm and 0.19 to 0.48 cm, respectively.

This analysis uses a smooth cochlear model, so no DPOAEs are expected to come from the reflection source near the iDP best place. However, even with using a raised cosine to transition between unaffected and damaged regions (Figure 5.20), the damage still causes a change in the impedance of the cochlear partition that can cause reflections. The impedance change likely generates some reflections and possibly explains the changes in DPOAE amplitude when the damaged region is near the iDP best place. The variations in the DPOAE when the third tone peaks at a position very apical to the iDP best place (Figures 5.25B-C) may be due to the relatively broad region affected by the third tone, especially at low frequencies (Figures 5.15 and 5.16).

For f_2/f_1 = 1.25 and 1.35 (Figures 5.25B-C), the extracellular potential, ϕ_{st}, has peaks at the $2f_1 - f_2$ and f_2 best places (like Figures 5.12 and 5.13). The peak at the f_2 best place is due to nonlinear distortion of the two primaries while the peak at $2f_1 - f_2$ is due to amplification of the iDP response by the cochlear amplifier. The peak in the iDP extracellular potential at the f_2 peak position corresponds to the positions that result in the largest decrease in the DPOAE when damage or a third tone is applied, indicating that most of the iDP generators that contribute to the DPOAE are located in this region.

An alternative approach for presenting the change in DPOAE when the third tone is applied is to change the abscissa from the third tone peak position to f_3/f_2 (Figure 5.26). This approach better relates to the results presented previously for various f_3/f_2 ratios (Figures 5.17, 5.19, and 5.18). For f_2/f_1=1.05 (Figure 5.26A), applying a third tone results in a >3 dB change in the DPOAE when f_3/f_2=0.58-1.5. At f_2/f_1=1.25 and 1.35 (Figures 5.26B-C), applying a third tone results in a >3 dB change in the DPOAE when f_3/f_2=0.28-1.15 and 0.38-1.20, respectively. These results are comparable with the findings by Martin et al. that suggesting basal DPOAE generators when f_3 was one-third octave above f_2

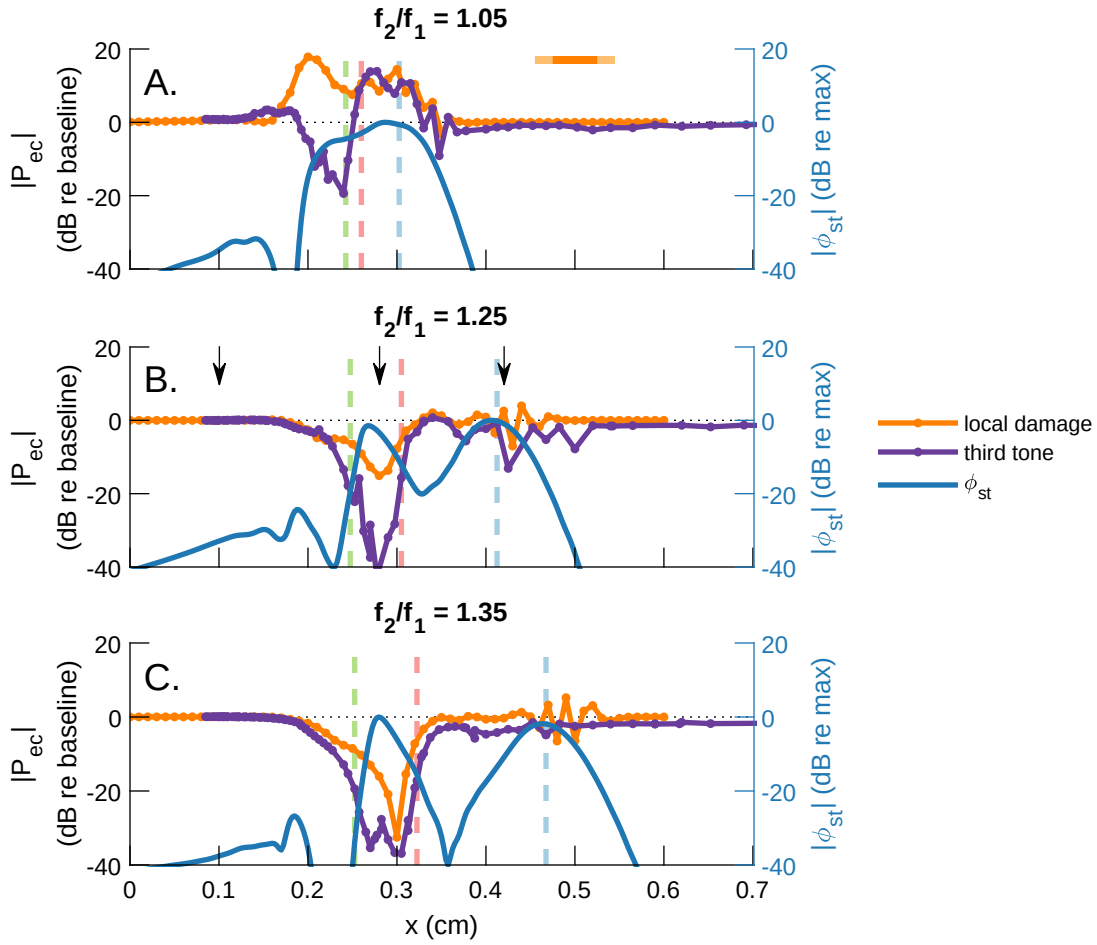

FIGURE 5.25. iDP ST potential and change in DPOAE level resulting from local damage or a third tone for several f_2/f_1 ratios with f_2=20 kHz at 80 dB SPL. The third tone stimulus level was set to 90 dB SPL and the abscissa is the peak position of the third tone response. For the local damage, the abscissa is given by x_c, is the center of the local damage (Figure 5.20). The vertical dashed lines denote, from left to right, f_2, f_1, and $2f_1 - f_2$. The arrows in panel B. indicate the DPOAEs corresponding to the spatial responses shown in, from left to right, Figures 5.22, 5.23, and 5.24, respectively. The scale bar in A. indicates the spatial extent of the local damage (Figure 5.20).

(f_3/f_2=1.26)[135]. These results are also comparable with measurements of DPOAEs in humans made by Martin et al.[148]; they reported a 2-4 dB change in the DPOAE even when f_3/f_2=2 (i.e. f_3 is a full octave above f_2). These results might suggest that the iDP generators that contribute the most to the DPOAE are located between the f_2 and f_1 peaks and that there are also iDPs generated at more basal positions that can contribute (albeit a small amount) to the DPOAE (as suggested by Martin et al.[135]). However, the effect of the

third tone is large for a relatively wide region after its peak (Figures 5.17 and 5.19), such that even when f_3 is reasonably higher than f_2, the third tone response can still affect the f_2 response at positions basal to the f_2 peak position.

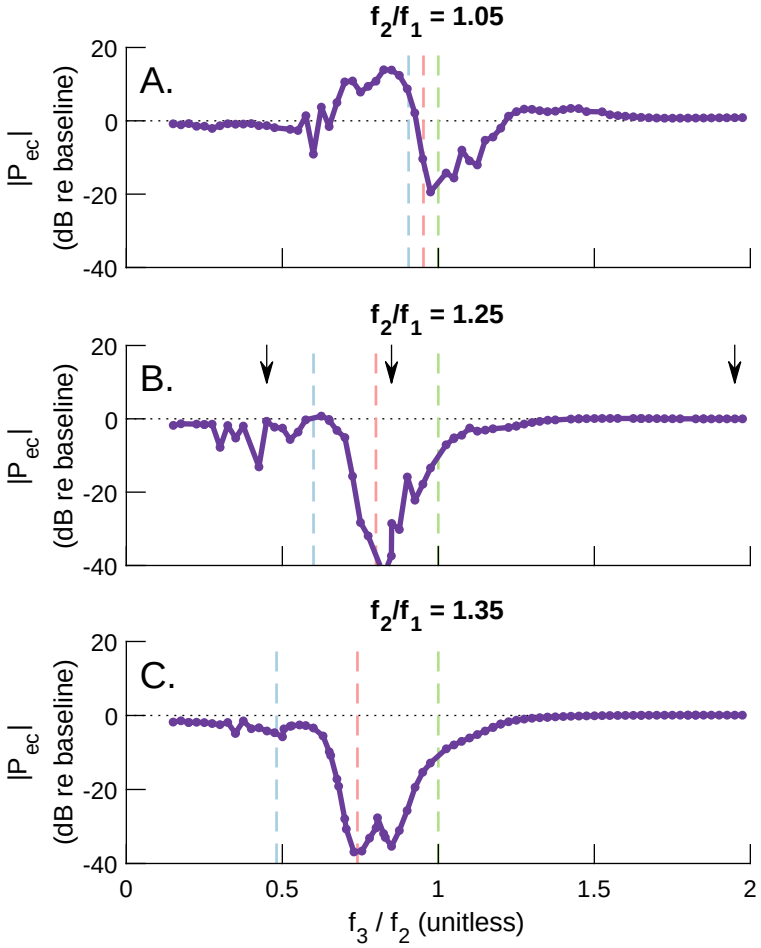

FIGURE 5.26. Change in DPOAE level resulting from a third tone for several f_2/f_1 ratios with f_2=20 kHz at 80 dB SPL. The third tone stimulus level was set to 90 dB SPL and the abscissa is f_3/f_2. The vertical dashed lines denote, from left to right, $2f_1 - f_2$, f_1, and f_2. The arrows in panel B. indicate the DPOAEs corresponding to the spatial responses shown in, from right to left, Figures 5.22, 5.23, and 5.24, respectively.

5.6.4 Estimating locations of DP generation for varied f_2/f_1 and primary stimulus levels

The results from Figure 5.25 are further expanded in Figure 5.27 for more f_2/f_1 ratios and shows many of the same trends. As in Figure 5.25A, at very narrow f_2/f_1 applying location

damage results in enhancement of the DPOAE (corresponds to the blue regions), while at wider ratios there is significant suppression (corresponding to the red regions, Figure 5.27A). Similarly, applying a third tone causes regions of enhancement and suppression at narrow f_2/f_1 but only suppression at wider f_2/f_1 ratios (Figure 5.27B). For $f_2/f_1 > 1.15$, the most dramatic decrease in the DPOAE occurs when the damage is applied between the f_2 and f_1 peak positions (Figure 5.27A, similar to Figure 5.25B-C). Similarly, when a third tone is applied (Figure 5.27B), the most dramatic decrease in the DPOAE occurs between f_2 and f_1. The results for applying local damage or a third tone indicate that most of the sources that contribute to the DPOAE occur in the region between the f_2 and f_1 peak positions. The regions of suppression that occur apical to the $2f_1 - f_2$ peak position when the third tone is applied are likely due to the relatively broad nature of the f_3 peak resulting from the high stimulus level (90 dB SPL, Figure 5.15).

The iDP extracellular voltage response for all f_2/f_1 =1.05-1.35 (Figure 5.27C) demonstrate many of the features already identified from the voltage responses in Figure 5.25. At f_2/f_1=1.05, the iDP extracellular voltage response is large over a relatively wide region compared to the locations of the primary and iDP peak locations. As f_2/f_1 is increased, this wide region separates into two distinct peaks: one between the f_2 and f_1 peak positions corresponding to nonlinear distortion and a second at the $2f_1 - f_2$ best place that corresponds to the amplification of the $2f_1 - f_2$ response by the cochlear amplifier. For f_2/f_1>1.2, the iDP extracellular voltage response is always >10 dB below the peak response for positions basal to the f_2 peak position, indicating a lack of iDP generation in these basal regions.

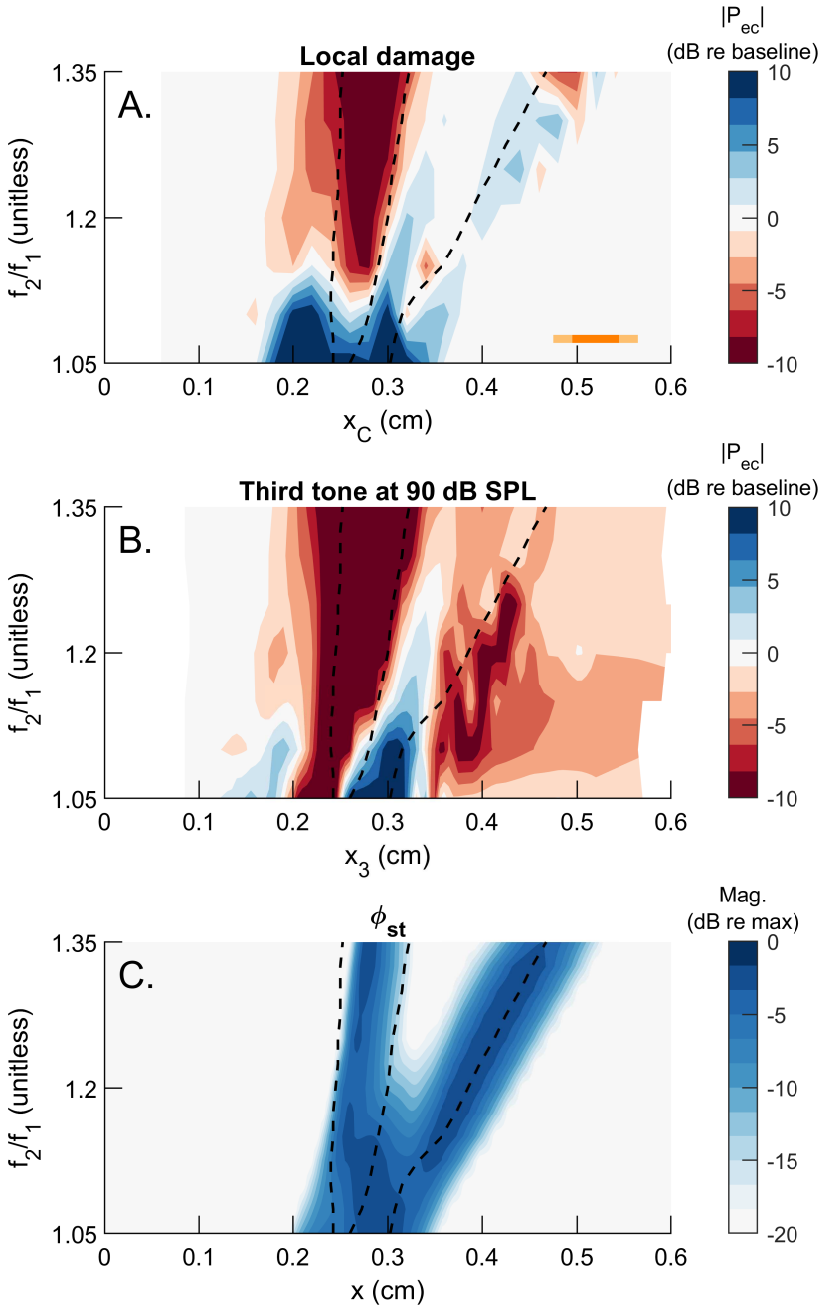

FIGURE 5.27. Locations of iDP generation that contribute to the DPOAE determined by the extracellular voltage, ϕ_{st}, and applying either local damage or a third tone. For all results, f_2 was set to 20 kHz with a stimulus level of 80 dB SPL. The dashed lines denote, from left to right, the f_2, f_1, and $2f_1 - f_2$ peak positions. (A.) Effect on DPOAE when local damage is applied for a 2-tone stimulus. The abscissa is the center of the applied local damage, x_C (Figure 5.20). The scale bar indicates the spatial extent of the local damage. (B.) Effect on DPOAE when a third tone at 90 dB SPL is applied. The abscissa is the peak position of f_3: x_3. (C.) Extracellular voltage of the undamaged model in response to a 2-tone stimulus normalized by the peak iDP response for each f_2/f_1.

5.7 Discussion

5.7.1 Strengths and limitations of the electrical model

Early analysis of the pure-tone response of the extracellular potential indicated that the model response was several orders of magnitude larger than the response reported experimentally (Figure 5.2). After the model was recalibrated, the model estimate of the extracellular potential around CF for a low level pure-tone stimulus was comparable to the values reported experimentally (Figure 5.3). Having the model predict a similar magnitude to the experiment around the peak is important for this work because most iDP generation is expected to occur around the f_2 and f_1 peaks. During model calibration, it was found that the model was unable to match the experiment at low frequencies relative to CF (Figure 5.3). However, if longitudinal electrical coupling was added to the scalae (referred to as electrical cables[79], Figure 5.28), the model was able to match the experiment voltage data both at CF and low frequencies relative to CF (Figure 5.29). These cables represent the flow of current through the cochlear ducts and allow neighboring OHCs to directly interact. When cables are included, the equation for the potential in the ST is:

$$\frac{1}{\lambda_{st}^2}\phi_{st} - \frac{\partial^2 \phi_{st}}{\partial x^2} = r_{st}\left(\frac{1}{R_m}\Delta\phi_{ohc} + C_m\Delta\dot{\phi}_{ohc} + i_{som}\right) \tag{5.5}$$

where r_{st} is the longitudinal resistance of the ST and the ST space constant, λ_{st}, is

$$\lambda_{st} = \sqrt{\frac{R_{tl}}{r_{st}}}. \tag{5.6}$$

The space constant provides an estimate of the length scale (and thus number of rows of OHCs) over which neighboring OHCs directly interact (the model without cables corresponds to $r_{st} = \infty$). Adjusting the resistances of the ST-ground and longitudinal ST coupling (R_{tl} and r_{st}, respectively) to match the experiment at low frequency and at the peak (Figure

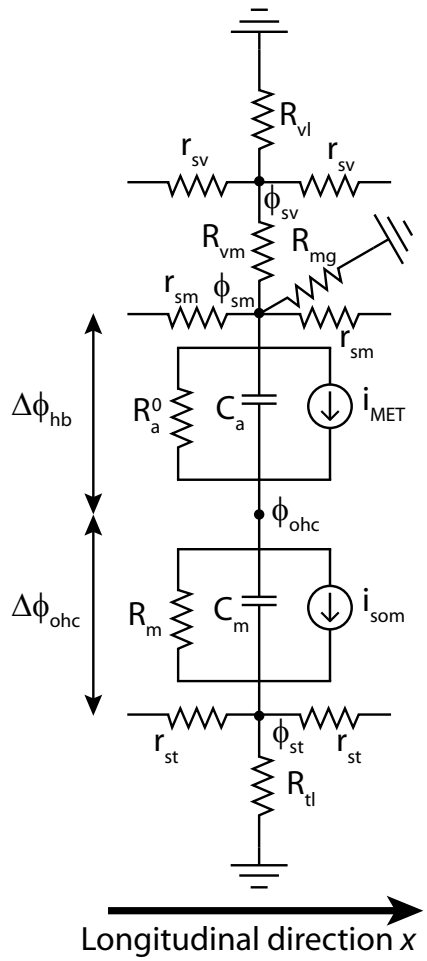

FIGURE 5.28. Circuit diagram of the electrical model with electrical cables included.

5.29) resulted in a space constant ($\lambda_{st} = \sqrt{R_{tl}/r_{st}}$ = 134 micron, "With cables, C" in Figure 5.29) that was larger than values reported experimentally (40-80 micron)[149,143]. A more significant issue that limits the use of the models with cables, however, is that including cables increases the stiffness of the system of ODEs that govern the nonlinear dynamics of the cochlear model (Equation 2.55). This increase in stiffness results in a dramatic decrease in the runtime performance of the time domain model (40x slower) that makes the use of the models with cables unfeasible. Despite efforts to improve the time domain runtime performance (Appendix D), this reduction in performance is similar to previous analysis by Meaud and Lemons[82], in which they reported a factor 46 reduction when cables are added to the model. A potential method for bypassing this computational issue is to solve for the

response with a nonlinear frequency domain model using a harmonic balance approach (as previously done by Meaud and Grosh[80,81]). Due to the significant runtime performance issues associated with adding electrical cables, all model results in this chapter, with the exception of Figure 5.29, were obtained from a model that does not include electrical cables (Figure 2.5).

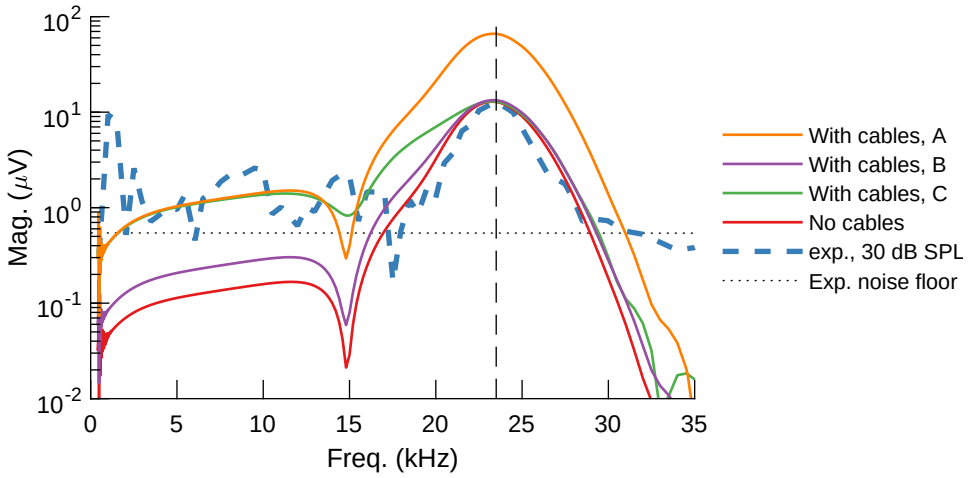

FIGURE 5.29. Response of extracellular voltage for linear active models that include electrical longitudinal cables with comparison to experimental data taken by Dong and Olson[143] at the 23.5 kHz best place. The electrical model parameters for the models are listed in Appendix C.

5.7.2 Comparison of model and experiment 2- and 3-tone responses

A comparison of model and experiment 2- and 3-tone responses was presented to validate the model and determine if the model OHC output is realistic. The peak magnitudes of the f_2 response at CF in the ST pressure were all within 10 dB of the magnitudes reported from the experiments (Figure 5.14). Like the pure-tone response, the model underpredicts the ST potential at low frequencies relative to CF for the 2-tone response when compared to the 2-tone experimental data.

When a third tone was added to the stimulus, both model and experiment results indicated suppression effects in the iDP response and ear canal DPOAE. The amount of suppression in the model results was consistent with that of the experiment when the third tone

was applied either well above f_2 (f_3/f_2=1.5, Figure 5.17) and near $2f_1 - f_2$ ($f_3 = f_1/1.35$, Figure 5.19). Additionally, like in the experiment, the model predicts suppression when the third tone is applied just above f_2 (f_3/f_2=1.15, Figure 5.17), although the model underpredicts the amount of suppression compared to the experiments. The results of these comparison studies have indicated that the model is able to match some key features in the iDP and DPOAE response, including the presence of a peak in the response of the ST pressure and potential located near f_2=CF and the suppression effects when a third stimulus tone is added. Given that the model matches several key features observed in the experimental data, and that the weaknesses of the model (e.g. the model underpredicts the extracellular potential at low frequencies relative to CF) have been identified and can be accounted for in analysis of the model results, the model is a useful tool to study the locations of iDP and DPOAE generation.

5.7.3 Locations of iDP and DPOAE generation

Distortion products are generated in the cochlea in response to a two-tone stimulus due to nonlinear distortion between the stimulus tones that is most significant between the two tones' peak positions. This nonlinear distortion appears as a peak in the iDP extracellular voltage response near f_2=CF, both in the model and experiment and as the transition between reverse-dominated traveling waves and forward-dominated traveling waves in the model iDP extracellular voltage response phase.

The locations of DP generation were investigated by applying either a third stimulus tone or local damage and then comparing the DP responses to that from the undamaged 2-tone DP response. The results suggest that the generation of iDPs that contribute to the DPOAE broadly spans the region between the primary frequency peaks. At narrow ratios, the overlap region of the primaries is relatively large and extends basal and apical to the f_2 and f_1, respectively, peak positions. Distortion sources with opposing phases can interact to reduce the overall DPOAE level[136,148], such that applying damage or a third tone can

result in enhancement of the DPOAE due to the elimination of some sources that would otherwise interfere and reduce the DPOAE. When damage or a third tone are applied to affect positions far basal to the f_2 peak, the response of the ST potential is reduced, but the BM and DPOAE are unaffected. This suggests that some iDPs are generated in the basal region, but they have a relatively small amplitude and do not contribute significantly to the DPOAE. When damage or a third tone are applied to affect positions between the f_2 and f_1 peak positions, the BM, ST potential, and DPOAE responses are reduced significantly, suggesting that most of the distortion source generators that contribute to the DPOAE are located between the f_2 and f_1 peak positions. Applying damage or a third tone to affect the region around the iDP peak results in a decrease in the BM and ST potential responses around the peak, but not the DPOAE, indicating that none, or very little, of the generators that contribute to the DPOAE are located around the iDP peak position.

Martin et al. reported changes in the DPOAE when a third tone was added one-third octave above f_2 and interpreted these results as evidence of basal DPOAE generators[135]. The results of this study, however, indicate that a third tone might overestimate the basal extent of the region of DPOAE generation due the third tone affecting the f_2 response at positions apical to the third tone's peak position. Additionally, the model does not predict that DPOAE originates from this basal region, in part because, for wider f_2/f_1, the iDP ST potential response is very small basal to the f_2 best place and thus implying that OHCs in this region are not generating significant iDPs.

5.8 Summary of contributions and conclusions

In this study, the computational model was used to estimate the locations of distortion product generation. The model was re-calibrated so that the model ST potential response to a low level pure-tone had a similar peak magnitude to that reported in experimental data. The model was then validated with 2- and 3-tone experimental data. This validation study revealed which aspects of the experimental data the model is able to match and those with

which it struggles. Model results show a prominent peak in the extracellular potential iDP response that corresponds approximately to nonlinear distortion around the f_2 best place. This peak corresponds to the location of most significant iDP and DPOAE generation and the position at which applying either local damage or a third stimulus tone has the most significant effect on the DPOAE. The results of this study indicate that using a third tone may overestimate the extent of basal DPOAE generation and should be considered when a third tone is applied to study the DPOAE in clinical and academic settings.

CHAPTER 6

EFFECTS OF REDUCED TECTORIAL MEMBRANE LONGITUDINAL COUPLING ON COCHLEAR STABILITY AND SPONTANEOUS OTOACOUSTIC EMISSIONS

6.1 Chapter overview

Recent experiments in genetically modified mice have demonstrated that mutations of the genes expressed in the tectorial membrane can significantly enhance the generation of SOAEs. Multiple untested mechanisms have been proposed to explain these unexpected results. In this study, a cochlear model (the Bowling 2019 model) is used to demonstrate that altering the viscoelastic properties of the TM tends to affect SOAE generation in a manner similar to what has been observed in the experiments. Furthermore, model results demonstrate that altering the viscoelastic properties of the TM affects the linear stability of the cochlea and the cochlear response to low amplitude stimuli.

6.2 Introduction

The tectorial membrane (TM, Figure 1.4) is an extracellular matrix that is located directly above the OHCs and whose role in cochlear amplification is actively debated[150,151,152,143,13,14]. The TM contains collagen fibrils embedded in a striated sheet matrix[153,154] that consists of

non-collageneous proteins, including α-tectorin (TECTA), β-tectorin (TECTB) and CEACAM16. Mutations of the genes that encode the TM proteins affect important characteristics of cochlear function, such as the sensitivity[155,156] and tuning[157] of the cochlear response to sound. Interestingly, recent experiments in transgenic mice have also shown that altering the properties, structure and morphology of the TM tends to enhance the generation of SOAEs[65,66,67]. This could imply that the TM helps maintain cochlear stability and prevent the generation of too many spontaneous oscillations. Beyond its fundamental scientific significance, studying the effect of TM genetic mutations could have clinical implications, since several TM mutations have been linked to hereditary hearing disorders in humans: for example, the $Tecta^{Y1870C/+}$ and *Ceacam16* knock-out (KO) mice are models for human deafness DFNA8[158] and DFNA4B[159], respectively.

However, TM mutations typically have multiple effects on the morphology and properties of the TM, making it difficult to link individual changes in TM properties to the observed changes in cochlear physiology using an approach based only on experiments. For example, multiple TM mutations are known to affect its mechanical properties: both the *Tectb* KO and the $Tecta^{Y1870C/+}$ mutations tend to reduce the shear stiffness of the TM[160,161,162] but only the $Tecta^{Y1870C/+}$ TMs have lower shear viscosity than the wild-type (WT) TMs[161]. Additionally, a loss of the Hensen's stripe[157] (a narrow ridge normally located on the bottom surface of the TM) is observed in *Tectb* KO mice; the presence of holes are observed in the TM of *Ceacam16* KO[65] and $Tecta^{Y1870C/+}$ mice[163].

Theoretical results[60], along with analysis of the relationship between cochlear tuning and the spatial extent of longitudinal TM waves[161], suggest that TM properties, and particularly the viscosity of the TM, influence the sharpness of cochlear tuning. Because tuning and linear stability are tightly linked in a dynamical system, the hypothesis of this work is that changes in the TM mechanical properties enhance the generation of SOAEs. A physiologically motivated computational model of the gerbil cochlea (Bowling 2019 model) is used to examine this hypothesis.

6.3 Changes to cochlear model

6.3.1 Adding longitudinal coupling to the TM-bending mode and model recalibration

Previous version of the model (Ref. 82 or the Bowling 2018 model) only included longitudinal coupling for the TM-shear mode, but not the TM-bending mode. Given the centrality of TM longitudinal coupling on this research, longitudinal coupling was added to the TM-bending mode (using the same coupling stiffness and viscosity as the TM shear mode, Equations 2.21 and 2.22). The addition of longitudinal coupling to the TM-bending mode necessitating a slight recalibration of the model relative to the Bowling 2018 model. Ultimately, only two parameters of the model were adjusted from the Bowling 2018 model: the TM-bending mass and the saturating hair bundle conductance, G_a^{max} (Equation 2.34, parameters are listed in Appendix C). As with the Bowling 2018 model, the saturating HB conductance was adjusted such that the sensitivity of the BM response is similar to experimental measurements.

The pure tone response of the model used in this chapter is compared to experimental data taken at two longitudinal positions in Figure 6.1. At the 34.6 kHz peak position (CF=34.6 kHz, Figure 6.1a), the model results are similar to the experimental data in terms of the sharpness of the peaks and relative levels of the gain (both show a difference of ≈21 dB between low and high SPL). At CF=13.3 kHz (Fig. 6.1b), the both model and experiment show a difference of ≈27 dB between low and high SPL and the peaks are similarly broad. However, there is a noticeable difference of 11 dB between the model and experiment that is possibly due to a mismatch in the structural properties or assumptions of the model. This mismatch also occurs for the Bowling 2018 model. Like the Bowling 2018 model, the phase rolls-off or decreases somewhat more rapidly than what is observed experimentally (Figures 6.1c and 6.1d) despite effort during calibration to mitigate this. The mismatch between the model and the experimental data is, however, noticeably smaller for

the 2019 model than that of the Bowling 2018 model.

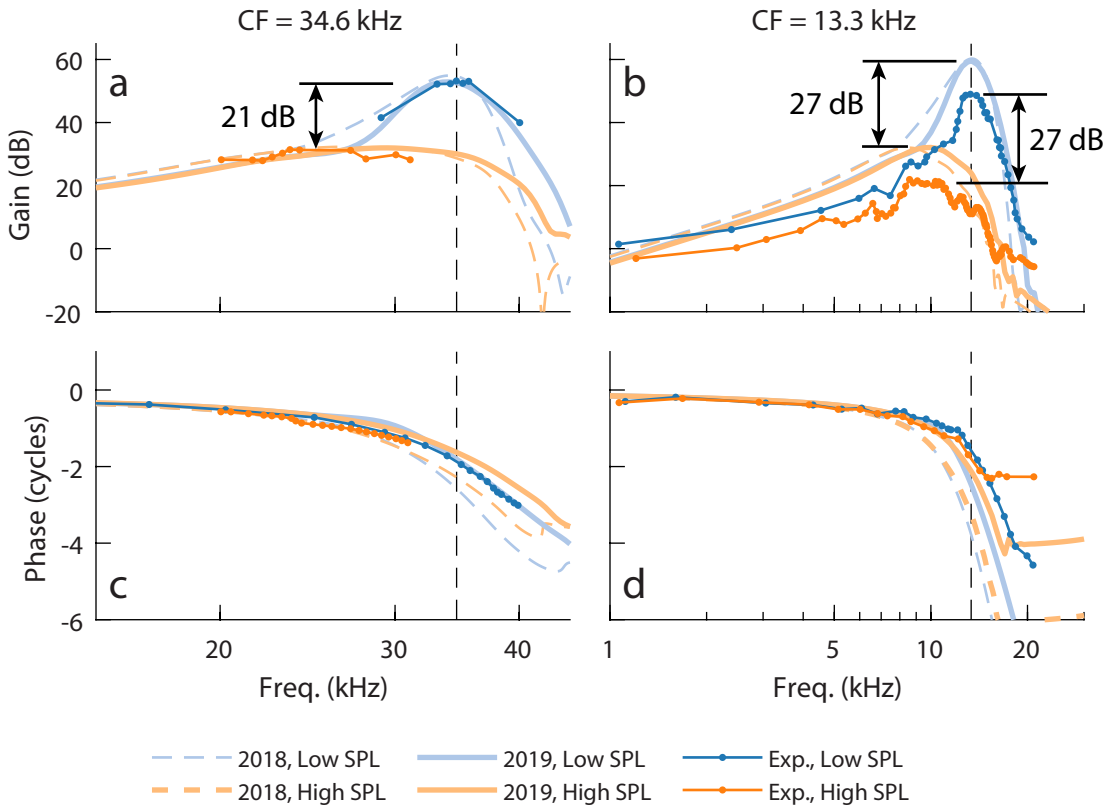

FIGURE 6.1. Comparison of BM pure tone response for the Bowling 2018 and 2019 models at two longitudinal positions with experimental data taken from Refs.[85] and[86]. (**a**) and (**b**) Gain of the BM velocity relative to the stapes velocity. (**c**) and (**d**) Phase of the BM velocity relative to the stapes velocity. (**a**) and (**c**) Experimental data from Ref.[86] is given. (**b**) and (**d**) Experimental data from Ref.[85] is given. (**a**) and (**c**) Results for 30- and 90 dB SPL and 50- and 90 dB SPL stimuli, respectively. (**b**) and (**d**) Results for 30 and 100 dB SPL stimuli. The vertical dashed lines denote CF.

The place-frequency map, BM gain at CF, and quality factor, Q_{10dB} are used to quantify the pure tone response of the smooth model at all longitudinal positions (Figure 6.2). These model results were obtained using the linear frequency domain model. Relative to the Bowling 2018 model, the active Bowling 2019 model place-frequency map is slightly lower in the basal half of the cochlea, and matches the data from Ren and Nutall and Overstreet et al. slightly better (Figure 6.2a). There are only minor differences in the BM gain and tuning for the Bowling 2019 model, although the 2019 model has slightly broader tuning (lower Q_{10dB}) between 17 and 40 kHz.

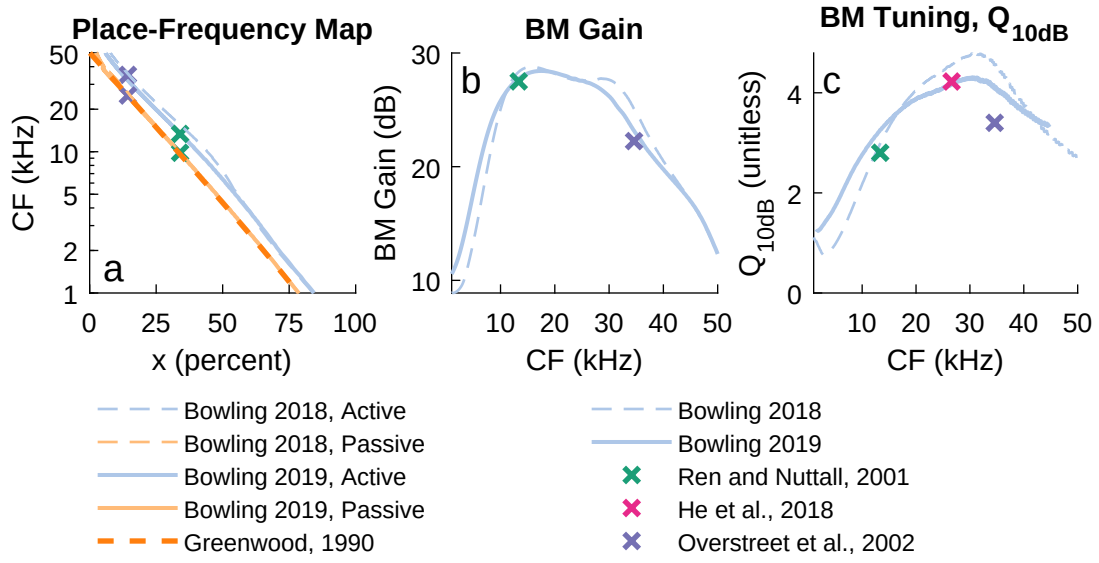

FIGURE 6.2. Comparison of BM pure tone response for the 2018 and 2019 models and experimental data from[4,85,86,75]. A. Place-frequency map of the passive and active models with experimental data[4,85,86]. B. Amplification of active model relative to passive model. C. Quality factor, Q10dB, of the tuning of the BM. Model results are compared with measurements from the 13 kHz[85], 27 kHz[75], and 34 kHz[86] best places. The stimulus levels used for computing the gain from the experimental data at the 13 and 34 kHz positions were 30 and 100; 30 and 90 dB SPL, respectively. The quality factors for the experiments were computed from the responses to a 30 dB SPL stimulus.

6.3.2 Cochlear roughness

As discussed in Section 1.2, reflection source OAEs arise due to impedance inhomogeneities[22]. As in Refs. 82, cochlear roughness can be included in the model by applying small random variations (of about 1%) to the OHC electromechanical coupling coefficient, ε_3 (see Equations 2.35 and 2.36). These random perturbations represent the effect of cellular disorganization and inhomogeneities in the number and properties of OHCs[24]. Roughness has previously been used with the model to study the response of the cochlea to an acoustic click and the fine structure in DPOAEs[82,43]. The value of $\varepsilon_3(x)$ can be written as

$$\varepsilon_3(x) = \varepsilon_3(x)|_{\text{smooth}} \times [1 + \Delta R \times r(x)], \tag{6.1}$$

where $\varepsilon_3(x)|_{\text{smooth}}$ is the value of $\varepsilon_3(x)$ in the smooth cochlear model, ΔR is a constant that measures the amplitude of the deviation from the smooth trend, and $r(x)$ is a dimensionless function of position that is generated using a random number generator with a normal distribution of average value 0 and standard deviation of 1. Because of the randomness, a random seed (RS) is chosen to initialize a random number generator. The electromechanical coupling coefficient for the smooth and rough models are shown in Figure 6.3.

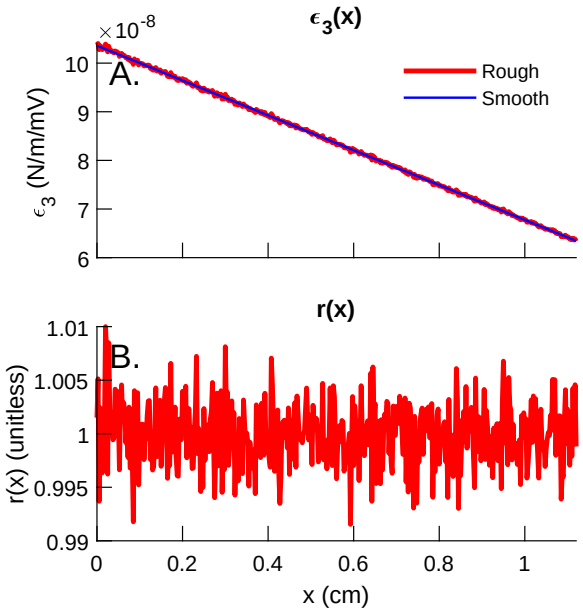

FIGURE 6.3. Spatial variations of electromechanical coupling coefficient and roughness. For the rough model, ΔR=1% and the random seed is RS=0. A. Electromechanical coupling coefficient, $\varepsilon_3(x)$, for the smooth and rough models. B. The roughness function, $r(x)$ for the rough model.

6.4 Results

6.4.1 Effect of roughness on cochlear stability

Because SOAEs are generated when the cochlea is linearly unstable[99], it is useful to first examine the poles, λ, of the model, which can be written in the following form (Equations 2.61 and 2.62):

$$\lambda = \sigma + i2\pi F \tag{6.2}$$

where σ is the real part and $2\pi F$ is the imaginary part. A positive value for σ indicates that the model has a linearly unstable mode that grows exponentially and oscillates at the frequency F[99]. The baseline smooth model does not have any linearly unstable modes and thus does not emit any SOAEs (Figure 6.4). Applying roughness to the model causes the real part of the poles to increase; at larger roughness amplitudes some of the poles become linearly unstable. Changing the random seed and thus random variations results in different poles and linearly unstable modes (Figure 6.4a vs Figure 6.4b). However, because by definition there is no randomness in the smooth model, varying the random seed does not affect the poles of the smooth model.

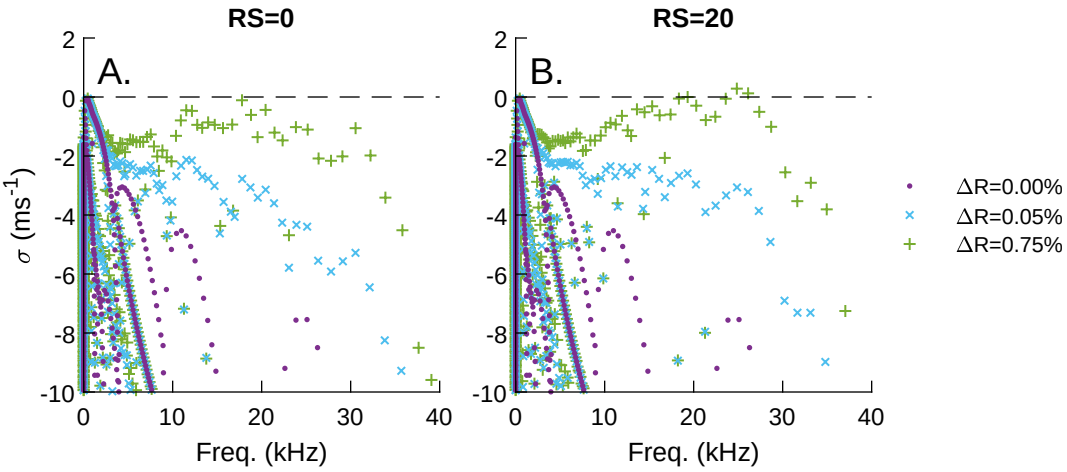

FIGURE 6.4. Effect of adding roughness on the linear stability diagram for two different random seeds. The smooth model corresponds to $\Delta R = 0\%$.

6.4.2 Limit cycle oscillations in the cochlear model

The actual cochlea emits SOAEs in the absence of any stimulus due to the presence of biological and thermal noise that causes the cochlea to move away from any unstable equilibrium. While noise could potentially be added at the stapes or in the cochlea (for example in the mechano-electrical transduction channels), for this work, as in previous work[64,164], a stimulus (an acoustic click of short duration) is applied at the stapes instead of directly modeling noise to move the model from its unstable equilibrium configuration. While the

ear canal pressure decays to 0 if the model is linearly stable, when linearly unstable modes are present, the ear canal pressure grows until limit cycle oscillations develop due to the saturation of the mechanoelectrical transduction channels. As in experiments[65], these limit cycle oscillations appear as narrow-band spectral peaks in the ear canal pressure and correspond to SOAEs. Only spectral peaks of amplitude > 0 dB SPL were counted as SOAEs in the model analysis since low amplitude peaks would be below the noise floor in an experiment.

For the model shown in Figure 6.5, there are two linearly unstables modes, at frequencies 17.0 and 24.8 kHz (Figure 6.5A). Due to these linearly unstable modes, limit cycle oscillations will develop in response to a click stimulus (Figure 6.5B). The 24.8 kHz limit cycle takes under 100 ms to reach steady state while the 17.0 kHz limit cycle takes approximately 500 ms to reach steady state (Figure 6.5E). The time required to reach steady state is related to the value of σ for the mode: a positive mode very close to σ=0 (e.g. the 17.0 kHz mode in Figure 6.5A) will take much longer (potentially $>$1 second) to reach steady state than a mode with a relatively large σ value (e.g. the 24.8 kHz mode in Figure 6.5A). The spectrum of the ear canal pressure (Figure 6.5D) shows two large peaks at the same frequencies as the linearly unstable modes and multiple smaller peaks below -50 dB SPL that are distortion products of the two large peaks. The phase portrait of the stapes response (Figure 6.5D) has an annular shape because the steady state waveform contains two frequency components of similar magnitude.

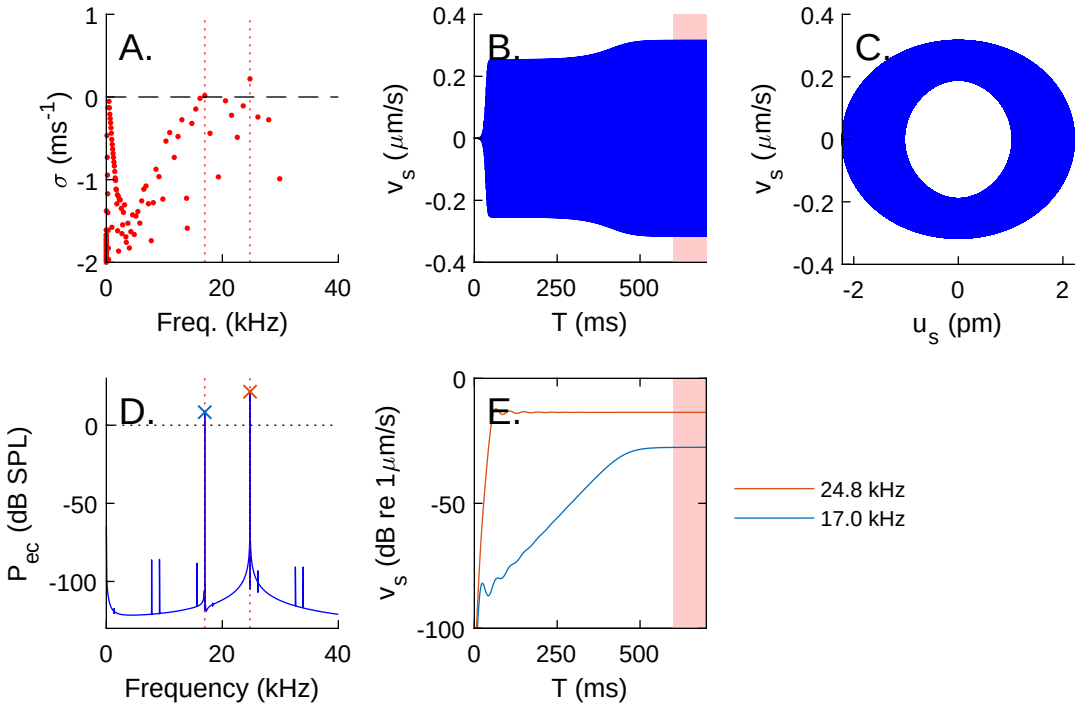

FIGURE 6.5. Limit cycles oscillations in the cochlear model for ΔR=1% and RS=4. A. Linear stability diagram. B. Waveform of the stapes velocity, v_s, for the first 700 ms of the simulation. C. Phase portrait of the steady state stapes response (velocity, v_s, vs. displacement, u_s) from t=600-700 ms (indicated by shaded region in B.). D. Ear canal pressure spectrum obtained from 500 ms of the steady stapes response. E. Spectrogram response of the stapes velocity at the two linearly unstable frequencies (17.0 and 24.8 kHz). The vertical dotted lines in (A.) and (C.) represent the frequencies of spectral peaks above 0 dB SPL.

6.4.3 Effect of reducing TM longitudinal coupling on SOAE generation for one seed number

The influence of TM viscoelastic coupling on SOAE generation was first determined for one RS (Fig. 6.6). While experiments with transgenic animals only allow for the characterization of the influence of TM properties on a population of animals, this model-based approach makes it possible to determine how varying TM properties affects individual SOAEs. To test the hypothesis is this study, four different models were considered: (1) the baseline model; (2) the "Reduced elastic" model (where the TM coupling stiffness, K_{tm}^{LC}, is reduced to 50% of its baseline value); (3) the "Reduced viscous" model (where the TM coupling viscosity, C_{tm}^{LC}, is reduced to 50% of its baseline value); (4) the "Reduced

both" model (where the stiffness and viscosity are reduced to the values of the "Reduced elastic" and "Reduced viscous" models, respectively). These changes in the TM properties are representative of the changes in the TM shear modulus and viscosity reported for $Tecta^{Y1870/+}$ mice [161].

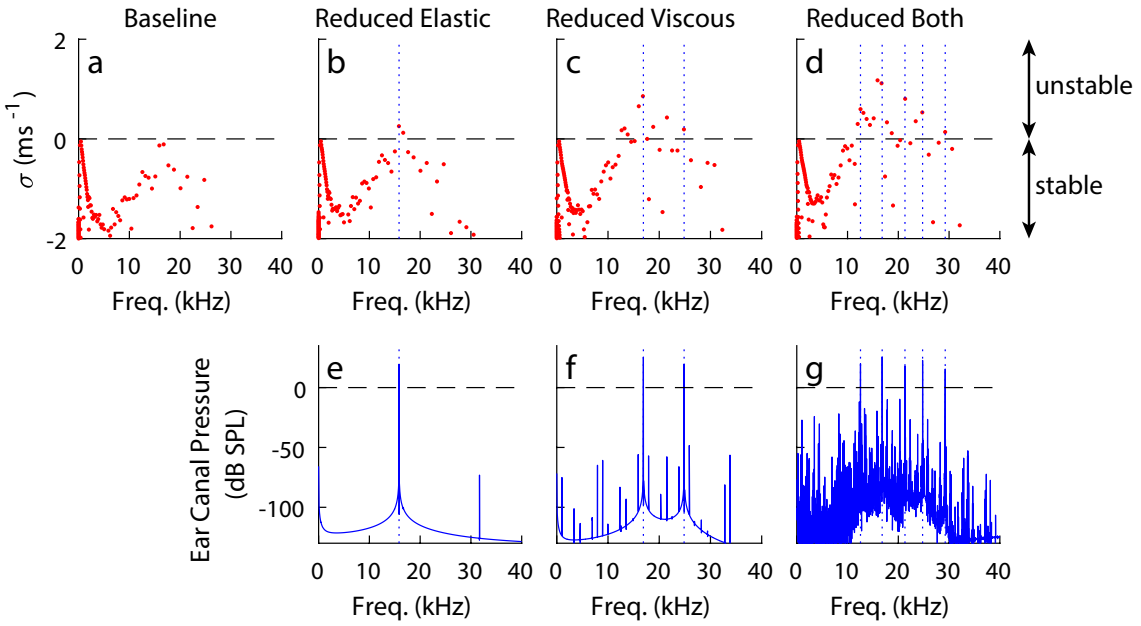

FIGURE 6.6. Influence of TM viscoelastic coupling on the linear stability diagram and SOAEs for one random seed (RS=3). Linear stability diagrams (**a**)-(**d**) and spectrum of the ear canal pressure (**e**)-(**g**) for models with baseline TM coupling (**a**), reduced elastic coupling (**b**) and (**e**), reduced viscous coupling (**c**) and (**f**), and reduced elastic and viscous coupling (**d**) and (**g**). ΔR was set to 0.75% for these results. The vertical dotted lines in (**e**)-(**g**) represent the frequencies of spectral peaks above 0 dB SPL.

The baseline model parameters were chosen so that the model does not have any unstable modes but is just on the verge on instability for the RS used in Figure 6.6, as evidenced by the presence of two nearly unstable modes (*i.e*, poles that are on the stable side and very close to the horizontal axis), of frequencies $F \approx 15.9$ and 16.8 kHz. These nearly-unstable modes become unstable in the "Reduced elastic" model (with almost the same frequency, $F \approx 15.8$ and 16.7 kHz). Reducing TM viscous coupling considerably reduces the linear stability: the "Reduced viscous" and "Reduced both" models have eight and fourteen linearly unstable modes, respectively. The linearly unstable modes seen in the "Reduced

viscous" and "Reduced both" models (Figures 6.6c and 6.6d) are either unstable or nearly unstable modes in the baseline and "Reduced elastic" models (Figures 6.6a-b).

For the RS used in Figure 6.6, no SOAEs are predicted by the baseline model due to a lack of linearly unstable modes. The "Reduced elastic", "Reduced viscous" and "Reduced both" models predict one, two and five SOAEs, respectively (Figure 6.6e-g). While the frequencies of SOAEs in Figure 6.6e-g correspond to the frequencies of some of the linearly unstable modes in Figure 6.6b-d, some of the linearly unstable modes do not appear as SOAEs; this is because some SOAEs dominate the overall response of the system[64].

6.4.4 Influence of TM longitudinal coupling on the average number of SOAEs

The numbers of linearly unstable modes and SOAEs depend on the RS used to initialize the random number generator. The results of multiple simulations (obtained with $N = 10$ different RS) were analyzed to mimic the recording of experimental data from multiple individuals within a population of WT or mutant animals (as done for example in[65]). As shown in Figure 6.7b, reducing viscoelastic coupling increases the average number of SOAEs emitted per model from 0.1 in the baseline model to 0.8 in the "Reduced elastic" model, 3.5 in the "Reduced viscous" model, and 5.5 in the "Reduced both" model. Changes in the average number of SOAEs are positively correlated with changes in the average number of linearly unstable modes (Figure 6.7a). However, because one dominant mode can suppress another mode for models with multiple unstable modes (as seen in Figure 6.6), the average number of unstable modes tends to be higher than the average number of SOAEs.

Because SOAE generation depends on the amplitude, ΔR, of the random perturbations used to introduce cochlear roughness (Equation 6.1), additional simulations were examined to determine whether the conclusions regarding the influence of TM viscoelastic longitudinal coupling are robust to changes in the value of ΔR. As shown in Figure 6.7c-d, increasing ΔR increases the number of linearly unstable modes and SOAEs for all TM coupling cases. However, for any given ΔR value, the average numbers of unstable modes and SOAEs are

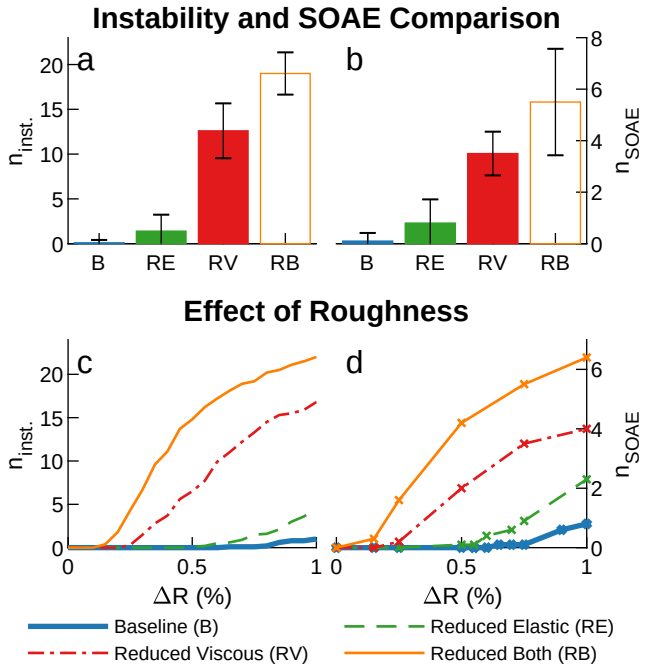

FIGURE 6.7. Influence of TM viscoelastic coupling on the number of linearly unstable modes and SOAEs, for $\Delta R = 0.75\%$ and $N = 10$ different RS. (**a**) and (**b**) Average number of instabilities (**a**) and SOAEs (**b**) for different TM longitudinal coupling cases. The error bar corresponds to $\pm$ one standard deviation. (**c**) and (**d**) Average number of unstable modes (**c**) and SOAEs (**d**) as function of the amplitude of the random perturbations, ΔR. Supplementary Fig. S6 shows the average number of unstable modes for a wider range ΔR values.

always ordered in the same manner:

$$\begin{aligned} n_{inst.}^{\text{reduced both}} &\geq n_{inst.}^{\text{reduced viscous}} \geq n_{inst.}^{\text{reduced elastic}} \geq n_{inst.}^{\text{baseline}} \\ n_{SOAE}^{\text{reduced both}} &\geq n_{SOAE}^{\text{reduced viscous}} \geq n_{SOAE}^{\text{reduced elastic}} \geq n_{SOAE}^{\text{baseline}} \end{aligned} \tag{6.3}$$

where $n_{inst.}$ and n_{SOAE} denote the average number of unstable modes and SOAEs, respectively. This implies that for all ΔR values, reducing either elastic or viscous coupling reduces linear stability and enhances SOAE generation.

While Figure 6.7 focuses on four different sets of values for the TM parameters, the influence of TM longitudinal coupling parameters on linear stability was also analyzed for more systematic variations in the parameters, where both the TM coupling stiffness and viscosity were allowed to vary between 0% and 150% of the baseline values. The results of

this parametric study, shown in Figure 6.8, demonstrate that reducing elastic and/or viscous coupling consistently increases the number of linearly unstable modes. This is consistent with results shown in Figure 6.7 and confirms that the effects of altering viscoelastic coupling on cochlear stability are robust to changes in TM parameter values.

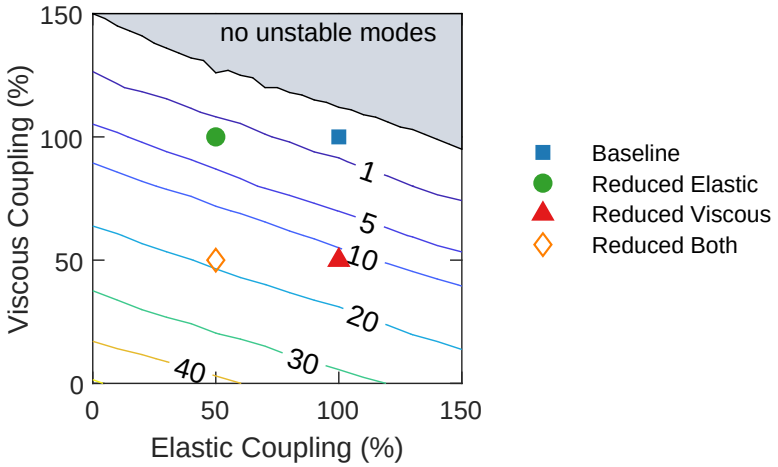

FIGURE 6.8. Contour plot of the average number of unstable modes as a function of the value of elastic and viscous coupling parameters as a percent change from the baseline values. $N = 20$ random seeds were analyzed. The symbols identify the parameter sets used in other figures for the baseline, "Reduced elastic", "Reduced viscous" and "Reduced both" cases.

In Figure 6.7c, the influence of varying the amplitude of the random perturbations, ΔR, on the average number of linearly unstable modes was examined for a relatively narrow range of ΔR values ($\Delta R \leq 1\%$). For larger random perturbations ($1\% \leq \Delta R \leq 40\%$), shown in Figure 6.9, the average number of unstable modes continues to increases as ΔR is increased, albeit at a slightly lower rate once ΔR exceeds 5%. While small random variations ($\Delta R \leq 1\%$) might be physically plausible, larger variations are not. However, it is useful theoretically to explore the influence of larger variations. In all cases, for a given random perturbation amplitude, reducing TM viscoelastic coupling results in a reduction in cochlear stability and an increase in the average number of linearly unstable modes.

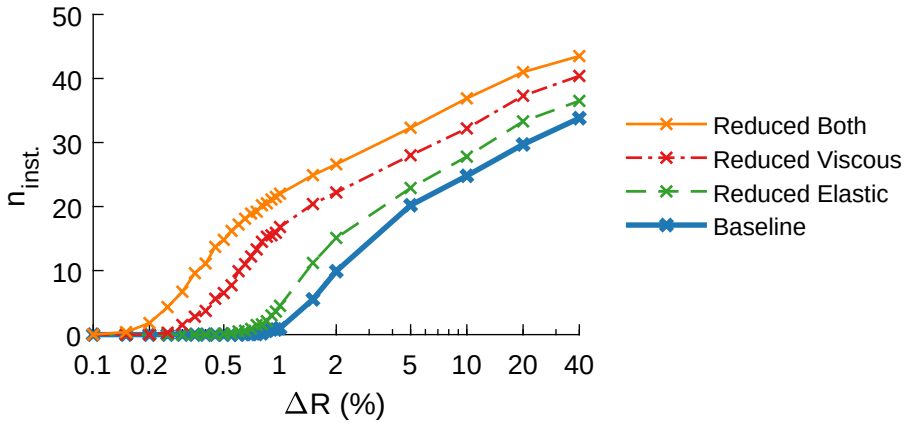

FIGURE 6.9. Influence of the amplitude of the random perturbation, ΔR, on the number of linearly unstable modes for $N = 10$ different RS.

6.4.5 Influence of finite element size and roughness length scale on linear stability

For all the results in this work (except for Appendix D), a finite element mesh with elements of longitudinal length Δx = 25 μm long was used (total of 448 elements along the BM). Furthermore, the roughness function, $r(x)$, is assumed to be a piecewise linear function with breakpoints that are separated by a distance Δx_r. Except for the results in Figure 6.11, Δx_r was chosen to be also equal to 25 μm.

The influence of Δx and Δx_r on the results was examined to determine how robust the findings on the effects of reducing the TM viscoelastic coupling were to changes in the roughness. Two different cases were considered: (1) Δx_r was fixed at 25 μm and the element size, Δx, was varied, shown in Figure 6.10 and (2) the roughness length-scale, Δx_r, was varied for a fixed element size (Δx = 25 μm) shown in Figure 6.11.

In the first case, the roughness is defined as

$$r(x) = r_{25\mu m}(x_1) + \frac{r_{25\mu m}(x_1) - r_{25\mu m}(x_0)}{x_1 - x_0}(x - x_0) \tag{6.4}$$

where $r_{25\mu m}(x)$ is the roughness computed using $\Delta x_r = 25\mu$m; x_0 and x_1 ($x_0 \leq x \leq x_1$) are nodal positions in the Δx= 25 μm mesh. The results (Figure 6.10), indicate a slight decrease in stability for models with Δx = 12.5 μm long elements. When the element size

is increased to $\Delta x = 50\ \mu$m, there is a noticeable decrease in the number of linearly unstable models (Figure 6.10d). The same roughness variations were used to allow for a meaningful comparison (Figures 6.10a and 6.10b); using different roughness variations would result in slightly different numbers of linearly unstable modes. For many of the models considered, using the finer mesh results in at most one more linearly unstable mode than using the mesh used in the manuscript. Shown in Figure 6.10c is a less common case, in which two nearly unstable modes for $\Delta x = 25\ \mu$m (indicated by the arrows) become unstable when the element size is reduced to $\Delta x = 12.5\ \mu$m. Such a small decrease in stability (increase in σ) for the finer mesh also affects n_{inst} when $N = 20$ models are considered, as shown in Figure 6.10d.

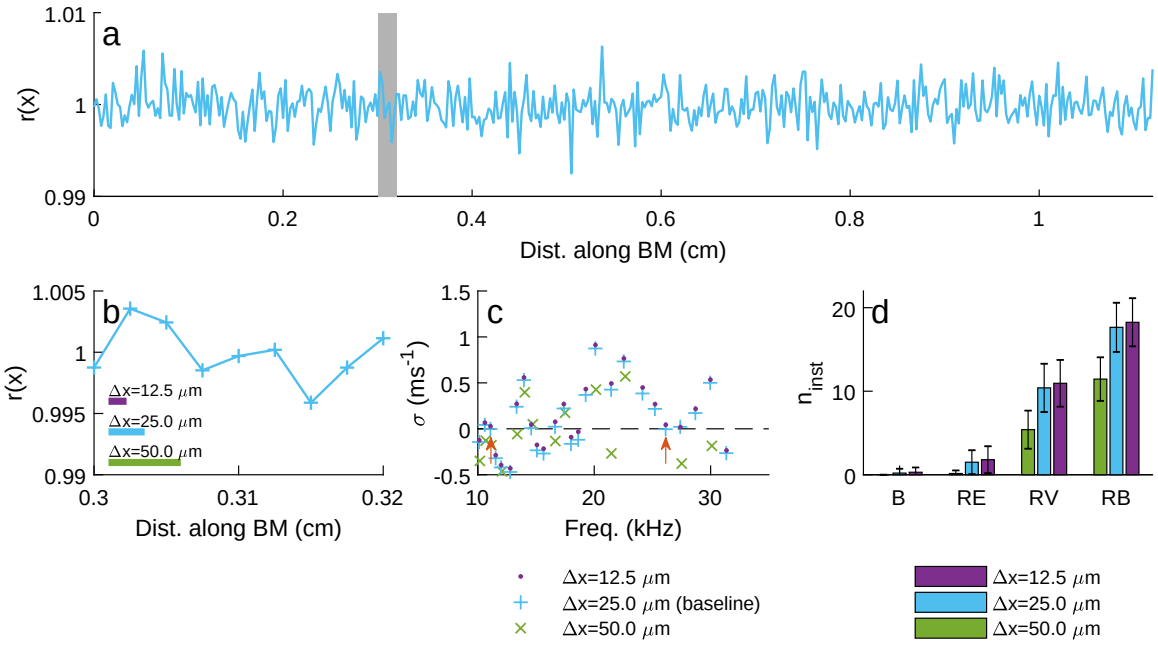

FIGURE 6.10. Influence of the finite element size, Δ_x, on linear stability for $\Delta R = 0.75\%$. Effects on linear stability for various meshes of different element size with a fixed roughness length scale ($\Delta x_r = 25\ \mu$m). (**a-b**) Roughness variations, $r(x)$ (Eq. 12), for RS=2. The narrow vertical shaded region in Panel (**a**) corresponds to the region shown in Panel (**b**). (**b**) The scale bars represent the element lengths considered (12.5, 25, and 50 μm). (**c**) Linear stability diagram for the "Reduced Both" model for RS=2. (**d**) Average number of linearly unstable models, n_{inst}, for N=20 RS for the four coupling cases, "Baseline" (B), "Reduced Elastic" (RE), "Reduced Viscous" (RV), and "Reduced Both" (RB). The error bar corresponds to $\pm$ one standard deviation.

Varying the length scale of the roughness, Δx_r, results in different roughness functions, $r(x)$ (Figure 6.11). In this case, the roughness is defined as

$$r_{\Delta x_r}(x) = r_{12.5\mu m}(x_1) + \frac{r_{12.5\mu m}(x_1) - r_{12.5\mu m}(x_0)}{x_1 - x_0}(x - x_0) \tag{6.5}$$

$$r(x) = r_{\Delta x_r}(x_1 + \frac{r_{\Delta x_r}(x_1) - r_{\Delta x_r}(x_0)}{x_1 - x_0}(x - x_0) \tag{6.6}$$

where $r_{12.5\mu m}$ is the roughness computed using a roughness length scale of 12.5 μm; $r_{\Delta x_r}$ is the roughness computed using a length scale of Δx_r; x_0 and x_1 are nodal positions in the $\Delta x = \Delta x_r$ mesh. Defining the $r_{\Delta x_r}$ roughness from the Δx_r=12.5 μm roughness ensures that the roughness variations will be the same at some nodal positions. Using a roughness length scale of 10-25 μm is reasonable given the value of the OHCs diameter (8-10 μm[6]) and the variability in OHC organization[24]. While identifying the related individual poles for the three meshes was straightforward in Figure 6.10c, there is no such correlation between poles for the results shown in Figure 6.11c since different $r(x)$ are used. This difference is due to the roughness having very different spatial variations (Figures 6.11a and 6.11b). More importantly, the average numbers of linearly unstable modes is not affected much by the changes in Δx_r (Figure 6.11d). The results of Figure 6.11d show that reducing TM viscoelastic coupling results in a reduction in cochlear stability and an increase in the average number of linearly unstable modes at all Δx_r values that were considered.

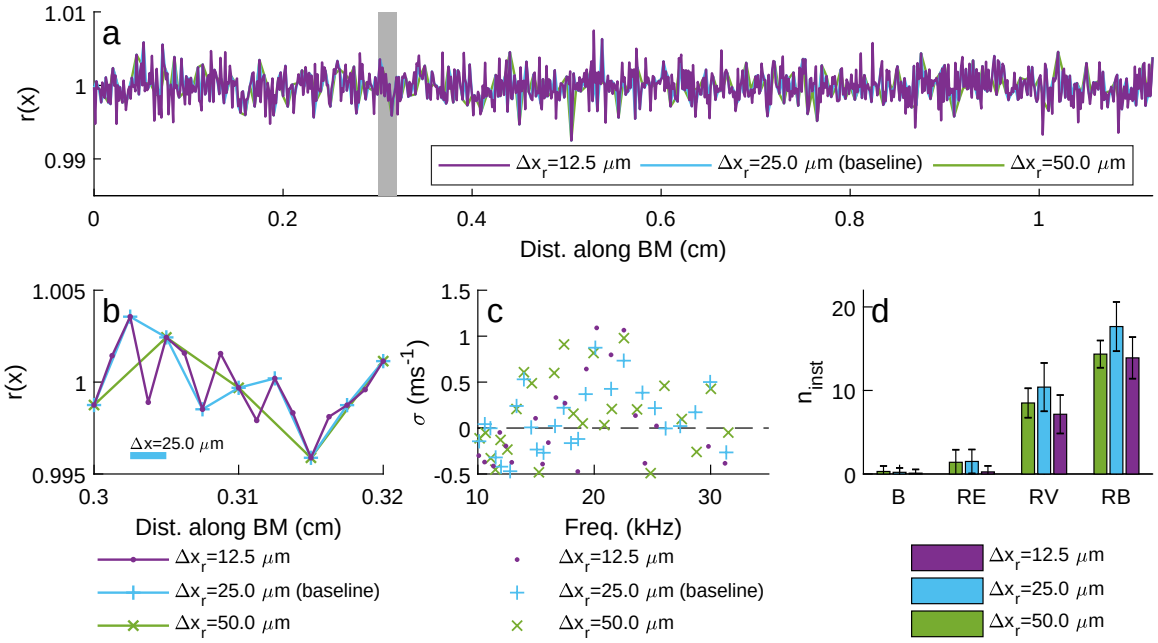

FIGURE 6.11. Influence of the roughness length scale (Δx_r) on linear stability for a fixed Δx = 25 μm mesh (indicated by the scale bar in Panel (**b**)). Other details are the same as Fig. 6.10.

6.4.6 Influence of TM longitudinal coupling on SOAE frequencies and amplitudes

Analysis of the results obtained for $N = 20$ different RS indicates that for all TM coupling cases, the model predicts that all SOAEs have a frequency between 11 and 32 kHz (Figure 6.12a-d). The frequency range of SOAEs predicted by the model corresponds to the frequency range where the cochlear amplifier has the most significant effect on the response of the cochlear model to a pure tone (Figure 6.2). While reducing TM viscous coupling does not significantly affect the frequency of individual SOAEs (see the discussion of the results of Figure 6.6), it broadens the frequency range of SOAEs due to the emergence of additional SOAEs: the frequency range changes from 14 to 26 kHz in the baseline case to 8 to 32 kHz in the "Reduced both" model. While all SOAEs have amplitudes below 26 dB SPL in the "Baseline" and "Reduced elastic" models, the maximum SOAE amplitude is slightly higher in the models with reduced viscous coupling and can reach up to about 31 dB SPL.

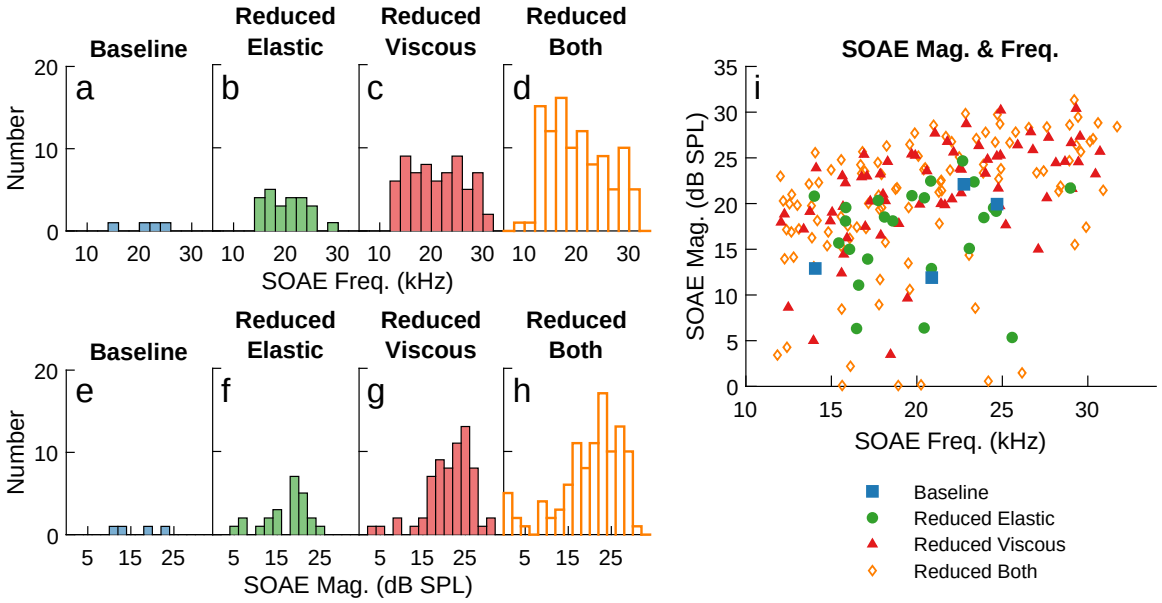

FIGURE 6.12. Influence of TM viscoelastic coupling on the amplitude and frequency of SOAEs. (**a**)-(**d**) Distribution of SOAE frequencies. (**e**)-(**h**) Distribution of SOAE amplitudes. (**i**) Amplitude vs frequency of SOAEs. The results for the four different models are analyzed for $\Delta R = 0.75\%$ and $N = 20$ different RS.

6.4.7 SOAEs: global phenomena or local instabilities?

The theory of coherent reflection predicts that SOAEs are not locally generated, but are instead due to a global phenomenon for which the cochlea acts like a laser cavity with standing waves building up within the cochlea, which acts like a tuned resonant cavity[61]. To test if SOAEs were locally generated, the linear stability of an isolated longitudinal cross-section of the organ of Corti was analyzed (Figure 6.13). This organ of Corti model neglects longitudinal coupling (coupling in the x-direction due to the intracochlear fluid or structural components of the organ of Corti) and fluid loading. Both the fully active model and a passive model were analyzed. As shown in Figure 6.13b, both the passive and active organ of Corti models are linearly stable. The parameters of the cochlear model vary spatially (Tables C.1 and C.3), so the stability of the organ of Corti at all other positions was analyzed. For all positions along the BM, the organ of Corti model remained stable.

Additionally, SOAE generation requires that some of the reverse traveling waves are reflected back into the cochlea by the stapes. To test whether SOAE generation is sensitive

to the condition of the stapes, the linear stability of the cochlear model was analyzed when the magnitude of the stapes reflection coefficient, $|R_{st}|$, is low (Section 3.3). The results of this test indicate that reducing the magnitude of the stapes reflection coefficient, $|R_{st}|$, significantly reduced the number of linearly unstable modes (Figure 6.14). Since SOAEs are only generated when linear unstable modes are present, this implies that SOAE generation requires the stapes reflection coefficient to have a sufficiently high magnitude. The findings that individual cross-sections of the organ of Corti are linearly stable, and that SOAE generation requires the stapes reflection coefficient to have a sufficiently high magnitude are consistent with the theory that SOAEs are caused by a global phenomenon instead of local instability.

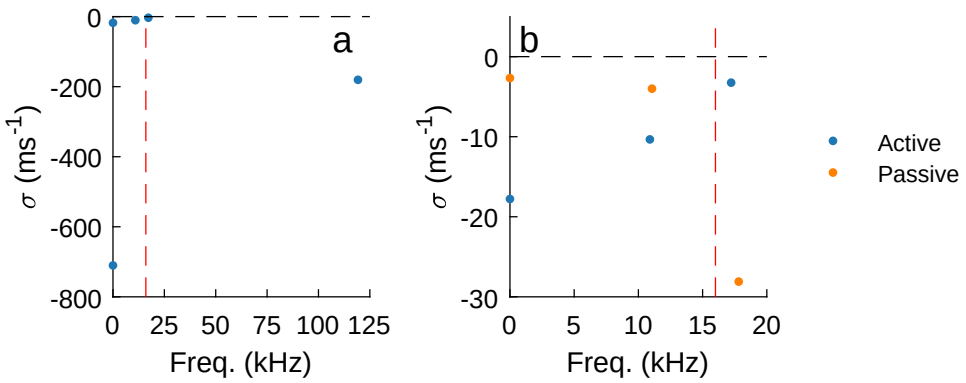

FIGURE 6.13. Stability of the organ of Corti model at the 16 kHz best place. CF is denoted by the vertical dashed line. (**a**) Linear stability diagram for the active model. (**b**) Zoom-in on the linear stability for low frequencies and frequencies near CF for the active and passive models.

6.4.8 Effect of reducing TM viscoelastic coupling on cochlear response to a pure tone

The influence of TM viscoelastic longitudinal coupling on the response of the BM to a pure tone of frequency $f_0 = 16$ kHz was analyzed for two different TM models: (1) the baseline model and (2) a model with no TM longitudinal coupling ("No TM coupling" model), obtained by setting $K_{tm}^{LC} = 0$ and $C_{tm}^{LC} = 0$. The Fast Fourier Transform (FFT), $V_{bm}(x,f)$, of the time-domain response to a pure tone, $v_{bm}(x,t)$, was calculated using MATLAB (The MathWorks, Natick, MA). For the baseline model that does not exhibit any SOAEs, the

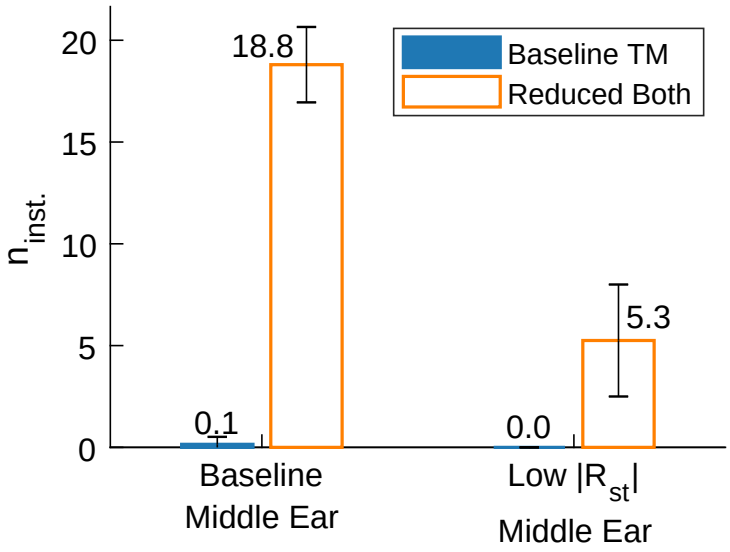

FIGURE 6.14. Influence of the stapes reflectance on the average number of linearly unstable modes. $N = 20$ random seeds were analyzed for each case. The error bar corresponds to $\pm$ one standard deviation.

BM at the 16 kHz peak position primarily vibrates at the frequency of the stimulus, with a secondary peak of lower amplitude at the frequency $2f_0$ due to harmonic distortion (Figure 6.15A). At a more basal location (x = 0.17 cm, Figure 6.15D), tuned to 30.5 kHz, the BM also vibrates primarily at 16 kHz but with a much lower amplitude (refer to vertical dotted lines in Figure 6.15B). However, the "No TM coupling" model exhibits many linearly unstable modes (more than 50 unstable modes), such that many spectral peaks are observed in the response to a pure tone of low level (Figures 6.15A and 6.15D). The peak at the frequency of the stimulus is significantly lower than the peaks due to linear instabilities. At each of the two locations, the BM primarily vibrates at frequencies around the corresponding CF, such that, even though the model is excited by a pure tone of frequency 16kHz, the basal location vibrates at frequencies around 30.5 kHz (Figure 6.15D). Because the response of the model remains dominated by instabilities rather than by the response directly evoked by the stimulus, the stimulus would likely be undetectable at low SPL.

To systematically evaluate whether the stimulus frequency component of the response is dominated by vibration at SOAE frequencies, the FFT of the BM velocity in response to a pure tone, $V_{bm}(x, f)$, is used to calculate the root mean square (RMS) values of the total

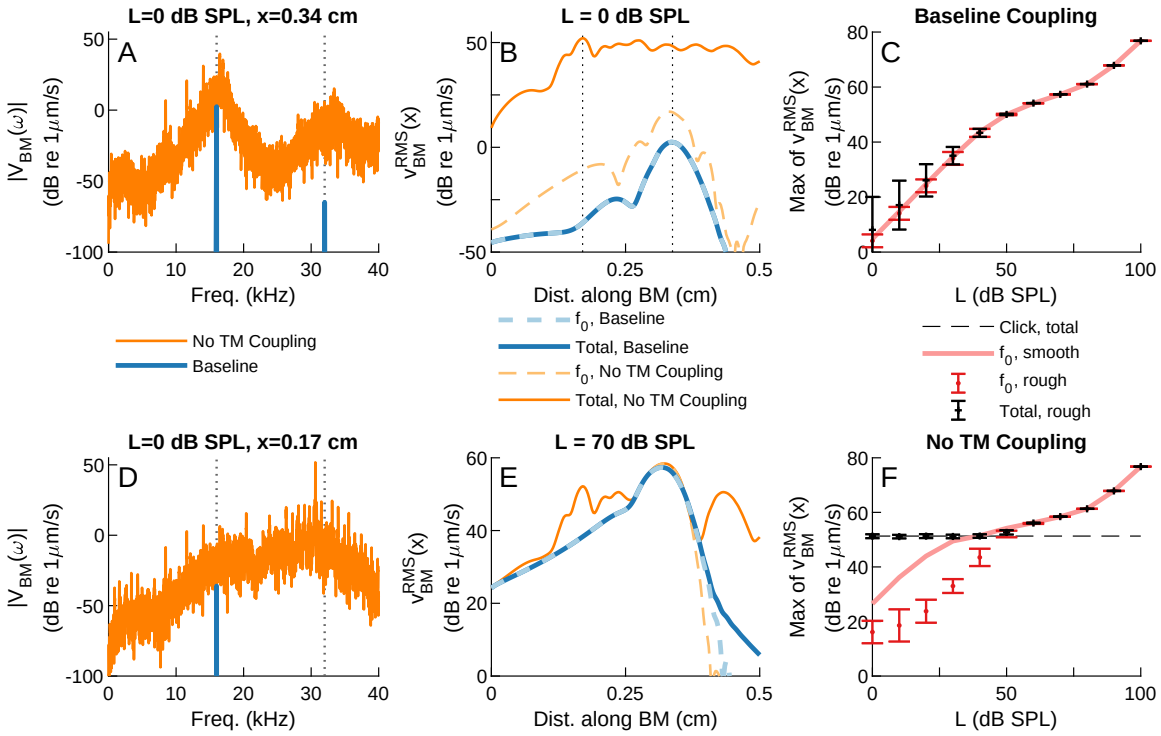

FIGURE 6.15. Effect of eliminating TM viscoelastic longitudinal coupling on the BM response to pure tones of stimulus frequency 16 kHz and different sound pressure levels, L. In all panels, "f_0" refers to the root mean square (RMS) value of the stimulus frequency component of the BM velocity, $v_{BM}^{RMS}\big|_{f_0}(x)$, while "Total" refers to the RMS value of the total BM velocity, $v_{BM}^{RMS}\big|_{tot}(x)$ (see Equation 6.7). Two coupling cases are considered: the baseline model and the "No TM coupling" model ($K_{tm}^{LC} = C_{tm}^{LC} = 0$). (**A**) and (**D**) Frequency spectrum of the BM at the 16 kHz peak position ($x = 0.34$ cm) and at a more basal position ($x = 0.17$ cm) for RS=0. The vertical dotted lines indicate the stimulus frequency, f_0= 16 kHz, and its second harmonic, $2f_0$=32 kHz. (**B**) and (**E**) Spatial response of the BM to pure tones of stimulus levels 0 and 70 dB SPL, respectively, for RS=0. (**C**) and (**F**) Maximum of the RMS value of the BM velocity for smooth model and rough ($\Delta R = 0.75\%$) models as a function of sound pressure level. The rough model results in Panels (**C**) and (**F**) include the average of $N = 10$ RS; the error bars correspond to $\pm$ 1 standard deviation. The click data in Panel (**F**) is the average RMS value of the total BM velocity in response to a click stimulus. The click response does not depend on the stimulus level, but is plotted as a horizontal line for easier comparison to the pure tone responses.

BM response, $v_{bm}^{RMS}\big|_{tot}(x)$, and the RMS value of the stimulus frequency component of the

BM velocity response, $v_{bm}^{RMS}\big|_{f_0}(x)$, using the following equations:

$$\begin{aligned} v_{bm}^{RMS}\Big|_{tot}(x) &= \sqrt{\frac{1}{2}\sum_{f=0}^{f_{max}}|V_{bm}(x,f)|^2} \\ v_{bm}^{RMS}\Big|_{f_0}(x) &= \frac{|V_{bm}(x,f_0)|}{\sqrt{2}} \end{aligned} \tag{6.7}$$

where $V_{bm}(x,f_0)$ corresponds to the component of frequency f_0 in the FFT of the time-domain response to a pure tone.

The values of $v_{bm}^{RMS}\big|_{tot}$ and $v_{bm}^{RMS}\big|_{f_0}$ are plotted as a function of position in response to a 16 kHz pure tone in Figures 6.15B and 6.15E. When the model has no unstable modes or SOAEs and thus only vibrates at the stimulus frequency, such as the baseline model shown in Figures 6.15B and 6.15E, $v_{bm}^{RMS}\big|_{tot}$ and $v_{bm}^{RMS}\big|_{f_0}$ nearly exactly match each other since the BM primarily vibrates at the stimulus frequency. At 0 dB SPL (Figure 6.15B), eliminating TM longitudinal coupling increases the total RMS value by about 30dB and the RMS value of the stimulus frequency component of the response, $v_{bm}^{RMS}\big|_{f_0}$, by only about 15 dB (close to its peak). In the case of a 70 dB stimulus (Figure 6.15E), the 16 kHz and total RMS velocities of the "No TM coupling" model peak at about the same location and have similar magnitudes, suggesting that the 16 kHz stimulus tone would be detectable.

The maxima of the RMS values of the stimulus frequency of the BM response and of total BM responses are plotted as a function of stimulus level in Figures 6.15C and 6.15F. If cochlear roughness is ignored (smooth model), both the baseline and "No TM coupling" models exhibit the compressive nonlinearity typically observed in measurements in live animals[12]. The low amplitude response of the smooth "No TM coupling" model is 15-20dB higher than the smooth baseline model. This increase in the maximum response of the smooth "No TM coupling" model, together with the 15 dB increase in the 16 kHz response, $v_{bm}^{RMS}\big|_{f_0}$, in Figure 6.15B indicate an increase in cochlear amplification when TM longitudinal coupling is eliminated. When cochlear roughness is introduced, the maxima of the stimulus frequency and total responses of the baseline model (Figure 6.15C) closely fol-

low the smooth model. For the "No TM coupling", rough models (Figure 6.15F), $v_{bm}^{RMS}\big|_{f_0}$ follows a similar trend to the corresponding smooth model, but the magnitude of the maxima are reduced by 10-20 dB at low SPL. The total responses, $v_{bm}^{RMS}\big|_{tot}$, exhibit a plateau of nearly constant value below $\approx$50 dB SPL due to the presence of numerous spontaneous oscillations on the BM. Indeed, this plateau coincides to the total response of the spontaneous oscillations from a click stimulus. The reduction of the 16 kHz response for the rough model relative to the smooth model may be due to suppression of the stimulus frequency response by these spontaneous oscillations. Additionally, the spontaneous oscillations are so large that the 16 kHz stimulus would be detectable only above $\approx$50 dB SPL, when the total RMS response begins to be dominated by the stimulus frequency component of the response.

In Figure 6.15, only two coupling cases were considered; in Figure 6.16 the viscoelastic longitudinal coupling is varied systematically for a low and moderate stimulus level. The max velocity of the smooth model increases as viscoelastic coupling is reduced for the smooth model at 0 dB SPL (Figure 6.16a, which confirms that reducing coupling increases cochlear amplification. For the rough model at 0 dB SPL, even a small $< 15\%$ reduction in coupling causes a significant increase in the max total response. For the response at 16 kHz with roughness and 0 dB SPL stimulus, however, there is little variation in the max total velocity until coupling is completely eliminated (100% reduction). As in Figure 6.15F, the 16 kHz rough response is below the 16 kHz smooth response, indicating that the numerous spontaneous oscillations may suppress the stimulus frequency response. When a slightly higher stimulus level is considered, there is much less variability in the maximum amplitudes (Figure 6.16b). This difference is likely due to the higher stimulus level causing more saturation.

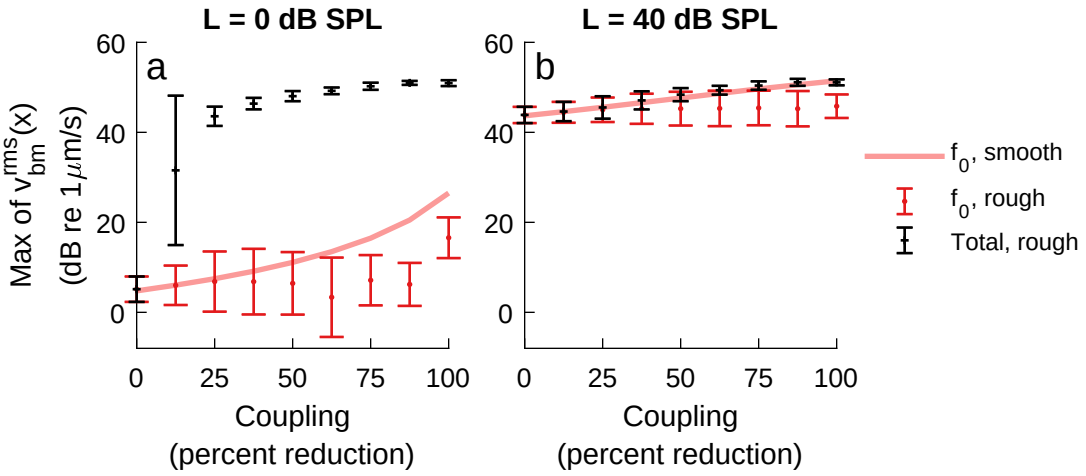

FIGURE 6.16. Effect of varying TM viscoelastic longitudinal coupling on the BM response to pure tones of stimulus frequency 16 kHz and two sound pressure levels, L. Viscous and elastic coupling where reduced by equal amounts relative to their baseline values. Two stimulus levels were considered: 0 and 40 dB SPL for $N = 5$ RS. All other details are the same as in Figures 6.15c and 6.15f.

6.5 Discussion

6.5.1 Lowering TM shear viscoelasticity significantly reduces cochlear stability and enhances SOAE generation

There are several important structures within the cochlea that provide longitudinal coupling: the BM[11], the TM, and Y-shaped elements formed by the basally slanted OHC, the apically slanted phalangeal process, and the supporting Deiters' cell[165,166,105]. In addition to longitudinal coupling of the TM, the model used for this study also includes longitudinal coupling of the BM, which is modeled using an orthotropic plate model (Chapter 2), but does not take into account the Y-shaped elements. BM longitudinal coupling likely has a relatively limited influence on SOAE generation since it has a relatively weak influence on the response to a pure tone[60]. However, longitudinal coupling by the Y-shaped elements, which play an essential role in cochlear amplification in some models[165,166,105], might have a more significant influence on SOAE generation. Because some genetic mutations are known to affect TM longitudinal coupling[160,161,162,167], longitudinal coupling of

the TM is particularly interesting and was the focus of this work.

Previous work has characterized the material properties of isolated segments of murine TMs based on a transversely isotropic and viscoelastic model within the auditory frequency range[167]. In that study, Lemons et al.[167] reported that the TM stiffness is about 25 times higher in the radial direction than in the longitudinal direction. The moel assumes the TM vibrates rigidly within each cross-section, which is consistent with the high stiffness in the radial direction. In the model, the viscoelastic coupling between longitudinal cross-section is directly proportional to the shear modulus, G_{tm}, and shear viscosity, η_{tm}, of the TM (Equations 2.21, 2.22, and 2.24). G_{tm} and η_{tm} are material properties that have been directly reported by Lemons et al.[167] and other previous studies[59,161,168] for the TM of the mouse cochlea. In the model, these parameters have values ($G_{tm} \approx 5$ kPa at the 20 kHz location and η_{tm}=0.03 Pa·s) that are lower than reported by Lemons et al. ($G_{tm} \approx 70$ kPa and $\eta_{tm} \approx 0.6$ Pa·s), Ghaffari et al.[59] ($G_{tm} \approx 47$ kPa and $\eta_{tm} \approx 0.19$ Pa·s) and Jones et al.[168] ($G_{tm} \approx 80$ kPa and $\eta_{tm} \approx 0.06$ Pa·s) for basal TM segments of the mouse cochlea. While some of these differences could be explained by the difference in the species, it is likely that we underestimate the effects of reducing viscoelastic coupling on cochlear stability. Development of a cochlear model of the mouse cochlea with a more detailed representation of the TM directly based on the reported anisotropic properties of the TM would be a useful extension of this study that would potentially allow for more quantitative predictions.

Even though the influence of TM mutations on SOAE generation has only been reported for the mouse cochlea, the model used for this work corresponds to a different species of rodents, the gerbil, which is a limitation of this study. The occurrence of SOAEs tends to vary among rodents: for example, they are much more common in guinea pigs[169] than in WT mice[65]. Only one (unsuccessful) attempt to observe SOAEs in the gerbil cochlea has been reported[170]. Reports of successful and unsuccessful attempts to measure SOAEs in large populations of gerbils and other rodents would be useful for validation of theoretical

studies. The baseline model of the gerbil cochlea is not inconsistent with an absence or near absence of SOAEs in the gerbil, since an average of only 0.1 SOAE per ear is predicted in the baseline model with $\Delta R = 0.75\%$: only one cochlear model out of 10 emits 1 SOAE. Prediction of a higher number of SOAEs is only obtained when either (1) ΔR is increased to larger values or (2) TM viscoelastic coupling is reduced significantly.

For the model of the gerbil cochlea used in this study, very robust conclusions were found regarding the influence of the shear viscosity and modulus of the TM. When the shear viscosity and/or modulus of the TM is reduced, the numbers of linearly unstable modes and SOAE peaks increase significantly. As seen in Figure 6.12, lowering TM viscous or elastic coupling has limited influence on the frequencies of individual SOAEs and causes moderate increases in the amplitude of SOAEs. The increase in the number of SOAEs with reduced viscoelastic coupling is correlated with a sharpening of cochlear tuning[60] caused by the weakened stabilization by neighboring longitudinal cross-sections. The enhancement of SOAEs when TM viscous coupling is lowered might be due to a decrease in energy dissipation within the TM.

The prediction of enhanced SOAE generation when TM elastic coupling is reduced is in contrast with a previous theoretical study that has investigated the effect of elastic coupling on the spontaneous oscillations of non-mammalian HB[171]. In that work, the authors found that elastic coupling tends to increase the amplitude and sharpen the frequency tuning of spontaneous HB oscillations in the presence of noise. A key difference in this work is that, because the focus is on the mammalian cochlea, organ-level fluid mechanics, organ of Corti mechanics, and the cochlear traveling wave are taken into account, while Dierkes et al.[171] only modeled individual nonlinear oscillators coupled by elastic springs. Indeed, SOAE generation is a global phenomenon that requires the collective action of OHCs over a finite extent of the cochlear partition in our model; individual sections of the organ of Corti model are stable (Figure 6.13). Additionally, SOAE generation is significantly inhibited if reflection of reverse traveling waves at the stapes is weak[95].

6.5.2 Changes in TM viscoelastic properties might be responsible for SOAE enhancement in transgenic mice

The conclusions regarding the enhancement of SOAEs when TM viscoelasticity is reduced are remarkably similar to observations of increased occurrence of SOAEs in genetically modified mice[65,67]: for example, while SOAEs are uncommon in WT mice (only $\sim 8.2\%$ emit SOAEs), about 52% of $Tecta^{Y1870C/+}$ mice emit SOAEs[67]. In the $Tecta^{Y1870C/+}$ mice, the TM has reduced shear viscosity and reduced shear stiffness[161,162] due to the increased porosity of the TM and the total loss of the striated sheet matrix. The results of this study show that models with both reduced coupling viscosity and stiffness emit significantly more SOAEs than baseline models, as observed in the experiments with the $Tecta^{Y1870C/+}$ mice. Similarly, the occurrence of SOAEs is significantly increased in the *Ceacam16* KO mice[65]; while the mechanical properties of the TM of *Ceacam16* KO mice have not been characterized, this study's theoretical results suggest that the enhancement of SOAEs in *Ceacam16* KO might also be due to a decreased viscosity and/or stiffness of the TM. Previous work has shown that the *Tectb* KO mutation primarily affects the shear viscosity of the TM, which is about 50% lower than its value in WT TMs[161,167]. The model predicts that if the mutation only affects the TM shear modulus, *Tectb* KO mice should emit slightly more SOAEs than WT mice, which is consistent with measurements by Cheatham *et al.*[67].

6.5.3 Possible other mechanisms for the enhancement of SOAEs in genetically modified mice

While the model predictions provide compelling evidence that reducing TM viscoelastic coupling enhances the generation of SOAEs, the model does not capture all of the experimental observations regarding SOAE generation in TM mutant mice. For example, the model does not give a mechanism for the increased occurrence of low frequency SOAEs in $Tecta^{Y1870C/+}$ mice[67]. The limited validity of the model at the apex of the cochlea, where

OHCs are predicted to have a nearly negligible influence on the BM response to sound (Figure 6.2b), is a likely cause for the absence of low frequency SOAEs predicted by the model when TM viscoelastic coupling is reduced.

6.5.4 The TM plays a key role in maintaining cochlear stability

Remaining on the stable side of a dynamic bifurcation might be desirable to maximize the sensitivity of the cochlea to low level inputs[45]. However, due to the inherent inhomogeneities present in a biological system such as the cochlea, for example due to variations in the OHC morphology and properties, being close to a dynamic instability without generating many SOAEs is challenging. Any small change in the parameters of the cochlea might cause the system to move to the oscillatory regime. Numerical results (Figure 6.15) demonstrate that the ability to detect low amplitude sound would be compromised if the cochlea had many SOAEs; furthermore, limit cycle oscillations of large amplitude on the BM would potentially be heard by the subject and cause objective tinnitus.

6.6 Summary of contributions and conclusions

Multiple roles have been proposed for the TM in the literature. The TM is essential for the stimulation of inner hair cells[156]. Furthermore, the TM applies an inertial load on the OHC hair bundles that might play a critical role in activating the cochlear amplifier[155,143]. The role of TM viscoelastic coupling in controlling the tuning of the BM has been demonstrated experimentally and theoretically[157,160,60]. In this study, the role of the TM viscoelasticity on cochlear stability and SOAE generation was investigated using a computational model of the cochlea. Given the focus on TM longitudinal coupling in this study, longitudinal coupling was added to the TM-bending mode and the model was then re-calibrated so that the model response to a pure-tone was similar to that measured experimentally. The effects of reducing TM viscoelasticity on cochlear stability and SOAE generation were analyzed; the results indicated that reducing TM viscoelasticity causes a decrease in cochlear stabil-

ity and enhancement of SOAEs. The theoretical results, and the previous experiments in transgenic mice by Cheatham *et al.*[65,66,67], suggest that another important function of the TM is to prevent the emergence of limit cycles oscillations of large amplitudes.

CHAPTER 7

CONCLUSION

7.1 Summary of contributions

This thesis improves our understanding of hearing mechanics and otoacoustic emission generation. This improved understanding was attained using a computational model of the mammalian cochlea.

The detailed and physiologically motivated model takes into account the acoustics in the cochlear fluid, vibrations of the organ of Corti structures, and electrical physics of the OHCs. This thesis provides a complete description of the model's formulation, as well as key assumptions of the model, that was lacking in the literature.

The computational model was calibrated such that the model response to an acoustic stimulus was representative of the gerbil cochlea. This computational model advanced research in the field of hearing mechanics by providing a high-fidelity physiologically based model of the gerbil; in addition to the work in this thesis, the gerbil model is also actively used by other members of the Meaud research group to study various aspects of hearing mechanics and otoacoustic emissions[43]. Prior to this thesis research, the model parameters were selected such that the model response to acoustic stimulus was representative of the guinea pig cochlea. A model of the gerbil cochlea was needed to provide the best comparison between the model and *in vivo* gerbil measurements. A description of the calibration process and parameter sensitivity study were provided. The sensitivity study is a useful reference for researchers looking to understand how the various mechanical properties affect

cochlear responses and thus the relative import of the related structures in hearing mechanics. After calibration, the model was validated against other experimental data sets not considered during calibration.

The computational model was used to determine how distortion products propagate within the cochlea. In this work, it was found that distortion products propagate as a slow reverse traveling wave along the basilar membrane and in the cochlear fluid. DPOAEs are commonly used in clinical and academic settings as a noninvasive hearing assessment; however, there remained questions as to where DPOAEs are generated in the cochlea and how they travel from their generation locations to the middle ear and ear canal. Prior to this thesis, two mechanisms were proposed for the propagation of distortion products (either as a slow reverse traveling wave or a fast compression wave). Additionally, for the first time, the use of a 3D 2-duct model of the cochlear fluid allowed for direct comparison of model results to intracochlear pressure measurements.

This thesis provides a better understanding of the locations of DPOAE generation, which was found to be most significant between the f_2 and f_1 peak positions. Distortion products are generated by the outer hair cells and measuring their extracellular potential provides a measure of the cells' electrical output. For the first time, model 2- and 3-tone responses of the extracellular potential were compared to experiment measurements. Three methods were considered for determining the locations of the DPOAE generation: examining the OHC extracellular potential, applying local damage, and applying a third tone. The results of this study also indicate that no intracochlear distortion products are generated on the basilar membrane at positions very basal to the f_2 best place. Additionally, the results indicate that using a third tone to estimate the locations of distortion product generation may overestimate the basal extent of generation.

The role of the tectorial membrane in maintaining cochlear stability was investigated using the computational model. Decreasing the viscoelastic longitudinal coupling of the tectorial membrane was found to cause a decrease in cochlear stability and an increase

in the number of SOAEs generated. This increase in the number of SOAEs predicted by the model is similar to experiment measurements using transgenic mice that found an increase in the number of SOAEs generated when the mutations affect the proteins in the tectorial membrane. Other studies have found that these mutations also cause a change in the mechanical properties (including the viscoelastic longitudinal coupling) of the tectorial membrane. When viscoelastic coupling was significantly reduced (or eliminated), the model generated many spontaneous oscillations such that a low level sound would be undetectable. Taken together, these results indicate that an important role for the tectorial membrane is to maintain cochlear stability and promote the detection of low level sounds.

7.2 Opportunities for future work

While this thesis research advanced knowledge regarding cochlear mechanics and otoacoustic emission generation, some opportunities for future research can be identified based on the known limitations of the model identified in this work.

The model is unable to match the magnitude of the potentials in the scala tympani reported from experimental measurements at low frequencies relative to CF. While including longitudinal electrical cables in the model provides the possibility of matching the low frequency experimental data, an increase in the stiffness of the ODE system makes running nonlinear time domain simulations with the model unfeasible. A way to side-step this numerical issue would be to develop a nonlinear frequency domain model. This approach was used in an earlier version of the model based on a FORTRAN code[80], but is not included in the current MATLAB code used in this thesis. In addition to enabling the use of the nonlinear model with electrical cables, this nonlinear frequency domain model would also likely be much faster than the current time domain implementation. However, this nonlinear frequency domain model would not be able to study SOAE generation because the frequencies of SOAEs are not know before the simulation is run.

Recent measurements using optical coherence tomography (and model predictions, not

shown) show that the basilar membrane and other structures in the organ of Corti do not vibrate as a single rigid body. One of the assumptions of the model is that the cochlear fluid is directly coupled only to the response of the basilar membrane. In the real cochlea, the tectorial membrane and reticular lamina are surrounded by the intracochlear fluid such that both are coupled to the fluid in the scala media and subtectorial space (i.e. the space between the reticular lamina and tectorial membrane). Additionally, there is also fluid within the organ of Corti that may interact with the motions of the organ of Corti structures. Including fluid coupling to the tectorial membrane, reticular lamina, and/or organ of Corti may be necessary for the model more accurately predict their responses and could be important for predicting realistic and significant OHC electrical response at low frequencies relative to CF.

The study to determine the locations of distortion product generation only considered distortion products arising from the nonlinear distortion source. In reality, distortion products are predicted to be generated not only by the distortion source, but also by the reflection source; the reflection source tends to become more prominent at low f_2/f_1 ratios[43] and so the reflection source probably does not affect the results of this study for f_2/f_1=1.2 to 1.35. These two sources occupy different longitudinal positions and interact, which complicates the analysis of DPOAEs when measured experimentally or predicted in models that include cochlear roughness[36,37]. As a result, there has been much effort to develop techniques for separating the two components[38,39,37,40,41,42] in the ear canal pressure, but these techniques cannot be applied to separate the two components from intracochlear measurements. Reapplying the methods used in Chapter 5 (and also varying the positions with roughness) in a model with cochlear roughness could provide an estimate of how cochlear damage affects the reflection source. Such information would be useful when trying to separate the distortion and reflection sources in a damaged cochlea.

APPENDIX A

KINEMATIC MODEL

A.1 Organ of Corti model

The geometric model of the organ of Corti is shown in Figure A.1. As mentioned previously, the geometric parameters (listed in Table A.1) were determined using images from Edge *et al.*[90]. These parameters were used for all three iterations of the model presented in this work.

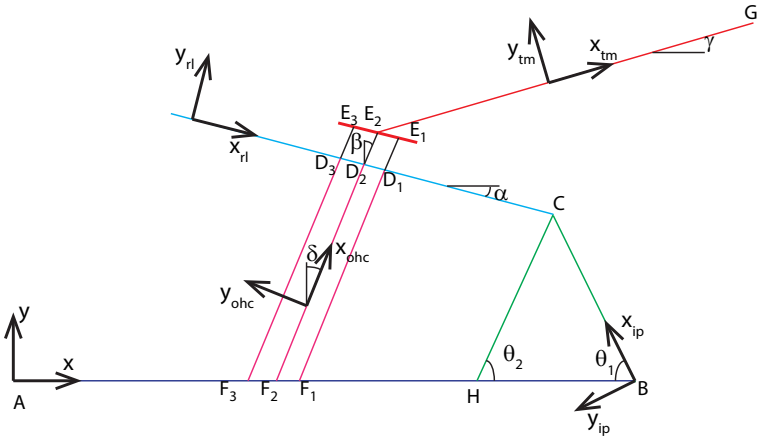

FIGURE A.1. Model of the organ of Corti

Coordinate systems are attached to several of the structures within the organ of Corti. The relationships between the basis vectors for these coordinate systems are:

$$\begin{aligned}
\vec{x}_{ip} &= -\cos\theta_1\vec{x} + \sin\theta_1\vec{y} & \vec{y}_{ip} &= -\sin\theta_1\vec{x} - \cos\theta_1\vec{y} \\
\vec{x}_{rl} &= \cos\alpha\vec{x} - \sin\alpha\vec{y} & \vec{y}_{rl} &= \sin\alpha\vec{x} + \cos\alpha\vec{y} \\
\vec{x}_{hb} &= \sin(\theta_1-\beta)\vec{x}_{ip} - \cos(\theta_1-\beta)\vec{y}_{ip} & \vec{y}_{hb} &= -\cos\beta\vec{x} + \sin\beta\vec{y} \\
\vec{x}_{tm} &= \vec{x}_{rl} & \vec{y}_{tm} &= \vec{y}_{rl} \\
\vec{x}_{ohc} &= \sin\delta\vec{x} + \cos\delta\vec{y}
\end{aligned} \tag{A.1}$$

The angle of the OHCs relative to vertical, δ is

$$\tan\delta = \frac{L_{02} - L_{Ro}\cos(\alpha) - L_{pc}\cos(\theta_1)\frac{\sin(\theta_1+\theta_2)}{\sin(\theta_2)}}{L_{Ro}\sin(\alpha) + L_{pc}\sin(\theta_1)\frac{\sin(\theta_1+\theta_2)}{\sin(\theta_2)}} \tag{A.2}$$

TABLE A.1. Anatomical parameters for the cochlea model (x in cm).

Param.	**Description**	**Value**
L	Length of BM	1.12 cm
L_h	Length of Helicotrema	0.1 cm
W	Width of cochlear ducts	0.1 cm
H	Height of each cochlear duct	0.1 cm
A_s	Cross-sectional area of stapes	$A_s = HW = 0.01$ cm^2
b	Width of BM	208μm (base) to 320μm (apex)
L_{tm}	Length of TM from pivot to middle HB	88μm (base) to 184μm (apex)
α	Angle between RL and BM	15° (base) to 26° (apex)
β	Angle between HB and vertical	15° (base) to 26° (apex)
γ	Angle between TM and BM	$-\alpha$
L_0	Distance between left edge of BM and contact of middle OHC with BM	$b/2$
L_1	Radial distance between HBs	13 μm
L_{pc}	Distance between left edge of BM and contact of outer pillar cell	58μm (base) to 100μm (apex)
L_{hb}	Length of HBs	1μm (base) to 6μm (apex)
L_{ro}	Distance between RL pivot and middle OHC	25.1μm (base) to 49μm (apex)
θ_1	Angle between inner pillar cell and BM	60°
θ_2	Angle between inner and outer pillar cells	60°

The distance between the right end of the BM (point B) and the i^{th} row of OHC are

$$L_{01} = L_0 - \frac{L_1}{\cos\delta} \tag{A.3}$$

$$L_{02} = L_0 \tag{A.4}$$

$$L_{03} = L_0 + \frac{L_1}{\cos\delta} \tag{A.5}$$

A.2 OHC motion

A.2.1 Motion of the OHC apex

The pillar cells are assumed rigid and rotate as the BM is displaced. The displacement of the tops of the pillar cells (point C in Figure A.1) is given as[79]:

$$u_{ap} = D_1 U_{bm} \tag{A.6}$$

where

$$D_1 = \psi(b/2 - L_{pc}) \frac{\sin(\theta_1 + \theta_2)}{\sin(\theta_2)} \tag{A.7}$$

The terms proportional to U_{bm} are found by assuming the TM is fixed, while the terms proportional to u_{tms} and u_{tmb} are found by assuming the BM is fixed. These terms can be added together through superposition to yield the apical displacement of the second OHC towards the BM in the OHC direction ($-\vec{x}_{ohc}$ direction) is:

$$u^a_{ohc2} = C_{21} U_{bm} + C_{23} u_{tms} + C_{24} u_{tmb} \tag{A.8}$$

where

$$C_{21} = -D_1 \left[\cos(\theta_1 - \delta) - \frac{\cos(\theta_1 - \beta)\cos(\delta - \alpha)}{\cos(\alpha - \beta)} \right] \tag{A.9}$$

$$C_{23} = -\cos(\delta - \alpha)\tan(\beta - \alpha) \tag{A.10}$$

$$C_{24} = -\cos(\delta - \alpha) \tag{A.11}$$

The motions of the tips of the first and third OHCs are easily found because the RL rotates about the top of the pillar cells:

$$u^a_{ohc_j} = C_{j1} U_{tmb} + C_{j3} u_{tms} + C_{j4} u_{tmb} \tag{A.12}$$

where $j = 1$ and $j = 3$ are for the first and third OHCs, respectively, and

$$C_{11} = -D_1\Big[\cos(\theta_1-\delta) - (1-\frac{L_1}{L_{Ro}})\frac{\cos(\theta_1-\beta)\cos(\delta-\alpha)}{\cos(\alpha-\beta)}\Big] \tag{A.13}$$

$$C_{31} = -D_1\Big[\cos(\theta_1-\delta) - (1+\frac{L_1}{L_{Ro}})\frac{\cos(\theta_1-\beta)\cos(\delta-\alpha)}{\cos(\alpha-\beta)}\Big] \tag{A.14}$$

$$C_{j3} = -\cos(\delta-\alpha)\tan(\beta-\alpha) \tag{A.15}$$

$$C_{j4} = -\cos(\delta-\alpha) \tag{A.16}$$

where j=1..3.

A.2.2 Motion of the OHC base

The motion of the base of the OHCs in the OHC direction ($\vec{x}_{ohc}$) is

$$u^b_{ohc_j} = E_{j1}U_{bm} \tag{A.17}$$

where j=1,2,3 for the respective OHCs and

$$E_{j1} = \psi(b/2 - L_{0j})\cos\delta \tag{A.18}$$

where

$$L_{01} = L_{02} - L_1\frac{1}{\cos\delta} \tag{A.19}$$

$$L_{03} = L_{02} + L_1\frac{1}{\cos\delta} \tag{A.20}$$

are the distances from the right edge of the BM (point B in Figure A.1) to the base of the first and third OHCs, respectively.

A.2.3 OHC compression

Lumping the three OHCs together, the sum of the displacements of the apical end of the OHC in the OHC direction is

$$\vec{u}^a_{ohc} = (C_1 u_{bm} + C_3 u_{tms} + C_4 u_{tmb})(-\vec{u}_{ohc}) \tag{A.21}$$

where

$$C_j = C_{1j} + C_{2j} + C_{3j} \tag{A.22}$$

where j=1,2,3. Similarly, the sum of the displacements of the basal end of the OHC in the OHC direction is

$$\vec{u}^b_{ohc} = E_1 U_{bm} \vec{x}_{ohc} \tag{A.23}$$

where

$$E_1 = E_{11} + E_{21} + E_{31}. \tag{A.24}$$

The OHC displacement in compression is then

$$\vec{u}^{comp}_{ohc} = \vec{u}^b_{ohc} - \vec{u}^a_{ohc} = \Big[(E_1 + C_1)u_{bm} + C_3 u_{tms} + C_4 u_{tmb}\Big]\vec{x}_{ohc} \tag{A.25}$$

A.3 Displacement of the reticular lamina

Using superposition, the displacement of the RL at the top of the second OHC (point D_2 in Figure A.1) may be written as

$$\begin{aligned} u_{rl_j} &= \vec{u}_{rl_j} \cdot \vec{y}_{rl} \\ &= B_{j1} U_{bm} + B_{j3} u_{tms} + B_{j4} u_{tmb} \end{aligned} \tag{A.26}$$

for j=1,2,3 where

$$B_{11} = (1 - \frac{L_1}{L_{ro}})B_{21} \tag{A.27}$$

$$B_{21} = -D_1 \frac{\cos(\theta_1 - \beta)}{\cos(\alpha - \beta)} \tag{A.28}$$

$$B_{31} = (1 + \frac{L_1}{L_{ro}})B_{21} \tag{A.29}$$

$$B_{j3} = \tan(\beta - \alpha) \tag{A.30}$$

$$B_{j4} = 1 \tag{A.31}$$

A.4 Deflection of the hair bundles

If the TM is fixed, the displacement of the top of the second OHC in the direction parallel to the RL ($\vec{x}_{rl}$) is given by:

$$\begin{aligned} u_{ohc2s} &= u_{ohc2}\vec{y}_{hb} \cdot \vec{x}_{rl} \\ &= A_{21}U_{bm} \end{aligned} \tag{A.32}$$

where

$$A_{21} = D_1 \sin(\theta_1 - \alpha) \tag{A.33}$$

If the BM is fixed, the displacement of the top of the second HB relative to the bottom of the HB in the direction parallel to the RL ($\vec{x}_{rl}$) is given by:

$$\begin{aligned} u_{ohc2tm} &= (\vec{x}_{E_2} - \vec{u}_{D_2}) \cdot \vec{x}_{rl} \\ &= -u_{tms} \end{aligned} \tag{A.34}$$

The total displacement of the second HB in the excitatory direction is then:

$$\begin{aligned} u_{hb2} &= -(u_{ohc2tm} - u_{ohc2s}) \\ &= A_{21}U_{bm} + A_{23}u_{tms} + A_{24}u_{tmb} \end{aligned} \tag{A.35}$$

where

$$A_{23} = 1 \tag{A.36}$$

$$A_{24} = 0 \tag{A.37}$$

The total displacements of the first ($j = 1$) and third HBs ($j = 3$) are similarly:

$$u_{hb_j} = A_{j1}U_{bm} + A_{j3}u_{tms} + A_{j4}u_{tmb} \tag{A.38}$$

where

$$A_{11} = D_1\left[\sin(\theta_1 - \beta)\cos(\alpha - \beta) - \left(1 - \frac{L_1}{L_{Ro}}\right)\cos(\theta_1 - \beta)\sin(\alpha - \beta)\right] \tag{A.39}$$

$$A_{31} = D_1\left[\sin(\theta_1 - \beta)\cos(\alpha - \beta) - \left(1 + \frac{L_1}{L_{Ro}}\right)\cos(\theta_1 - \beta)\sin(\alpha - \beta)\right] \tag{A.40}$$

$$A_{j3} = 1 \tag{A.41}$$

$$A_{j4} = 0 \tag{A.42}$$

APPENDIX B

METHOD FOR ESTIMATING EFFECTIVE FLUID MASS

B.1 Fluid domain

By assuming a harmonic propagating wave (of angular frequency ω) in the x direction in the antisymmetric component of the fluid pressure (Equation 3.13):

$$P_{as}(x,y,z) = P_{as}(y,z)e^{ik_x x}e^{i\omega t}, \tag{B.1}$$

the governing equation and boundary conditions for the fluid (Section 2.2.1) yield:

$$P_{as}(y,z) = \sum_{m=0}^{\infty} B_m \phi_m(y) \cosh\left[\bar{k}_{zm}(z-H)\right] \tag{B.2}$$

where B_m will be determined later and

$$\bar{k}_{zm} = \sqrt{k_x^2 + \left[\frac{m\pi}{W}\right]^2}. \tag{B.3}$$

B.2 Mechanical domain

In the structural domain, the BM is assumed to be uncoupled beams in the radial direction (this assumption ultimately has no effect on the estimation of the effective fluid mass):

$$E\frac{h^3}{12}\frac{\partial^4 u_{bm}(x,y)}{\partial y^4} + \rho_s \ddot{u}_{bm}(x,y) = -2P_{as}(x,y,z=0) \tag{B.4}$$

where E is the Young's modulus, h is the thickness of the BM, and ρ_s is the mass of the BM per unit area. Assuming a harmonic response, that the BM vibrates in its first mode, and there is a propagating wave in the x direction yields:

$$u_{bm}(x,y,t) = U_{bm}\psi(y)e^{ik_x x}e^{i\omega t} \tag{B.5}$$

where U_{bm} is the amplitude of the response (assumed constant) and $\psi(y)$ is defined by Equation 2.9. Using these assumptions, Equation B.4 becomes

$$E\frac{h^3}{12}\left(\frac{\pi}{b}\right)^4\psi(y)-\rho_s\omega^2\psi(y)=-2\sum_{m=0}^{\infty}B_m\phi_m(y)\cosh\left[\bar{k}_{zm}(z-H)\right]. \tag{B.6}$$

B.3 Coupled equations

Multiplying Equation B.6 by $\psi(y)$ and integrating over the width of the BM (from $-b/2$ to $b/2$) yields:

$$K_{bm}-\omega^2M_{bm}=-2\sum_{m=0}^{\infty}B_m\cos(\bar{k}_{zm}H)C_{m1} \tag{B.7}$$

where K_{bm} and M_{bm} are the effective BM stiffness and mass, respectively:

$$K_{bm}=E\frac{h^3}{12}\left(\frac{\pi}{b}\right)^4\Gamma_1 \tag{B.8}$$

$$M_{bm}=\rho_s\Gamma_1 \tag{B.9}$$

Γ_1 and C_{m1} are given by

$$\Gamma_1=\int_{-b/2}^{b/2}\psi(y)^2dy=\frac{b}{2} \tag{B.10}$$

$$C_{m1}=\int_{-b/2}^{b/2}\psi(y)\phi_m(y)dy \tag{B.11}$$

Evaluating the integral in Equation B.11 yields:

$$C_{m1}=\begin{cases}\frac{b}{2}\cos\frac{\pi m}{2} & W=bm\\ \frac{(-1)^{m/2}W^2b}{\pi(W^2-b^2m^2)}\cos\left(\frac{\pi bm}{2W}\right)\left((-1)^m+1\right) & W\neq bm\end{cases} \tag{B.12}$$

The value of B_m can be found by multiplying the linearized Euler relationship at the BM (Equation 2.2) by the fluid radial mode shape, $\phi_m(y)$, and then integrating over the

width of the cochlear duct:

$$B_m = -\frac{\rho_0 \omega^2 C_{m1} U_{bm}}{2\Lambda_m \bar{k}_{zm} \sinh(\bar{k}_{zm} H)} \tag{B.13}$$

where

$$\Gamma_m = \int_{-W/2}^{W/2} \phi_m(y)^2 dy \tag{B.14}$$

$$\Lambda_0 = W \tag{B.15}$$

$$\Lambda_m = \frac{W}{2} \tag{B.16}$$

Equation B.7 can then be rewritten as:

$$K_{bm} - \omega^2 M_{bm} = \rho_0 \omega^2 \Gamma_1 H_{eq}(k_x) \tag{B.17}$$

where H_{eq} is the effective fluid thickness, which is given by

$$H_{eq}(k_x) = \frac{1}{\Gamma_1} \sum_{m=0}^{\infty} \frac{C_{m1}^2}{\Lambda_m} \frac{1}{\bar{k}_{zm} \tanh(\bar{k}_{zm} H)} \tag{B.18}$$

B.4 Effective fluid mass

The effective thickness (Equation B.18) can be separated into near field ($k_x H \ll 1$) and far field ($k_x H \gg 1$) terms [172]:

$$H_{eq}(k_x) = H_{eq}^{FF}(k_x) + H_{eq}^{NF} \tag{B.19}$$

where

$$H_{eq}^{FF}(k_x) = \frac{8b}{HWk_x^2\pi^2} \tag{B.20}$$

$$H_{eq}^{NF} = \frac{8b}{3\pi^2} + \sum_{m=1}^{\infty} \frac{4C_{m1}^2}{bm\pi} \frac{1}{\tanh(m\pi)} \tag{B.21}$$

Equation B.17 can be rewritten as:

$$K_{bm} - (M_{bm} + M_f)\omega^2 = \rho_0 \omega^2 \Gamma_1 H_{eq}^{FF}(k_x) \tag{B.22}$$

where M_f is the added fluid mass, which is given by:

$$M_f = \rho_0 \frac{4b^2}{3\pi^2} + \rho_0 \sum_{m=1}^{\infty} \frac{2C_{m1}^2}{m\pi \tanh(m\pi)} \tag{B.23}$$

APPENDIX C

MODEL PARAMETERS

C.1 Mechanical parameters

The mechanical parameters for the cochlea model are provided in Table C.1 and the middle ear parameters are provided in Table C.2. The 2018 and 2019 models used the same baseline middle ear parameters (2018 parameters in Table C.2). The baseline middle ear parameters used for the current model were determined by Meaud lab group member Haiqi Wen to give a stapes reflection coefficient (R_{st}, Equation 3.4) magnitude of approximately 0.5. All cochlea parameters except for the TM-bending mass, M_{tmb}, are the same for all models; the TM-bending mass for the 2019 and current models was increased by 30% from the 2018 model value. By assuming the TM has the same density as water (reasonable since the TM is mostly water), the cross-sectional area of the TM can be estimated. Because the model parameters for the TM in shear and bending are different, the effective cross-sectional areas are also different. The cross-sectional area of the TM from the model is compared to experiment measurements[173,174] taken in the gerbil hemicochlea (i.e. the cochlea was cut in half) in Figure C.1. The effective area of the TM-shear model is nearly identical to the measurements by Richter et al., 2007[174].

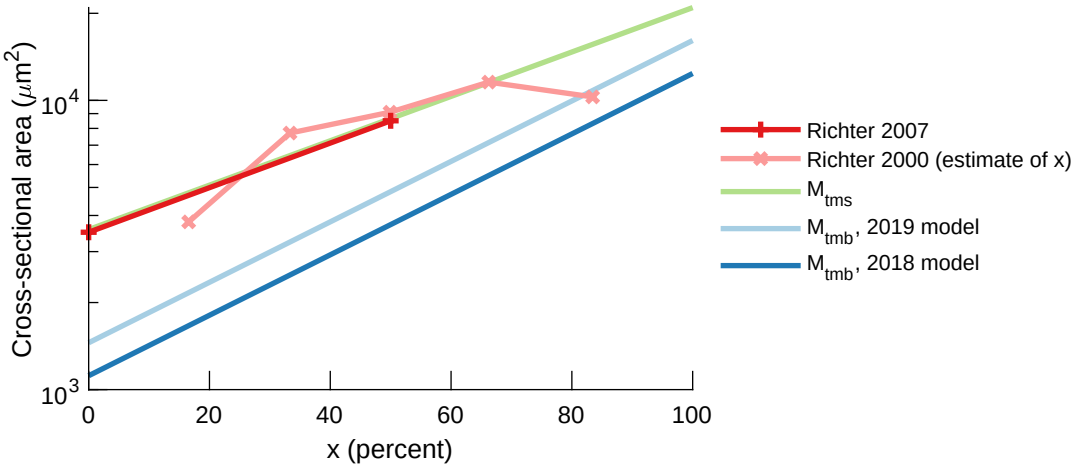

FIGURE C.1. Comparison of model values for the TM cross-sectional area with experimental measurements in the hemicochlea by Richter et al.[173,174]. The cross-sectional area of the model TM is computed by assuming the TM has the same density as water (1 gram/cm^3). The positions shown for the experimental data are rough estimates.

TABLE C.1. Mechanical parameters for the Bowling 2018 cochlear model (where x is the longitudinal position in cm). Parameters denoted * are defined per unit length.

Param.	**Description**	**Value**	**Ref.**
K_{bm}	BM stiffness *	$18.4\exp(-7.54x)\cdot 10^5$ N/m^2	assumed
D_{xx}	BM plate bending stiffness (xx) *	$10^{-10}\exp(-0.5x)$ N.m	60
D_{xy}	BM plate bending stiffness (xy) *	$10^{-10}\exp(-0.5x)$ N.m	60
D_{shear}	BM plate bending stiffness (shear) *	$4.3\exp(-0.5x)\cdot 10^{-11}$ N.m	60
K_{tms}	TM shear stiffness *	$2.31\exp(-1.32x^2-6.42x)\cdot 10^5$ N/m^2	assumed
K_{tmb}	TM bending stiffness *	$3.84\exp(-7.54x)\cdot 10^4$ N/m^2	assumed
K_{rl}	RL stiffness *	$2.78\exp(-7.54x)\cdot 10^3$ N/m^2	assumed
K_{ohc}	OHC stiffness *	$5.07\exp(-7.54x)\cdot 10^3$ N/m^2	assumed
K_{hb}	HB stiffness	$291\exp(-7.54x)$ mN/m	assumed
M_{bm}	BM mass *	$2.8\cdot 10^{-7}$ kg/m	175
M_{tms}	TM shear mass *	$3.58\exp(1.58x)\cdot 10^{-6}$ kg/m	based on 173, 174
M_{tmb}	TM bending mass *	*2018*: $1.12\exp(2.15x)\times 10^{-6}$ kg/m *2019*: $1.46\exp(2.15x)\times 10^{-6}$ kg/m	based on 173, 174
c_{bm}	BM damping coefficient *	$8.5\cdot 10^{-2}$ N.s/m^2	assumed
c_{hb}	HB damping coefficient	$\eta_f \frac{L_{tm}}{3L_{hb}}$, where $\eta_f = 1.0\cdot 10^{-3}$ N.s/m^2 is the viscosity of the fluid	60
c_{tmb}	TM bending damping coefficient *	0.1 N.s/m^2	assumed
c_{tms}	TM shearing damping coefficient *	$3\cdot 10^{-3}$ N.s/m^2	assumed
G_{tm}	TM modulus	$7.0\exp(-3.75x)$ kPa	174, 60
η_{tm}	TM viscosity	0.03 Pa.s	based on 59
ρ_f	fluid density	1000 kg/m^3	

TABLE C.2. Mechanical parameters for the middle ear model.

Parameters	Description	Baseline	High $\lvert R_{st}\rvert$	Low $\lvert R_{st}\rvert$
M_s	Stapes mass (kg)	2018: 3.0×10^{-7} Current: 3.15×10^{-9}	3.0×10^{-7}	6.6×10^{-7}
C_s	Stapes damping coefficient (N.s/m)	6.0×10^{-2} Current: 9.6×10^{-1}	1.0×10^{-3}	3.4×10^{-1}
K_s	Stapes stiffness (N/m)	5.0×10^2 Current: 7.8×10^3	5.0×10^2	2.3×10^4

C.2 Electrical parameters

The electrical parameters for the cochlea models are provided in Table C.3. The value of the basolateral conductance and capacitance were set to the values reported by Johnson et al.[145]. The HB saturating conductance, G_a^{max}, was chosen to be a free parameter whose value was varied during the calibration process to give BM gain values that matches the experimental data[85,86].

C.2.1 Comparison of model HB saturating conductance with values computed from measurements

The values of the HB saturating conductance for the three model iterations considered in this work are compared to values calculated from measurements taken in vivo in the rat and gerbil by Johnson, et al.[145] in Figure C.2. For all three model iterations, the model values are higher than those from the experiments.

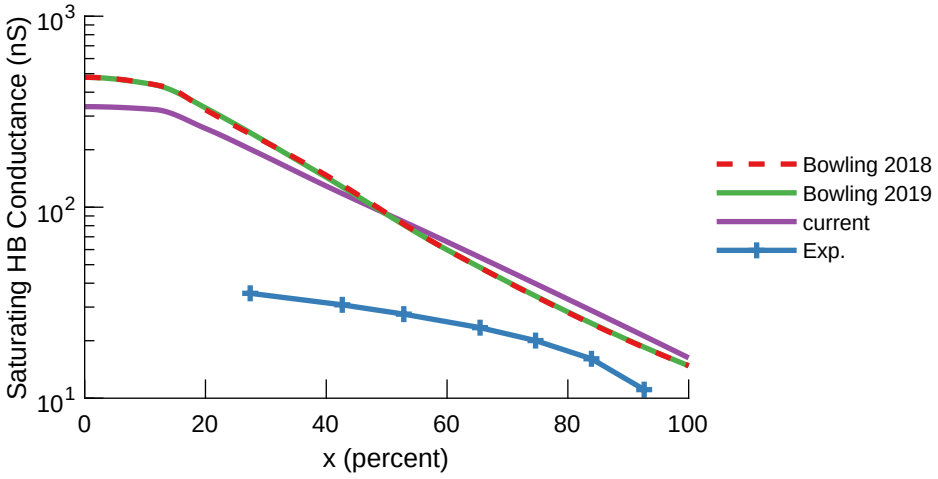

FIGURE C.2. Comparison of model values for HB saturating conductance with values calculated from in vivo measurements in rats and gerbils by Johnson, et al.[145]. The positions shown for the experimental data were estimated using Greenwood's[4] place frequency map.

C.2.2 Parameters for models with longitudinal cables

The electrical properties for the models with longitudinal cables shown in Figure 5.28 that are different from the values for the 2019 model listed in Table C.3 are listed in Table C.4.

TABLE C.3. Electrical parameters for the three model iterations (x in cm). Parameters denoted * are defined per unit length and parameters denoted † are defined per OHC assuming 1000 rows of OHCs per centimeter[6] and 3 OHCs per row.

Param.	**Description**	**2018 Value**	**2019 Value**	**Current Value**	**Ref.**
G_a^{max}	saturating HB conductance *	Interpolated from 479 nS at x=0 cm 427 nS at x=0.15 cm 324 nS at x=0.224 cm 151 nS at x=0.44 cm 60 nS at x=0.67 cm 14.8 nS at x=1.12 cm	Interpolated from 479 nS at x=0 cm 438 nS at x=0.13 cm 422 nS at x=0.15 cm 331 nS at x=0.224 cm 148 nS at x=0.44 cm 60 nS at x=0.67 cm 14.8 nS at x=1.12 cm	Interpolated from 336 nS at x=0 cm 325 nS at x=0.13 cm 258 nS at x=0.224 cm 193 nS at x=0.32 cm 132 nS at x=0.44 cm 66 nS at x=0.67 cm 16 nS at x=1.12 cm	assumed
R_{mg}	resistance from SM to ground *	Infinite		27 Ωm	based on 92
R_{tl}	resistance from ST to ground *	4 Ωm		2.73×10^{-2} Ωm	assumed
R_{vm}	resistance from SV to SM *	25 Ωm			based on 92
R_{vl}	resistance from SV to ground *	10 Ωm			based on 92
C_m	basolateral capacitance †	$17.45x$ pF			based on 145
G_m	basolateral conductance †	$192 - 148.9x$ nS			based on 145
ε_3	electromechanical coupling coefficient *	$(-1.04 + 0.36x) \times 10^{-5}$ N/m/mV			based on 146
R_a^0	apical resistance *	$58.1\exp(2.05x)$ Ωm			80
C_a	apical capacitance*	50 nF/m			based on 176
ΔV_{hb}^0	resting value of potential difference between SM and intracellular OHC potential	$150 - 10x$ mV			80
P_0^s	resting probability	0.4			80
f_{gs}	single channel gating force in the tip link direction	10 pN			177, 178
γ	geometric gain factor	0.5 μm / L_{hb}			179, 180
T	temperature	310 K			

TABLE C.4. Electrical parameters for model with longitudinal cables (where x is the longitudinal position in cm).

Param.	**Description**	**Model A**	**Model B**	**Model C**	**Ref.**
r_{st}	ST longitudinal resistance *	16 MΩ/m	31 MΩ/m	14 MΩ/m	assumed
R_{tl}	ST-ground resistance*	0.25 Ωm	0.05 Ωm	0.25 Ωm	assumed
r_{sv}	SV longitudinal resistance *	3 MΩ/m			based on 92
r_{sm}	SM longitudinal resistance *	2000 MΩ/m			based on 93
R_{mg}	SM-ground resistance*	1 Ωm			93
G_a^{max}	saturating HB conductance *	Interpolated from 282 nS at x=0 cm 263 nS at x=0.15 cm 226 nS at x=0.224 cm 175 nS at x=0.31 cm 119 nS at x=0.44 cm 55.0 nS at x=0.67 cm 15.8 nS at x=1.12 cm			assumed

APPENDIX D

RUNTIME PERFORMANCE IMPROVEMENTS

D.1 Overview and baseline mesh

This Appendix details the runtime performance of model simulations. Several relatively minor changes were made to the model code that resulted in significant improvements in the runtime performance. These improvements are characterized for different mesh parameters. The baseline mesh has 448 elements along the BM (25 μm elements) and 40 elements for the fluid in the vertical direction (z-direction) in each of cochlear ducts. Running the same code multiple times on the same processor or node can result in vastly difference computational times. To obtain accurate performance metrics, $n = 10$ iterations were run for each simulation case. All results are obtained from simulations using the 2019 model run using MATLAB 9.5 R2018b (The Mathworks, Natick, MA). The vast majority of simulations results presented in this thesis were run on the Partnership for an Advanced Computing Environment (PACE) cluster at Georgia Tech. The Meaud research group has access to a dedicated queue (appropriately named the "cochlea" queue) with 9 nodes that contain a total of 224 cores (CPUs). For analyzing the runtime performance of the model, all simulations were run on the newest set of nodes on the queue. The characteristics of these nodes are listed in Table D.1.

TABLE D.1. Technical specifications for several of the nodes on the "cochlea" queue on PACE.

Node	**Cores**	**Processor**	**Total Memory (GB)**
rich133-k35-27-l	28	Intel Xeon E5-2680 v4 (2.4 GHz)	254
rich133-k35-27-r	28	Intel Xeon E5-2680 v4 (2.4 GHz)	254
rich133-k35-28-l	28	Intel Xeon E5-2680 v4 (2.4 GHz)	254
rich133-k35-28-r	28	Intel Xeon E5-2680 v4 (2.4 GHz)	254

D.2 Fluid matrix assembly

The baseline mesh used in this work has thousands of mechanical and electrical DOFs and 40,000 pressure DOFs per fluid mode for a total of over one million pressure DOFs when

25 fluid modes are used. As a result, the fluid stiffness matrix, $\mathbf{K_f}$, is a large 1,000,400 x 1,000,400 sparse matrix with approximately 8.9 million nonzero entries (density of $8.8 \times 10^{-4}\%$). The fluid-structure mass ($\mathbf{M_{sf}}$) and stiffness ($\mathbf{K_{fs}}$) matrices are large 1,000,400 x 1,797 and 1,797 x 1,000,400 matrices, respectively, with approximately 135,000 nonzero entries (density of $7.5 \times 10^{-3}\%$). The assembly of the fluid stiffness and fluid-structure coupling matrices were originally[82] performed with commands like the following (for $\mathbf{K_f}$):

```
Kf(index(i),index(j))=Kf(index(i),index(j)) + Kfe(i,j);
```

where `Kfe` is the fluid element stiffness matrix, `index` maps the local element nodes to the global nodes, and `i` and `j` are for loop variables. Due to the data structure used for sparse matrices in MATLAB, this kind of indexing is not computationally efficient. The computational time required to assemble the FEM matrices (fluid, structural, and electrical) increases as number of fluid modes increases (shown in Figure D.1A) or the number of elements increases (Figure D.1B). The bulk of the matrix assembly computational time is spent assembling the fluid matrices, whereas assembling the much smaller structural and electrical matrices is relatively quick. Using the original 2015 formulation[82], assembling the FEM matrices for $N_m = 25$ fluid modes would take approximately 15.5 hours. Assembling the fluid matrices for every simulation would become very computationally expensive. While the structural and electrical FEM matrices may vary depending on the specific simulation being performed (e.g. reducing TM longitudinal coupling or adding local damage), the fluid matrices are always the same for all simulations for a given mesh. To bypass the assembly time issue, the fluid FEM matrices ($\mathbf{K_f}$, $\mathbf{K_{fs}}$, and $\mathbf{M_{sf}}$) were loaded from a data file instead of being reassembled for each simulation. This approach does have drawbacks, however, in that it required the user to always keep track of these data files and any simulations using a different mesh would require first reassembling all the matrices and saving them to a data file for later use for the actual simulations of interest. Within the MATLAB documentation, an alternative approach for assembling sparse matrices is recommended (especially for FEM applications) in which the nonzero entries of the matrices

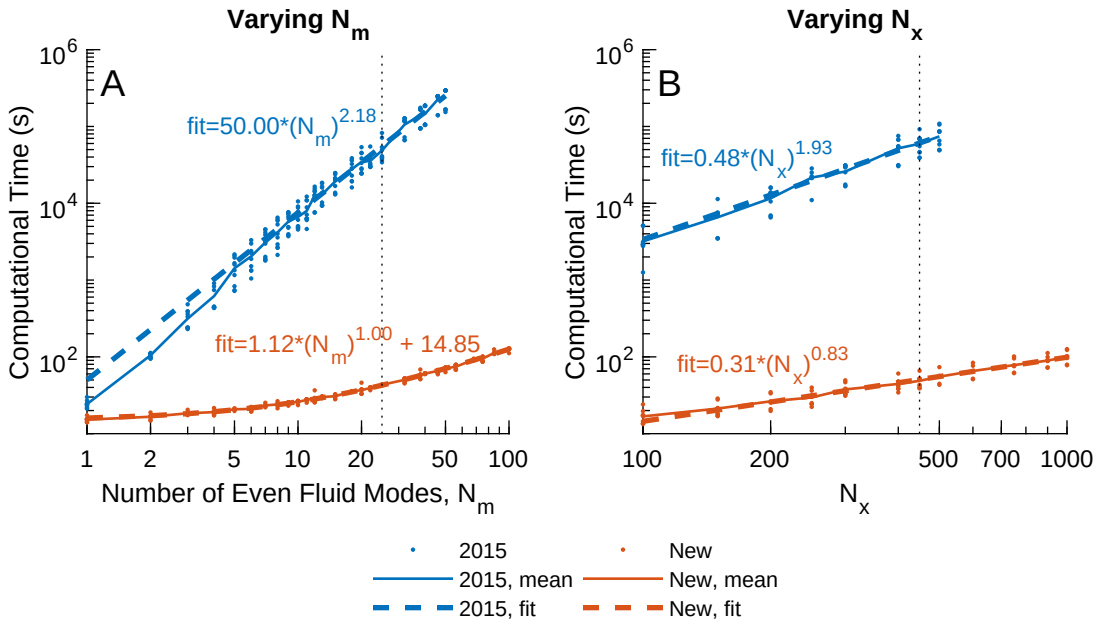

FIGURE D.1. Computational time required for FEM matrix assembly (includes fluid, structure, and electrical matrices) as a function of the number of fluid modes (A) and number of nodes along the BM (B) for the original and new assembly methods. A total of $n = 10$ iterations were run for each fluid mode and assembly method. All simulations were run on the rich133-k35-28-l node on PACE with 20 GB of memory and 12 GB of disk space requested for each iteration. A power series fit is also included for each of the assembly formulations.

are assembled using a row-column-value triplet vectors, `i`, `j`, and `v`, such that for a sparse matrix, `S`:

```
S(i(k), j(k)) = v(k);
```

MATLAB adds together any elements in `v` that have duplicate row (`i`) and column (`j`) values. To implement this approach within the model, it is first necessary to determine the total number of triplets that will occur in the fluid stiffness and coupling matrices based on the mesh parameters so that the row, column, and value vectors can be preallocated. Entries from the element matrices are added to the vectors by commands like the following (for $\mathbf{K_f}$):

```
KfNtriplets = KfNtriplets + 1;
KfI (KfNtriplets) = indexF(i);
```

```
KfJ (KfNtriplets) = indexF(j);
KfX (KfNtriplets) = Kf_e(i,j);
```

where `KfNtriplets` is a counter, `KfI` is a vector of the rows, `KfJ` is a vector of the columns, and `KfX` is a vector of values of the nonzero entries in $\mathbf{K_f}$. Once all the fluid elements have been added, the fluid stiffness matrix is assembled by calling MATLAB's `sparse` function:

```
Kf = sparse(KfI, KfJ, KfX);
```

An idential approach was used for assembling the fluid-structure coupling mass and stiffness matrices. Assembling the fluid matrices in this manner results in a dramatic increase in performance (see Figure D.1). While the computational time for the original 2015 formulation would increase at $O((N_m)^{2.18})$, the new method is much faster and the computational time increases linearly $O(N_m)$ (see fits in Figure D.1A), where N_m is the number of even fluid modes. The constant appearing in the fit for the new formulation (14.85 seconds) in Figure D.1A corresponds to the time spent assembling the mechanical and electrical matrices. For the baseline N_m=25 case, the new assembly method is almost 1,200 times faster than the original method.

D.3 Improvements in time domain performance

Most simulations run by the model are in the time domain, which involves integrating a system of ordinary differential equations (ODEs) using MATLAB's `ode45` function. In the extreme, a single simulation can involve hundreds of millions of integration steps and take more than one month to complete (e.g. many of the SOAE simulations in Chapter 6). At each time step, MATLAB calls a function (referred to henceforth as the "ODE function") that implements the ODE system of equations:

$$\dot{\mathbf{v}} = \mathbf{f}(\mathbf{v}, t). \tag{D.1}$$

This section describes two sets of improvements that were made to the ODE function's computation of $\mathbf{f}(\mathbf{v},t)$. The first improvement was modifying how the nonlinear force vector, $\mathbf{F}_{\mathbf{es}}^{\mathbf{NL}}$ was computed and the second was to take better advantage of MATLAB's built-in matrix functionality. In the state space formulation described in Section 2.4.2, the mass matrix, $\mathbf{M}$ was left on the left-hand side of the state space equation (Equation 2.55). However, in the original 2015 formulation[82] , the state space equation solved in the ODE function is

$$\mathbf{M_{orig}}\dot{\mathbf{v}} = \mathbf{a_{lin}}\mathbf{v} + \mathbf{NL}(\mathbf{v}) + \mathbf{f} \tag{D.2}$$

where $\mathbf{v} = [\dot{\mathbf{u}}, \mathbf{u}, \phi]^T$ is the state variable (as in Section 2.4.2) and:

$$\mathbf{M_{orig}} = \begin{pmatrix} \mathbf{I} & \mathbf{0} & \mathbf{0} \\ \mathbf{0} & \mathbf{I} & \mathbf{0} \\ \mathbf{0} & \mathbf{0} & \mathbf{C_{es}} \end{pmatrix} \tag{D.3}$$

$$\mathbf{a_{lin}} = -\begin{pmatrix} \mathbf{M_{eff}}^{-1}\mathbf{C_s} & \mathbf{M_{eff}}^{-1}\mathbf{K_s} & \mathbf{M_{eff}}^{-1}\mathbf{K_{se}} \\ -\mathbf{I} & \mathbf{0} & \mathbf{0} \\ \mathbf{C_{es}} & \mathbf{K_{es}^{lin}} & \mathbf{K_e} \end{pmatrix} \tag{D.4}$$

$$\mathbf{f} = \begin{pmatrix} \mathbf{M_{eff}}^{-1}\mathbf{F_u} \\ \mathbf{0} \\ \mathbf{0} \end{pmatrix} \tag{D.5}$$

In the MATLAB implementation, the matrices $\mathbf{a_{lin1}}$ and $\mathbf{a_{lin3}}$corresponds to the first and third rows of block matrices in $\mathbf{a_{lin}}$:

$$\mathbf{a_{lin1}} = \begin{pmatrix} \mathbf{M_{eff}}^{-1}\mathbf{C_s} & \mathbf{M_{eff}}^{-1}\mathbf{K_s} & \mathbf{M_{eff}}^{-1}\mathbf{K_{se}} \end{pmatrix} \tag{D.6}$$

$$\mathbf{a_{lin3}} = \begin{pmatrix} \mathbf{C_{es}} & \mathbf{K_{es}^{lin}} & \mathbf{K_e} \end{pmatrix} \tag{D.7}$$

In the original formulation, the computations performed by the ODE function can be

split into four tasks:

1. Compute the nonlinear force vector, $\mathbf{F_{es}^{NL}}$
2. Compute $\mathbf{a_{lin1}} \times \mathbf{v}$
3. Solve the electrical model equation, $\mathbf{C_e}\dot{\boldsymbol{\phi}} = \mathbf{a_{lin3}}\mathbf{v} + \mathbf{F_{es}^{NL}}$
4. Compute the stimulus forcing term, $\mathbf{F_u}$

Preliminary profiling results indicated that up to 95% of the overall computational time of a simulation was spent in the ODE function. Because the ODE function is called for each integration step, efforts to optimize the function can potentially result in a dramatic reduction in the computational time. In the original 2015 formulation, a significant part of the time spent computing the nonlinear force vector was spent computing the HB deflection relative to the RL, $u_{hb/rl}$ from the BM, TM-shear, and TM-bending displacements (i.e. the geometric coupling coefficients A_{ij}, B_{ij}, E_{ij} in Equations 2.12 and 2.13). These geometric coupling coefficients do not depend on time and can thus be computed once during matrix assembly. Similarly, other variables needed for computing $\mathbf{F_{es}^{NL}}$ can be computed once during matrix assembly instead of at each time step. These improvements not only sped up the runtime performance of time domain simulations, but also improved the readability of the code.

For the baseline mesh, $\mathbf{a_{lin1}}$ is a relatively dense matrix with a density of 72.5% (due to the $\mathbf{M_{eff}}^{-1}$ terms), but in the original 2015 formulation[82] the matrix was defined to be sparse. Through tests on both a PC work station and PACE, it was determined that it is computationally faster to define $\mathbf{a_{lin1}}$ as a full matrix. For the runtime performance results discussed later in this section, the improvements discussed thus far are referred to as the "2019 formulation."

One of the options for MATLAB's ODE solvers is to specify a mass matrix, so that the following system is solved:

$$\mathbf{M}\dot{\mathbf{v}} = \mathbf{f}(t, \mathbf{v}). \tag{D.8}$$

Through further testing, it was determined that the runtime performance could be improved dramatically by solving Equation 2.55 instead of using the inverse of the effective mass, $\mathbf{M_{eff}}$ to solve Equation D.2. In this case, all matrices in Equation 2.55 (except for $\mathbf{M_{eff}}$, which is $\approx 25\%$ dense for the baseline mesh) are sparse, making the computation of $\mathbf{f}(t, \mathbf{v})$ very efficient.

The runtime performance for all three methods are compared in Figure D.2. For all methods, increasing N_x results in a dramatic increase in the computational time ($\geq O((N_x)^4$, Table D.2), as shown in Figure D.2A. The 2019 formulation results in increased performance and is approximately 2 times faster than the original 2015 formulation for $N_x = 449$, but the speedup decreases as N_x increases (Figure D.2E). The decrease in speedup is due to computing $\mathbf{A_{lin1}} \times \mathbf{v}$ taking a larger percentage of the overall computational time as N_x increases (Figure D.2C). Using the 2019 formulation with the mass matrix results in performance more than 5 times faster than the original formulation for N_x=449, and this speedup increases as N_x increases.

As N_x increases, the percent of time spent computing $\mathbf{F_{es}^{NL}}$ for the 2019 formulation becomes negligible compared to the total computation time (Figure D.2D). For the 2019 formulation with the mass matrix, the time spent computing $\mathbf{A_{lin1}} \times \mathbf{v}$ is significantly reduced compared to the 2015 and 2019 formulations (Figure D.2C) due to the increased matrix sparsity. The percent of time spent computing the nonlinear force (Figure D.2D) increases when the mass matrix is included because, although the calculations are identical for both formulations, other operations complete quicker and the total time is less. Using the 2019 formulation with the mass matrix, a single simulation with the baseline mesh (N_x=449) will cover approximately 460 ms per day (Figure D.2B). It should also be noted that these results are for a pure tone simulation; running a two-tone or click simulation, for example, may result in slightly different results although the general trends reported here should still hold true.

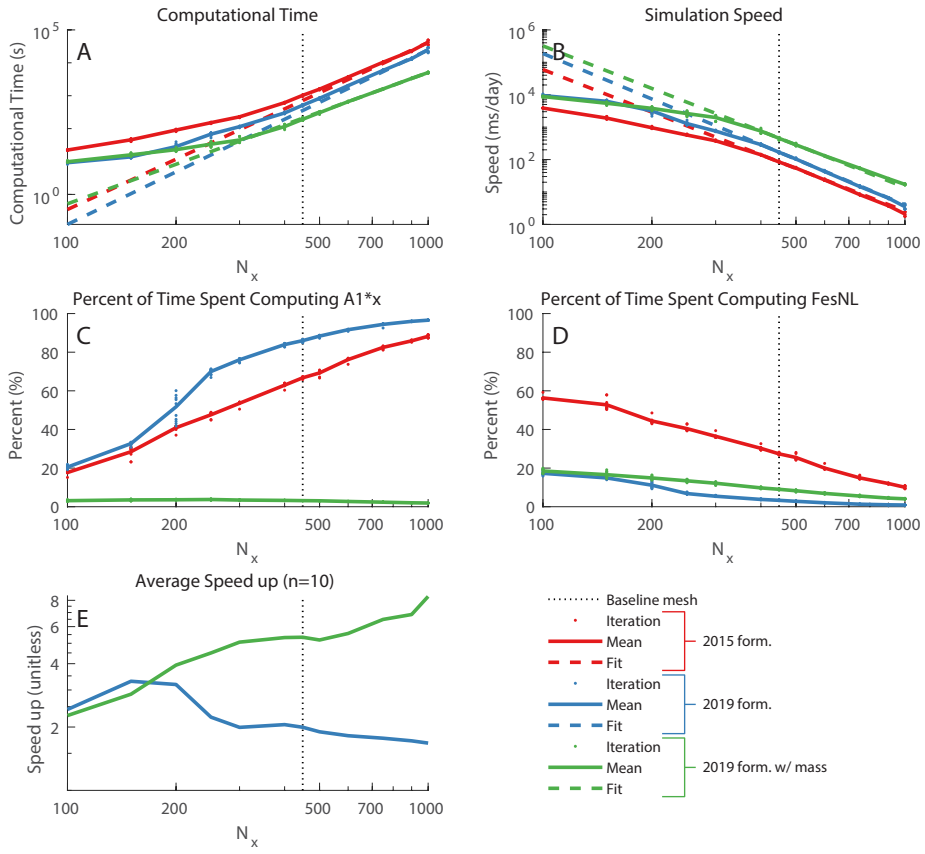

FIGURE D.2. Comparison of code performance for original and improved model formulations. All results are for 1 ms duration time domain simulations with a stimulus at 20 kHz and 100 dB SPL. A total of $n = 10$ iterations were run for each mesh and formulation combination. All simulations were run on the rich133-k35-28-r node on PACE with 20 GB of memory and 12 GB of disk space requested for each simulation. (A) Computational time required for the simulation (does not include matrix assembly or state space formulation). (B) Speed of the simulation (computed by dividing 1 ms by the computational time from (A) to provide an estimate of how much simulation time can be covered in one day. (C and D) The percent of the total computational time spent computing $\mathbf{A_{lin1}} \times \mathbf{v}$ and $\mathbf{F_{es}^{NL}}$, respectively. (E) The average speed up for the improved model formulation calculated by dividing the original computational time by the new computational time. (A and B) The fit curves were computed using a power series fit to the results for $N_x \geq 400$; the fit formulae are listed in Table D.2.

TABLE D.2. Fits for runtime performance from Figure D.2.

Method	**Computational Time (s)**	**Simulation Speed (ms/day)**
2015	$2.43 \times 10^{-11}(N_x)^{5.08}$	$3.21 \times 10^{13}(N_x)^{-4.37}$
2019	$2.99 \times 10^{-12}(N_x)^{5.31}$	$4.02 \times 10^{14}(N_x)^{-4.67}$
2019 with mass matrix	$5.41 \times 10^{-9}(N_x)^{3.99}$	$1.71 \times 10^{14}(N_x)^{-4.36}$

D.4 Methods for solving frequency domain response

In the frequency domain, the FEM matrix equation (Equation 2.51) becomes:

$$\left(-\omega^2 \begin{pmatrix} \mathbf{M_s} & \mathbf{0} & \mathbf{0} \\ \mathbf{M_{sf}} & \mathbf{0} & \mathbf{0} \\ \mathbf{0} & \mathbf{0} & \mathbf{0} \end{pmatrix} + i\omega \begin{pmatrix} \mathbf{C_s} & \mathbf{0} & \mathbf{0} \\ \mathbf{0} & \mathbf{0} & \mathbf{0} \\ \mathbf{C_{es}} & \mathbf{0} & \mathbf{C_e} \end{pmatrix} + \begin{pmatrix} \mathbf{K_s} & \mathbf{K_{fs}} & \mathbf{K_{se}} \\ \mathbf{0} & \mathbf{K_f} & \mathbf{0} \\ \mathbf{K_{es}^{lin}} & \mathbf{0} & \mathbf{K_e} \end{pmatrix} \right) \begin{pmatrix} \mathbf{u} \\ \mathbf{p} \\ \phi \end{pmatrix} = \begin{pmatrix} \mathbf{F_u} \\ \mathbf{0} \\ \mathbf{0} \end{pmatrix} \tag{D.9}$$

The model response in the frequency domain may be obtained by solving one of two equations: either the FEM matrix equation (Equation D.9) or the state space equation (Equation 2.60), where the pressure DOFs have been condensed out. Assembling the FEM matrices in Equation D.9 with the baseline mesh results in large (1 million x 1 million element) very sparse matrices ($< 10^{-3}$ percent dense). Assembling the state space matrices (Equation 2.60) results in a much smaller (4,500 x 4,500 element) but denser (47 percent dense) matrix. This increase in density is due to the M_{eff}^{-1} term in Equation D.4. Increasing the number of fluid modes increases the size of the block matrices in Equation D.9, but does not change the size of the state space matrices. The runtime speed of solving the model response in the frequency domain for these two methods are compared in Figure D.3. For small number of fluid modes ($N_m < 3$), the sparsity of the FEM matrices results in computing the model response quicker than solving with the much denser state space matrix. The computational time required to solve the model response using the FEM equation at a single frequency grows at slightly worse than $O(n)$ as the number of fluid modes increases while the computational time for the state space method is essentially constant. For the baseline mesh (N_m=25), using the state space method is nearly 10x faster than solving the FEM equation. If a 2D fluid model was used (i.e. $N_m = 1$; only the plane wave mode is

included), then solving the FEM equation is approximately 3.6 times faster than solving with the state space method.

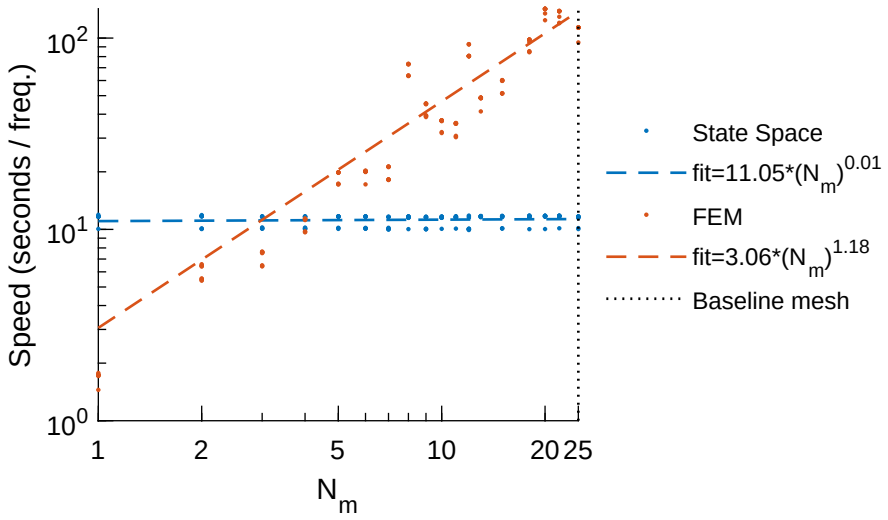

FIGURE D.3. Speed comparison of methods for solving the model in the frequency domain for varied numbers of fluid modes. All results are from linear frequency domain simulations with the response solved for 50 frequencies. A total of $n = 10$ iterations were run for each fluid mode number and solution method. All simulations were run on the rich133-k35-28-r node on PACE with 20 GB of memory and 12 GB of disk space requested for each simulation. The speed was calculated by dividing the total simulation time by the number of frequencies solved in the simulation (50 in this case). The fit curves were computed using a power series.

APPENDIX E

REUSE PERMISSIONS

SPRINGER NATURE LICENSE
TERMS AND CONDITIONS

Jul 10, 2019

This Agreement between Thomas Bowling ("You") and Springer Nature ("Springer Nature") consists of your license details and the terms and conditions provided by Springer Nature and Copyright Clearance Center.

License Number	4625570208511
License date	Jul 10, 2019
Licensed Content Publisher	Springer Nature
Licensed Content Publication	Nature Reviews Neuroscience
Licensed Content Title	The sensory and motor roles of auditory hair cells
Licensed Content Author	Robert Fettiplace et al
Licensed Content Date	Jan 1, 2006
Type of Use	Thesis/Dissertation
Requestor type	academic/university or research institute
Format	print and electronic
Portion	figures/tables/illustrations
Number of figures/tables/illustrations	2
High-res required	no
Will you be translating?	no
Circulation/distribution	<501
Author of this Springer Nature content	no
Title	Computational Modeling of Otoacoustic Emissions
Institution name	Georgia Institute of Technology
Expected presentation date	Aug 2019
Portions	Figures 1 and 2
Requestor Location	Thomas Bowling 771 Ferst Drive ATLANTA, GA 30318 United States Attn: Thomas Bowling
Total	0.00 USD
Terms and Conditions	

Springer Nature Customer Service Centre GmbH
Terms and Conditions

This agreement sets out the terms and conditions of the licence (the **Licence**) between you and **Springer Nature Customer Service Centre GmbH** (the **Licensor**). By clicking

'accept' and completing the transaction for the material (**Licensed Material**), you also confirm your acceptance of these terms and conditions.

1. Grant of License

1. 1. The Licensor grants you a personal, non-exclusive, non-transferable, world-wide licence to reproduce the Licensed Material for the purpose specified in your order only. Licences are granted for the specific use requested in the order and for no other use, subject to the conditions below.

1. 2. The Licensor warrants that it has, to the best of its knowledge, the rights to license reuse of the Licensed Material. However, you should ensure that the material you are requesting is original to the Licensor and does not carry the copyright of another entity (as credited in the published version).

1. 3. If the credit line on any part of the material you have requested indicates that it was reprinted or adapted with permission from another source, then you should also seek permission from that source to reuse the material.

2. Scope of Licence

2. 1. You may only use the Licensed Content in the manner and to the extent permitted by these Ts&Cs and any applicable laws.

2. 2. A separate licence may be required for any additional use of the Licensed Material, e.g. where a licence has been purchased for print only use, separate permission must be obtained for electronic re-use. Similarly, a licence is only valid in the language selected and does not apply for editions in other languages unless additional translation rights have been granted separately in the licence. Any content owned by third parties are expressly excluded from the licence.

2. 3. Similarly, rights for additional components such as custom editions and derivatives require additional permission and may be subject to an additional fee. Please apply to Journalpermissions@springernature.com/bookpermissions@springernature.com for these rights.

2. 4. Where permission has been granted **free of charge** for material in print, permission may also be granted for any electronic version of that work, provided that the material is incidental to your work as a whole and that the electronic version is essentially equivalent to, or substitutes for, the print version.

2. 5. An alternative scope of licence may apply to signatories of the STM Permissions Guidelines, as amended from time to time.

3. Duration of Licence

3. 1. A licence for is valid from the date of purchase ('Licence Date') at the end of the relevant period in the below table:

Scope of Licence	Duration of Licence
Post on a website	12 months
Presentations	12 months
Books and journals	Lifetime of the edition in the language purchased

4. Acknowledgement

4. 1. The Licensor's permission must be acknowledged next to the Licenced Material in print. In electronic form, this acknowledgement must be visible at the same time as the figures/tables/illustrations or abstract, and must be hyperlinked to the journal/book's homepage. Our required acknowledgement format is in the Appendix below.

5. Restrictions on use

5. 1. Use of the Licensed Material may be permitted for incidental promotional use and minor editing privileges e.g. minor adaptations of single figures, changes of format, colour and/or style where the adaptation is credited as set out in Appendix 1 below. Any other changes including but not limited to, cropping, adapting, omitting material that affect the meaning, intention or moral rights of the author are strictly prohibited.

5. 2. You must not use any Licensed Material as part of any design or trademark.

5. 3. Licensed Material may be used in Open Access Publications (OAP) before publication by Springer Nature, but any Licensed Material must be removed from OAP sites prior to final publication.

6. Ownership of Rights

6. 1. Licensed Material remains the property of either Licensor or the relevant third party and any rights not explicitly granted herein are expressly reserved.

7. Warranty

IN NO EVENT SHALL LICENSOR BE LIABLE TO YOU OR ANY OTHER PARTY OR ANY OTHER PERSON OR FOR ANY SPECIAL, CONSEQUENTIAL, INCIDENTAL OR INDIRECT DAMAGES, HOWEVER CAUSED, ARISING OUT OF OR IN CONNECTION WITH THE DOWNLOADING, VIEWING OR USE OF THE MATERIALS REGARDLESS OF THE FORM OF ACTION, WHETHER FOR BREACH OF CONTRACT, BREACH OF WARRANTY, TORT, NEGLIGENCE, INFRINGEMENT OR OTHERWISE (INCLUDING, WITHOUT LIMITATION, DAMAGES BASED ON LOSS OF PROFITS, DATA, FILES, USE, BUSINESS OPPORTUNITY OR CLAIMS OF THIRD PARTIES), AND
WHETHER OR NOT THE PARTY HAS BEEN ADVISED OF THE POSSIBILITY OF SUCH DAMAGES. THIS LIMITATION SHALL APPLY NOTWITHSTANDING ANY FAILURE OF ESSENTIAL PURPOSE OF ANY LIMITED REMEDY PROVIDED HEREIN.

8. Limitations

8. 1. ***BOOKS ONLY:***Where **'reuse in a dissertation/thesis'** has been selected the following terms apply: Print rights of the final author's accepted manuscript (for clarity, NOT the published version) for up to 100 copies, electronic rights for use only on a personal website or institutional repository as defined by the Sherpa guideline (www.sherpa.ac.uk/romeo/).

9. Termination and Cancellation

9. 1. Licences will expire after the period shown in Clause 3 (above).

9. 2. Licensee reserves the right to terminate the Licence in the event that payment is not received in full or if there has been a breach of this agreement by you.

Appendix 1 — Acknowledgements:

For Journal Content:
Reprinted by permission from [**the Licensor**]: [**Journal Publisher** (e.g. Nature/Springer/Palgrave)] [**JOURNAL NAME**] [**REFERENCE CITATION** (Article name, Author(s) Name), [**COPYRIGHT**] (year of publication)

For **Advance Online Publication papers:**
Reprinted by permission from [**the Licensor**]: [**Journal Publisher** (e.g. Nature/Springer/Palgrave)] [**JOURNAL NAME**] [**REFERENCE CITATION** (Article name, Author(s) Name), [**COPYRIGHT**] (year of publication), advance online publication, day month year (doi: 10.1038/sj.[JOURNAL ACRONYM].)

For Adaptations/Translations:
Adapted/Translated by permission from [**the Licensor**]: [**Journal Publisher** (e.g. Nature/Springer/Palgrave)] [**JOURNAL NAME**] [**REFERENCE CITATION** (Article name, Author(s) Name), [**COPYRIGHT**] (year of publication)

Note: For any republication from the British Journal of Cancer, the following credit line style applies:

Reprinted/adapted/translated by permission from [**the Licensor**]: on behalf of Cancer Research UK: : [**Journal Publisher** (e.g. Nature/Springer/Palgrave)] [**JOURNAL NAME**] [**REFERENCE CITATION** (Article name, Author(s) Name), [**COPYRIGHT]** (year of publication)

For **Advance Online Publication** papers:
Reprinted by permission from The [**the Licensor**]: on behalf of Cancer Research UK: [**Journal Publisher** (e.g. Nature/Springer/Palgrave)] [**JOURNAL NAME**] [**REFERENCE CITATION** (Article name, Author(s) Name), [**COPYRIGHT**] (year of publication), advance online publication, day month year (doi: 10.1038/sj.[JOURNAL ACRONYM])

For Book content:
Reprinted/adapted by permission from [**the Licensor**]: [**Book Publisher** (e.g. Palgrave Macmillan, Springer etc) [**Book Title**] by [**Book author**(s)] [**COPYRIGHT**] (year of publication)

Other Conditions:

Version 1.2

Questions? customercare@copyright.com or +1-855-239-3415 (toll free in the US) or +1-978-646-2777.

AIP PUBLISHING LICENSE TERMS AND CONDITIONS

Jul 08, 2019

This Agreement between Thomas Bowling ("You") and AIP Publishing ("AIP Publishing") consists of your license details and the terms and conditions provided by AIP Publishing and Copyright Clearance Center.

License Number	4624261179646
License date	Jul 08, 2019
Licensed Content Publisher	AIP Publishing
Licensed Content Publication	The Journal of the Acoustical Society of America
Licensed Content Title	Evoked otoacoustic emissions arise by two fundamentally different mechanisms: A taxonomy for mammalian OAEs
Licensed Content Author	Christopher A. Shera, John J. Guinan
Licensed Content Date	Feb 1, 1999
Licensed Content Volume	105
Licensed Content Issue	2
Type of Use	Thesis/Dissertation
Requestor type	Student
Format	Print and electronic
Portion	Figure/Table
Number of figures/tables	1
Title of your thesis / dissertation	Computational Modeling of Otoacoustic Emissions
Expected completion date	Aug 2019
Estimated size (number of pages)	1
Requestor Location	Thomas Bowling 771 Ferst Drive ATLANTA, GA 30313 United States Attn: Thomas Bowling
Total	**0.00 USD**

Terms and Conditions

Acoustic Society of America -- Terms and Conditions: Permissions Uses

Acoustic Society of America ("ASA") hereby grants to you the non-exclusive right and license to use and/or distribute the Material according to the use specified in your order, on a one-time basis, for the specified term, with a maximum distribution equal to the number that you have ordered. Any links or other content accompanying the Material are not the subject of this license.

1. You agree to include the following copyright and permission notice with the reproduction of the Material:"Reprinted with permission from [FULL CITATION]. Copyright [PUBLICATION YEAR], Acoustic Society of America." For an article, the copyright and permission notice must be printed on the first page of the article or book chapter. For photographs, covers, or tables, the copyright and permission notice may appear with the Material, in a footnote, or in the reference list.
2. If you have licensed reuse of a figure, photograph, cover, or table, it is your responsibility to ensure that the material is original to ASA and does not contain the copyright of another entity, and that the copyright notice of the figure, photograph, cover, or table does not indicate that it was reprinted by ASA, with permission, from another source. Under no circumstances does ASA, purport or intend to grant permission to reuse material to which it does not hold copyright.

3. You may not alter or modify the Material in any manner. You may translate the Material into another language only if you have licensed translation rights. You may not use the Material for promotional purposes. ASA reserves all rights not specifically granted herein.
4. The foregoing license shall not take effect unless and until ASA or its agent, Copyright Clearance Center, receives the Payment in accordance with Copyright Clearance Center Billing and Payment Terms and Conditions, which are incorporated herein by reference.
5. ASA or the Copyright Clearance Center may, within two business days of granting this license, revoke the license for any reason whatsoever, with a full refund payable to you. Should you violate the terms of this license at any time, ASA, Acoustic Society of America, or Copyright Clearance Center may revoke the license with no refund to you. Notice of such revocation will be made using the contact information provided by you. Failure to receive such notice will not nullify the revocation.
6. ASA makes no representations or warranties with respect to the Material. You agree to indemnify and hold harmless ASA, Acoustic Society of America, and their officers, directors, employees or agents from and against any and all claims arising out of your use of the Material other than as specifically authorized herein.
7. The permission granted herein is personal to you and is not transferable or assignable without the prior written permission of ASA. This license may not be amended except in a writing signed by the party to be charged.
8. If purchase orders, acknowledgments or check endorsements are issued on any forms containing terms and conditions which are inconsistent with these provisions, such inconsistent terms and conditions shall be of no force and effect. This document, including the CCC Billing and Payment Terms and Conditions, shall be the entire agreement between the parties relating to the subject matter hereof.

This Agreement shall be governed by and construed in accordance with the laws of the State of New York. Both parties hereby submit to the jurisdiction of the courts of New York County for purposes of resolving any disputes that may arise hereunder.

Questions? customercare@copyright.com or +1-855-239-3415 (toll free in the US) or +1-978-646-2777.

REFERENCES

[1] L. Chittka and A. Brockmann, "Anatomy of the human ear," 2009. [Online; accessed July 10, 2019].

[2] R. Fettiplace and C. M. Hackney, "The sensory and motor roles of auditory hair cells," *Nature Reviews Neuroscience*, vol. 7, no. 1, pp. 19–29, 2006.

[3] R. Patuzzi, "Cochlear micromechanics and macromechanics," in *The cochlea* (P. Dallos, A. N. Pupper, and R. R. Fay, eds.), pp. 186–257, Springer, 1996.

[4] D. D. Greenwood, "A cochlear frequency-position function for several species - 29 years later," *The Journal of the Acoustical Society of America*, vol. 87, no. 6, pp. 2592–2605, 1990.

[5] N. B. Slepecky, "Structure of the mammalian cochlea," in *The cochlea* (P. Dallos, A. N. Pupper, and R. R. Fay, eds.), pp. 44–129, Springer, 1996.

[6] P. Dallos, "Overview: cochlear neurobiology," in *The cochlea* (P. Dallos, A. N. Pupper, and R. R. Fay, eds.), pp. 1–43, Springer, 1996.

[7] J. Ashmore, P. Avan, W. E. Brownell, P. Dallos, K. Dierkes, R. Fettiplace, K. Grosh, C. M. Hackney, A. J. Hudspeth, F. Jülicher, *et al.*, "The remarkable cochlear amplifier," *Hearing Research*, vol. 266, no. 1, pp. 1–17, 2010.

[8] O. Ropshkow, "Cross section of the cochlea," 2010. [Online; accessed July 12, 2019].

[9] W. E. Brownell, C. R. Bader, D. Bertrand, and Y. de Ribaupierre, "Evoked mechanical responses of isolated cochlear outer hair cells.," *Science*, vol. 227, pp. 194–196, Jan. 1985.

[10] A. Hudspeth, "Making an effort to listen: mechanical amplification in the ear," *Neuron*, vol. 59, no. 4, pp. 530–545, 2008.

[11] G. von Békésy, *Experiments in Hearing*. McGraw-Hill, New York, 1960.

[12] L. Robles and M. A. Ruggero, "Mechanics of the mammalian cochlea," *Physiological reviews*, vol. 81, no. 3, pp. 1305–1352, 2001.

[13] H. Y. Lee, P. D. Raphael, J. Park, A. K. Ellerbee, B. E. Applegate, and J. S. Ogha-

lai, "Noninvasive in vivo imaging reveals differences between tectorial membrane and basilar membrane traveling waves in the mouse cochlea," *Proceedings of the National Academy of Sciences*, vol. 112, no. 10, pp. 3128–3133, 2015.

[14] H. Y. Lee, P. D. Raphael, A. Xia, J. Kim, N. Grillet, B. E. Applegate, A. K. E. Bowden, and J. S. Oghalai, "Two-dimensional cochlear micromechanics measured in vivo demonstrate radial tuning within the mouse organ of Corti," *Journal of Neuroscience*, vol. 36, no. 31, pp. 8160–8173, 2016.

[15] T. Ren, W. He, and D. Kemp, "Reticular lamina and basilar membrane vibrations in living mouse cochleae," *Proceedings of the National Academy of Sciences*, vol. 113, no. 35, pp. 9910–9915, 2016.

[16] N. P. Cooper, A. Vavakou, and M. van der Heijden, "Vibration hotspots reveal longitudinal funneling of sound-evoked motion in the mammalian cochlea," *Nature communications*, vol. 9, no. 1, p. 3054, 2018.

[17] J. B. Dewey, B. E. Applegate, and J. S. Oghalai, "Amplification and suppression of traveling waves along the mouse organ of Corti: evidence for spatial variation in the longitudinal coupling of outer hair cell-generated forces.," *The Journal of Neuroscience*, vol. 39, pp. 1805–1816, Mar. 2019.

[18] D. Kim, S. Neely, C. Molnar, and J. Matthews, "An active cochlear model with negative damping in the partition: comparison with rhode's ante-and post-mortem observations," *Psychophysical, physiological and behavioural studies in hearing*, pp. 7–14, 1980.

[19] S. T. Neely and D. Kim, "A model for active elements in cochlear biomechanics," *The journal of the acoustical society of America*, vol. 79, no. 5, pp. 1472–1480, 1986.

[20] D. T. Kemp, "Otoacoustic emissions: concepts and origins," in *Active processes and otoacoustic emissions in hearing*, pp. 1–38, Springer, 2008.

[21] R. Probst, B. L. Lonsbury-Martin, and G. K. Martin, "A review of otoacoustic emissions," *The Journal of the Acoustical Society of America*, vol. 89, no. 5, pp. 2027–2067, 1991.

[22] C. A. Shera and J. J. Guinan Jr, "Evoked otoacoustic emissions arise by two fundamentally different mechanisms: a taxonomy for mammalian OAEs," *Journal of the Acoustical Society of America*, vol. 105, no. 2, pp. 782–798, 1999.

[23] G. Zweig and C. A. Shera, "The origin of periodicity in the spectrum of evoked otoacoustic emissions," *The Journal of the Acoustical Society of America*, vol. 98, no. 4, pp. 2018–2047, 1995.

[24] B. Lonsbury-Martin, G. Martin, R. Probst, and A. Coats, "Spontaneous otoacoustic emissions in a nonhuman primate. ii. cochlear anatomy," *Hearing research*, vol. 33,

no. 1, pp. 69–93, 1988.

[25] C. A. Shera and J. Guinan, John J., "Mechanisms of mammalian otoacoustic emission," in *Active Processes and Otoacoustic Emissions in Hearing*, Springer, Jan. 2008.

[26] D. Kemp, "Otoacoustic emissions, travelling waves and cochlear mechanisms," *Hearing research*, vol. 22, no. 1, pp. 95–104, 1986.

[27] L. Robles, M. A. Ruggero, and N. C. Rich, "Two-tone distortion in the basilar membrane of the cochlea," *Nature*, vol. 349, no. 6308, p. 413, 1991.

[28] L. Robles, M. A. Ruggero, and N. C. Rich, "Two-tone distortion on the basilar membrane of the chinchilla cochlea," *Journal of neurophysiology*, vol. 77, no. 5, pp. 2385–2399, 1997.

[29] N. Cooper and W. Rhode, "Mechanical responses to two-tone distortion products in the apical and basal turns of the mammalian cochlea," *Journal of neurophysiology*, vol. 78, no. 1, pp. 261–270, 1997.

[30] W. Dong and E. S. Olson, "Two-tone distortion in intracochlear pressure," *The Journal of the Acoustical Society of America*, vol. 117, no. 5, pp. 2999–3015, 2005.

[31] W. Dong and E. S. Olson, "Supporting evidence for reverse cochlear traveling waves," *The Journal of the Acoustical Society of America*, vol. 123, no. 1, pp. 222–240, 2008.

[32] R. Kalluri and C. A. Shera, "Distortion-product source unmixing: a test of the two-mechanism model for DPOAE generation," *Journal of the Acoustical Society of America*, vol. 109, no. 2, pp. 622–637, 2001.

[33] E. Dalhoff, D. Turcanu, H.-P. Zenner, and A. Gummer, "Distortion product otoacoustic emissions measured as vibration on the eardrum of human subjects," *Proceedings of the National Academy of Sciences*, vol. 104, no. 5, pp. 1546–1551, 2007.

[34] D. Kim, "Cochlear mechanics: implications of electrophysiological and acoustical observations," *Hearing research*, vol. 2, no. 3-4, pp. 297–317, 1980.

[35] C. L. Talmadge, A. Tubis, G. R. Long, and P. Piskorski, "Modeling otoacoustic emission and hearing threshold fine structures," *The Journal of the Acoustical Society of America*, vol. 104, no. 3, pp. 1517–1543, 1998.

[36] J. Heitmann, B. Waldmann, and P. Plinkert, "Limitations in the use of distortion product otoacoustic emissions in objective audiometry as the result of fine structure," *European archives of oto-rhino-laryngology*, vol. 253, no. 3, pp. 167–171, 1996.

[37] M. Mauermann and B. Kollmeier, "Distortion product otoacoustic emission (dpoae) input/output functions and the influence of the second dpoae source," *The Journal of the Acoustical Society of America*, vol. 116, no. 4, pp. 2199–2212, 2004.

[38] D. Kemp and A. Brown, "A comparison of mechanical nonlinearities in the cochleae of man and gerbil from ear canal measurements," in *Hearing. Physiological Bases and Psychophysics* (R. Klinke and R. Hartmann, eds.), pp. 82–88, Springer Berlin Heidelberg, 1983.

[39] C. L. Talmadge, G. R. Long, A. Tubis, and S. Dhar, "Experimental confirmation of the two-source interference model for the fine structure of distortion product otoacoustic emissions.," *The Journal of the Acoustical Society of America*, vol. 105, pp. 275–292, Jan. 1999.

[40] A. Vetešník, D. Turcanu, E. Dalhoff, and A. W. Gummer, "Extraction of sources of distortion product otoacoustic emissions by onset-decomposition.," *Hearing research*, vol. 256, pp. 21–38, Oct. 2009.

[41] D. Zelle, A. W. Gummer, and E. Dalhoff, "Extraction of otoacoustic distortion product sources using pulse basis functions.," *The Journal of the Acoustical Society of America*, vol. 134, pp. EL64–EL69, July 2013.

[42] D. Zelle, E. Dalhoff, and A. W. Gummer, "Comparison of time-domain source-separation techniques for short-pulse distortion-product otoacoustic emissions," *The Journal of the Acoustical Society of America*, vol. 142, no. 6, pp. EL544–EL548, 2017.

[43] H. Wen, T. Bowling, and J. Meaud, "Investigation of the 2f1-f2 and 2f2-f1 distortion product otoacoustic emissions using a computational model of the gerbil ear," *Hearing Research*, vol. 365, pp. 127–140, Aug. 2018.

[44] T. Gold, "Hearing ii: The physical basis of the action of the cochlea," *Proceedings of the Royal Society of London Series B – Biological Sciences*, vol. 135, no. 881, pp. 492–498, 1948.

[45] A. J. Hudspeth, F. Jülicher, and P. Martin, "A critique of the critical cochlea: Hopf-a bifurcation–is better than none," *Journal of Neurophysiology*, vol. 104, no. 3, pp. 1219–1229, 2010.

[46] P. M. Zurek, "Spontaneous narrowband acoustic signals emitted by human ears," *The Journal of the Acoustical Society of America*, vol. 69, no. 2, pp. 514–523, 1981.

[47] M. J. Penner and T. Zhang, "Prevalence of spontaneous otoacoustic emissions in adults revisited," *Hearing Research*, vol. 103, pp. 28–34, 1997.

[48] P. van Dijk, B. Maat, and E. de Kleine, "The effect of static ear canal pressure on human spontaneous otoacoustic emissions: spectral width as a measure of the intra-cochlear oscillation amplitude," *Journal of the Association for Research in Otolaryngology*, vol. 12, no. 1, pp. 13–28, 2011.

[49] A. J. Hudspeth, "Hair-bundle mechanics and a model for mechanoelectrical transduction by hair cells.," *Society of General Physiologists series*, vol. 47, p. 357, 1992.

[50] P. Dallos, X. D. Wu, M. A. Cheatham, J. G. Gao, J. Zheng, C. T. Anderson, S. P. Jia, X. Wang, W. H. Y. Cheng, S. Sengupta, D. Z. Z. He, and J. Zuo, "Prestin-based outer hair cell motility is necessary for mammalian cochlear amplification," *Neuron*, vol. 58, no. 3, pp. 333–339, 2008.

[51] F. Nin, T. Reichenbach, J. A. N. Fisher, and A. J. Hudspeth, "Contribution of active hair-bundle motility to nonlinear amplification in the mammalian cochlea," *Proceedings of the National Academy of Sciences*, vol. 109, no. 51, pp. 21076–21080, 2012.

[52] D. Ó. Maoiléidigh and A. J. Hudspeth, "Effects of cochlear loading on the motility of active outer hair cells," *Proceedings of the National Academy of Sciences*, p. 201302911, 2013.

[53] J.-H. Nam and R. Fettiplace, "Optimal electrical properties of outer hair cells ensure cochlear amplification," *PLOS ONE*, vol. 7, p. e50572, 11 2012.

[54] J. Meaud and K. Grosh, "Coupling active hair bundle mechanics, fast adaptation, and somatic motility in a cochlear model," *Biophysical Journal*, vol. 100, no. 11, pp. 2576–2585, 2011.

[55] A. C. Crawford and R. Fettiplace, "The mechanical properties of ciliary bundles of turtle cochlear hair cells," *The Journal of Physiology*, vol. 364, p. 359, 1985.

[56] P. Martin, D. Bozovic, Y. Choe, and A. J. Hudspeth, "Spontaneous oscillation by hair bundles of the bullfrog's sacculus," *Journal of Neuroscience*, vol. 23, no. 11, pp. 4533–4548, 2003.

[57] D. K. Chan and A. J. Hudspeth, "Ca^{2+} current-driven nonlinear amplification by the mammalian cochlea in vitro," *Nature Neuroscience*, vol. 8, no. 2, pp. 149–155, 2005.

[58] H. J. Kennedy, A. C. Crawford, and R. Fettiplace, "Force generation by mammalian hair bundles supports a role in cochlear amplification," *Nature*, vol. 433, no. 7028, pp. 880–883, 2005.

[59] R. Ghaffari, A. J. Aranyosi, and D. M. Freeman, "Longitudinally propagating traveling waves of the mammalian tectorial membrane," *Proceedings of the National Academy of Sciences*, vol. 104, no. 42, pp. 16510–16515, 2007.

[60] J. Meaud and K. Grosh, "The effect of tectorial membrane and basilar membrane longitudinal coupling in cochlear mechanics," *The Journal of the Acoustical Society of America*, vol. 127, no. 3, pp. 1411–1421, 2010.

[61] C. A. Shera, "Mammalian spontaneous otoacoustic emissions are amplitude-stabilized cochlear standing waves," *The Journal of the Acoustical Society of America*, vol. 114, pp. 244–262, July 2003.

[62] A. Vilfan and T. Duke, "Frequency clustering in spontaneous otoacoustic emissions

from a lizard's ear," *Biophysical journal*, vol. 95, no. 10, pp. 4622–4630, 2008.

[63] F. Fruth, F. Jülicher, and B. Lindner, "An active oscillator model describes the statistics of spontaneous otoacoustic emissions," *Biophysical journal*, vol. 107, no. 4, pp. 815–824, 2014.

[64] E. M. Ku, S. J. Elliott, and B. Lineton, "Limit cycle oscillations in a nonlinear state space model of the human cochlea," *The Journal of the Acoustical Society of America*, vol. 126, no. 2, pp. 739–750, 2009.

[65] M. A. Cheatham, R. J. Goodyear, K. Homma, P. K. Legan, J. Korchagina, S. Naskar, J. H. Siegel, P. Dallos, J. Zheng, and G. P. Richardson, "Loss of the tectorial membrane protein CEACAM16 enhances spontaneous, stimulus-frequency, and transiently evoked otoacoustic emissions," *The Journal of Neuroscience*, vol. 34, no. 31, pp. 10325–10338, 2014.

[66] M. A. Cheatham, A. Ahmad, Y. Zhou, R. J. Goodyear, P. Dallos, and G. P. Richardson, "Increased spontaneous otoacoustic emissions in mice with a detached tectorial membrane," *Journal of the Association for Research in Otolaryngology*, vol. 17, no. 2, pp. 81–88, 2016.

[67] M. A. Cheatham, A. Ahmad, P. Dallos, and G. P. Richardson, "*Tecta*$^{Y1870C/+}$ mice with alterations in the structure and porosity of the tectorial membrane display large numbers of spontaneous emissions," *AIP Conference Proceedings*, vol. 1965, no. 1, p. 040001, 2018.

[68] F. R. Lin, J. K. Niparko, and L. Ferrucci, "Hearing loss prevalence in the united states," *Archives of internal medicine*, vol. 171, no. 20, pp. 1851–1853, 2011.

[69] D. L. Blackwell, J. W. Lucas, and T. C. Clarke, "Summary health statistics for US adults: national health interview survey, 2012," *Vital and health statistics. Series 10, Data from the National Health Survey*, no. 260, pp. 1–161, 2014.

[70] E. Daniel, "Noise and hearing loss: a review," *Journal of School Health*, vol. 77, no. 5, pp. 225–231, 2007.

[71] A. F. Ryan, "Protection of auditory receptors and neurons: evidence for interactive damage," *Proceedings of the National Academy of Sciences*, vol. 97, no. 13, pp. 6939–6940, 2000.

[72] T. Janssen and J. Müller, "Otoacoustic emissions as a diagnostic tool in a clinical context," in *Active Processes and Otoacoustic Emissions in Hearing*, pp. 421–460, Springer, 2008.

[73] B. L. Lonsbury-Martin and G. K. Martin, "The clinical utility of distortion-product otoacoustic emissions.," *Ear and hearing*, vol. 11, no. 2, pp. 144–154, 1990.

[74] W. Dong, "Simultaneous intracochlear pressure measurements from two cochlear locations: Propagation of distortion products in gerbil," *Journal of the Association for Research in Otolaryngology*, vol. 18, no. 2, pp. 209–225, 2017.

[75] W. He, D. Kemp, and T. Ren, "Timing of the reticular lamina and basilar membrane vibration in living gerbil cochleae," *eLife*, vol. 7, p. e37625, 2018.

[76] E. Fallah, C. E. Strimbu, and E. S. Olson, "Nonlinearity and amplification in cochlear responses to single and multi-tone stimuli," *Hearing research*, vol. 377, pp. 271–281, 2019.

[77] E. S. Olson, "Direct measurement of intra-cochlear pressure waves," *Nature*, vol. 402, no. 6761, pp. 526–529, 1999.

[78] A. A. Parthasarathi, K. Grosh, and A. L. Nuttall, "Three-dimensional numerical modeling for global cochlear dynamics," *The Journal of the Acoustical Society of America*, vol. 107, no. 1, pp. 474–485, 2000.

[79] S. Ramamoorthy, N. V. Deo, and K. Grosh, "A mechano-electro-acoustical model for the cochlea: response to acoustic stimuli," *The Journal of the Acoustical Society of America*, vol. 121, no. 5, pp. 2758–2773, 2007.

[80] J. Meaud and K. Grosh, "Response to a pure tone in a nonlinear mechanical-electrical-acoustical model of the cochlea," *Biophysical Journal*, vol. 102, no. 6, pp. 1237–1246, 2012.

[81] J. Meaud and K. Grosh, "Effect of the attachment of the tectorial membrane on cochlear micromechanics and two-tone suppression," *Biophysical Journal*, vol. 106, no. 6, pp. 1398–1405, 2014.

[82] J. Meaud and C. Lemons, "Nonlinear response to a click in a time-domain model of the mammalian ear," *The Journal of the Acoustical Society of America*, vol. 138, no. 1, pp. 193–207, 2015.

[83] S. M. Echteler, R. R. Fay, and A. N. Popper, "Structure of the mammalian cochlea," *Comparative Hearing: Mammals*, Jan. 1994.

[84] M. Muller, "The cochlear place-frequency map of the adult and developing mongolian gerbil," *Hearing Research*, vol. 94, no. 1-2, pp. 148–156, 1996.

[85] T. Ren and A. L. Nuttall, "Basilar membrane vibration in the basal turn of the sensitive gerbil cochlea," *Hearing Research*, vol. 151, no. 1, pp. 48–60, 2001.

[86] E. H. Overstreet, A. N. Temchin, and M. A. Ruggero, "Basilar membrane vibrations near the round window of the gerbil cochlea," *JARO-Journal of the Association for Research in Otolaryngology*, vol. 3, no. 3, pp. 351–361, 2002.

[87] S. Ramamoorthy, *Passive and active structural acoustic filtering in cochlear mechanics*

– *analysis and applications*. PhD thesis, University of Michigan, 2004.

[88] S. T. Neely, "Finite difference solution of a two-dimensional mathematical model of the cochlea," *The Journal of the Acoustical Society of America*, vol. 69, no. 5, pp. 1386–1393, 1981.

[89] P. Dallos, "Organ of corti kinematics," *JARO - Journal of the Association for Research in Otolaryngology*, vol. 4, no. 3, pp. 416–421, 2003.

[90] R. Edge, B. Evans, M. Pearce, C.-P. Richter, X. Hu, and P. Dallos, "Morphology of the unfixed cochlea," *Hearing research*, vol. 124, no. 1, pp. 1–16, 1998.

[91] S. S. Rao, *Vibration of continuous systems*. John Wiley & Sons, 2007.

[92] D. Strelioff, "A computer simulation of the generation and distribution of cochlear potentials," *The Journal of the Acoustical Society of America*, vol. 54, no. 3, pp. 620–629, 1973.

[93] P. D. Teal and G. Ni, "Finite element modelling of cochlear electrical coupling," *The Journal of the Acoustical Society of America*, vol. 140, no. 4, pp. 2769–2779, 2016.

[94] T. Bowling and J. Meaud, "Forward and reverse waves: modeling distortion products in the intracochlear fluid pressure," *Biophysical Journal*, vol. 114, no. 3, pp. 747–757, 2018.

[95] T. Bowling, C. Lemons, and J. Meaud, "Reducing tectorial membrane viscoelasticity enhances spontaneous otoacoustic emissions and compromises the detection of low level sound," *Scientific Reports*, vol. 9, no. 1, 2019.

[96] E. S. Olson, "Intracochlear pressure measurements related to cochlear tuning," *The Journal of the Acoustical Society of America*, vol. 110, no. 1, pp. 349–367, 2001.

[97] W. Dong and E. S. Olson, "Middle ear forward and reverse transmission in gerbil," *Journal of Neurophysiology*, vol. 95, no. 5, pp. 2951–2961, 2006.

[98] T. J. R. Hughes, *The Finite Element Method: Linear Static and Dynamic Finite Element Analysis*. Dover, 2000.

[99] S. J. Elliott, E. M. Ku, and B. Lineton, "A state space model for cochlear mechanics," *The Journal of the Acoustical Society of America*, vol. 122, no. 5, pp. 2759–2771, 2007.

[100] C. A. Shera and G. Zweig, "Reflection of retrograde waves within the cochlea and at the stapes," *The Journal of the Acoustical Society of America*, vol. 89, no. 3, pp. 1290–1305, 1991.

[101] S. Puria, "Measurements of human middle ear forward and reverse acoustics: implications for otoacoustic emissions," *The Journal of the Acoustical Society of America*, vol. 113, no. 5, pp. 2773–2789, 2003.

[102] O. de La Rochefoucauld, W. F. Decraemer, S. M. Khanna, and E. S. Olson, "Simultaneous measurements of ossicular velocity and intracochlear pressure leading to the cochlear input impedance in gerbil," *Journal of the Association for Research in Otolaryngology*, vol. 9, pp. 161–177, Jun 2008.

[103] E. H. Overstreet III and M. A. Ruggero, "Development of wide-band middle ear transmission in the Mongolian gerbil," *The Journal of the Acoustical Society of America*, vol. 111, no. 1, pp. 261–270, 2002.

[104] Y.-J. Yoon, S. Puria, and C. R. Steele, "Intracochlear pressure and derived quantities from a three-dimensional model," *The Journal of the Acoustical Society of America*, vol. 122, no. 2, pp. 952–966, 2007.

[105] H. Motallebzadeh, J. A. M. Soons, and S. Puria, "Cochlear amplification and tuning depend on the cellular arrangement within the organ of Corti," *Proceedings of the National Academy of Sciences*, vol. 115, no. 22, pp. 5762–5767, 2018.

[106] W. Dong, A. Xia, P. D. Raphael, S. Puria, B. Applegate, and J. S. Oghalai, "Organ of corti vibration within the intact gerbil cochlea measured by volumetric optical coherence tomography and vibrometry," *Journal of neurophysiology*, vol. 120, no. 6, pp. 2847–2857, 2018.

[107] L. Peterson and B. Bogert, "A dynamical theory of the cochlea," *The Journal of the Acoustical Society of America*, vol. 22, no. 3, pp. 369–381, 1950.

[108] S. S. Kale and E. S. Olson, "Intracochlear scala media pressure measurement: implications for models of cochlear mechanics," *Biophysical journal*, vol. 109, no. 12, pp. 2678–2688, 2015.

[109] C. R. Steele and L. A. Taber, "Comparison of wkb calculations and experimental results for three-dimensional cochlear models," *The Journal of the Acoustical Society of America*, vol. 65, no. 4, pp. 1007–1018, 1979.

[110] Y. Wang, C. R. Steele, and S. Puria, "Cochlear outer-hair-cell power generation and viscous fluid loss," *Scientific reports*, vol. 6, 2016.

[111] C. A. Shera, J. J. Guinan, and A. J. Oxenham, "Revised estimates of human cochlear tuning from otoacoustic and behavioral measurements," *Proceedings of the National Academy of Sciences*, vol. 99, no. 5, pp. 3318–3323, 2002.

[112] D. T. Kemp, "Otoacoustic emissions, their origin in cochlear function, and use," *British medical bulletin*, vol. 63, no. 1, pp. 223–241, 2002.

[113] T. Ren, "Reverse propagation of sound in the gerbil cochlea," *Nature neuroscience*, vol. 7, no. 4, pp. 333–334, 2004.

[114] W. He, A. Fridberger, E. Porsov, K. Grosh, and T. Ren, "Reverse wave propagation

in the cochlea," *Proceedings of the National Academy of Sciences*, vol. 105, no. 7, pp. 2729–2733, 2008.

[115] E. De Boer, C. Kaernbach, P. König, and T. Schillen, "Forward and reverse waves in the one-dimensional model of the cochlea," *Hearing research*, vol. 23, no. 1, pp. 1–7, 1986.

[116] W. He, A. Fridberger, E. Porsov, and T. Ren, "Fast reverse propagation of sound in the living cochlea," *Biophysical journal*, vol. 98, no. 11, pp. 2497–2505, 2010.

[117] C. A. Shera, A. Tubis, and C. L. Talmadge, "Four counter-arguments for slow-wave oaes," *Auditory mechanisms: processes and models. Singapore: World Scientific*, pp. 449–457, 2006.

[118] E. de Boer, "Forward and reverse waves in nonclassical models of the cochlea," *The Journal of the Acoustical Society of America*, vol. 121, no. 5, pp. 2819–2821, 2007.

[119] X. Zhang and D. C. Mountain, "Distortion product emissions: Where do they come from?," in *Concepts and Challenges in the Biophysics of Hearing: Proceedings of 10th International Workshop on the Mechanics of Hearing, edited by Cooper NP, and Kemp DT,(World Scientific Publishing*, pp. 48–54, 2009.

[120] R. Sisto, A. Moleti, T. Botti, D. Bertaccini, and C. A. Shera, "Distortion products and backward-traveling waves in nonlinear active models of the cochlea," *The Journal of the Acoustical Society of America*, vol. 129, no. 5, pp. 3141–3152, 2011.

[121] J. A. Young, S. J. Elliott, and B. Lineton, "Investigating the wave-fixed and place-fixed origins of the 2 f 1-f 2 distortion product otoacoustic emission within a micromechanical cochlear model," *The Journal of the Acoustical Society of America*, vol. 131, no. 6, pp. 4699–4709, 2012.

[122] A. Vetešník and A. W. Gummer, "Transmission of cochlear distortion products as slow waves: A comparison of experimental and model data," *The Journal of the Acoustical Society of America*, vol. 131, no. 5, pp. 3914–3934, 2012.

[123] E. d. Boer, A. L. Nuttall, and C. A. Shera, "Wave propagation patterns in a "classical" three-dimensional model of the cochlea," *The Journal of the Acoustical Society of America*, vol. 121, no. 1, pp. 352–362, 2007.

[124] E. de Boer, J. Zheng, E. Porsov, and A. L. Nuttall, "Inverted direction of wave propagation (IDWP) in the cochlea," *The Journal of the Acoustical Society of America*, vol. 123, no. 3, pp. 1513–1521, 2008.

[125] E. De Boer, "Mechanics of the cochlea: modeling efforts," in *The cochlea* (P. Dallos, A. N. Pupper, and R. R. Fay, eds.), pp. 258–317, Springer, 1996.

[126] E. S. Olson, "Observing middle and inner ear mechanics with novel intracochlear

pressure sensors," *The Journal of the Acoustical Society of America*, vol. 103, no. 6, pp. 3445–3463, 1998.

[127] S. C. Chapra and R. P. Canale, *Numerical methods for engineers*. McGraw Hill, sixth ed., 2010.

[128] J. S. Lamb and R. S. Chadwick, "Dual traveling waves in an inner ear model with two degrees of freedom," *Physical review letters*, vol. 107, no. 8, p. 088101, 2011.

[129] J. Cormack, Y. Liu, J.-H. Nam, and S. M. Gracewski, "Two-compartment passive frequency domain cochlea model allowing independent fluid coupling to the tectorial and basilar membranes," *The Journal of the Acoustical Society of America*, vol. 137, no. 3, pp. 1117–1125, 2015.

[130] Y. Liu, S. M. Gracewski, and J.-H. Nam, "Consequences of location-dependent organ of corti micro-mechanics," *PLOS ONE*, vol. 10, no. 8, p. e0133284, 2015.

[131] G. K. Martin, D. Jassir, B. B. Stagner, M. L. Whitehead, and B. L. Lonsbury-Martin, "Locus of generation for the $2f_1 - f_2$ vs $2f_2 - f_1$ distortion-product otoacoustic emissions in normal-hearing humans revealed by suppression tuning, onset latencies, and amplitude correlations," *The Journal of the Acoustical Society of America*, vol. 103, no. 4, pp. 1957–1971, 1998.

[132] G. K. Martin, B. B. Stagner, and B. L. Lonsbury-Martin, "Time-domain demonstration of distributed distortion-product otoacoustic emission components," *The Journal of the Acoustical Society of America*, vol. 134, no. 1, pp. 342–355, 2013.

[133] P. Avan, B. Büki, and C. Petit, "Auditory distortions: origins and functions," *Physiological Reviews*, vol. 93, no. 4, pp. 1563–1619, 2013.

[134] R. H. Withnell and J. Lodde, "In search of basal distortion product generators.," *Journal of the Acoustical Society of America*, vol. 120, no. 4, pp. 2116–2123, 2006.

[135] G. K. Martin, B. B. Stagner, and B. L. Lonsbury-Martin, "Evidence for basal distortion-product otoacoustic emission components," *Journal of the Acoustical Society of America*, vol. 127, no. 5, pp. 2955–2972, 2010.

[136] P. Martin and A. J. Hudspeth, "Active hair-bundle movements can amplify a hair cell's response to oscillatory mechanical stimuli," *Proceedings of the National Academy of Sciences*, vol. 96, no. 25, pp. 14306–14311, 1999.

[137] M. A. Ruggero, L. Robles, and N. C. Rich, "Two-tone suppression in the basilar membrane of the cochlea: mechanical basis of auditory-nerve rate suppression," *Journal of Neurophysiology*, vol. 68, no. 4, pp. 1087–1099, 1992.

[138] C. Geisler, "Two-tone suppression by a saturating feedback model of the cochlear partition," *Hearing Research*, vol. 63, no. 1–2, pp. 203 – 210, 1992.

[139] G. K. Martin, B. B. Stagner, W. Dong, and B. L. Lonsbury-Martin, "Comparing distortion product otoacoustic emissions to intracochlear distortion products inferred from a noninvasive assay," *Journal of the Association for Research in Otolaryngology*, vol. 17, no. 4, pp. 271–287, 2016.

[140] V. Vencovsky and A. Vetesnik, "Analysis of level dependence of $2f_1 - f_2$ component of otoacoustic emissions using nonlinear 2D cochlear model," *Acta Acustica united with Acustica*, vol. 104, no. 5, pp. 891–894, 2018.

[141] V. Vencovskỳ, D. Zelle, E. Dalhoff, A. W. Gummer, and A. Vetešník, "The influence of distributed source regions in the formation of the nonlinear distortion component of cubic distortion-product otoacoustic emissions," *The Journal of the Acoustical Society of America*, vol. 145, no. 5, pp. 2909–2931, 2019.

[142] I. Russell and M. Kössl, "The voltage responses of hair cells in the basal turn of the guinea-pig cochlea.," *The Journal of physiology*, vol. 435, no. 1, pp. 493–511, 1991.

[143] W. Dong and E. S. Olson, "Detection of cochlear amplification and its activation," *Biophysical Journal*, vol. 105, no. 4, pp. 1067–1078, 2013.

[144] J. J. Zwislocki, "Analysis of cochlear mechanics," *Hearing Research*, vol. 22, pp. 155–169, 1986.

[145] S. L. Johnson, M. Beurg, W. Marcotti, and R. Fettiplace, "Prestin-driven cochlear amplification is not limited by the outer hair cell membrane time constant," *Neuron*, vol. 70, no. 6, pp. 1143–1154, 2011.

[146] K. H. Iwasa and M. Adachi, "Force generation in the outer hair cell of the cochlea," *Biophysical Journal*, vol. 73, no. 1, pp. 546–555, 1997.

[147] W. Dong. Personal communication, May 2019.

[148] G. K. Martin, E. I. Villasuso, B. B. Stagner, and B. L. Lonsbury-Martin, "Suppression and enhancement of distortion-product otoacoustic emissions by interference tones above< i> f</i>< sub> 2</sub>. ii. findings in humans," *Hearing research*, vol. 177, no. 1, pp. 111–122, 2003.

[149] A. Fridberger, J. B. de Monvel, J. Zheng, N. Hu, Y. Zou, T. Ren, and A. Nuttall, "Organ of corti potentials and the motion of the basilar membrane," *Journal of Neuroscience*, vol. 24, no. 45, pp. 10057–10063, 2004.

[150] J. J. Zwislocki, "Symposium on cochlear mechanics - where do we stand after 50 years of research," *The Journal of the Acoustical Society of America*, vol. 67, no. 5, pp. 1679–1679, 1980.

[151] A. W. Gummer, W. Hemmert, and H. P. Zenner, "Resonant tectorial membrane motion in the inner ear: its crucial role in frequency tuning," *Proceedings of the National*

Academy of Sciences, vol. 93, no. 16, pp. 8727–8732, 1996.

[152] N. Gavara, D. Manoussaki, and R. S. Chadwick, "Auditory mechanics of the tectorial membrane and the cochlear spiral," *Current opinion in otolaryngology & head and neck surgery*, vol. 19, no. 5, p. 382, 2011.

[153] D. J. Lim, "Fine morphology of the tectorial membrane: its relationship to the organ of Corti," *Archives of Otolaryngology*, vol. 96, no. 3, pp. 199–215, 1972.

[154] N. Gavara and R. S. Chadwick, "Collagen-based mechanical anisotropy of the tectorial membrane: implications for inter-row coupling of outer hair cell bundles.," *PLOS ONE*, vol. 4, p. e4877, 2009.

[155] P. K. Legan, V. A. Lukashkina, R. J. Goodyear, M. Kossl, I. J. Russell, and G. P. Richardson, "A targeted deletion in alpha-tectorin reveals that the tectorial membrane is required for the gain and timing of cochlear feedback," *Neuron*, vol. 28, no. 1, pp. 273–285, 2000.

[156] A. N. Lukashkin, P. K. Legan, T. D. Weddell, V. A. Lukashkina, R. J. Goodyear, L. J. Welstead, C. Petit, I. J. Russell, and G. P. Richardson, "A mouse model for human deafness DFNB22 reveals that hearing impairment is due to a loss of inner hair cell stimulation," *Proceedings of the National Academy of Sciences*, vol. 109, no. 47, pp. 19351–19356, 2012.

[157] I. J. Russell, P. K. Legan, V. A. Lukashkina, A. N. Lukashkin, R. J. Goodyear, and G. P. Richardson, "Sharpened cochlear tuning in a mouse with a genetically modified tectorial membrane," *Nature Neuroscience*, vol. 10, no. 2, p. 215, 2007.

[158] K. Verhoeven, L. Van Laer, K. Kirschhofer, P. K. Legan, D. C. Hughes, I. Schatteman, M. Verstreken, P. Van Hauwe, P. Coucke, A. Chen, *et al.*, "Mutations in the human α-tectorin gene cause autosomal dominant non-syndromic hearing impairment," *Nature genetics*, vol. 19, no. 1, pp. 60–62, 1998.

[159] J. Zheng, K. K. Miller, T. Yang, M. S. Hildebrand, A. E. Shearer, A. P. DeLuca, T. E. Scheetz, J. Drummond, S. E. Scherer, P. K. Legan, *et al.*, "Carcinoembryonic antigen-related cell adhesion molecule 16 interacts with α-tectorin and is mutated in autosomal dominant hearing loss (DFNA4)," *Proceedings of the National Academy of Sciences*, vol. 108, no. 10, pp. 4218–4223, 2011.

[160] R. Ghaffari, A. J. Aranyosi, G. P. Richardson, and D. M. Freeman, "Tectorial membrane travelling waves underlie abnormal hearing in *tectb* mutant mice," *Nature Communications*, vol. 1, p. 96, 2010.

[161] J. B. Sellon, R. Ghaffari, S. Farrahi, G. P. Richardson, and D. M. Freeman, "Porosity controls spread of excitation in tectorial membrane traveling waves," *Biophysical Journal*, vol. 106, no. 6, pp. 1406–1413, 2014.

[162] G. P. Jones, S. J. Elliott, I. J. Russell, and A. N. Lukashkin, "Modified protein expression in the tectorial membrane of the cochlea reveals roles for the striated sheet matrix," *Biophysical Journal*, vol. 108, no. 1, pp. 203–210, 2015.

[163] P. K. Legan, V. A. Lukashkina, R. J. Goodyear, A. N. Lukashkin, K. Verhoeven, G. Van-Camp, I. J. Russell, and G. P. Richardson, "A deafness mutation isolates a second role for the tectorial membrane in hearing," *Nature Neuroscience*, vol. 8, pp. 1035–1042, August 2005.

[164] B. Epp, J. L. Verhey, and M. Mauermann, "Modeling cochlear dynamics: Interrelation between cochlea mechanics and psychoacoustics," *The Journal of the Acoustical Society of America*, vol. 128, no. 4, pp. 1870–1883, 2010.

[165] J. H. Nam and R. Fettiplace, "Force transmission in the organ of corti micromachine," *Biophysical Journal*, vol. 98, no. 12, pp. 2813 – 2821, 2010.

[166] Y.-J. Yoon, C. R. Steele, and S. Puria, "Feed-forward and feed-backward amplification model from cochlear cytoarchitecture: an interspecies comparison," *Biophysical journal*, vol. 100, no. 1, pp. 1–10, 2011.

[167] C. Lemons, J. B. Sellon, E. Boatti, D. Filizzola, D. M. Freeman, and J. Meaud, "Anisotropic material properties of wild-type and *tectb*$^{-/-}$ tectorial membranes," *Biophysical Journal*, 2019.

[168] G. Jones, V. Lukashkina, I. Russell, S. Elliott, and A. Lukashkin, "Frequency-dependent properties of the tectorial membrane facilitate energy transmission and amplification in the cochlea," *Biophysical Journal*, vol. 104, no. 6, pp. 1357 – 1366, 2013.

[169] K. Ohyama, H. Wada, T. Kobayashi, and T. Takasaka, "Spontaneous otoacoustic emissions in the guinea pig," *Hearing research*, vol. 56, no. 1-2, pp. 111–121, 1991.

[170] R. A. Schmiedt and J. C. Adams, "Stimulated acoustic emissions in the ear canal of the gerbil," *Hearing research*, vol. 5, no. 2-3, pp. 295–305, 1981.

[171] K. Dierkes, B. Lindner, and F. Jülicher, "Enhancement of sensitivity gain and frequency tuning by coupling of active hair bundles," *Proceedings of the National Academy of Sciences*, vol. 105, no. 48, pp. 18669–18674, 2008.

[172] S. J. Elliott, B. Lineton, and G. Ni, "Fluid coupling in a discrete model of cochlear mechanics," *The Journal of the Acoustical Society of America*, vol. 130, no. 3, pp. 1441–1451, 2011.

[173] C.-P. Richter, R. Edge, D. Z. He, and P. Dallos, "Development of the gerbil inner ear observed in the hemicochlea," *JARO-Journal of the Association for Research in Otolaryngology*, vol. 1, no. 3, pp. 195–210, 2000.

[174] C.-P. Richter, G. Emadi, G. Getnick, A. Quesnel, and P. Dallos, "Tectorial membrane

stiffness gradients," *Biophysical Journal*, vol. 93, no. 6, pp. 2265–2276, 2007.

[175] C. Fernández, "Dimensions of the cochlea (guinea pig)," *The Journal of the Acoustical Society of America*, vol. 24, no. 5, pp. 519–523, 1952.

[176] P. Dallos and B. N. Evans, "High-frequency motility of outer hair cells and the cochlear amplifier," *Science*, vol. 267, no. 5206, p. 2006, 1995.

[177] M. Beurg, J. H. Nam, A. Crawford, and R. Fettiplace, "The actions of calcium on hair bundle mechanics in mammalian cochlear hair cells," *Biophysical Journal*, vol. 94, no. 7, pp. 2639–2653, 2008.

[178] B. Sul and K. H. Iwasa, "Effectiveness of hair bundle motility as the cochlear amplifier," *Biophysical Journal.*, vol. 97, no. 10, pp. 2653–2663, 2009.

[179] W. Howard, J. Roberts and A. Hudspeth, "Mechanoelectrical transduction by hair cells," *Annual Review of Biophysics and Biophysical Chemistry*, vol. 17(1), pp. 99–124., 1988.

[180] V. S. Markin and A. J. Hudspeth, "Gating-spring models of mechanoelectrical transduction by hair-cells of the internal ear," *Annual Review Of Biophysics And Biomolecular Structure*, vol. 24, pp. 59–83, 1995.